ABSTRACT

Title of Thesis: **DEVELOPMENT AND TESTING OF A VARIABLE ASPECT RATIO WING USING PNEUMATIC TELESCOPIC SPARS**

Julie E. Blondeau, Masters of Science, 2004

Thesis Directed By: **Professor Darryll Pines**
Department of Aerospace Engineering

The purpose of this thesis is to discuss the design, development and testing of a pneumatic telescopic wing using pneumatic actuators that permit a change in the aspect ratio while simultaneously supporting structural wing loads. The key element of the wing is a pressurized telescopic spar that can undergo large-scale spanwise changes while under loadings in excess of 15 lbs/ft^2. The wing cross-section is maintained by NACA0013 rib sections; telescopic skin sections preserve the span wise airfoil geometry and ensure compact storage and deployment of the telescopic wing. Several iterations led to a full-scale telescopic wing assembly that was tested in the Glenn L. Martin Wind Tunnel at the University of Maryland. These tests included measurements of Lift, Drag, and Lift to Drag ratio at a variety of Reynolds numbers. The telescopic wing was tested in several configurations and experimental results were compared to finite wing theory results. Preliminary aerodynamic results are promising for the variable aspect ratio telescopic wing.

Development and Testing of a Pneumatic Variable Aspect Ratio Wing Using Telescopic Spars

By

Julie E. Blondeau

Thesis submitted to the Faculty of the Graduate School of the
University of Maryland, College Park, in partial fulfillment
of the requirements for the degree of
Master of Science
2004

Advisory Committee:

Associate Professor Darryll Pines, Chair
Associate Professor Alison Flatau
Assistant Professor Christopher Cadou

© Copyright by
Julie E. Blondeau
2004

DEDICATION

I dedicate this work to my parents and my entire family
who never failed to support me in the happiest and hardest times,
and despite the 7000 kms between us…

ACKNOWLEDGEMENTS

I first want to acknowledge my academic advisor, Dr Darryll Pines, for being a such strong support during the last 2 years. Thanks for your academic advice but also for being present at all times and not letting me quit when personal issues made the working difficult. It has been an immense pleasure to work under your direction.
A very big thanks to Bernie for the uncountable hours spent on my project, for his good sense of humor and his precious help in design. Thanks to the Glenn Martin Wind Tunnel team for their help in testing, especially to Les. Thanks to Kevin for his friendship and his patience with my computers….

Very special thanks to my family and close friends. Merci Maman et Papa d'etre toujours prêt de moi et de me soutenir en toutes circonstances. Mon plus grand desir est de vous rendre fiers, j'espere toucher au but après toutes ces annees de labeur! Merci David et Sophie pour etre la, tout simplement. Merci a tous les autres membres de la famille egalement pour votre presence dans ma vie. Merci aussi a mes amis Isabelle, Fanny, Fred, Myriam, Arno et bien d'autres encore, pour me prouver chaque jour que la distance ne tuera pas nos liens.

Merci a Lapin et Yaya pour m'avoir accueillie a mon arrivee aux States. A big thanks to all the students of the Rotorcraft Center, it's been fun to work with you all, and to be in the same boat. I also want to say a very loud "Sorry!!!" to Jaye and Josh for getting "caught" listening to me during classes. Thanks to the old-timers for making

me part of the “lab”, especially to Jayant, Felipe, Ron, Ashish, and Paul of course. I had good times with you all, and I’m sure there will be a lot more partying in the coming years. Good luck to you all.

Paul, I could give you a thousand pages in this section, but that would make my thesis look miserable. So I wilL just say “thank you” fOr your support, for trusting me and making me belieVe in mysElf, for making mY days bright and happy, and fOr making my fUture look blissful.

TABLE OF CONTENTS

Chapter 5: Second Generation Prototype – Development and Testing 76

LIST OF TABLES

LIST OF FIGURES

TABLE OF SYMBOLS

α	Angle of attack, deg
Λ	Sweep angle,deg
c	Chord, ft
b	Wing span, ft
AR	Aspect Ratio
S	Wing Reference Surface Area, ft^2
ρ	Air density, slug/ft^3
V_∞	Wind Velocity, mph or ft/s
L	Lift Force, lb/ft^2
D	Drag Force, lb/ft^2
a	Lift Curve Slope, deg or rad
a_0	Theoretical Lift Curve Slope, deg or rad
C_L	Lift Coefficient
C_D	Drag Coefficient
$C_{D,i}$	Induced Drag Coefficient
$C_{D,0}$	Parasite Drag Coefficient
Re	Reynolds number
M	Mach number
R	Range, miles or km
E	Endurance, hours or minutes

η	Propeller Efficiency
c_f	Nominal fuel consumption, litter/ft
W_0	Gross take-off weight, lbs
W_1	Gross weight, lbs
p	Power, hp
e	Oswald factor
I	Moment of Inertia, in^4
V	Shear Force, lb
M	Bending moment, lb/ft
σ	Flexural Stress, lb/ft^2
m	Mass, lbs
P	Pressure Force, lbs/ft^2
A_p	Piston Area, ft^2
F_b	Friction Force, lbs/ft^2
C_0	Frictional Losses coefficient
e	Oswald factor
Γ	Circulation
Γ_0	Maximum Circulation

Chapter 1: Introduction

1.1. Background and Motivation

In the US over the past 20 years, research on fixed-wing unmanned air vehicles (UAVs) has been spearheaded by DARPA, the Air Force, Navy, and DARO (Defense Airborne Reconnaissance Office).[1] These activities have the goal of achieving a variety of military objectives to aid the "war fighter" in the air, over land, and in the sea. Toward this goal, the Department of Defense (DoD) has fielded numerous vehicle configurations to meet various mission objectives including reconnaissance, surveillance, target acquisition and search and rescue. Figure 1 shows the wingspan and takeoff weights of the best known vehicles. Note that the vehicles span a three-order of magnitude range in wingspan and a six-order of magnitude range in gross-takeoff weight (GTOW).[2]

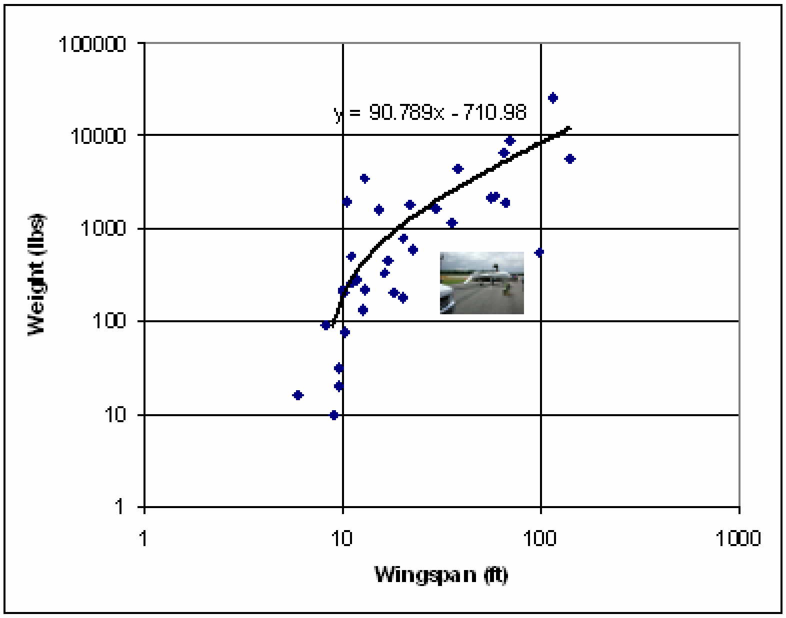

Figure 1: UAV GTOW Weights vs. Wingspan

However, closer inspection of this figure reveals that the majority of fixed-wing aircraft have wingspans in the range between 5 to 30 feet with gross takeoff weights varying from approximately 10 lbs to 2000 lbs. These vehicles are typically designed to achieve a single mission objective such as reconnaissance, surveillance or combat. While many of the current operational platforms have given the “war fighter” an advantage in the military battlefield, the full potential of UAVs is still emerging as evidenced by the success of General Atomic’s Predator in the Afghanistan and Iraq theaters.

New tactical advantages provided by UAVs include situational awareness, standoff weaponry, forward pass targeting, and logistic support. It is anticipated that such autonomous agents will contribute to a new age in war fighting for today’s military.
In the future, vehicles may be required to achieve multiple mission objectives in a single platform. To enable this capability the concept of variable geometry has been proposed as a means to extend the capability of current air vehicle platforms. This requires the development of seamless aerodynamic structures that can undergo large-scale changes in wing geometry. In addition, such vehicles must have adaptive control architectures to maintain robust stability and control capability over an expanded flight regime.

With such a capability, one might envision that vehicles with short wingspans could seamlessly morph into vehicles with longer wingspans to achieve a longer time on station in a military theatre. Figure 2 is a plot on UAV endurance vs. wingspa. It suggests that increasing wingspan tends to increase endurance. As a result, figure 2 also suggests that one could achieve a significant gain in endurance performance, if current UAVs could morph its wing to increase wingspan from 100% to 200%.

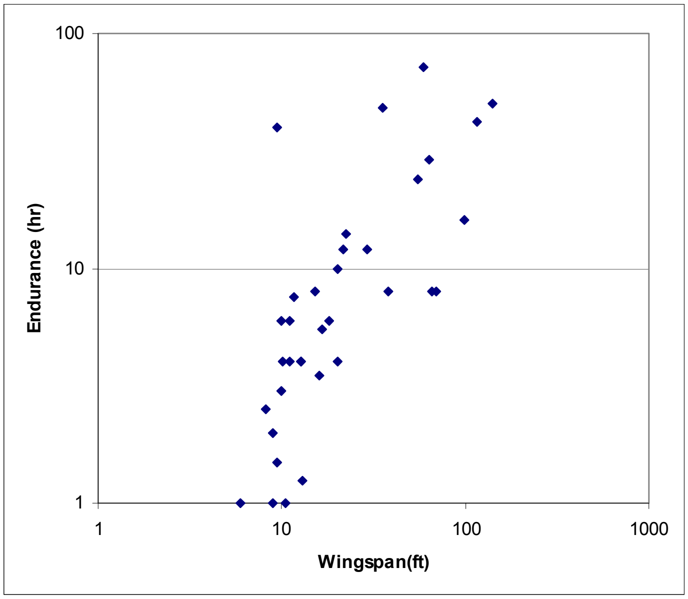

Figure 2: UAV Endurance vs. Wingspan[2]

However, a morphed aircraft wing must be able to sustain a sufficient wing loading as the lift increases at a given altitude, which implies a reinforcement of the structure. This consequently increases the GTOW of the vehicle and is a penalty compared to a conventional aircraft of same dimensions. Hence, the requirement to morph an aircraft's wing must be accomplished with a minimal addition in GTOW while meeting anticipated wing loading requirements as the lift over the airfoil increases. Moreover, the propulsion system of the UAV must also be able to operate efficiently over an expanded flight envelope.

In spite of the apparent complexity of variable geometry aircraft, nature has evolved thousands of flying machines (insects and birds of prey) that perform far more difficult missions routinely. Observations by experimental biologists reveal that birds like falcons are able to loiter on-station in a high aspect ratio configuration using air currents and thermals to circle above until they detect their prey. Upon detection, the bird morphs into a strike configuration to swoop down on unsuspecting prey. This overwhelming superiority of biological fliers over existing fixed-wing UAVs stems from two fundamental factors: the first factor involves an ability to generate seamless aerodynamic lift and maneuverability more efficiently while undergoing shape changes; the second factor involves the ability to store and release energy more efficiently than man-made machines. Thus, bio-mimetic "morphing" flight may offer many advantages over traditional uninhabited air vehicles (MAVs, UAVs, UCAVs, etc). The first advantage would be the capability of a morphing air vehicle to transform itself into multiple geometries, enabling multiple mission objectives with one vehicle. The second advantage of a morphing vehicle would be its aerodynamic efficiency, thanks to its capability to adapt its shape and power precisely to the flight conditions requirements.

In response to the need of such revolutionary aircraft, DARPA solicited in September 2001 innovative research proposals on Morphing Aircraft Structures, and defined a few specific goals: "Examples of specific controlled geometry changes include, but are not limited to, the following: 200% change in aspect ratio, a 50% change in wing area, a 5° change in wing twist, and a 20° change in wing sweep. The effort will culminate with a wind tunnel test of a flight traceable wing."[3]

Along the lines set by DARPA, the Aerospace Department at the University of Maryland initiated in 2002 a three-fold Morphing Aircraft research project including: camber morphing, sweep morphing, and aspect ratio morphing concepts. Variation of camber can be used not only to steer an airplane, but also to improve its flying capabilities at specific times by directly influencing the amount of lift and drag produces on the airfoil. Variation of sweep allows not only for stability control, but also control over Mach number in subsonic flight and over the wave drag in supersonic flight. Finally, variation of aspect ratio affects directly the amount of lift produced on the wing and could provide roll control by means of differential lift.

1.2. Performance Benefit of Morphing Aspect Ratio[4]

Morphing in general is considered to improve the performance or maneuverability of an aircraft. In order to determine which vehicle characteristics should be modified to achieve the desired level of performance, structured design methods such as decomposition of the figure-of-merit matrix can be used. For example, suppose that turn radius is a metric of performance given by:

$$\widehat{R}_t = \frac{V_{true}^2}{g\left(q\frac{C_L}{W/S} + \frac{T}{W}\sin\varepsilon\right)} \qquad (1)$$

In this equation, several parameters can be modified by morphing technologies, such as the wing area S – modified by fowler flaps and telescopic wings, the lift coefficient C_L - modified by leading edge flaps/slats and trailing edge slats, airfoil shape change and the thrust gimbal angle ε. Other typical performance metrics such as range and endurance can be decomposed in a similar fashion in order to identify the morphing technologies' influences. In terms of geometric shape changes, range and endurance are directly driven by the surface area of the wing, through the aspect ratio. As a result, a variation of the wingspan will result in a variation of range and endurance as further described. Mathematically, these performance parameters can be written as[6,7]:

$$R = \frac{\eta}{c_f}\frac{C_L}{C_D}\ln\left(\frac{W_0}{W_1}\right) \tag{2}$$

$$E = \frac{\eta}{c_f}\frac{C_L^{3/2}}{C_D}\sqrt{2\rho_\infty S}\left(\frac{1}{\sqrt{W_1}}-\frac{1}{\sqrt{W_0}}\right) \tag{3}$$

where

$$\left(\frac{C_L}{C_D}\right)_{\max} = \frac{\left(C_{D,0}\,\pi eAR\right)^{1/2}}{2C_{D,0}} \tag{4}$$

$$\left(\frac{C_L^{3/2}}{C_D}\right)_{\max} = \frac{\left(3C_{D,0}\,\pi eAR\right)^{3/4}}{4C_{D,0}} \tag{5}$$

Notice that both range and endurance are strongly dependent on C_L/C_D and $C_L^{3/2}/C_D$ respectively, and each of these ratios is dependent on the wing aspect ratio AR. Thus, an increase in wing aspect ratio results in an increase in both range and endurance. In addition, endurance is further enhanced for a variable aspect ratio wing since the wing surface area also increases with aspect ratio. By tailoring the wing geometry one can adapt the lift and drag characteristics to a variety of missions.

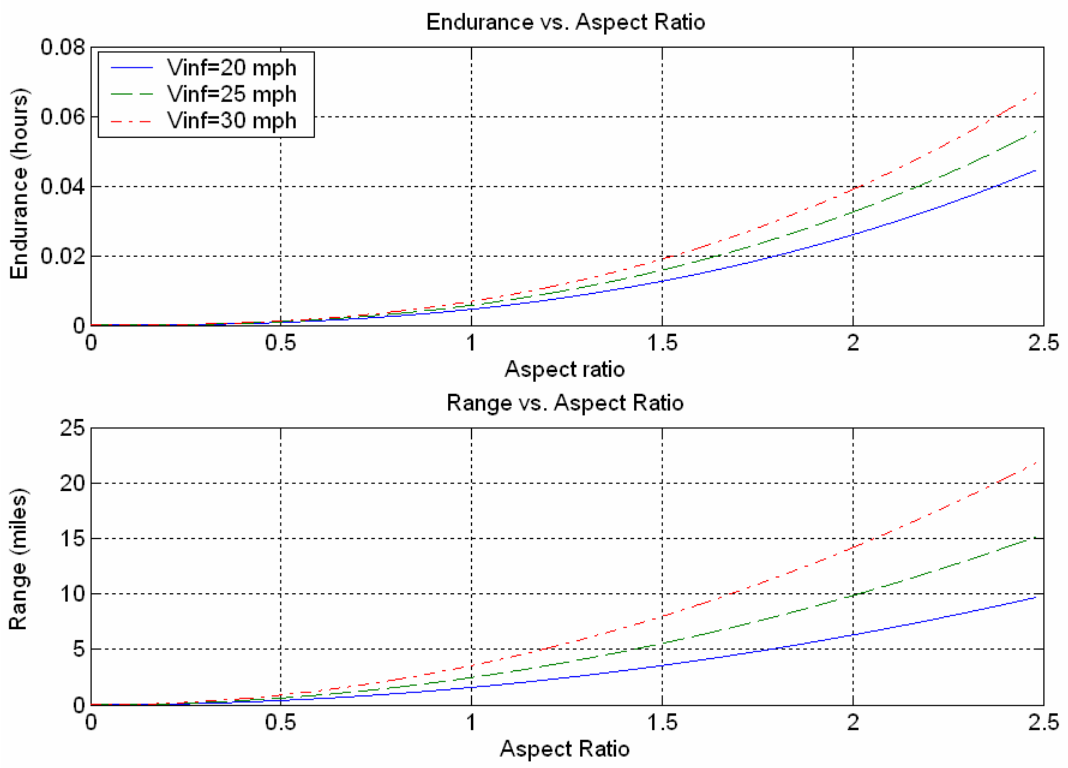

Figure 3: Endurance and Range versus Aspect Ratio for Sample Aircraft

Table 1: Sample Aircraft Characteristics

Propeller efficiency (Zinger 22x12)	$\eta = 0.75$
Specific fuel Consumption (Zenoah 62 cc)	c_f = 3e-7 1/ft
Power at Sea Level (Zenoah 62 cc)	p = 4.75 hp
Aircraft Gross weight (w/ fuel and payload)	W_0 = 60.182 lbs
Normal capacity of fuel	W_f =2.182 lbs
Wing Chord	c = 1 ft
Wing Surface	Rectangular
Airfoil Section	NACA 0012
Parasitic Drag Coefficient[16]	$C_{d,0}$ = 0.0087
Oswald factor	e=0.8
Varying Span	b =2' to 8'

In this work we will be restricting our attention to small UAVs of about 8' to 10' wingspan in fully extended configuration. In order to evaluate the impact of wingspan on endurance and range, we chose a sample aircraft of dimensions and power plant's characteristics, summarized in Table1, similar to those we expect for our aircraft. Figure 3 displays endurance and range versus aspect ratio curves calculated for the chosen sample aircraft. A significant increase in endurance and range can be observed as aspect ratio is increased. For instance, at a cruise speed of 30 mph, the Endurance and Range of Sample Aircraft are almost quadrupled when the Aspect Ratio is increased from 1 to 2.

1.3. Existing work

While the development of variable geometry has primarily been associated with high speed manned fighter aircraft (Tornado, F-111, Mirage, etc.), variable geometry wings with seamless aerodynamic capability would enable a new generation of uninhabited air vehicles with greater mission flexibility. Specifically, telescopic morphing aspect ratio wings have been sporadically designed over the course of the past century. Some were invented as early as 1936 in the form of telescopic wing tips[8] (US Patent 2,056,188), some as recent as 1990[9], and some are presently being designed, the Gevers Aircraft for example[10]. However, there is little evidence that these designs have ever been built, let alone tested. In addition, the telescopic designs previously cited were created for habited flying structures, but none have been documented for use on an uninhabited air vehicle and nearly all-telescopic designs incorporated a lead-screw mechanism to control extension and retraction of the wing elements. Although lead-screw mechanisms have advantageous characteristics, they produce a sizeable increase in the wing's structural weight. This additional weight is detrimental in the aerospace field due to its associated costs. Thus, a pneumatic system is an attractive alternative to achieve morphing. The choice of a pneumatic telescopic wing to achieve morphing on UAV's wing would have numerous advantages over conventional wing technologies including weight, compactness, compliance tailoring, and minimal moving parts. Thus, motivated by the success of recent NASA inflatable Wing Projects[11,12], this research project focuses on the concept of a variable geometry wing with a pneumatic telescopic spar and hollow skin elements.

Chapter 2: Literature Survey

2.1. Introduction

Morphing technologies appeared with the first powered flight vehicles at the beginning of the last century when Wilbur and Orville Wright introduced wing warping on the Wright Flyer. This was the first practical application of a variable camber wing, or morphing technologies. In this case, a series of cables connecting the wing tips to the pilot's pedals allowed the pilot to change the shape of the outer panel of the wing[13] thereby to control and maneuver the aircraft.

This section will present a state of the art for three major types of morphing: variable sweep, variable camber, and variable aspect ratio. The last section will focus on existing morphing technologies applied to UAVs.

2.2. Variable Sweep: Swing Wings

As early as 1924, Max Munk refers to sweep, in a NACA technical note and mentions the effect of a small dihedral on stability[14]. It's only in 1937 that the benefits of sweep at high speeds and the disadvantage at low speeds were demonstrated by Dr Alexander Lippisch, confirming Busemann's theory[15,16]. In 1942, Lippisch built a prototype, the Messerschmitt P-1101, capable of achieving a 40 degree sweep. In 1949, Bell began the X-5 program which was intended to be a new experimental platform for swing wing technology. The X-5 first flew in 1951 with a sweeping mechanism such that the wing was moved forward as it was swept aft. The same year, Grumman implemented swing wing technology on a new high speed aircraft, the XF10F-1. It used a similar sweeping mechanism as the X-5.

The F-111 was the first swing wing aircraft to enter service in the US air Force, but it happened to be penalized by large trim downloads and poor maneuverability at high velocities due to its excessive longitudinal stability.

Since then, all swing wing aircraft have adopted the outboard pivot design, first created at NASA Langley. This design was a breakthrough since it made possible to get the same stall margin in both swept and un-swept configurations, by choosing a proper pivot location. The proper location depended on the wingspan ratio between the two extreme positions[17,18].

The swing-wing concept only is truly useful for aircrafts that fly at a wide range of speeds; therefore it has been used primarily in various military aircraft. The F-111[19] was followed by the F-14 Tomcat and MiG-23 in the 1970s. Despite its clear aerodynamic advantages, variable sweep remains a relatively unusual feature in military aircraft, because of its high cost and weight penalties. Nevertheless, several other swing-wing aircraft have followed, including the Soviet Sukhoi Su-17 (1966), MiG-23 (1967), Tupolev Tu-160 bomber (1981), the US F-14 Tomcat naval fighter (1970), bomber (1974), and the European Panavia Tornado (1974). As of 2004, the F-111 remains in service in Australia's RAAF.

The B-1B and F-14 will be discussed in more detail after a short presentation of the simple sweep theory.

2.2.1. Simple Sweep Theory

Swing-wing aircrafts use a pivoted wing planform in order to combine the advantages of a swept wing at high speeds, while avoiding its weaknesses at lower speeds. According to Simple Sweep Theory[6], wing sweep has two beneficial aerodynamic effects at high speed: it increases the critical Mach number in subsonic flight, and decreases the wave drag in supersonic flight.

Figure 4 illustrates the first effect by comparing the flow across an un-swept wing and a swept wing: only the component of the flow normal to the leading edge (M_n) sees the shape of the wing but the tangent component (M_t) does not contribute to the pressure variation.

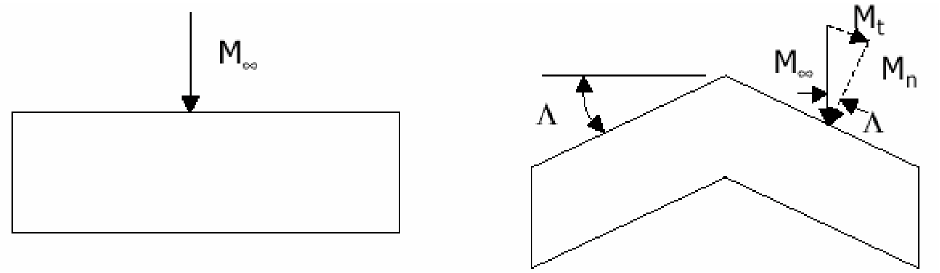

Figure 4: Effect of Sweep on the Mach

The Mach number on the wing is consequently reduced by $\mathrm{Cos}(\Lambda)$, so the critical Mach number for a swept wing is:

$$M_{cr,swept.wing} = \frac{M_{cr,airfoil}}{\mathrm{Cos}(\Lambda)} \tag{6}$$

Figure 5 illustrates the second effect by comparing two cases: If the leading edge is outside the Mach cone, the velocity normal to the leading edge is supersonic therefore every segment of the leading edge produces its own shock wave, resulting in a high wave drag. However, if the leading edge is inside the Mach cone, the velocity is subsonic everywhere along the leading edge; no shocks are formed except at the point of the delta itself. This results in low wave drag. Clearly, sweep is highly advantageous at high speeds.

Sweep also has disadvantages. It generates poor stall behavior and it harms low speed performance such as lift to drag ratio. It also adds large torsional loads.

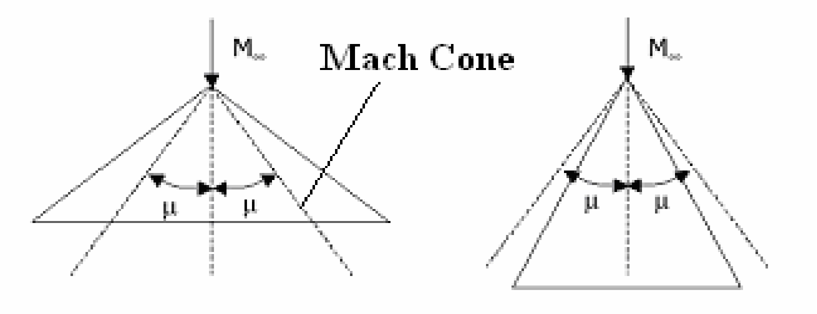

Figure 5: Effect of Sweep on Wave Drag

2.2.2. The B-1B Lancer

The B-1B[20,21] is a multi-role bomber with a variable sweep wing designed to fly intercontinental missions without refueling and to penetrate sophisticated enemy defenses. It is capable of performing a variety of missions, including that of a conventional weapons carrier for theater operations.

Through 1991, the B-1 was dedicated to the nuclear deterrence role as part of the single integrated operational plan. The B-1B has a blended wing and body configuration, and uses variable-geometry design to improve range and speed. They also can enhance survivability: wings are swept at the full-forward position to allow a short takeoff roll and a fast base-escape profile for airfields under attack. Once flying, the wings are swept to maximum cruise distance configuration or high-speed penetration.

Aft wing settings are used in both high subsonic and supersonic flight to enhance the aircraft's maneuverability. The B-1B holds several world records for speed, payload and distance and was recognized by the National Aeronautic Association recognized for completing one of the 10 most memorable record flights for 1994.

As illustrated in figure 6, the B-1B's wingspan varies between 137 feet (41.8 meters) when extended forward and 79 feet (24.1 meters) when swept aft.

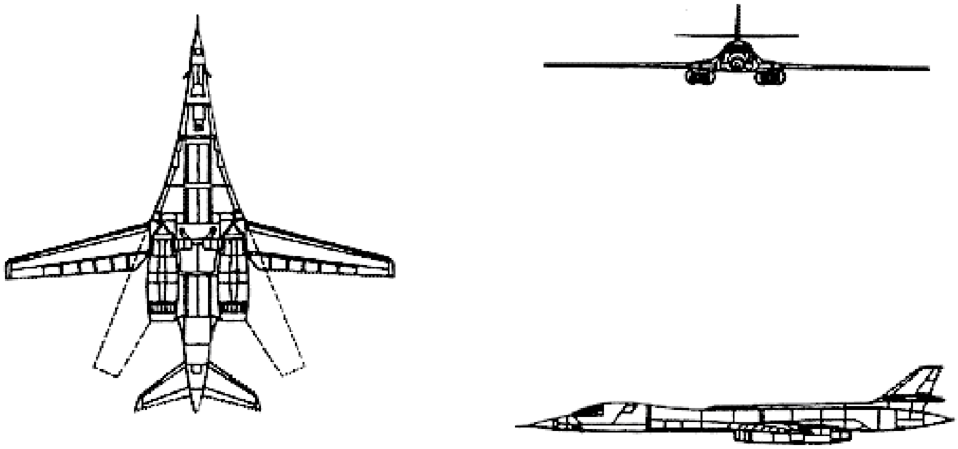

Figure 6: B-1B Lancer

2.2.2. The F-14 Tomcat

The F-14 *Tomcat*[22,23] is a supersonic variable sweep wing fighter designed to attack enemy aircraft at night and in all weather conditions. Its wings are shoulder-mounted and are programmed for automatic sweep during flight, along with a manual override at a sweep speed of 7.5 deg per second. The 22 ft (6.7 m) long wing pivot carry-through crosses the central structure. The normal sweep range of F-14 is 20 to 68 degrees with a 75 degrees "oversweep" position provided for shipboard hangar stowage. For unswept, low-speed combat maneuvering, the outer 2 sections of trailing edge flaps can be deployed at 10 deg and the nearly full-span leading-edge slats are drooped to 8.5 degrees. Finally, at speeds above Mach 1.0, glove vanes in the leading edge of the fixed portion of the wing extend to move the aerodynamic center forward and reduce loads on the tail plane. As illustrated on the next figure, the Tomcat's wingspan varies between 64 feet (19 meters) when unswept and 38 feet (11.4 meters) when swept.

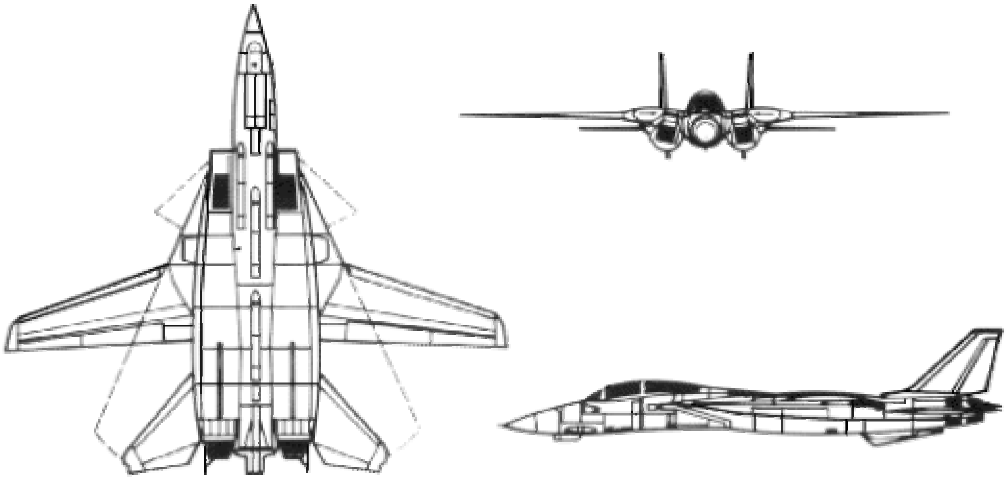

Figure 7: F-14 Tomcat

2.3. Variable Cambered Wings [24,25]

In the history on human flight, the idea of building a variable camber wing is not a new one. For instance, the Wright Brothers in their Wright Flyer used wing warping, a technique that allows the pilot to roll the aircraft by changing the camber of the outboard tip of the wing. In 1920, the Dayton Wright Airplane Company creates the

R. B. Racer, which appears to be one of the first practical applications for a variable cambered wing. A hand crank was manually actuated by the pilot to change the shape of the wing's leading and trailing edge sections. The plane gained more aerodynamic efficiency and speed by flattening the surface once it had taken off.

Among the properties associated with the camber of the airfoil are the chordwise load distribution, the angle of zero-lift, and the pitching coefficient. This explains why variable camber is now a widely used technique. The next sections will present the principal variable camber techniques: high lift devices, adaptive and aeroelastic wings, and inflatable concepts.

2.3.1. High Lift devices

High lift devices[25] appeared for the first time as early as 1914 on the British S.E.4 biplane, not only to steer the airplane, but also to improve its flying capabilities at specific times, particularly during takeoff and landing.

The elevators, rudder, and ailerons are the primary control surfaces on an airplane and allow the pilot to control pitch, yaw and roll respectively. Wing flaps can be extended to increase the wing camber and the angle of attack of the wing. This makes it possible to achieve a steeper descent when landing without increasing airspeed and also allows the airplane get off the ground in a short distance. Flaps increase wing lift but also increases drag. Several types of flaps are shown on figure 8.

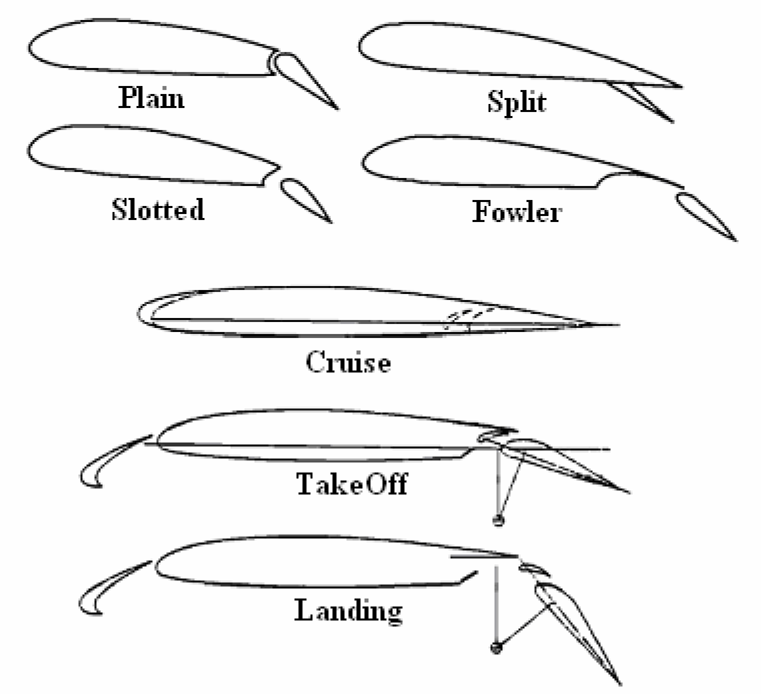

Figure 8: Several Types of Flaps and Typical double-slotted flap/ leading-edge slat high lift system

Slats are protrusions from the leading edge of the wing. They are used to increase the lift of a wing. Figure 8 displays an example of a slat. Note that slats and flaps are used together to maintain laminar flow over the top of the wing, as shown on the following figure.

Figure 9 illustrates the lift coefficient vs. drag coefficient of a three element airfoil. In slow flight conditions where high lift is required, the wing with slats and flaps clearly is the best solution. However, it has a small drag penalty in cruise and it has a relatively small low drag range, which means a narrow economical cruise speed range.

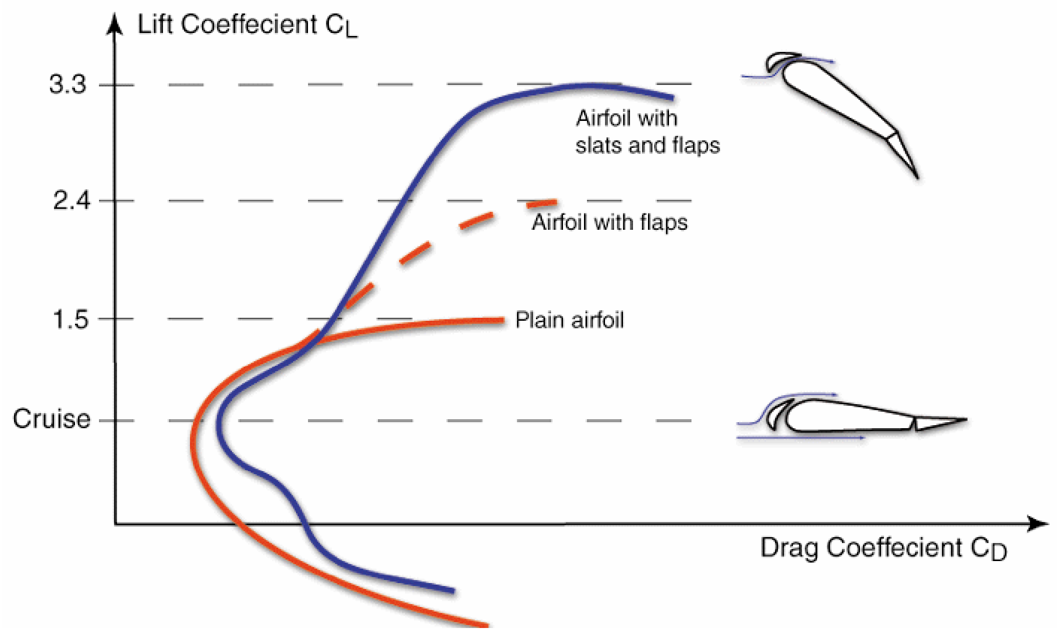

Figure 9: Fixed Leading Edge Slat Lift vs. Drag[26]

Spoilers or airbrakes are control surfaces more commonly found on gliders and jet aircraft, and are used to slow down the aircraft and to reduce lift. They are mounted on either the top or bottom of the center portion of the wings and protrude from the wing surface into the airflow to break the laminar flow over a portion of the wing.

These high-lift devices improve significantly the aerodynamic performance of the aircraft in desired flight conditions. However, they require bulky and reliable actuation devices that add complexity and weight to the aircraft.

2.3.2. Mission Adaptive Wing (MAW - AFTI / F-111)

For a tactical fighter airplane, the wing is typically designed for a relatively narrow range of flight conditions such as a specific Mach number, altitude and load-factor combination, or 1-g cruise. However, the airplane still has to be able to operate over a wide range of flight conditions.

The National Aeronautics and Space Administration (NASA) and the United States Air Force (USAF) joined to conduct a series of flight tests on an advanced fighter technology integration F-111A (AFTI/F-111) aircraft to investigate advanced wing designs. The aircraft was modified with a variable-sweep supercritical mission adaptive wing (MAW). The MAW[26] leading and trailing-edge variable-camber surfaces were deflected once airborne in order to provide a near-ideal wing camber shape for the flight condition.

The MAW features smooth, flexible upper surfaces and fully enclosed lower surfaces. These features distinguish it from conventional flaps that create discontinuous surfaces and exposed or semi-exposed mechanisms.

The MAW allows the leading-edge of the wing to travel from +2 to -21 degrees and the trailing-edge of the wing to travel from +4 to -22 degrees. The sweep angles are similar to those of the conventional F-111 aircraft. Several flight tests were conducted and the MAW design proved to minimize penalties for off-design flight conditions through the combination of smooth skin variable camber and variable sweep.

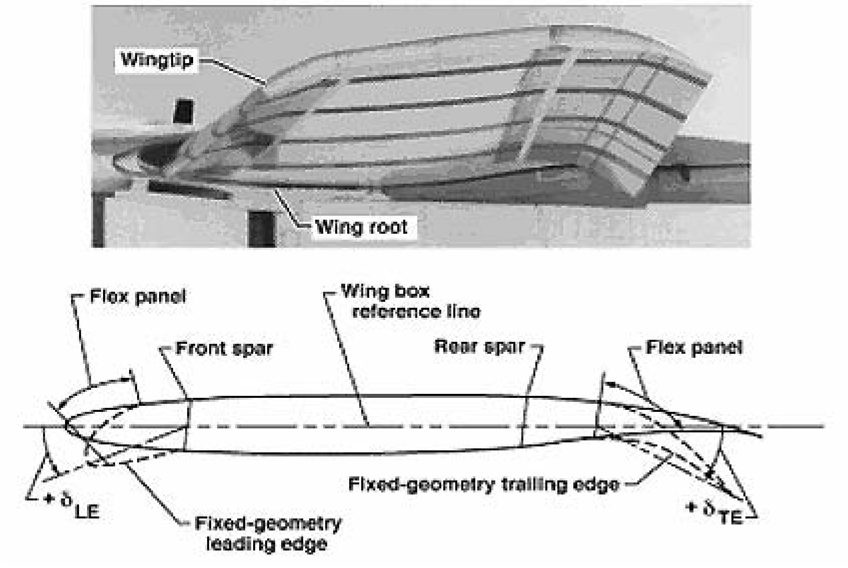

Figure 10: The MAW smooth, variable-camber flap shape

2.3.3 F/A-18A Hornet with Active Aeroelastic Wing

The Active Aeroelastic Wing[27,28] (AAW) concept was introduced in the 1980s by Rockwell International Corporation as a novel way of providing powerful rolling control forces for high performance aircraft. This wing concept has been developed extensively by DARPA, US Air Force, Boeing and NASA for use on the fighter aircraft to solve the aeroelastic control reversal problem.

Active aeroelastic wing (AAW) technology integrates air vehicle aerodynamics, active controls, and structures to maximize air vehicle performance. The idea is to turn the aeroelastic wing flexibility into a net benefit through the use of multiple leading and trailing edge control surfaces, as illustrated on figure 11, which are digitally activated. The energy of the air stream is used to achieve the desired wing twist with very little control surface motion. As a result, the wing creates the needed control forces with outstanding effectiveness. Additionally, AAW control surfaces are used as "tabs" at high dynamic pressures in order to promote wing twist for added control force capability. AAW technology can also be used to minimize drag at low wing strain conditions and/or minimize structural loads at high wing strain conditions. The technology allows designers more freedom to exploit highly efficient, thin, higher aspect ratio aerodynamic wing planforms. A NASA Dryden's F/A-18 wings were recently modified to incorporate the AAW flight hardware for the AAW flight research program. This aircraft was chosen for this project because its pre-production wings were initially too flexible at high speeds. These wings ended up being used for the same trait that they were originally discarded for.

The benefits to future aircraft using AAW technology air vehicles are significant. Besides a substantial increase in control authority through the flight envelope, the AAW wing can reduce aerodynamic drag through programmed optimum control surface deflection. This, in turn, reduces aircraft structural weight because stiffness and hinge moment requirements can be relaxed.

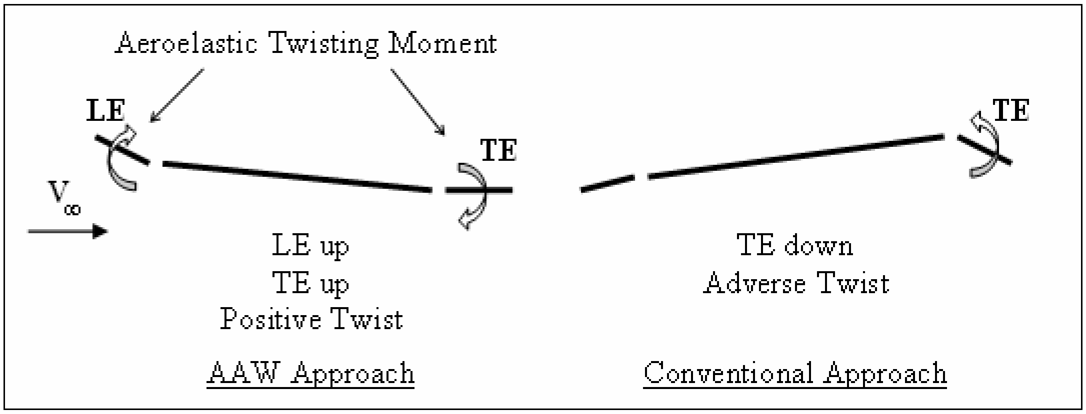

Figure 11: AAW vs. Conventional Control

2.3.4 Inflatable Wings

Inflatable structures are of particular interest to small scale aircrafts since fabrication costs and test range costs are reduced with smaller vehicles, and test flight operations are simplified when the mass of the test vehicle is lowered. In addition, reducing weight also reduces the power needed to fly and control the airfoil. In the 1950's, inflatable aircraft started being designed to carry aerodynamic loads while using low-pressurized airfoil shape. Examples include the Goodyear Inflatoplane and the ML Aviation Utility[30]. In the 1960's, new inflatable designs were using tubular structures. Both segmented wing designs and multiple pressurized spar designs were used to define the airfoil shape and carry the aerodynamic load.

2.3.4.1. Inflatable Wing by NASA Dryden

This NASA Dryden concept[31] relies on pressurized tubular structures to define the airfoil shape and carry the aerodynamic loads. The inflatable aerodynamic wing comprises at least two inflatable cylindrical spars made out of a flexible material, extendible in spanwise direction and butted lengthwise together. This structure provides inflatable support and airfoil cross-section definition to the wing, which is covered by a collapsible fabric skin. The inflatable chambers are rigidly connected together by a rib at the tip of the wing, as illustrated on figure 12.

This structure forms a taut smooth airfoil that can be operated in two configurations: un-inflated or inflated. The structure is compartmentalized to increase the wing strength and minimize air pressure losses. The cylinders can be inflated independently but simplicity favors simultaneous inflation. Check valves are used on each cylinder to prevent a leak in one cylinder from deflating the whole structure. Figure 12 shows that the airfoil cross-section can be tailored by controlling the diameter of the tubular elements: both length and camber of the airfoil can be modified.

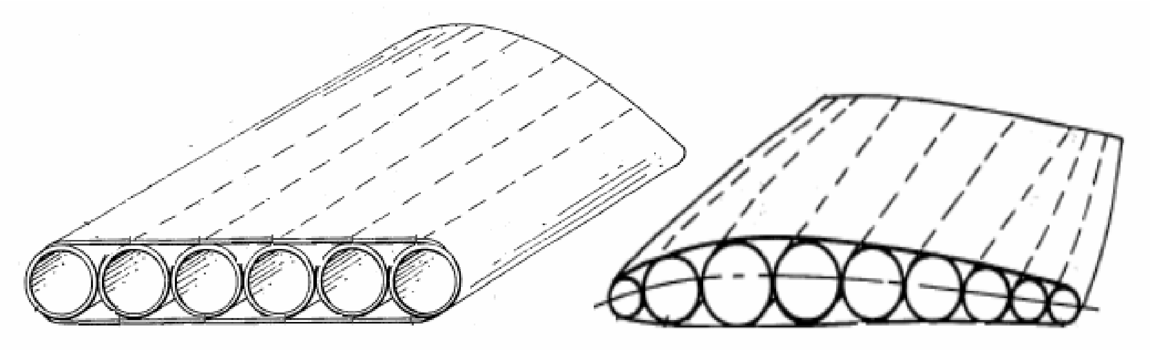

Figure 12: NASA Dryden Inflatable Wing

Possible variations of this concept:

- The inflatable spars, when bonded together, can also have axes of unequal length forming a terminating edge of the structure that is not perpendicular to the means axes. In this case, no rib is used to connect the spars together.
- The inflatable tubular enclosures do not have to be bonded together. In this case, open-cell foam is used between the spars and at the trailing edge to maintain the rigidity of the airfoil surface.
- The wing can be inflated in two ways: pre-inflated if the aircraft is powered, or in-flight inflated if the aircraft is un-powered (dropped in ballistic flight by a carrier aircraft).

Since inflatable structures tend to inflate to a circular geometry, the basic geometry of the cylinders matches the membrane state of stress and yielding a stronger structure, which is less subject to distortion from external forces. It also makes the structure particularly stable with variations in pressure beyond the initial pressurization required for inflation. This is an advantage for aerodynamics surface whose shape is critical. As a result, inflatable aerodynamic structure can provide high structural strength and great stability with minimal risks associated with deflation.

An inflatable wing was tested at the NASA Dryden Flight Research Center and compared to a geometrically similar rigid wing for its trim, aerodynamic performance, longitudinal stability and control characteristics. A tip-rib would rigidly connect all the spars to establish wing torsional stiffness, and open cell-foam was bonded to the spars and to a rib-top nylon outer skin.

The study of the NASA Dryden Inflatable Wing proved that the aerodynamic performance of the inflatable wing is comparable to a rigid wing of the same dimensions.

2.3.4.2. Variable Section configuration airfoil: the semi-rigid aircraft wing.

This concept[32] involves changing the shape of the airfoil cross-section, thus the lift-distribution, to adapt the wing to the mission requirements or to the flight conditions.

The semi-rigid aircraft wing is composed of a rigid spar forming the leading-edge of the wing, a flexible cable forming the trailing edge of the wing, a flexible covering extending between the spar and the cable forming upper and lower wing surfaces, and an inflatable air bag situated within the wing between the two surfaces, which extends along the leading edge.

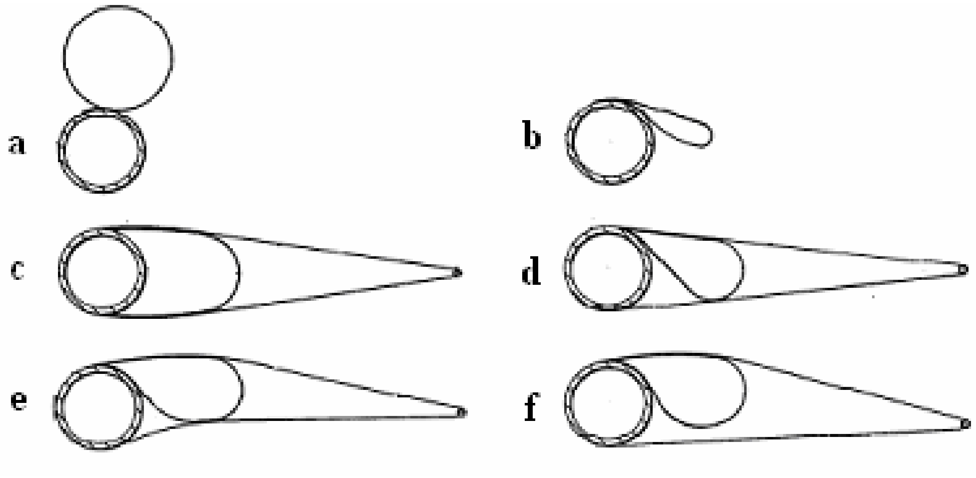

Figure 13: Semi-Rigid Wing

The air bag is attached to the upper surface of the rigid spar and adapted to engage at least one of the surfaces when inflated to cause the wing to take the desired airfoil configuration.

Figure 13 shows the wing section in several configurations:

- Configurations a and b: The air bag attached to the rigid spar in deflated and inflated configuration.
- Configuration c: The air bag encloses the front spar and extends rearwards only through part of the wing chord. It extends chord wise from the rigid

spar, which is enclosed, to the first third or quarter of the chord. This configuration permits to attain the aerodynamics efficiency of symmetric airfoils.

- Configuration d: The air bag in its deflated state in the complete wing, it has no influence on the airfoil shape.
- Configuration e: The air bag is affixed not only to the front spar of the wing but also to the fabric of the underside of the wing, leading to an airfoil of hollow camber suitable for very slow flight
- Configuration f: The air bag is inflated and lifts the upper wing surface into a convex position, creating an unsymmetrical flat-bottom airfoil, which has a high lift capability.

This concept is intended for use on a light airplane and allows short take-off and landing performance by making the airfoil variable in flight.

Experimentation showed that the air bag removes the flutter instability and can safely be used for human transportation[32]. Additionally, it was proved that the pilot could change the lift-to-drag ratio during the flight by varying the pressure of inflation of the air bag. In a low state of inflation the airfoil is suitable for rapid flight; in its fully inflated state the wing is suitable for slow flight.

2.4. Variable Aspect Ratio Wings

The idea of changing the area of the wing - thus the lift repartition along the span - provides a solution to the most classic problem of aircraft design: a large thick chord wing won't go faster after creation of lift without dramatic power increases, and a small thin chord wing will not generate enough lift without greater velocity.

This section reviews several concepts that were found in the literature referring to variable aspect ratio wings.

2.4.1. Varigeowing

This concept[33] involves increasing or decreasing the area of a fixed wing to provide all the benefits of a multiple-size triangular wing. Two fabric airfoils are rolled on a drum and driven in and out on tracks attached to the leading edge that run from fuselage to wingtip (See figures 14 and 15). The foils provide a changeable wing size and the leading edge guides the foils. A continuous drive loop (actuated by a motor) extends and retracts the foils along the tracks.

Figure 14 displays the various possible configurations of the Varigeowing. Takeoff requires more wing area (and more power) than the initial climb, and flight configuration requires the smallest area possible that corresponds to the enrolled airfoils, and leave only the fixed wing clear.

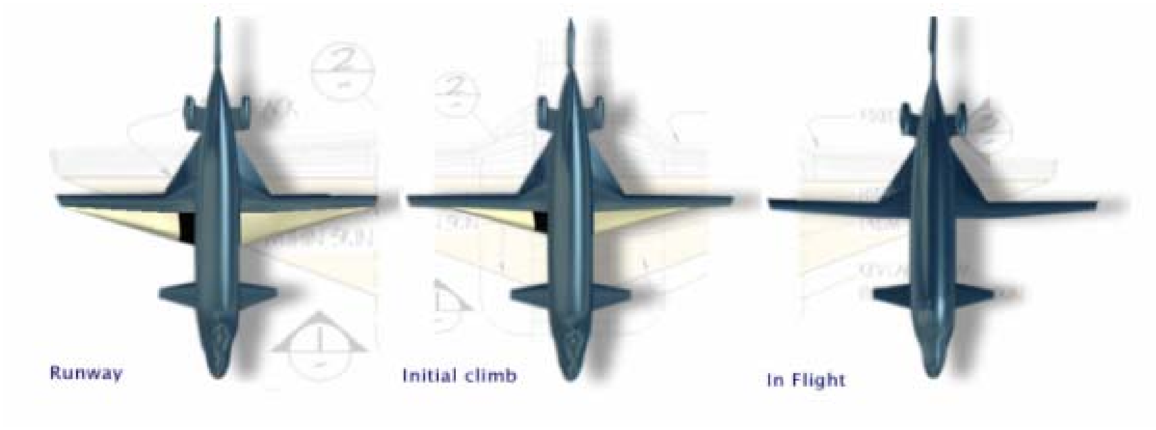

Figure 14: Varigeowing Aircraft in Several Configurations

The technical realization includes a static tube acting as an axle, which an outer tube rotates. A motor rotates the outer tube to extend or retract the foils. The airfoils are made of a Kevlar reinforced Dalron/Nylon material that can be rolled easily and remains taut in flight. The described structure allows increasing or decreasing the area of a fixed wing by a factor of three or more, to adapt (thus decrease) power requirements. The tensile skin can be designed to maximize lift at low speeds, and the fixed wing can be designed for high speeds, minimizing power requirements at cruise.

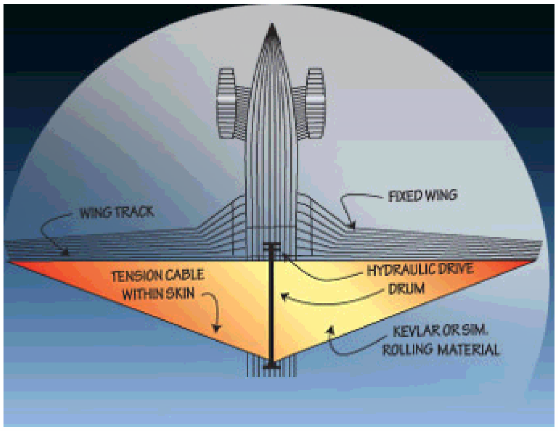

Figure 15: Varigeowing Aircraft Concept

At take off, the skin is fully deployed to maximize lift, and at cruise it is fully retracted, leaving the fixed wing clean. The increased lift of the airfoil allows lower take-off and climb-speeds, reducing takeoff roll by up to 40%, and can facilitate steeper climb and descents. Altitude to distance downrange could also be increased by 50%.

2.4.2. Telescopic Wings

Telescopic wing technologies[34,9] such as Telescopic Wing Tips or Convertible Fixed Wing were proposed as early as the 1940s but there is little evidence that those early designs were ever built, or flown. The only information about those design were found in US Patents, which give manufacturing guidelines and technical drawing but do not refer to any aerodynamic or structural studies or testing.

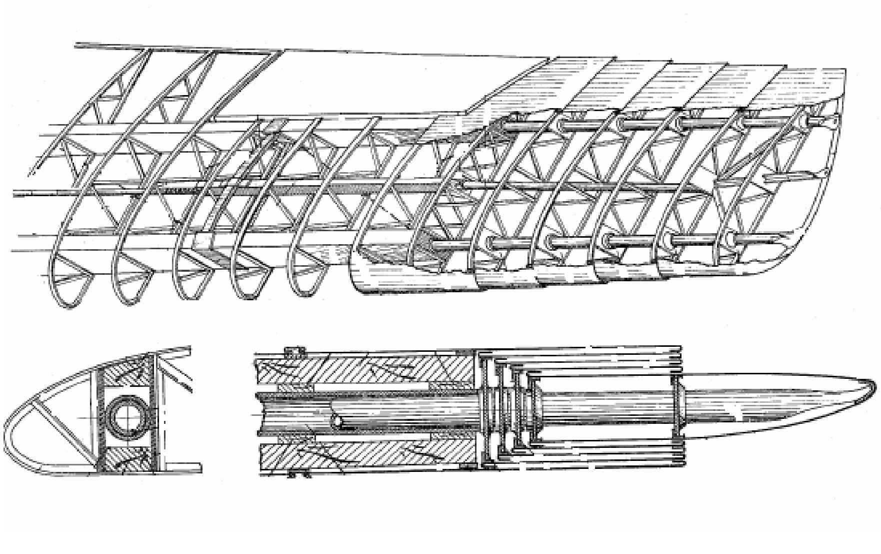

Figure 16: Telescopic Wing Tips[34]

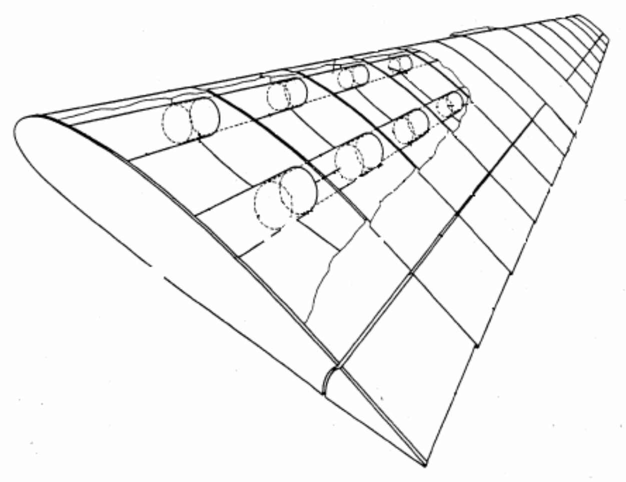

Figure 17: Convertible fixed wing[9]

More recently, in 1997, GEVERS AIRCRAFT, INC. developed a 6-seat 'triphibious' aircraft designed for unprecedented speed, utility, safety, and ruggedness. It uses a telescopic wing to adapt the aircraft geometry to the flight conditions.

The wing is designed for high-speed cruise when retracted and enhanced low speed capabilities when extended. It is composed of a fixed center section and two extendable outer sections, using an overlapping extension spar system. The center section is a high-speed wing (low drag and strong) and the completely retractable high lift section moves in a span-wise direction. It appears that the aircraft actually flew, but no flight test data could be found[10].

Figures 18 and 19 show the Gevers aircraft in fully extended and fully retracted configurations.

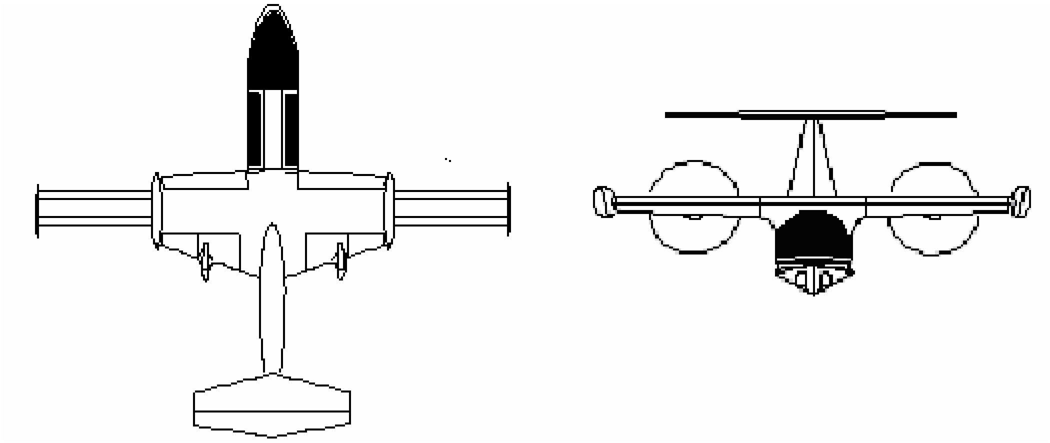

Figure 18: Gevers Aircraft[10]

Figure 19 shows the extension/retraction mechanism as a simple system of cables that prevent asymmetric extension and the extendable spars interlock guided on rollers to drive the span-wise increase. Ailerons are on both the center section and the extendable section and are fully functional at all time during the extension/retraction process.

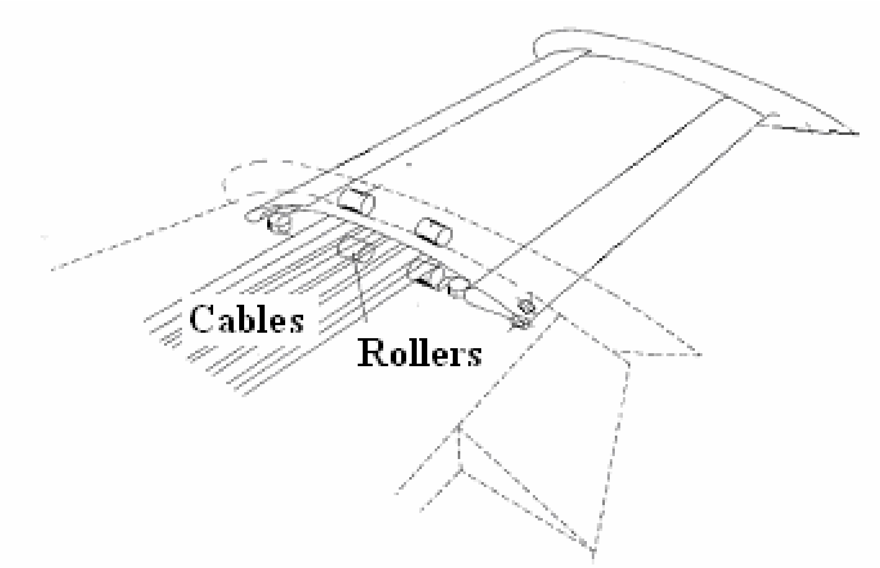

Figure 19: Gevers Aircraft's Telescopic Wing Tip[10]

2.5 Morphing Technologies applied to UAVs

Recent extensive use of Unmanned Aerial Vehicles (UAVs) has led to a need for improved endurance and range capabilities. UAVs are now capable of undertaking missions from a fraction of hour up to 40 hours. The issue is now that these aircrafts have already been optimized for their current mission objectives and are limited by their storage capacity for fuel. An alternative to improve the power systems is to improve the fuel efficiency by adapting the geometry of the vehicle to the flight conditions. Again, morphing seems to be the appropriate solution, and is beginning to be applied in the UAV field. This section presents an example of morphing technologies applied to UAVs.

2.5.1 Inflatable and Rigidizable Wings for UAVs

The Inflatable and Rigidizable Wing[35] developed by ILC is a one-time inflated wing. The idea is to store the aircraft in a very small space and release it airborne. The rigidization process is the action by which the flexible inflatable structure is converted into a rigid composite structure. Once the wing surface is rigidized, the wing no longer relies on pressure to maintain its shape. The rigidization of the structure can be done using thermal-chemical reactions, UV-chemical reactions, and inflation gas-chemical reactions. Maturation of the materials used in inflatable structures such as space suits has led to an improved understanding of high strength fibers and laminates that were used to create the Inflatable and Rigidizable wing. Material with high strength to weight ratio such as Kevlar, Vectran and PBO permit the design of a new generation of inflatable wings that can be stored in volumes tens of times smaller than their deployed volume without damaging their structural integrity. Figure 20 presents the wing in both inflated and packed configuration.

Figure 20: Inflatable UAV Wing (ILC Dover)

This design uses a multi-spar approach in which the wing stiffness is dictated by the internal pressure and the modulus of elasticity of the material. The higher the strength and modulus of the material, the higher the internal pressures the wing can withstand, the stiffer the wing. The wing can be covered with a skin to improve aerodynamics.

The inflation system can be configured from compressed gas, a chemical gas generator, or feed lines from engines and compressors. Advanced technologies in rigidization lead to high stiffness deployable wings, multi-functional structures that are very promising for UAV technologies.

Chapter 3: Conceptual Design

3.1. Introduction

As presented in chapter 1, there is a need to enhance the range and endurance of Unmanned Aerial Vehicles. Previously designed for a unique task, or a limited mission, UAVs can now adapt themselves for various missions. This can be achieved using morphing to alter wing geometry. Changing parameters like camber, wing sweep and aspect ratio are very efficient ways for adapting an aircraft's geometry and power requirements to the flight conditions and the mission requirements. For example, morphing could be used to increase the surface area of the wing is increased when lift requirements are higher, as in take-off, low-speed flight, and landing. This section describes the basics of a morphing aspect ratio wing concept for achieving multiple mission objectives. Such changes have been achieved before, but it is a major concern to accomplish this using seamless designs.

The main objective is to achieve a seamless change in aspect ratio approaching 200% in a controlled manner. This should be accomplished without adding too much weight and complexity to the wing. Additionally, it is important to minimize cost.

3.2. Description of the Concept

The primary elements of the pneumatic telescopic wing include one or several actuator(s) to perform the change in aspect ratio and its control system, a system of structural elements to sustain the aerodynamic loads on the wing, and a type of skin that allows the geometric transformation while maintaining the airfoil shape and permitting the transfer the aerodynamic loads to the structural elements.

Considering the general requirements described above, a basic design was developed for the telescopic morphing aspect ratio wing. It is composed of:

- A pneumatic telescopic spar and an extension/ retraction control mechanism
- Length sensors embedded in the wing
- Ribs fixed at the end of each section of the pneumatic telescopic spar
- Telescopic skin sections
- A source of pressurized gas

Figure 21 presents conceptual design drawings developed using the Ideas software. The telescopic wing is represented in three different stages of extension, with and without the skin.

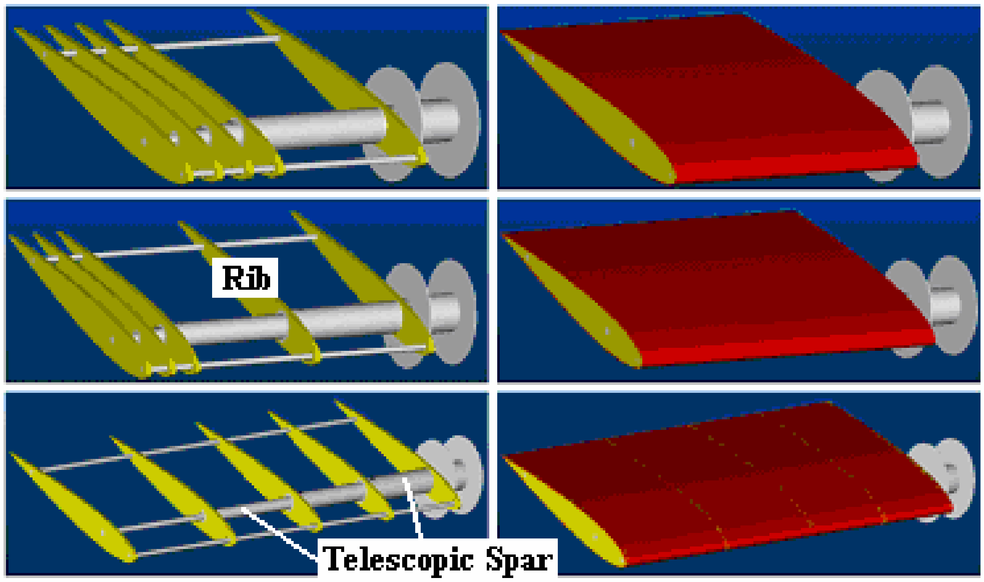

Figure 21: Conceptual Drawings of the Pneumatic Telescopic Wing

The concept and design challenges of each element of the pneumatic telescopic wing are now described below.

3.2.1. The Actuator and Control System

An important challenge is to perform the change in aspect ratio while avoiding the heavy and bulky rack/pinion or cable/pulley systems that were used in previous morphing aspect ratio concepts. The problem with these previous systems is that they add considerable non-structural weight and introduce number of moving parts in the wing, which increases complexity. Using the concept of a pneumatic telescopic spar permits the development of a variety of pneumatic morphing wing designs as it allows large-scale changes in the aspect ratio.

The telescopic spar design consists of concentric circular tubes of decreasing diameter and increasing length, ended by pistons that deploy under pressure to produce various wingspan configurations. The telescopic elements are linked by linear bearings to avoid misalignment when sliding inside each other and sealed so that they can maintain pressure at any position. The sealed pistons, located at the root of each moving element of the spar, provide the necessary surface area for the pressure force to be applied in order to move the free tubes with respect to the outer ones.

Additionally, it was decided that the telescopic spar/actuator will also carry the loads in static case (no motion of the actuator) and dynamic case (extension or retraction of the wing). For this reason, the design of the pneumatic actuator is crucial step in the development of the pneumatic telescopic spar concept.

A control system also needs to be developed. It should not involve moving parts if possible and it should be light-weight and easy to embed into the wing structure. This system should allow a real-time, closed-loop, control of the wing span.

3.2.2. The Ribs

The rib sections should be designed so that it is possible to find data that can be used to predict the aero forces. Accordingly, the NACA 4-digit series were chosen as they are widely recognized and well understood. Furthermore, a symmetrical airfoil is desirable in order to facilitate theoretical predictions as well as manufacturing. It is relatively easy to cut rib sections out of a 0.25” thick aluminum plate using a programmable milling machine.

3.2.2. The Skin

The choice of the wing skin design is a complicated but important part of the pneumatic telescopic wing development. Being structurally stiff (in order to maintain the shape of the airfoil and transfer the aerodynamic loads to the wing structure) at any stage of the wing deployment or retraction creates a design dilemma: as in any flying structure, weight is not desirable, but stiff designs tend to be much bulkier, hence heavier, than softer desins. Two options will be presented. Using hollow shells to create a telescopic skin, which is the most straightforward solution. A more complex solution is to use a soft “foldable” or “rollable” fabric to create the skin. This would allow a larger stroke but would require a rolling and unrolling system or a complex auto-folding skin structure.

3.3. In the next Chapters

The next chapters (chapter 4 and chapter 5) will describe in detail the evolution of the actuator, the ribs and the skin design and sizing, as well as the challenges encountered and the solutions developed to provide a robust and reliable control. Chapter 4 will present the first generation study, in which two conceptual prototypes will be designed and built. The capabilities of both skin options and several sensors and control systems will be demonstrated. Chapter 5 will present the second generation study, which led to the construction and testing of a full-size, controlled, UAV wing prototype.

Chapter 4: First Generation Prototype – Spar and Wing Design

4.1. The Actuator

4.1.1. Design and Manufacturing

The telescopic spar design pictured in figure 22 consists of three concentric circular aluminum tubes of decreasing diameter and increasing length (see Table 2) that deploy under air pressure to produce various wingspan configurations.

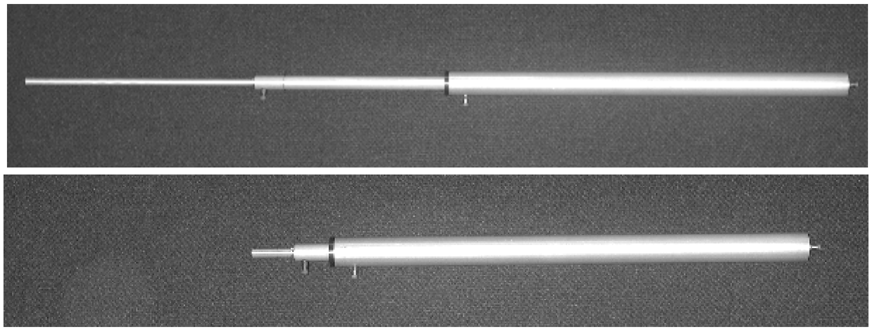

Figure 22: Telescopic Spar in extended/retracted configuration

The three telescopic elements are linked by ceramic linear bearings to avoid misalignment when sliding inside each other. Each of these bearings is equipped with two seals to allow the spar to be hermetic while morphing. Two sealed pistons, located at the root of each moving element of the spar, provide the necessary surface area for the pressure force to be applied in order to move the free tubes with respect to the outer one.

Table 2: Dimensions of Telescopic Spar Elements

	OD (in)	ID (in)	Length (in)
Tube – Large	1.25	1.12	19.7
Tube – Medium	0.75	0.62	11.3
Tube – Small	0.375	0.245	12.5
Bearing – Large	1.12	0.75	1.625
Bearing – Small	0.62	0.375	0.875
Fittings	Thread and Tube OD: 0.125”		
Release Valves	0 to 105 psi @ 12 VDC		
Tubing	OD: 0.125”		

Three cavities exist in between the tubes and are used as pressure chambers. Each of the chambers is pressure fed by an input/output fitting connected to a set of two miniature electronically-operated pneumatic solenoid valves (one for the input, the other one for the output of pressure). See Figure 23.

The extension or retraction of the telescopic spar can be completely controlled by changing the pressure in the chambers by opening certain release valves independently. This is carried out by a feedback loop given by two length sensors that are fixed at the tip of each moving element of the spar. An input of pressure in chamber “1” when opening the release valve of the chamber “2” and/or chamber “3” deploys the middle and/or the small element of the telescopic tube (see Figure 24).

Conversely, an input of pressure in the chamber “2” and/or chamber “3” when opening the release valve of the chamber “1” retracts the middle and/or small elements of the telescopic spar (see Figure 25).

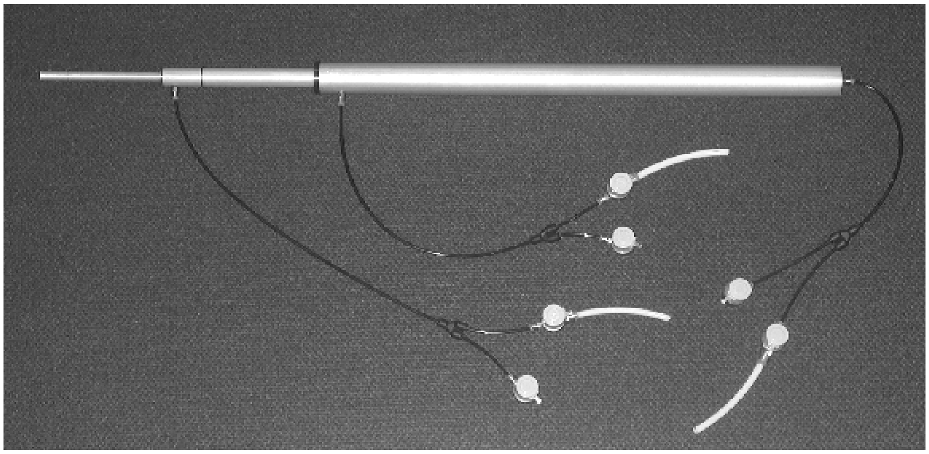

Figure 23: Telescopic spar and input/ output control valves

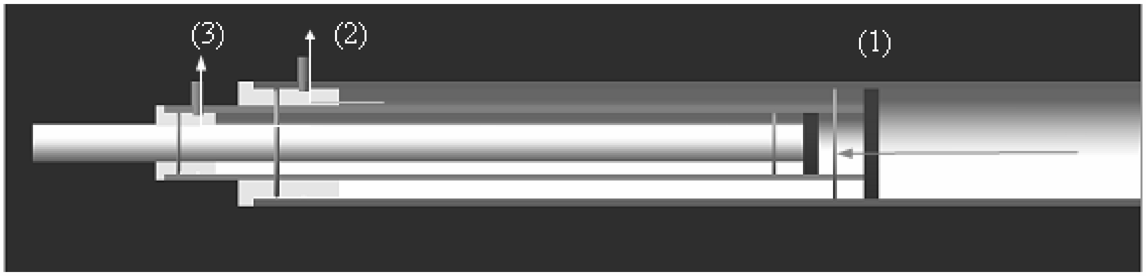

Figure 24: Pressure Scheme for Spar Deployment

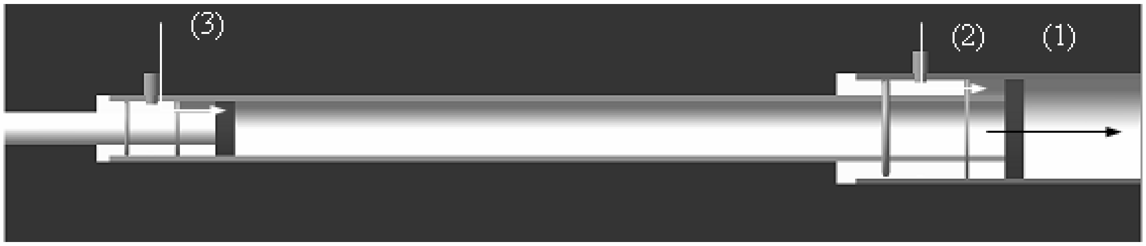

Figure 25: Pressure Scheme for Spar Retraction

Manufacturing of the Pneumatic Telescopic Spar

The pneumatic telescopic spar elements are seamless tubes constructed from aluminum alloy 6061-T6. Aluminum was chosen for its lightweight, strength and corrosion resistance characteristics. The tubes were cut, polished and machined before being anodized. Anodizing gives the tube surfaces a very low friction property that is important at the contact location (inside the bearings and on the lateral surface of the pistons). The contact-surface of the bearings is covered with a Frelon layer to reduce friction. The outside shell of the linear bearings is made out of aluminum 6061-T6 for the same physical characteristics noted earlier and for ease of machining. This outside shell is cut at the inside dimensions of the tube with a very low clearance and each of the bearings is provided with a spring-loaded Teflon seal at both end. Figure 26 shows some details of the bearings after machining, mounted on the tubes.

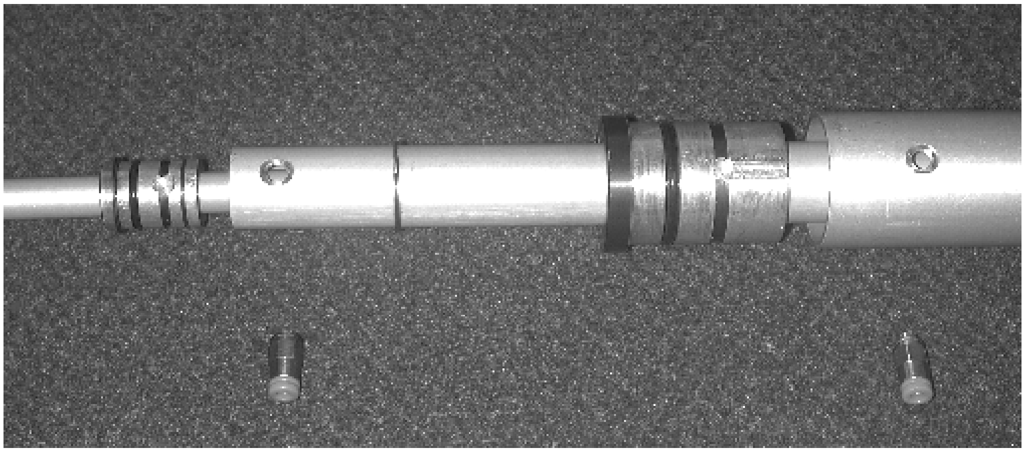

Figure 26: Details of linear bearings

Low-friction, chemical-resistant and highly reliable Teflon is combined with a stainless steel canted-coil spring to create a seal that adjusts to wear, dimension and temperature changes, and mechanical inconsistencies and provides a near-constant spring force that greatly enhances sealing efficiency. The instant (push-to-connect) fittings seal on the outside of the tubing for a quick connection and are easy to replace. The fitting threads are nickel-plated brass with a Teflon sealant for increased strength and impact resistance.

An important part of the design is the choice of the length sensors. It has been decided to use sets of racks and pinions mounted on potentiometers. The main advantage of this sensor is that it is perfectly linear and its output signal can be used directly for the feedback without treatment. Moreover, it is an inexpensive. The potentiometer/pinion assembly is fixed directly on the outside of the telescopic elements. The materials and parts were chosen or designed to be easily removable or replaceable without damaging the assembly.

4.1.2. Structural Study

The tubes and linear bearings that comprise the telescopic spar are made of the same aluminum alloy 6061-T6 and are fit closely enough to consider the spar as a single element. Therefore, it can be modeled as a stepped beam by reproducing the dimensions of the tubes and bearings. To define the structural performance of the spar, the fully deployed case was studied. The moment of inertia was calculated as a function of the axial location by measuring the length and thicknesses of the different tubes and bearings.

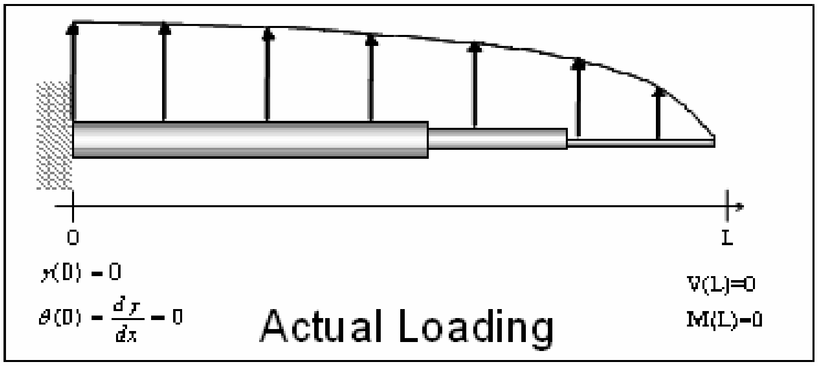

Figure 27: Elliptical Loading on the Spar

The distribution of bending moment has been derived by assuming various loading distribution amplitudes and profiles (tip force, uniform loading, or elliptical loading – see figure 27) using the following relations[36]:

$$\frac{dV}{dx} = -\omega \tag{7}$$

and

$$\frac{dM}{dx} = V \tag{8}$$

where ω is the distributed load, V is the shear force and M is the bending moment. The normal stress distribution (flexural stress) can then be calculated using the following relation:

$$\sigma = \frac{M(x)y(x)}{I(x)} \tag{9}$$

where y(x) is the distance from the center line and I(x) is the area moment of inertia at location x. The stress in the telescopic spar was compared to the maximum yield stress of the material at every location along the wingspan. Figure 28 shows that in the case of a uniform loading or a quadratic loading (the latter being a closer representation of an actual lift distribution along the wing), the structure can withstand up to 30 lbs/ft^2 for a 13" chord airfoil, which is approximately twice the typical loading for a UAVs. Plotting the maximum stress distribution and the maximum yield strength of the material together for a given loading distribution is useful for identifying the failure point(s). Figure 29 displays the stress along the spar for a uniform loading of 35lbs/ft^2. For this given loading condition, it can be seen on the maximum stress profile that failure occurs at the root of the smallest telescopic element. The maximum allowable wing loading is 32lbs/ft^2.

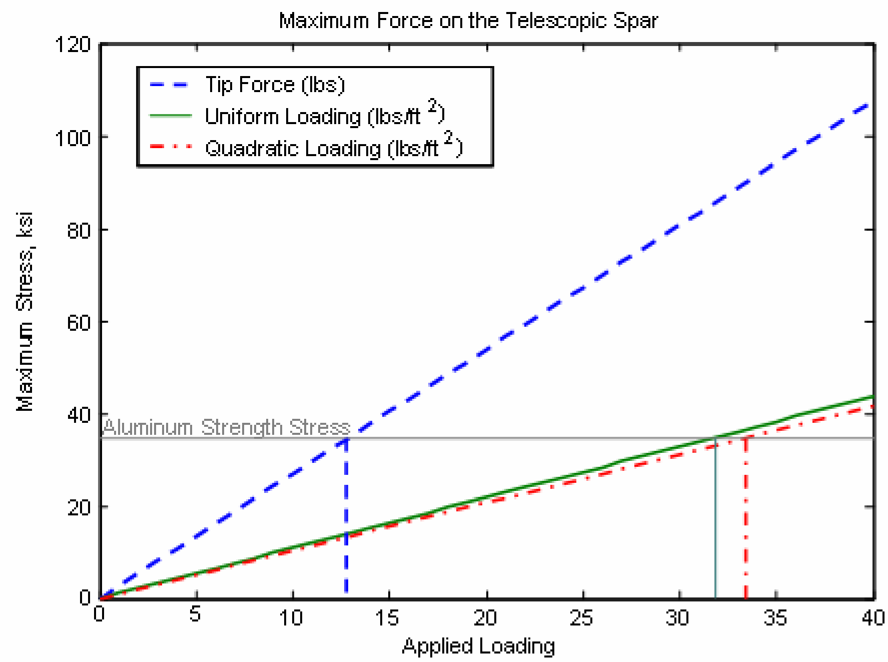

Figure 28: Maximum Force vs. Loading

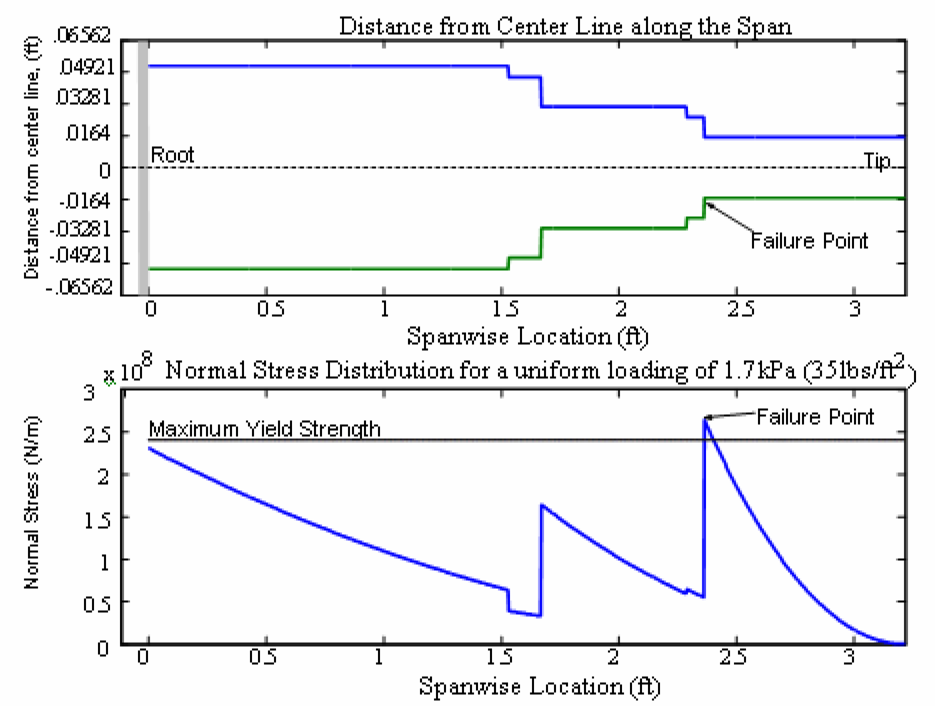

Figure 29: Distribution of Normal Stress under uniform Loading

4.1.3. Dynamic Deployment Model

Experiments have shown that the full-scale telescopic spar can be smoothly deployed and retracted using input pressures of 50 - 90 psi. A dynamic study was done to prove these results theoretically.

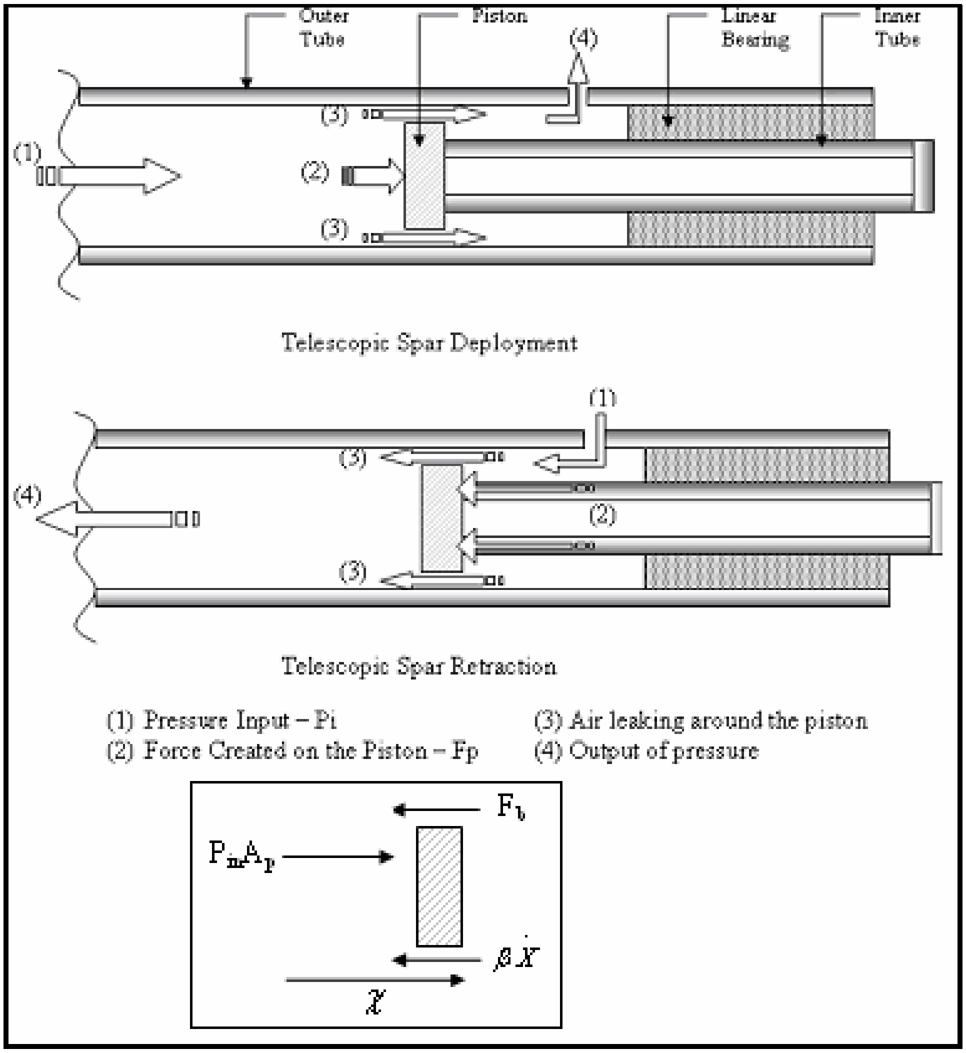

Figure 30: Extension and Retraction of the telescopic Spar and Free Body Diagram

A control system instantly manages the motion of the telescoping sections while preventing unstable transitions. For structural strength reasons, it has been decided that the small element of the telescopic spar will not deploy until the middle element reaches its maximum position.

Therefore, the motion of the telescopic spar was described using two uncoupled models, one for each moving element. See figure for Free Body Diagram 30.

Let's consider one of the moving tubes in motion (extension) with respect to the outer one. A force is created on the piston (1) to achieve the motion, but a small leakage (3) has to be considered around the piston, as it could not be tight fitted for friction reasons. The exit of the pressurized air is done through a small orifice that can also be considered as a "V^2 Damper[37]". Finally, a friction force F_b appears when the aluminum tube slides inside the linear bearing. Therefore, we used the following model for each moving element (tube and piston):

$$m\ddot{X} + \left(\frac{\rho A_p^{\ 3}}{2 A_{0p}^3 C_{0p}^3} \right) \dot{X} \left| \dot{X} \right| + \left(\frac{\rho A_p^{\ 3}}{2 A_{0.out}^3 C_{0.out}^3} \right) \dot{X} \left| \dot{X} \right| = P_{in} * A_p - F_b \qquad (10)$$

where A_p is the area of the piston; A_{0p} and $A_{0\ out}$ are the areas of the orifices around the piston and of the pressure output; $C_{0\ p}$ and $C_{0\ out}$ are factors that account for frictional losses through the orifices. They were given the value of 0.7, as the surface areas of the orifices are very small (in the order of 8.10^{-4} in^2).

A similar model can be used for the retraction of the telescopic spar, again assuming that the biggest tube doesn't retract until the small tube is completely retracted.

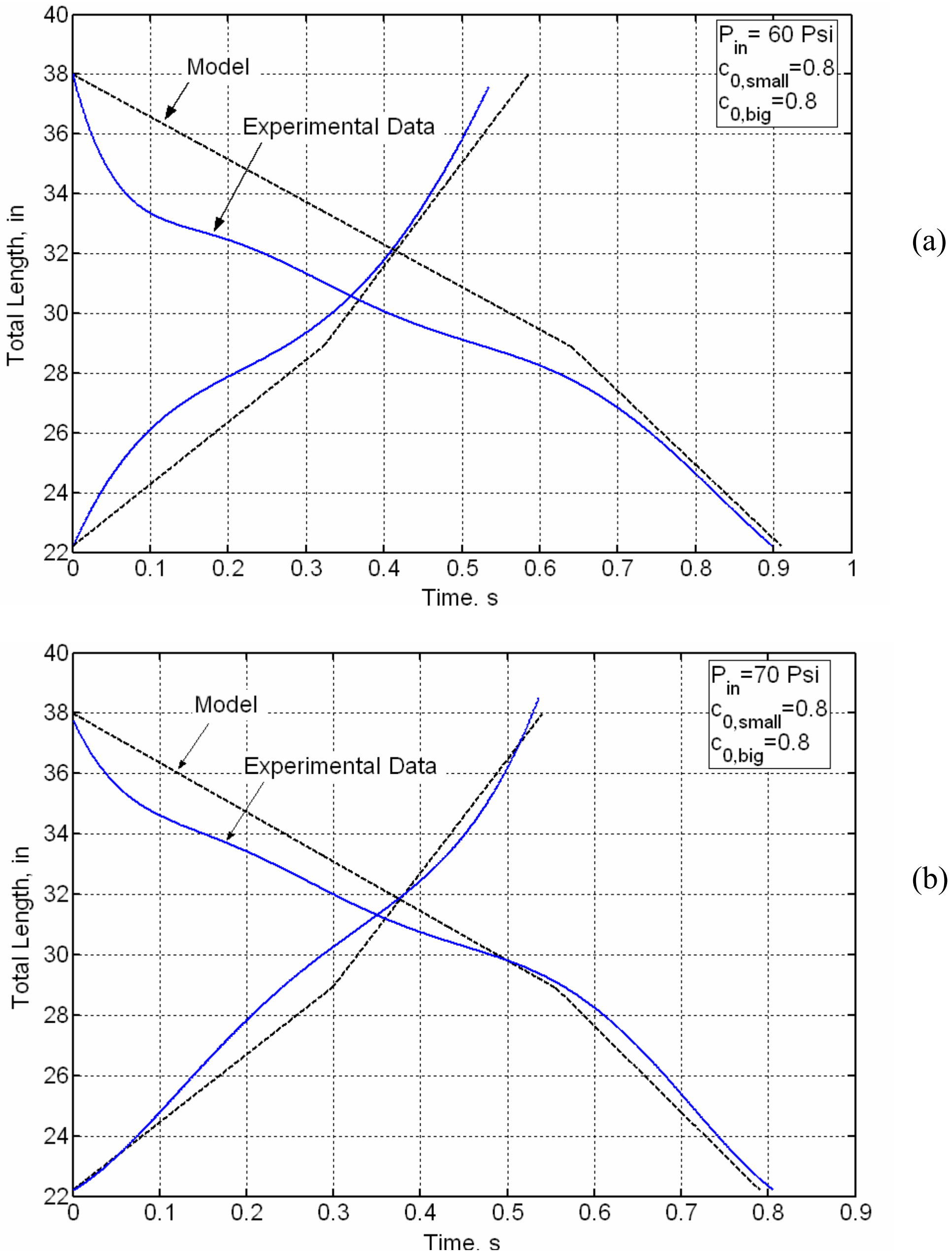

Figure 31: Total Length of the Spar during Extension and Retraction at 60Psi and 70Psi

Figure 31 shows the predicted and measured times required to extend and retract the telescopic spar when it is operated at different pressures. These results confirm the extension and retraction time-scale that was observed while testing. However, it appears that the model does not fit exactly the trends observed during testing. It is assumed that this difference in trends is due to an effect of static friction between the elements of the spars, which is not accurately accounted for in the model.

4.2. The Control System

4.2.1. General Concept

The objective was to create a closed-loop control system to manage the deployment of the wing. The primary requirement is being able to sense the instantaneous length of the wing, and respond in a timely manner to a length command given by the user. It was decided to use the software LabView from National Instruments to create the control program. This program had to be able to receive indicative data from length sensors embedded in the wing, and respond to the user command by managing the opening and closing of solenoid valves. This task is completed by sending a +5V signal to the valves to cause the opening, or a +0V signal otherwise (the rest state of the solenoid valves being “closed”), through a data acquisition card (DAC) and a terminal block.

The solenoid valves command the input and output of pressure in the actuator to generate its extension or retraction. The primary constraint for those valves is to provide a sufficient flow rate in order to create a fast response of the actuator. However, such valves require +12V supply at high current, and the control program/ associated hardware can only provide up to 5V at low current. Therefore, an electronic circuit including a relay was created to allow the control signal current opening or closing an electronic switch to command the opening/closing of the valves.

The next two figures display the elements mentioned above (valves, electronic circuit, DAC, etc…) as well as a functional diagram of the electronic circuit.

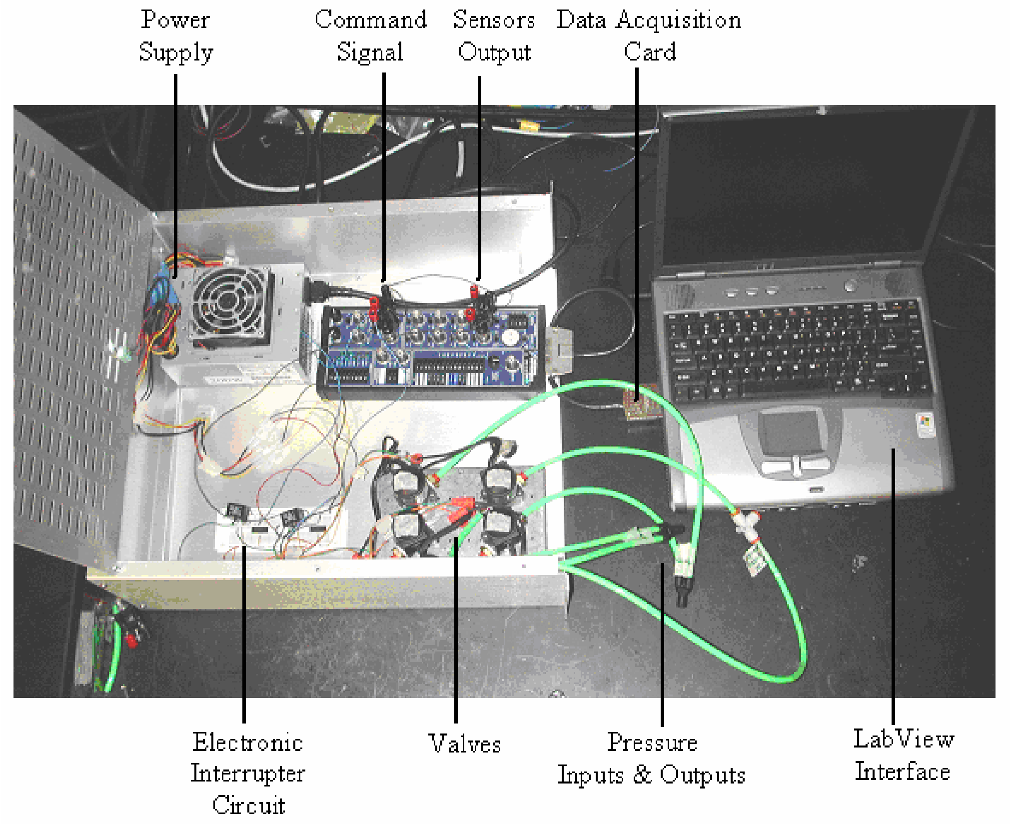

Figure 32: Components of Spar Control System

As described in earlier sections, the first generation prototype uses a fully controllable actuator: each stage of the telescopic spar can be prescribed to extend or retract independently of the other stages. However, it was decided for structural reasons that the weaker stage (tip) would not deploy (extend) until the intermediate stage is completely extended, and that it had to be completely retracted before the intermediate stage could start to retract.

4.2.2. First Iteration: Discrete Sensing

The goal of the first iteration was to create a very simple control system since it was initially decided to use each moving element of the telescopic spar in only two definite positions: fully extended or fully retracted - even though all intermediate position could be reached. Only two positions needed to be sensed for each of these moving elements, therefore a discrete sensing device can be used.

Additionally, the design of the fully integrated wing leaves very little space for sensors and wiring. It was then decided to use a simple control concept that involves Hall Effect Sensors, as they are very small and relatively easy to connect. Hall Effect sensors work as follows: when a magnetic field is applied perpendicularly to the conductor, a voltage (the Hall voltage) is generated transversely to the current flow direction in the electric conductor (semi-conductive platelet).

Therefore, the position of each moving element of the telescopic spar, thus the telescopic wing, can be characterized using a set of two magnets embedded at the on the surface of each lateral anti-rotation rod at its extremities, and sensed by a Hall Effect Sensor. One of the magnets has its positive pole facing the sensor, inducing a positive peak output out of the sensor, which characterizes the extended position of the corresponding element of the telescopic spar. The other magnet has its negative pole facing the sensor, inducing a negative peak output that characterizes the retracted position. Any intermediate position of the moving tube will generate an intermediate voltage comprised between the positive and negative output boundary voltages of the sensor. Figure 33 illustrates this first design.

The control program, developed using the Labview software, receives the output data from these two Hall Effect sensors through a data acquisition device, and compares them to the command given by the user. The two symmetric segments that compose the full telescopic wing can be controlled separately.

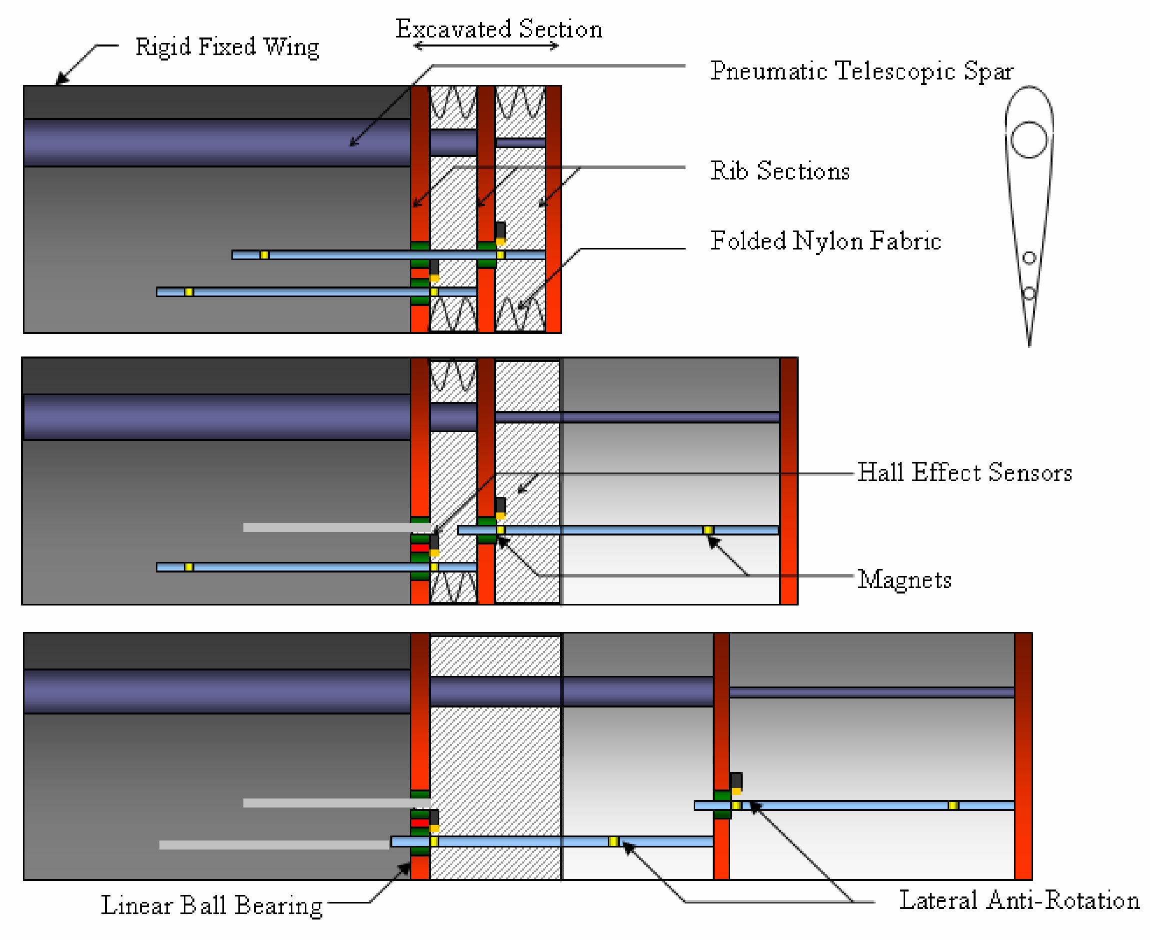

Figure 33 : Telescopic Wing Assembly – First Generation Prototype with Discrete Sensing

Three choices are offered to determine the total span of the wing:

- Choice 0: the wing is fully retracted
- Choice I: the tip element is extended while the middle element is retracted
- Choice II: both mobile elements are extended.

Each of these choices is associated to a set of two reference voltages corresponding to the reference outputs of the two sensors. The user command, through these choices, will generate the reference sensors output set, to which the actual sensors outputs are compared. For each comparison case, (sensor output higher/included/lower than high/low reference boundaries) a number of actions is defined in the Labview program in order to match the reference and the actual sensors outputs.

Each action corresponds a set of four voltages (of value 0V or 5V) acting as switches (through simple resistor-transistor-diode circuits), allowing or not a 12V voltage to be fed to the solenoid valves that control the input or output of pressure in the different chambers of the actuating telescoping spar.

The control logic is inserted into a time loop that allows a constant check to maintain the wing's length. The following figure describes briefly the control process, where V_1 and V_2 represent the output voltages from the Hall Effect Sensors and V_1Ref and V_2 Ref represent the Reference voltages defined corresponding to the users command.

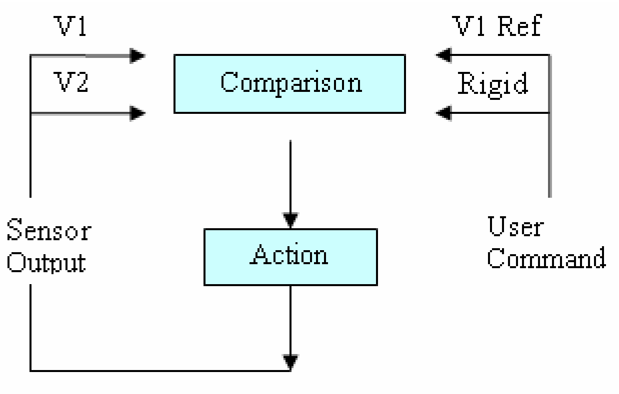

Figure 34: Discrete Sensing - Control Logic

Advantages and Disadvantage of this control design:

The advantage of this control method is simplicity. The sensors are easy to install, are reliable, and do not require high currents. The Labview-based program is simple, and it was easy to create a user-friendly interface by giving only three options to the user. However, Hall effect sensors happen to be extremely fragile devices, and were not a good solution since they had to be mounted on moving parts, resulting in a too frequent breakage of the electrical connections. Additionally, a clear disadvantage of this control method is that the system is discrete and does not match the capabilities of the spar: the spar is able to attain an infinite number of locations between its two extreme configurations, but the sensing scheme is only able to detect a discrete number of positions. The next iteration is to include a continuous sensing scheme in the control of the spar.

4.2.3. Second Iteration: Continuous Sensing

For the second iteration, it was decided to use the full range of capabilities of the pneumatic spar. Each moving element of the telescopic spar can have an infinite number of positions between its fully extended and retracted states. Thus, a continuous sensing device will be used. It is important to mention that the full integrated wing leaves very little space for sensors and wiring. Therefore, it was decided to use optoelectronic distance measuring sensors (model SHARP GP2Y0D21YK). These sensors are supplied 12 Vcc, detect a distance in the range of 10 to 80cm, and weigh about 3.6 grams.

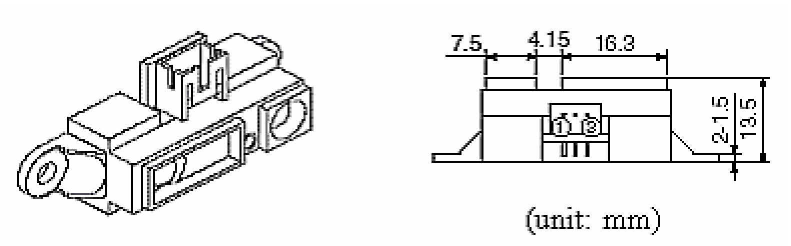

Figure 35: Optoelectronics Distance Measuring Sensor - SHARP GP2Y0D21YK

The position of each moving element of the telescopic spar, can be characterized using two sensors placed inside the wing that are fixed on the previous static element, and a reflective surface at the tip of the element for which the distance has to be measured. In this case, the ribs can be used as the reflective surface so the design is very simple. The sensors need to be calibrated in order to be included in the control program so a set of experimental data is acquired and a curve is fit to the data in order to provide a mathematical description of the output of the sensor. Figure 36 shows a set of experimental data and the Polynomial Least-Square Curve Fit over the applicable range. Table 3 displays the coefficients of the polynomial curve fit and its maximum error with respect to experimental data.

Polynomial Curve Fit: $C_1X^8 + C_2X^7 + C_3X^6 + C_4X^5 + C_5X^4 + C_6X^3 + C_7X^2 + C_8X^1 + C_9 = Y$

Table 3: Optical Sensor Calibration: Polynomial Curve Fit Coefficients

C_1	0.7716
C_2	-11.9724
C_3	77.1366
C_4	-270.464
C_5	565.851
C_6	-726.773
C_7	568.983
C_8	-264.842
C_9	72.623
Error (%)	6.6984e-05

The control program, written in Labview, receives the output voltage from the optical sensor through a data acquisition device, and compares it to the command given by the user. Recall that the actuator is composed of one fixed section (at the root) and two mobile sections, and the small element of each telescopic spar cannot deploy until the middle element reaches its maximum position.

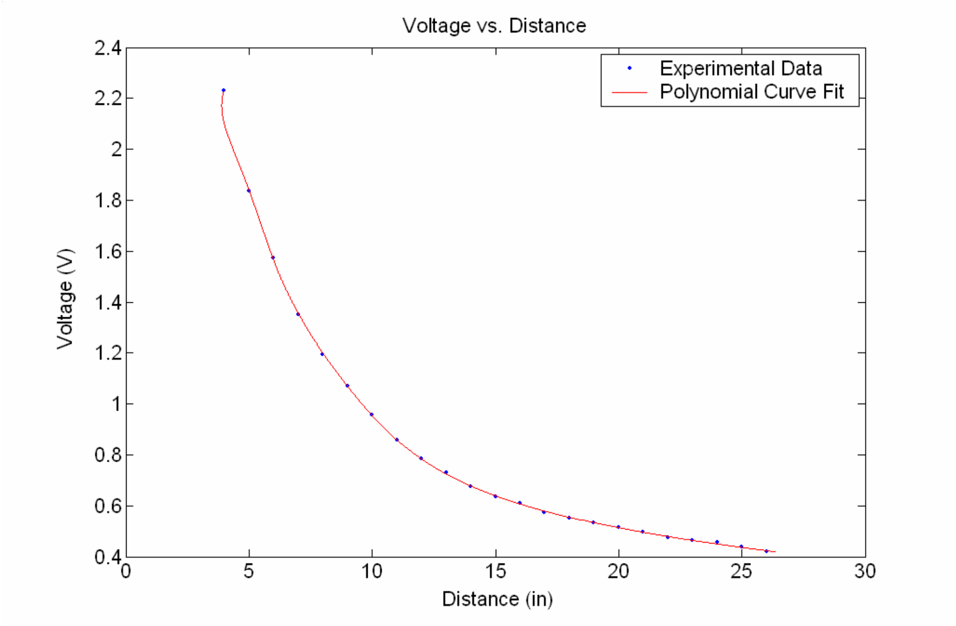

Figure 36: Voltage vs. Distance - Experimental Data and Polynomial Curve Fit

As in the previous control scheme, actuation is controlled via a set of four voltages (0V or 5V) acting as switches (through simple resistor-transistor-diode circuits), allowing or not a 12V voltage to be fed to the solenoid valves that control the input or output of pressure in the different chambers of the actuating telescoping spar. Figure 37 illustrates the terminology used for the control logic.

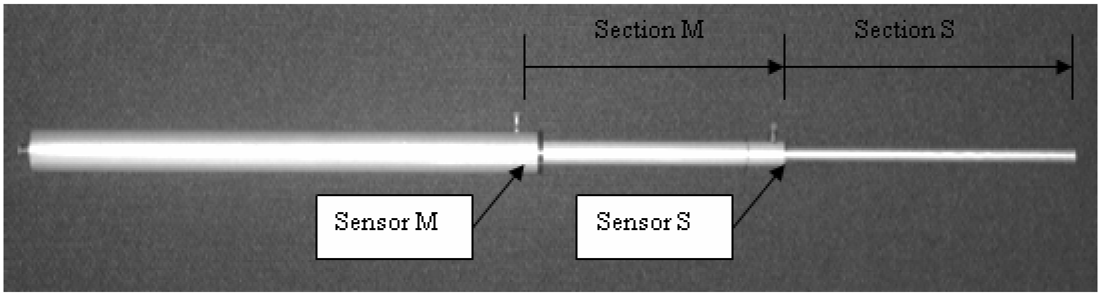

Figure 37: Sensor Location and Spar Sections

Let us now illustrate the control logic with a general example using figures 38 and 39.

(1) - The control logic is inserted into a time loop that allows a periodic check on the wing's length.

(2) - Select case: Case1- The command is in section M; Case2 - The command is in section S

(3) - Case 1 - First Frame: Check that section S is completely Retracted; If not: Do So (While Loop)

(4) - Case 1 - First Frame: Send Control Outputs to the valves based on the While Loop Timer

(5) - Case 1 - Second Frame: Then only, check the output of M Sensor; compare to the command (Figure 39)

(6) - Case 1 - Second Frame: Adjust Control Outputs to match Sensor M Signal and Command (Figure 39)

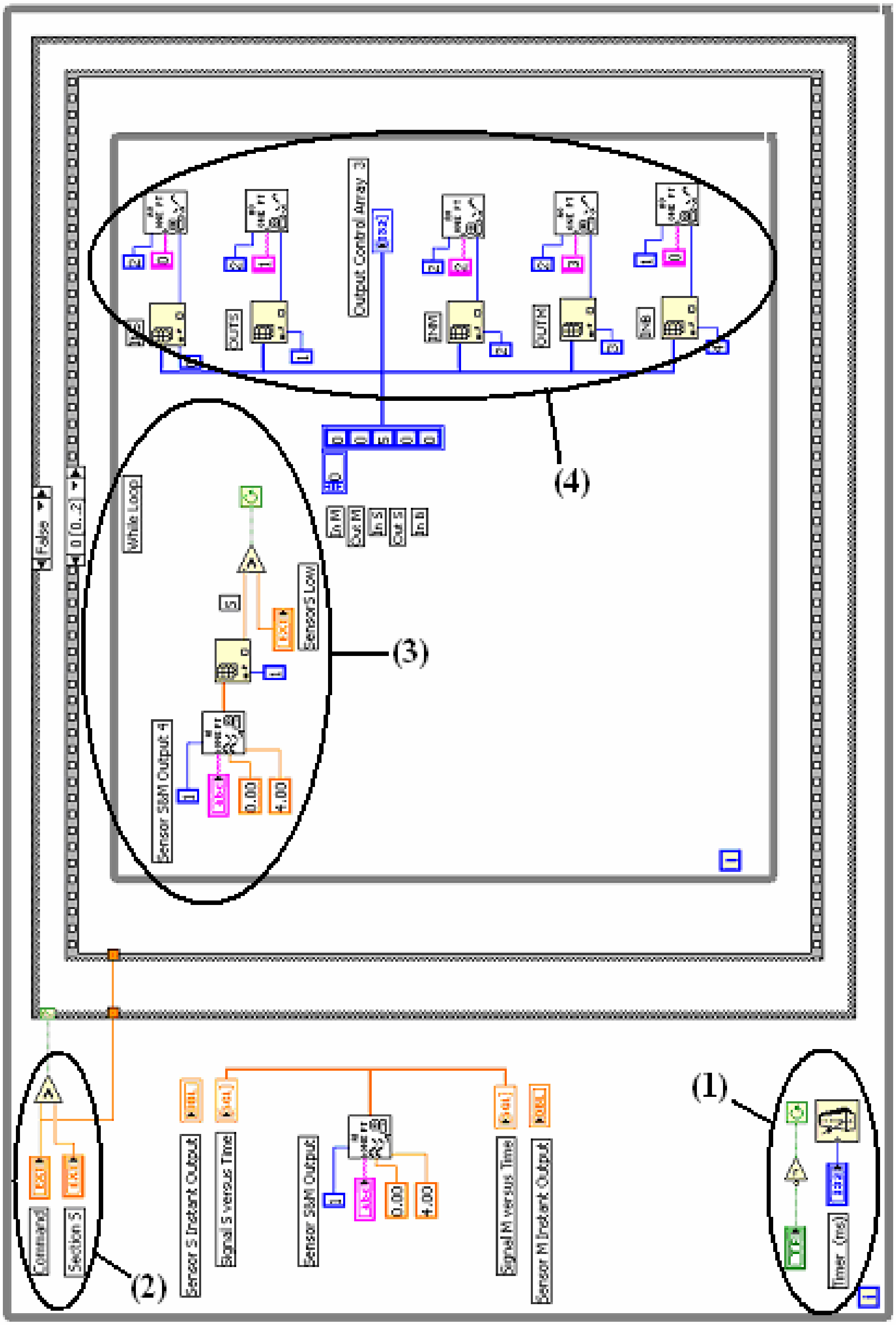

Figure 38: LabView Code: Case1 - First Frame of the Sequence

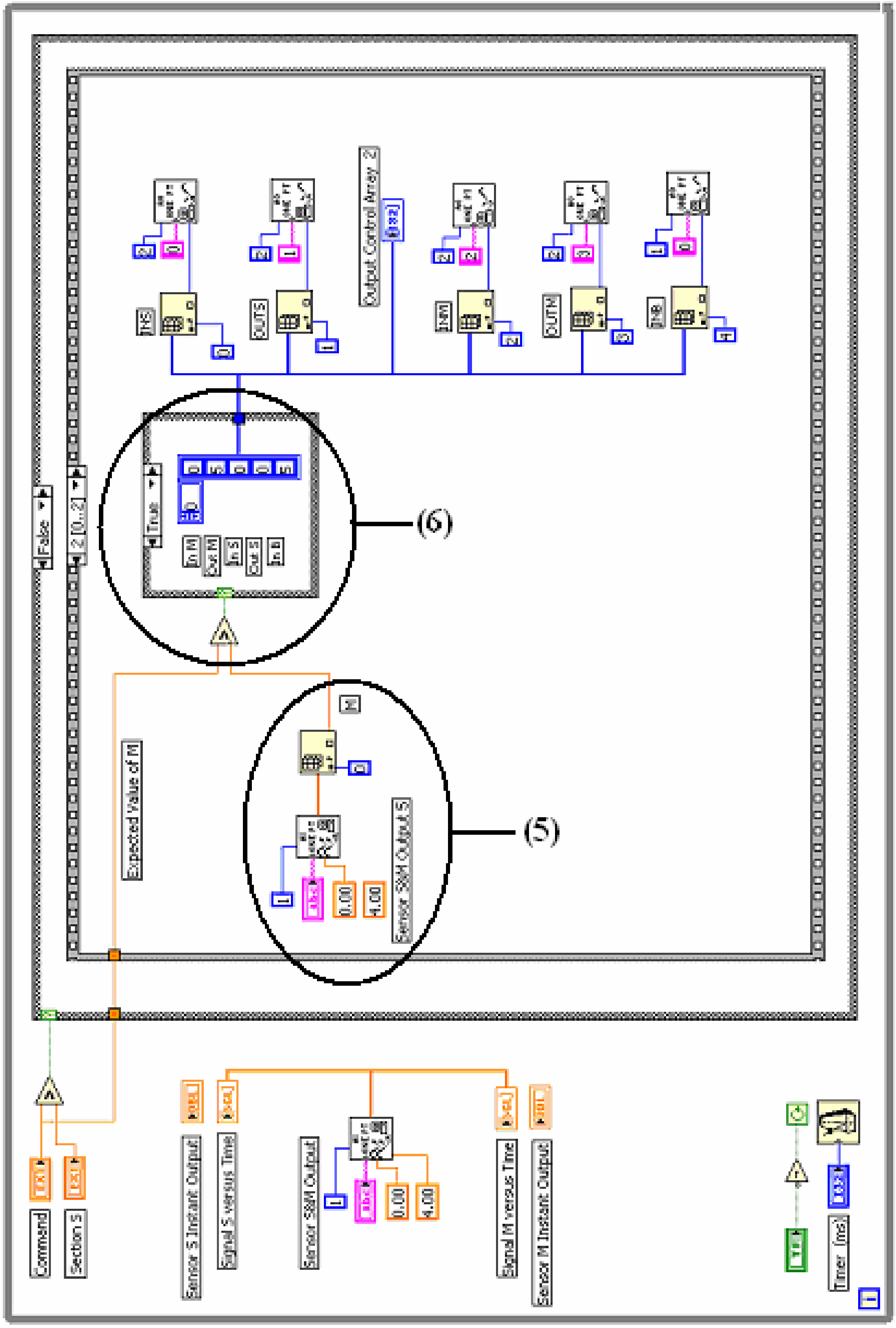

Figure 39: LabView Code: Case 1 - Second Frame of Sequence

Case 2 uses the same sequence of actions: Check that Section M is completely extended, then only adjust Section S's position to match the Command.

<u>Advantages and Disadvantage of this control method:</u>

The main advantage is the simplicity of the optical sensor: there is no part in contact and the output voltage can directly be converted in a distance. However, the use of this sensor revealed a few problems: the sensors are very sensitive to the lighting environment, therefore they have to be used in the exact same condition every time or the calibration has to be done again. Additionally, it was not possible to use the chosen sensor in the desired configuration due to the proximity of the skin elements: hence the sensor would detect the skin before it detects the rib facing it because it emits a conic group of rays rather than a unique perpendicular ray of light.

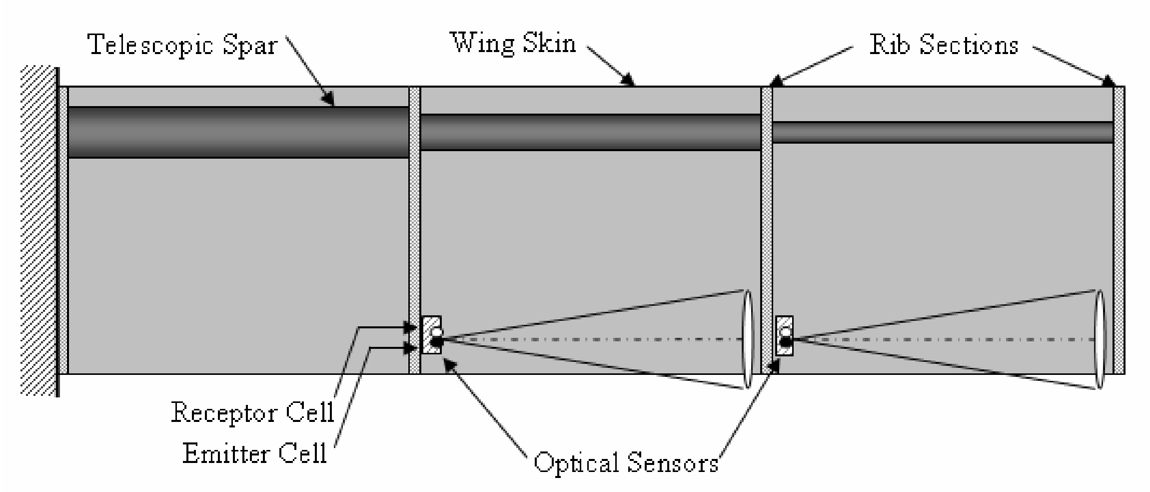

Figure 40 : Telescopic Wing Assembly – First Generation Prototype with Continuous Sensing

4.3. The Telescopic-Wing Skin

4.3.1. Soft Fabric Skin

Two different concepts are explored to provide a stiff skin for the telescopic wing. The first option is to use a foldable fabric skin on the two extendable sections of the telescopic wing. The choice of the fabric used for the skin is a critical part of the manufacturing process since it has to transmit aerodynamic loads to the main spar, and be easily storable. Kite fabric (¾ oz. Polyurethane coated 1.9 oz. Ripstop) was chosen for various reasons: light weight, easy to glue or sew, high resistance (not damaged by folding or tension), and non-porosity. However, it is an issue to ensure that the skin elements fold nicely inside the fairing when the wing sections retract.

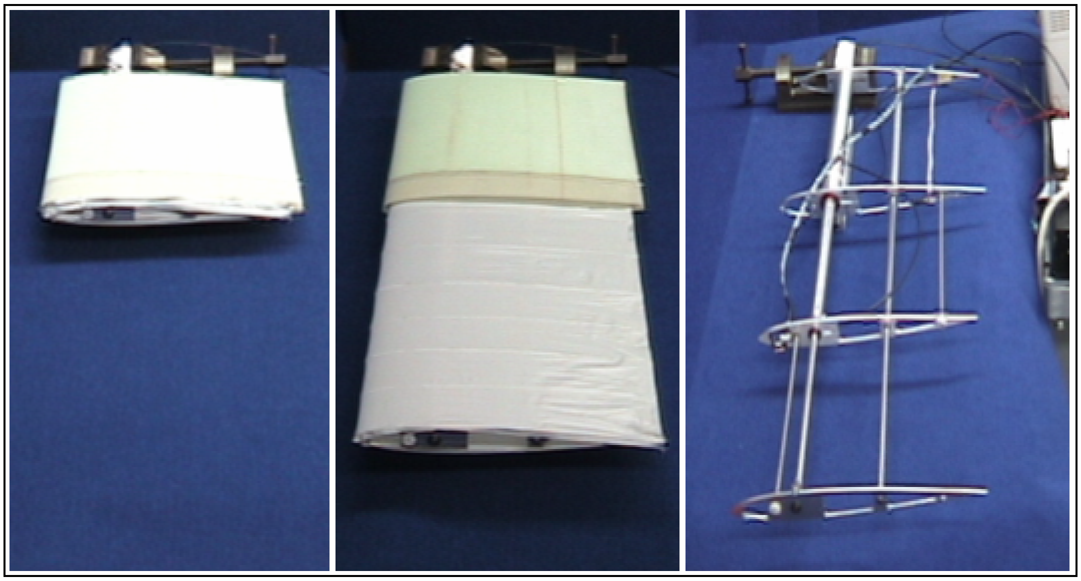

Figure 41: Pneumatic Telescopic Wing using Fabric Soft Skin

Figure 41 shows a prototype manufactured at the University of Maryland in its retracted and extended configurations. Kite fabric was glued to every rib and at the trailing edge. Note that between the fixed rib, 3 or 4 floating ribs, free to slide on the spar, were used to maintain the shape of the airfoil. The issue encountered with this material was that it was hard to stow and deploy the skin consistently. This part of the project was temporarily abandoned to focus on another option.

4.3.2. Hollow Shells

While a smart flexible skin was originally considered for the telescopic wing, finding a material that could stretch over twice its original length while continuing to support an aerodynamic load, proved difficult. Therefore a rigid telescopic skin proved to be the most feasible solution because it allowed for several rigid sections to support the aerodynamic loads while in any configuration. A preliminary fiberglass shell was fabricated by making a conventional foam core wing with a fiberglass coating and then removing the inner foam core. This shell proved that a skin made from fiberglass would be sturdy enough to support an aerodynamic loading when ribs are attached at each end. The skin prototype was constructed from 4 sheets of fiberglass and had an average total thickness of 0.040”. Using this skin as a baseline, aluminum molds were designed to produce skins of a consistent 0.045” thickness. The additional 0.005” in thickness increased its structural rigidity and minimized flexing at the quarter-chord. In order to manufacture skins that would telescope tightly over each other, three sets of aluminum molds were designed and manufactured. The first set consisted of a pair of female molds that produced a NACA0012 airfoil with 8” chord and a male mold that was 0.045" smaller than a NACA0012 in the unit normal direction. The second set of molds consisted of female molds that produced the same geometry as the larger male mold and a smaller male mold that was 0.090" smaller than a NACA0012 in the unit normal direction. The final set was a pair of female molds that produced the same geometry as the smaller male mold. This last set was used to make a foam core wing instead of a fiberglass skin so that the wing base was solid and to reduce the number of molds manufactured.

Wire EDM (electrical discharge machining) was used to produce the two male molds and the two pairs of smaller female molds, guaranteeing very tight tolerances. The largest pair of female molds was readily available in the Smart Structures Laboratory as it was made for a previous project. See figure 42 for a photograph of the molds.

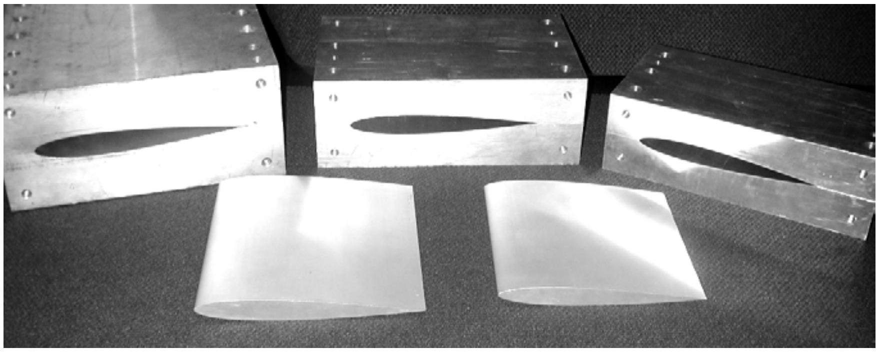

Figure 42: Aluminum Male/Female Molds

Note that the cost for this process was significantly higher than building the shells as described above. However, the shells produced with the mold were of a much superior quality.

4.4. Integrated Wing

The wing assembly must be rigid enough to resist turbulent loads that would result in an oscillating twisting of the wing. Therefore, the rib sections are rigidly fixed to the telescopic spar and to the lateral rods. Additionally, all sliding surfaces are inserted into bearings to avoid misalignments. Various cavities are machined into the rigid fixed part of the wing to host the main telescopic spar, the lateral rods, the pressure feeding tubes, and the sensor wiring. These cavities are carefully located so the stiffness of the section is not affected. After calibration, the distance sensors are fixed on the ribs and placed close to the rods to ensure an accurate position reading. Table 4 summarizes the test wing characteristics and concept, and figure 43 shows the first generation prototype's spar and ribs assembly with the hollow fiberglass shells.

Table 4: Test Wing Characteristics

Wing Section	Naca 0012
Chord	c=12”
Wingspans	2 - 8 ft
Aspect Ratios	2 - 8

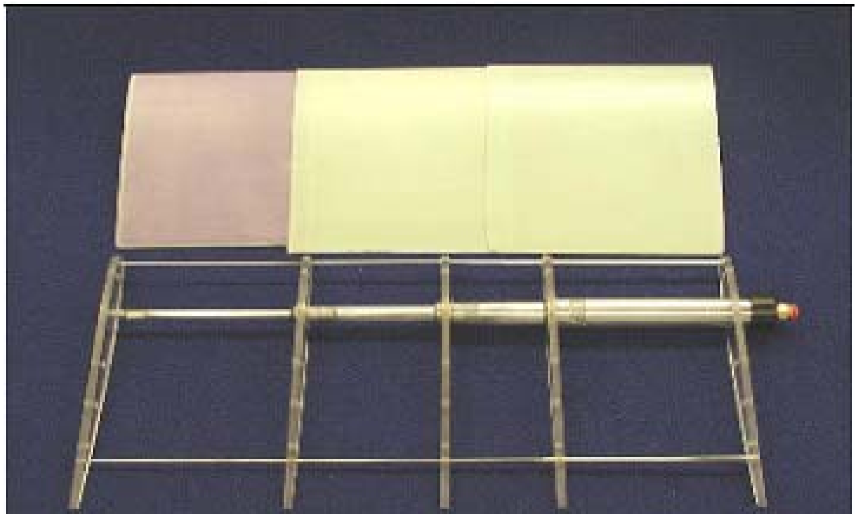

Figure 43: First Generation Prototype using hollow fiberglass shells

4.5. Analysis of Telescopic Wing Aerodynamic Performance

4.5.1. Theoretical Aerodynamic Performance

The principle behind making a morphing aspect ratio wing lies in finite wing theory.[10] According to this theory, a finite wing produces a wingtip vortex that redirects the free-stream flow down, thereby effectively reducing the lift characteristics of a given airfoil and increasing drag. Equation 11 shows lift coefficient. The reduction in lift is a result of the overall lift curve slope being lowered by Equation 12, where a_0 is the theoretical lift curve slope, equal to 2π for thin airfoils. The induced drag coefficient, $C_{D,i}$, is also a function of the aspect ratio as given in Equation 13.

$$C_L = a\alpha \tag{11}$$

$$a = \frac{a_0}{1 + a_0/(\pi AR)} \tag{12}$$

$$C_{D,i} = \frac{C_L{}^2}{\pi AR} \tag{13}$$

As seen in the above equations, the aspect ratio, and thus wingspan in the case of a rectangular wing, is the driving variable in the aerodynamic performance of a finite wing. Further, the effect of a large scale variation in wingspan will result in a wide variation of L/D, especially in the regime of low aspect ratios, as seen by the denominator of Equation 9.

The theoretical determination of parasite drag, composed of profile drag and skin friction drag, could not be expressed by simple analytic solutions. The CFD program X-Foil[38], originally developed at MIT, was used to predict the parasite drag at various angles of attack and Reynolds numbers. Parasite drag values for the first prototype are shown respectively in tables 5 and 7.

Lift and induced drag theoretical values were calculated as described by equations 11 to 13. The parasite drag values for the first generation prototype are shown in the following table for 4 different speeds.

Table 5: Profile Drag Coefficient for given Reynolds Number

	Reynolds Number			
α (˚)	182,000	273,000	363,000	454,000
0	0.01103	0.00814	0.00696	0.00635
1	0.01101	0.00844	0.00724	0.00659
2	0.01110	0.00918	0.00798	0.00722
3	0.01137	0.00998	0.00894	0.00816
4	0.01211	0.01079	0.01000	0.00930
5	0.01345	0.01198	0.01117	0.01063
6	0.01561	0.01373	0.01267	0.01195
7	0.01841	0.01583	0.01442	0.01356
8	0.02186	0.01841	0.01665	0.01524
10	0.03167	0.02524	0.02227	0.02014
12	0.05010	0.03593	0.03032	0.02760
14	0.15653	0.06123	0.04707	0.04106
16	0.18936	0.18230	0.14884	0.07401
18	0.21792	0.21712	0.17060	0.17072
20	0.24593	0.24578	0.19256	0.19302
22	0.27311	0.27321	0.21558	0.21588

The CFD results obtained were compared with NACA experimental results for an infinite wing[12]. The maximum c_d for the NACA0012 airfoil is approximately 0.020. Therefore, the CFD profile drag past an 8˚ angle of attack was not used to model the theoretical total drag coefficient because it was greater than one would expect. Instead, the profile drag coefficients above 8˚ were set equal to the 8˚ profile drag for the given Re. The lift is estimated using thin airfoil theory beyond this angle of attack.

4.5.2. Wind Tunnel Testing: Setup

Wind tunnel testing of the small scale telescopic wing and solid NACA0012 wings of 8” chord and 7”, 11.5” and 15” wingspans was conducted in the Aerospace Laboratories at the University of Maryland. A subsonic free jet wind tunnel with a 22” x 22” square test section was used for the testing. The speed of the wind tunnel was controlled by a Variac, which when at maximum voltage produced a maximum dynamic pressure of 13.5 lb/ft^2 and a 107 ft/s top wind speed. A Pitot tube attached to the side of the test section was connected to a manometer to measure the wind speed at the test section.

A lift and drag balance designed and manufactured for this project was mounted to a tripod stand and positioned in front of the test section, as shown in Figure 44. The balance employed two load cells, each consisting of an aluminum cantilever beam with a full Wheatstone bridge, to measure the aerodynamic forces. Each load cell was calibrated before and after each test specimen with a series of known weights to determine the linear strain to force relationship in the lift and drag direction.

When testing at high angles of attack, a constant value of strain was unable to be determined. To get the best estimates at these angles, the RMS option on the voltmeters was used.

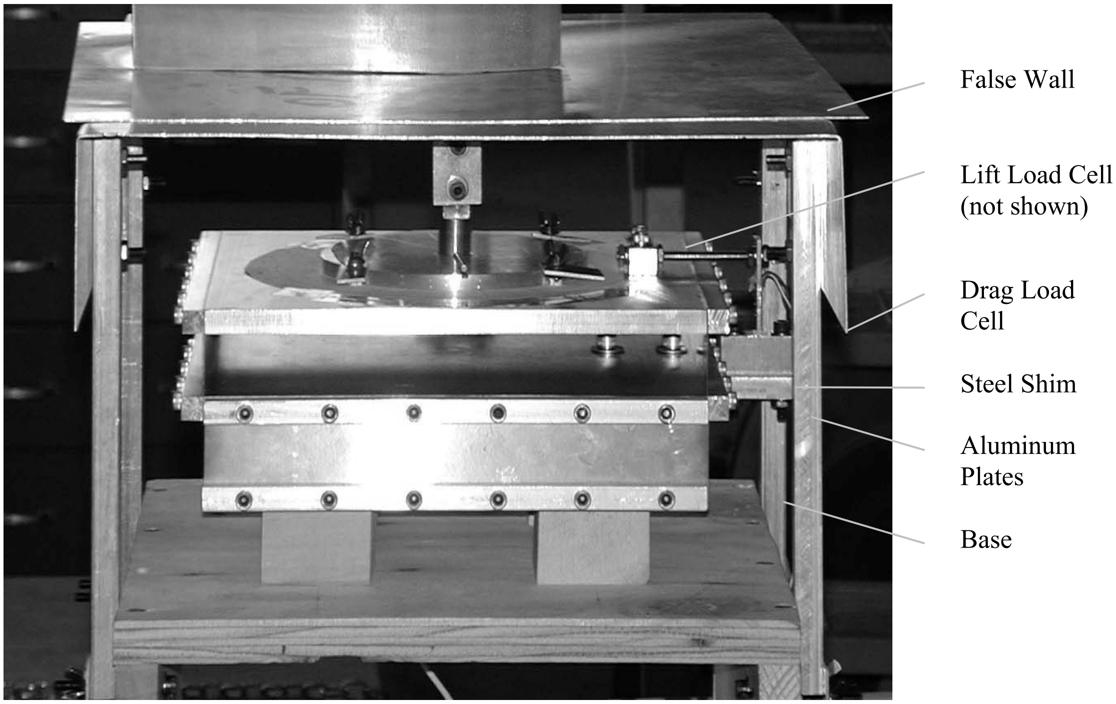

Figure 44: Lift and Drag Balance

4.5.3. Characteristics of the First Generation Prototype and Test Matrix

Six different tests were conducted in the wind tunnel. Half of the tests were devoted to fixed wings of 7”, 11.5” and 15” wingspans. The second half investigated the telescopic wing in the three different stages of deployment. The 7” wingspan corresponds to the fully collapsed wing where all the skins are at the root.

The 11.5” configuration is when the inner spar and outer skin is extended 4.5”, leaving 1.5” inside the medium spar. The final configuration occurs when the two skins extend another 3.5” out from the solid wing at the root. This gives a complete wingspan of 15” and leaves 1.5” of the medium spar inside the largest spar affixed at the root. The three configurations are shown in Figure 45. Each wing was measured from a 0˚ angle of attack to several degrees after stall to test the aerodynamic performance throughout the entire angle of attack range. The solid wings were tested first to provide a baseline comparison to the telescopic wing configurations.

The solid 7” wingspan was tested up to a 22˚ angle of attack, 2˚ degrees after it experienced stall. The solid wings of 11.5” and 15” wingspans stalled earlier at 16˚, but were tested up to 22˚ and 20˚, respectively. The three telescopic wing configurations were tested throughout the same angles of attack as their solid wing counterparts. As expected, each configuration stalled at approximately the same angle of attack as the corresponding fixed wing.

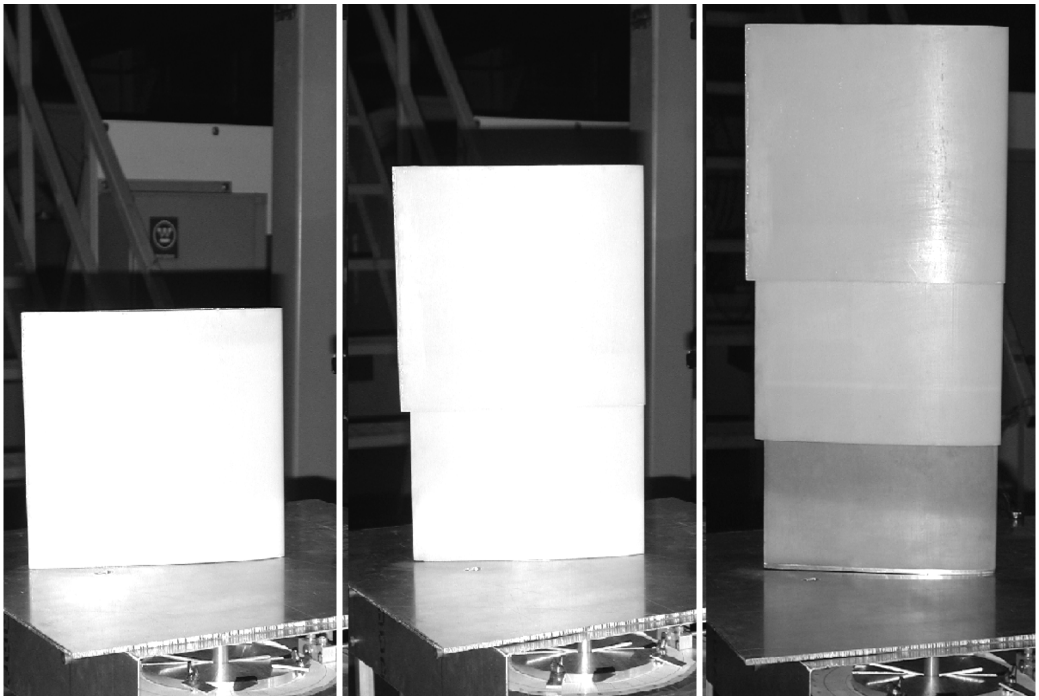

Figure 45: Telescopic Wing in Testing Configurations

While testing at each given angle of attack, the wing was also tested at four wind speeds and thus Reynolds numbers (182,000, 273,000, 363,000, and 454,000). The maximum Re was calculated to be 454,000 for an 8” chord length and 107 ft/s free stream velocity.

The other Re tested were 80%, 60%, and 40% of the maximum Re. The test matrix for the telescopic and solid wings is shown below as Table 6.

Table 6: Test Matrix of Angles of Attack for given Re and Wingspan Configuration

	Wingspan		
Re	7”	11.5”	15”
182,000	0° – 22°	0° – 22°	0° – 20°
273,000	0° – 22°	0° – 22°	0° – 20°
363,000	0° – 22°	0° – 22°	0° – 20°
454,000	0° – 22°	0° – 22°	0° – 20°

4.5.4. Wind tunnel tests results

A summary of all tests results is presented in Appendix I. This section focuses on significant results for the fully retracted and fully extended cases at a Reynolds Number of 454,000.

Figures 46 through 51 display the lift, drag and Lift to Drag polars for the fixed wing and telescopic wing at the two extreme wingspan conditions, i.e. 7” and 15”, and at a Reynolds number of 454,000. In addition, each figure displays the theoretical predictions based on finite wing theory. For both wingspans, theoretical predictions are within reasonable agreement.

4.5.4.1. 7” Wingspan Results

Careful inspection of figures 46 through 48 reveals that the theoretical results (from finite wing theory combined with CFD) and experimental results for the Lift curves are fairly close. For all angles of attack the telescopic wing has a higher lift coefficient than the rigid fixed wing of the same dimensions.

The drag coefficients are in better agreement except near stall conditions and at very low angles of attack.

However, the drag coefficient for the telescopic wing is always below the drag coefficient for the fixed wing. These two effects are profoundly displayed in Figure 44 where lift to drag ratio is plotted versus angle of attack. Here the telescopic wing consistently out performs the rigid fixed wing at all angles of attack, except near the stall conditions.

The maximum L/D value is approximately 15% higher for the telescopic wing. This is rather surprising, considering that both wing specimens have approximately the same dimensions. The only difference is that in the fully collapsed condition, the outer wing skins conform over the final rigid root portion of the telescopic wing.

Thus, a possible explanation for the enhanced performance of the telescopic wing may be the fact that it suffers less skin friction drag and is a bit more flexible than the rigid wing. Flexibility tends to change the airfoil flow characteristics by increasing the tip angle of attack. However, drag is expected to go up too but it does not.

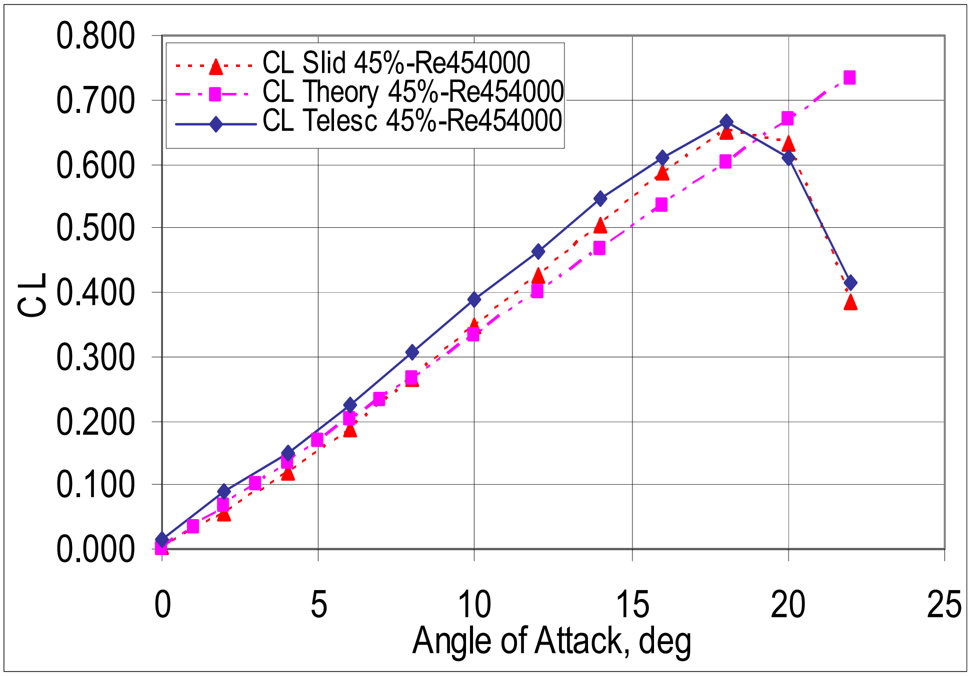

Figure 46: Comparison of Lift Coefficients for 7" Wingspan at Re = 454,000

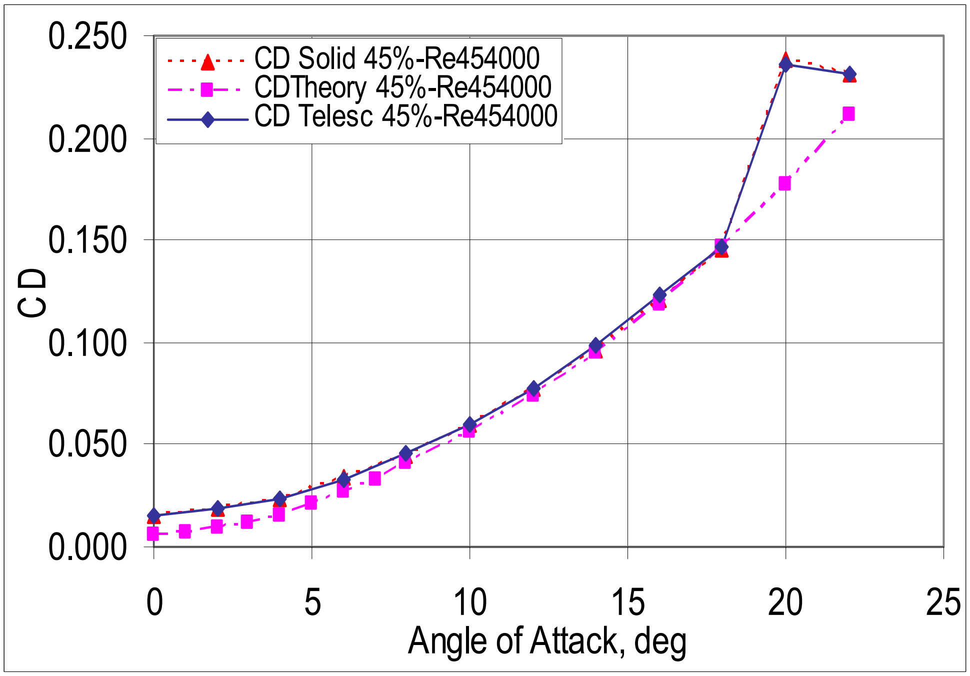

Figure 47: Comparison of Drag Coefficients for 7" Wingspan at Re = 454,000

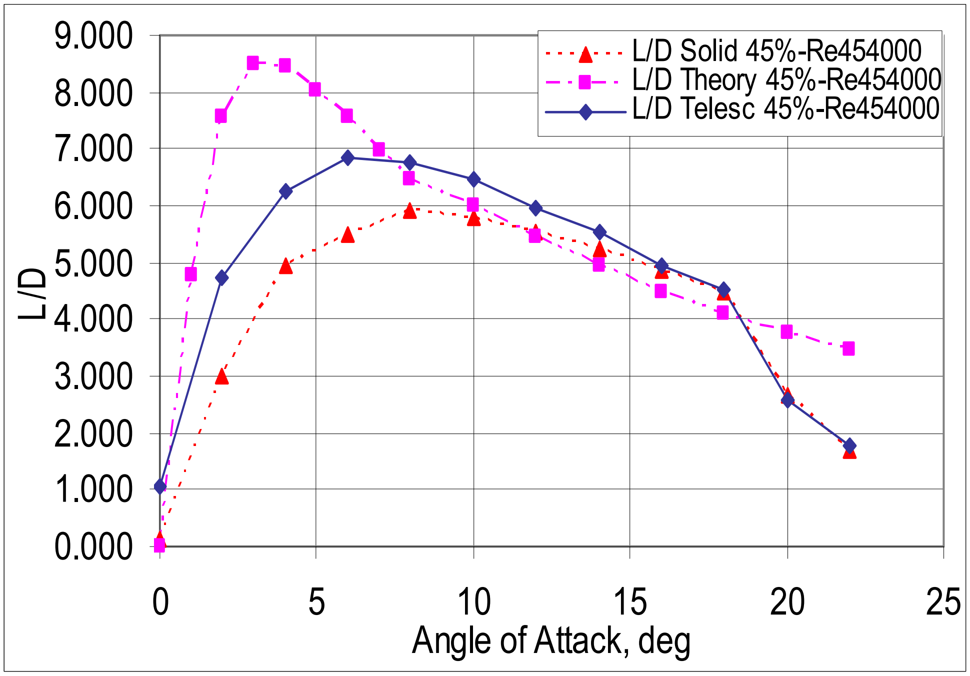

Figure 48: Comparison of Lift / Drag for 7” Wingspan at Re = 454,000

4.5.4.2. 15” Wingspan Results

Figures 49 to 51 display the lift coefficient, drag coefficient and lift to drag ratio as a function of angle of attack for the 15” wingspan configuration.

Unlike the 7” wingspan results, the rigid fixed wing out performs the telescopic wing. Figure 49 reveals that the lift coefficient of the telescopic wing is consistently lower than the rigid fixed wing test specimen of the same wingspan.

In addition, the drag coefficient for the telescopic wing is also higher than its rigid fixed wing counterpart for all angles of attack (See Figure 50).

It is likely that the loss of lift and the increase in drag of the telescopic wing is probably created by the fact that the aerodynamics are not completely seamless. The wing skins are constructed in sections and at the interfaces provide regions for flow interference. This may lead to an increase in wing section drag for the telescopic wing. In addition, the wing surface area of the telescopic wing is approximately 3.1% lower than that of the rigid fixed wing. This may also have a small effect on the lift to drag ratio.

However, this cannot completely explain the 25% difference in the peak lift to drag ratio between the rigid and telescopic wings. During experimental testing it was observed that the telescopic wing at 15" wingspan underwent noticeable twist deformation at angles of attack greater than 5 degrees.

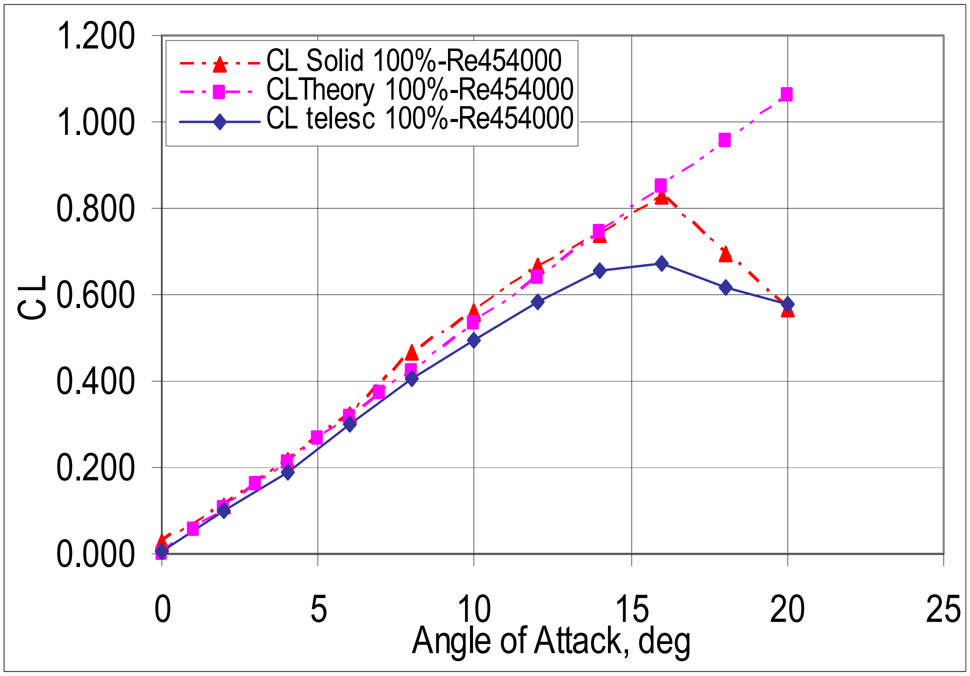

Figure 49: Comparison of Lift Coefficients for 15" Wingspan at Re = 454,000

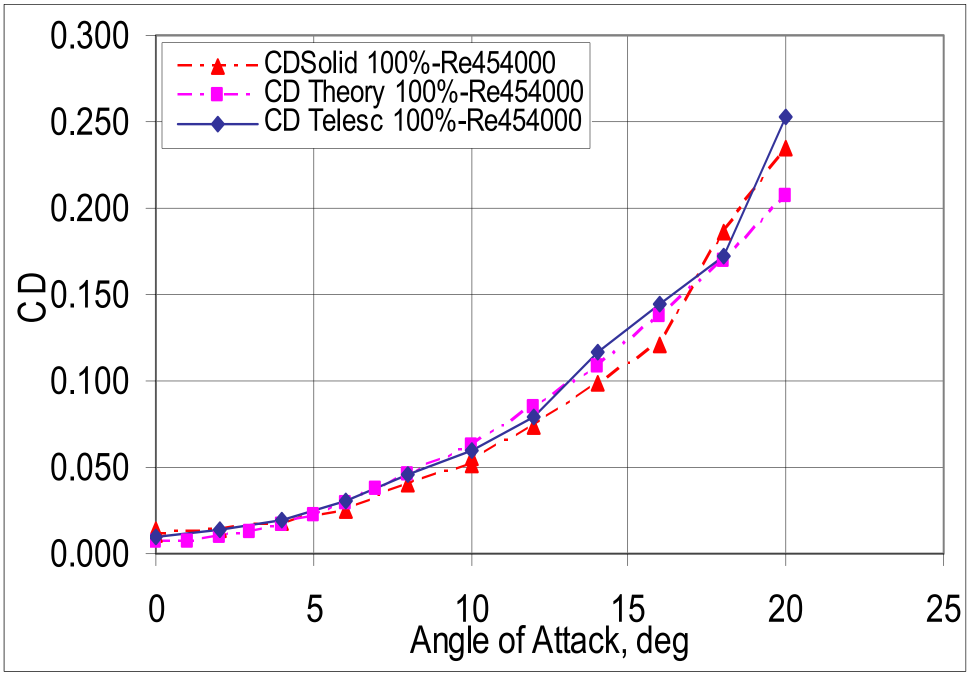

Figure 50: Comparison of Drag Coefficients for 15” Wingspan at Re = 454,000

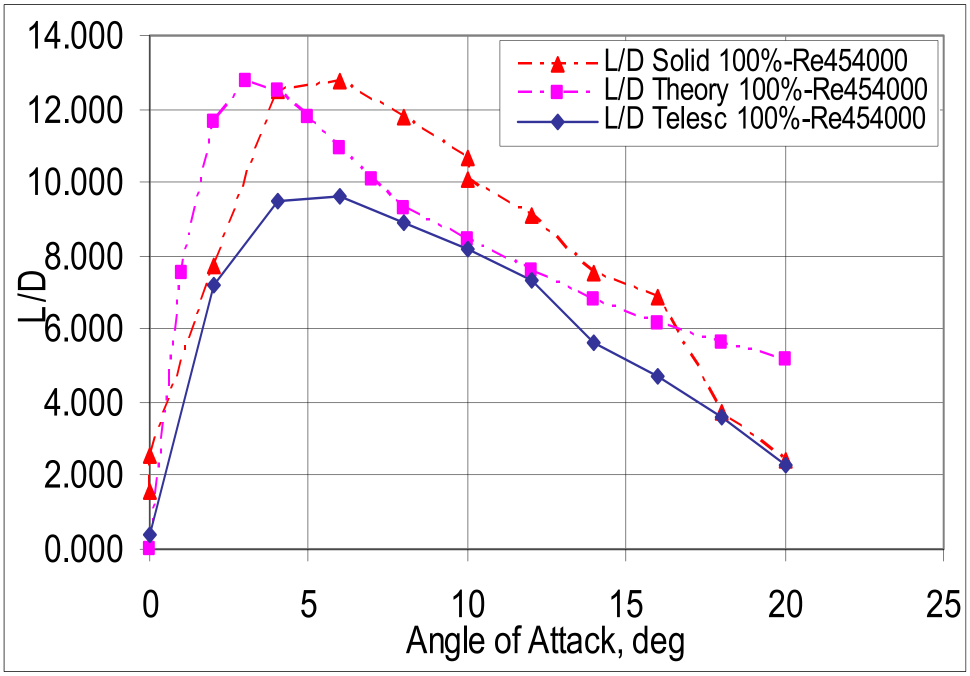

Figure 51: Comparison of Lift / Drag for 15” Wingspan at Re = 454,000

Chapter 5: Second Generation Prototype – Development and Testing

5.1. Actuator

5.1.1. Design and Manufacturing: Ergo-Help Double Spars

The integrated first generation prototype with the UMD telescopic spar and the soft-skin proved several facts:

- The sizing of the spars had to be reconsidered if we wanted the wing to handle the aerodynamic loads
- The manufacturing of the spars needed to be greatly improved in terms of “air-tightness” in order to minimize the amount of gas required to operate the spars.
- Wing twist and fluttering could not be avoided if only one actuator is used in the wing since the cylindrical elements that compose the spar are free to rotate with respect to each other. The side rods that were added for this purpose were shown to be too weak.

As a result of these observations, two decisions were made:

- Two telescopic spars were going to be coupled and used side by side to prevent uncontrolled twisting of the wing and provide more strength and actuation force to the wing.

- The pneumatic telescopic spars were going to be redesigned, and manufactured by a subcontractor company specializing in high-lift pneumatic telescopic tubes.

The Ergo-Help company[39], based in Arlington Heights, IL, was chosen to assist us in the design and manufacturing of the spars. The desired dimensions were given to Ergo-help as well as operating requirements (the spars had to be designed to support loads in horizontal configuration and with low actuation pressures). Figure 52 presents the design adopted.

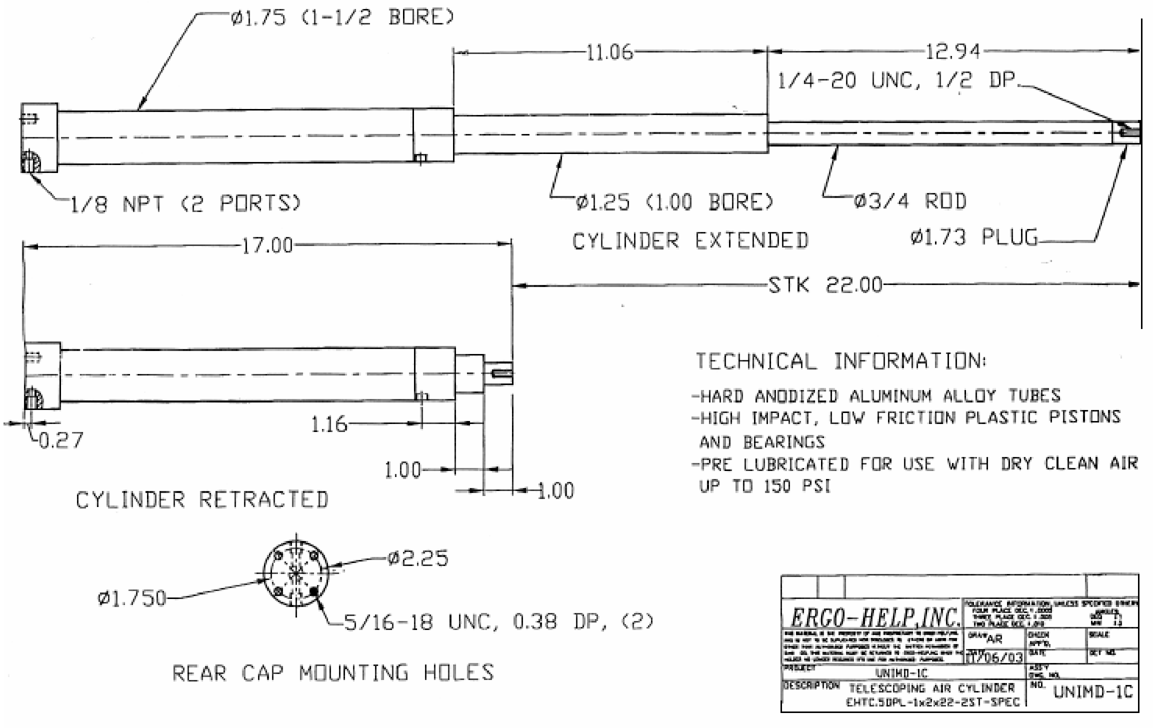

Figure 52: Ergo-Help Pneumatic Telescopic Spar Dimensions

Figure 53 presents details of the extension and retraction mechanism for the Ergo-Help Pneumatic Telescopic Spar. The extension mode is comparable to the used in the UMD pneumatic telescopic spar: a pressure input at the root (1) generates motion of the two mobile section with pressure applied on both pistons (2&3). As a result of the motion, air is exhausted behind the two pistons (4).

Recall that the input and output of pressure orifices are closed (by the solenoid valves) when they are not being used. Hence, the spar is sealed under pressure at every time. However, the retraction scheme is slightly different that the UMD pneumatic telescopic spar's, since the Ergo-Help pneumatic telescopic spar has only one, fixed, input of pressure to generate the retraction of the spar. While pressurized gas is input in location (5), the retraction of the middle element of the telescopic spar is initiated by the back-pressure on the piston (6) and exhaust of pressure at the root of the spar (7). On the other hand, the tip element of the telescopic spar does not move until the middle element is completely retracted. When this occurs, the middle element is retracted completely, orifices at the tip of the middle element allow the air to push the small piston and initiate retraction of the tip telescopic element.

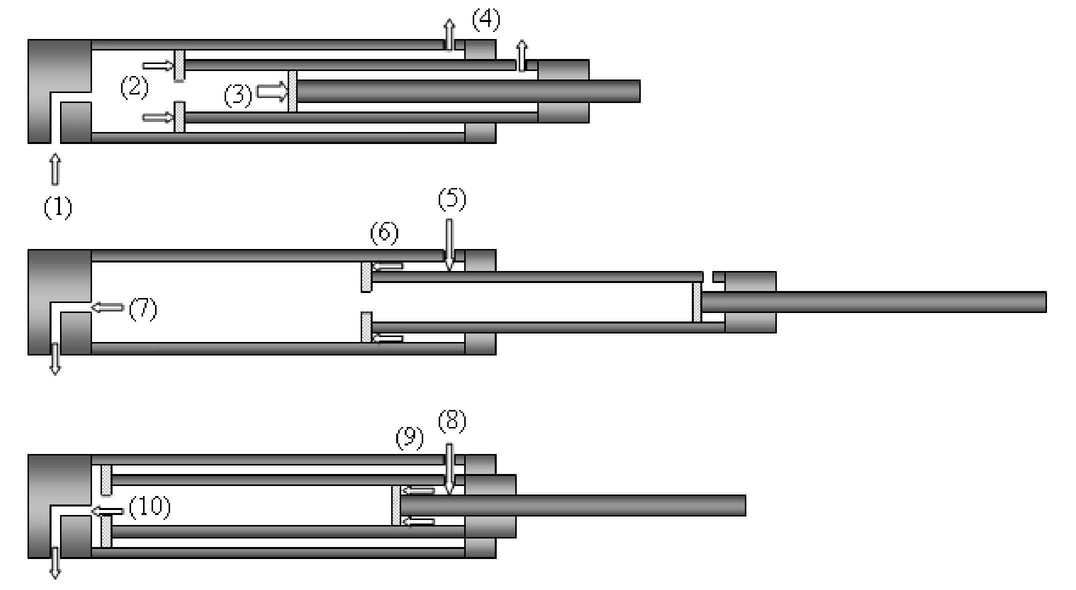

Figure 53: Ergo-Help Pneumatic Telescopic Spar Functional Design

Therefore, actuation of the span resumes in an input of pressure in location (1) for extension associated with opening of orifices (4) for the extension, and an input of pressure in location (5,8) for extension associated with opening of orifices (7,10) for the extension.

As previously mentioned, it was decided to use two Ergo-Help pneumatic telescopic spars to actuate the second generation prototype. The two identical spars are placed side by side and mechanically coupled by the ribs at the root, and at the tip of each section. The design of the ribs will be discussed in section 5.3.

5.1.2. Dynamic characterization of the spars.

In order to characterize the behavior of the spars under loading, experimental testing was performed. The spars were placed side by side and the loading was simulated upwards as in the actual wing configuration. In order to avoid the inertia effects, the weights were mounted on pulleys and placed 10 feet away from the spars. In that situation, when the mobile elements of the spars are in motion, they experience a load but do not have to lift or accelerate the weights. The varying wingspan (extension and retraction) was measured using a potentiometer and a wheel on a string. This experiment was performed at three different pressures (30PSI, 40PSI and 50PSI) and in three different loading cases (No load, Load A, Load B), and repeated 5 times in each case.

In order to define the experimental/simulation loading cases A and B, the moment over the wing had to be calculated by integrating the lift distribution.

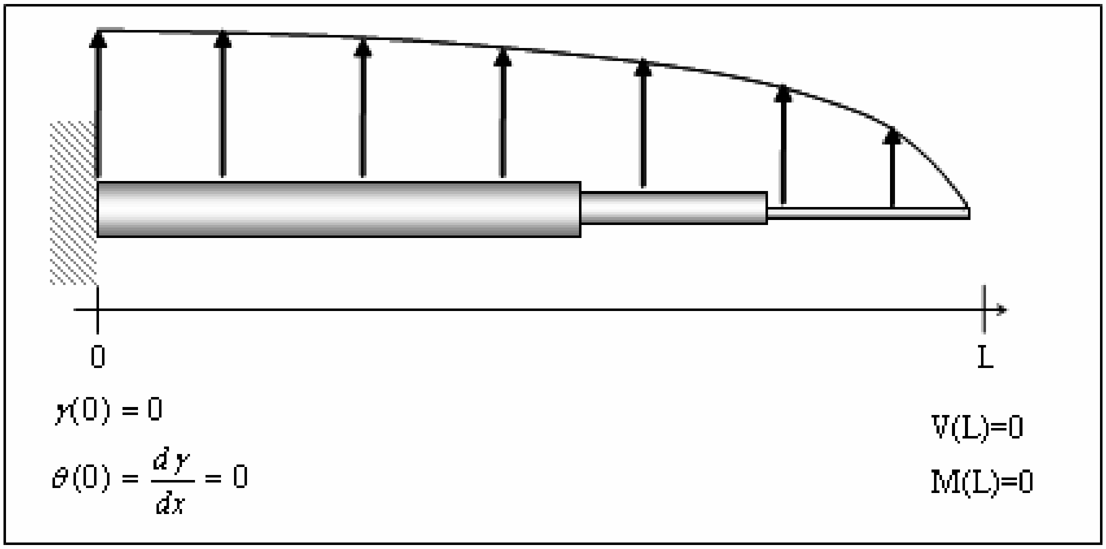

Figure 54: Elliptical Distribution of Load on the Spars

The lift force over a rectangular wing can be modeled by Prantl's lifting-line theory[7] using the expression of circulation for an elliptical lift distribution (it is the case for a rectangular wing). Calculations for α=6 deg. and V_∞ = 30mph = 44 ft/s.

Circulation distribution: $$\Gamma(x) = \Gamma_o \sqrt{1 - \left(2\frac{x}{b}\right)^2} \quad (14)$$

Maximum circulation: $$\Gamma o = bV_\infty \alpha \left(\frac{\pi}{180}\right) \quad (15)$$

Local lift distribution: $$L_l(x) = \rho_\infty . V_\infty . \Gamma(x) \quad (16)$$

Shear and Moment: $$\frac{dV}{dx} = -L(x) \quad \text{and} \quad \frac{dM}{dx} = V(x) \quad (17)$$

Constants: $$C_1 = \rho_\infty . V_\infty . \Gamma o \quad \text{and} \quad C_2 = \frac{4}{b^2} \quad (18)$$

$$a = \frac{1}{\sqrt{C_2}} \quad \text{and} \quad b = 2.L \quad (19)$$

Integration of the lift distribution then integration of the shear gives the expression for the maximum bending stress (moment at the root), that was calculated (see Appendix IV) the values of angle and speed mentioned earlier and in the most critical case (L is the maximum length L=38”):

$$M(0) = \frac{C_1.\sqrt{C_2}}{2}.\frac{\left(a^2\right)^{\frac{3}{2}}}{3} + \frac{C_1.\sqrt{C_2}}{2}.\left[-\left(a^2 - L^2\right)^{\frac{3}{2}}\right] + \frac{C_1.\sqrt{C_2}.a^2}{2}.\left[a.\ln\left(\tan\frac{L}{2a}\right)\right]$$

$$+ L.C_1.\sqrt{C_2}.\left[\frac{L}{2}.\sqrt{a^2 - L^2} + \frac{a^2}{2}.\sin^{-1}\left(\frac{L}{a}\right)\right] = 10.3 \text{ lbf.ft} \qquad (20)$$

This result was compared to a uniform loading and triangular loading with the same maximum loading at the root ($L_l(0)$) to ensure that the order of our result was right.

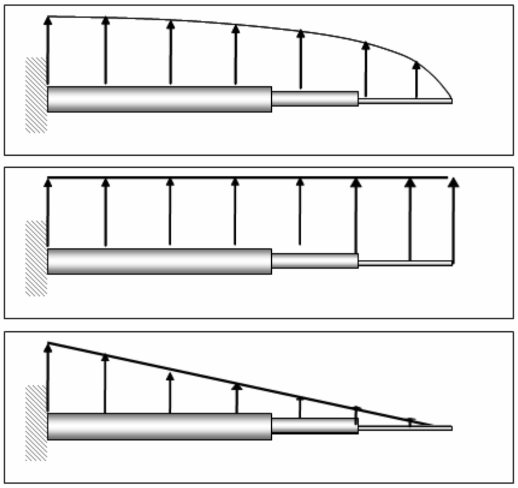

$M(0)_{\text{elliptical loading}}$= 10.3 lbf.ft

$M(0)_{\text{uniform loading}}$=5.328 lbf.ft

$M(0)_{\text{triangular loading}}$=15.9 lbf.ft

Figure 55: Spar under Different types of loading

For the experiment, the Root moment was simulated using 3 equal weights distributed and attached using pulleys, as described earlier, at the end of each section of the spars.

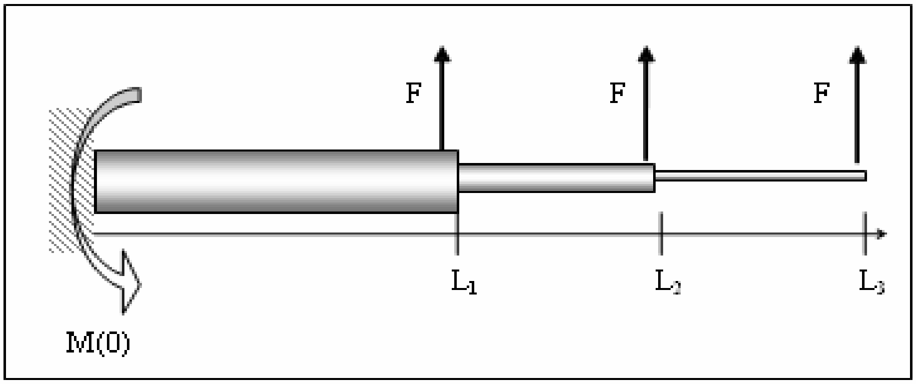

Figure 56: Experimental/Simulation Loading

Moment at the Root: $M_{\text{distributed}}(0) = F.(L_1+L_2+L_3) = M(0)_{\text{elliptical Loading}}$ (21)

The most critical case corresponds to the spar being totally extended (highest moment), therefore we choose: L_1=16.5”, L_2=27.5”, L_3=38”. As a result: F= 1.5 lbs. Using the available weights for the experiments, loading case A corresponds to F_A=1.58 lbs, and loading case B corresponds to F_B=2.68 lbs. The next series of plots display plots of extension and retraction of the two coupled spars at the three different pressures and for the three different loading cases. Each test was repeated 5 times and the curves presented on these plots are averages of all the tests. Nominal standard deviation for these tests is about 0.85, which proves a good repeatability of the motion.

Several expected facts can be observed in both extension and retraction cases:

-The higher the pressure, the faster the motion

-The higher the load the slower the motion

Also, in the extension case, almost every plot shows a sudden change in curve slope. Before that change, both the middle section and the tip section are in motion. After that break, the slope decreases since it corresponds to the motion of the tip section of the spars only.

In the retraction case however, the part before the change of slope corresponds to the middle section on the spars retracting, then only the tip section of the spars can retract. Comparing figures 57 to 59, notice that the break observed is longer when the load increases and shorter when the pressure increases. This is partly explained by a phenomenon of stiction (static friction) observed when the spars are bent by the load. The higher the bending, the higher the force required to overcome the stiction. Note that in loading case B, a pressure of 30Psi is barely sufficient to overcome the stiction. The same phenomenon of stiction is observed at the very beginning of the retraction and followed by a short steep slope.

Close examination of figure 60 to 62 shows an anomaly that could not be explained: in every case, when the load is increased, the time required to complete extension is also increased and the break in curve slope is more pronounced, except in the case of Load B – 30PSI. Experiments were performed several times and the result was consistent.

The phenomenon of stiction that was observed during simulation of the loading likely explains why it was extremely difficult to actuate the wing in the wind, in addition to the fact that the bending of the skin causes additional friction to overcome in order to generate the motion of the mobile sections of the wing.

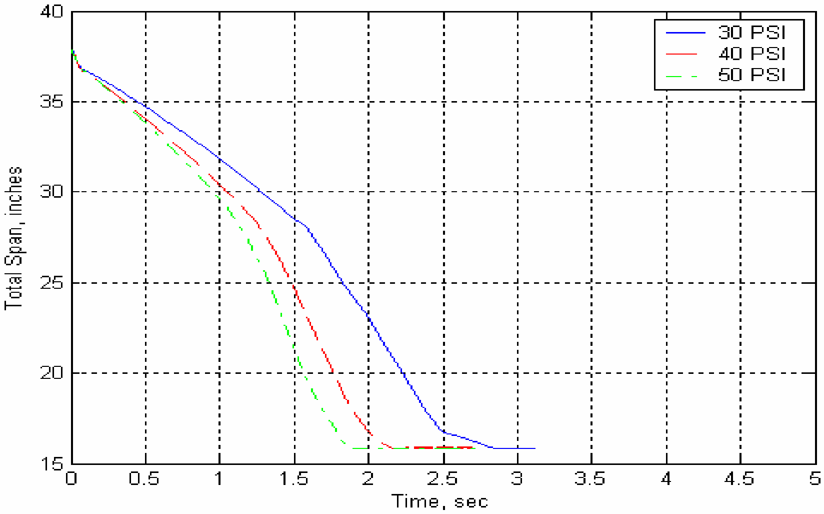

Figure 57: Retraction of the Spars - No Load

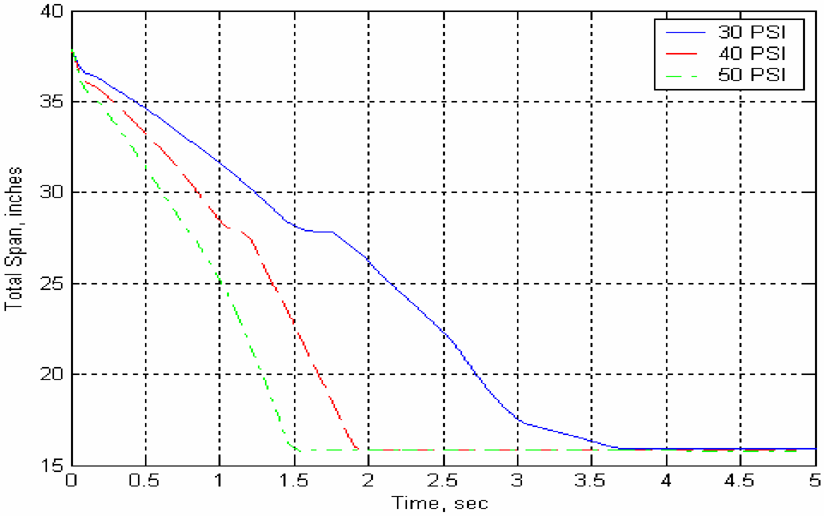

Figure 58: Retraction of the Spars - Load A

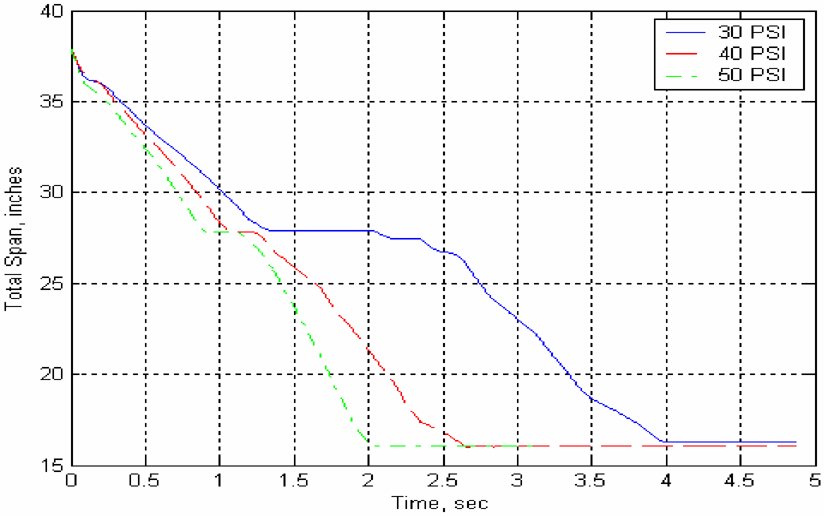

Figure 59: Retraction of the Spars - Load B

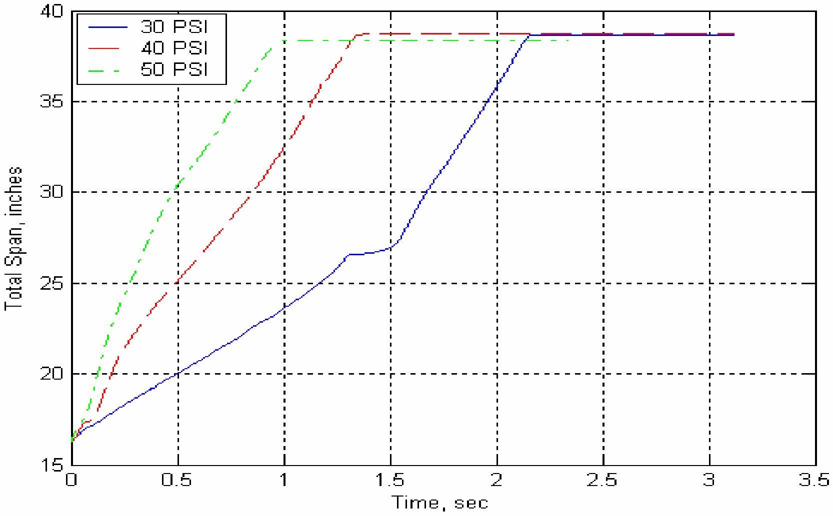

Figure 60: Extension of the Spars - No Load

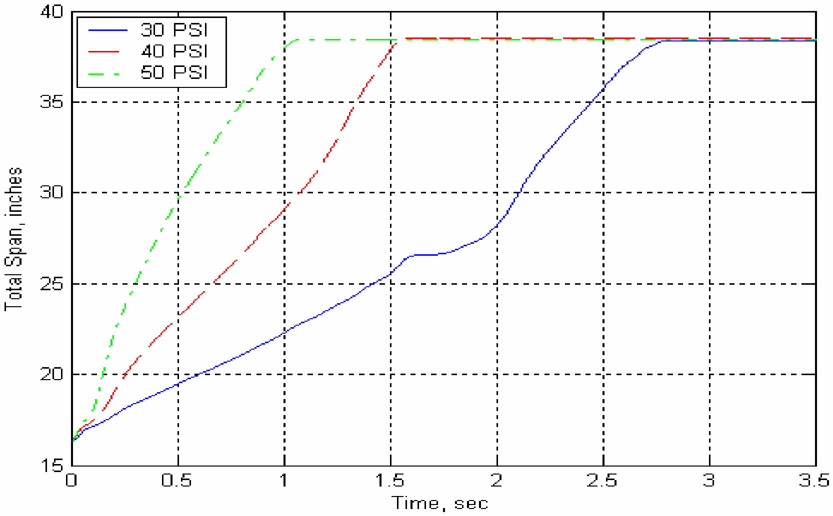

Figure 61: Extension of the Spars - Load A

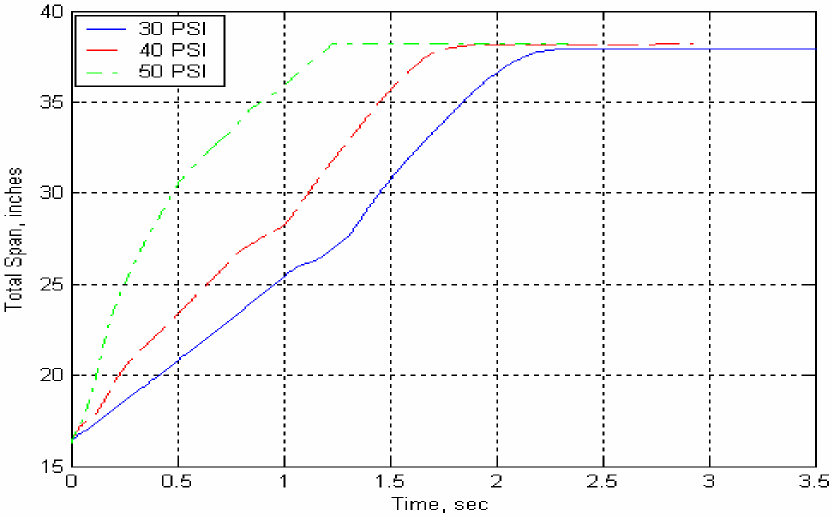

Figure 62: Extension of the Spars - Load B

5.2. Control System

5.2.1. Control System Design

The second generation prototype's control design was critical since the wing was going to be tested in the Glenn Martin Wind Tunnel, and possibly tested in flight. The next step was to integrate a continuous sensing device in the wing assembly and test its reliability. The ideal case would have been to find a length sensor that would have no moving part in contact, but the only option satisfying this requirement, which was the optical sensor, has found to be unusable in the wing assembly for the reasons specified in part 5.1.2.

Therefore it was decided to use a rack and pinion system driving potentiometer to sense the displacement. This choice was motivated by its simplicity and a good durability. A rack was solidly mounted on the each of the two moving ribs and was aligned with the pinion-potentiometer that was solidly mounted to the lower rib.

Consequently, the relative displacement of each section with respect to the lower section could be sensed. Additionally, the potentiometer is a really simple device and has a linear characteristic. It was decided to use a limited-number-of-turns potentiometer in order to avoid counting the turns in the control program, so the characteristics would only be a straight line as opposed to a teeth-like characteristic for an infinite-number-of-turns potentiometer. Figure 63 shows the characteristics of the potentiometers that were used in the Second Generation Prototype

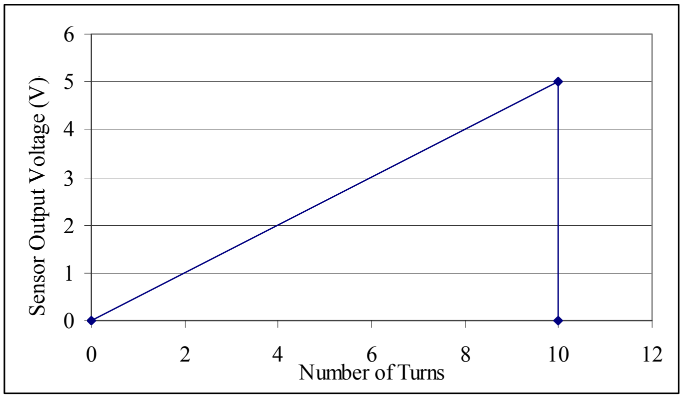

Figure 63: Potentiometer Characteristic

Figure 64 shows the pinion mounted on the potentiometer with the rack that are used in the Second Generation Prototype.

Figure 64: Pinion Mounted on the potentiometer

Figure 65 shows the potentiometer mounted on the Middle section of the wing. The rack that generates the rotation of the pinion is mounted inside the tip element of the wing.

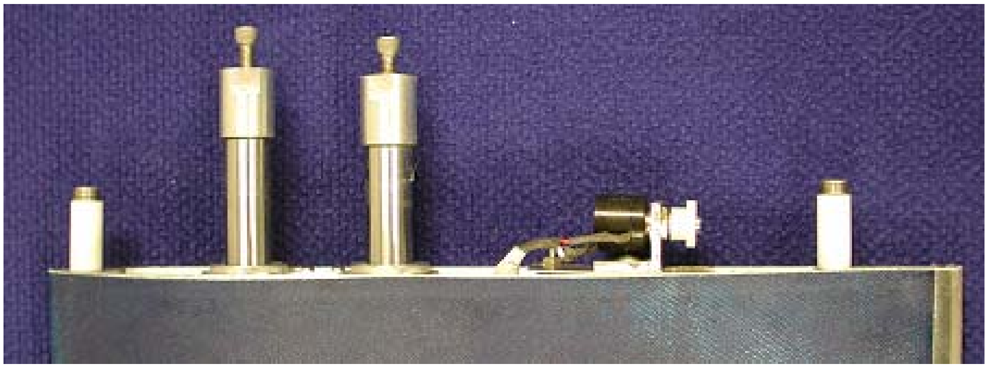

Figure 65: SGP - Potentiometer Mounted on Middle Element

The control logic and program will now be further described.

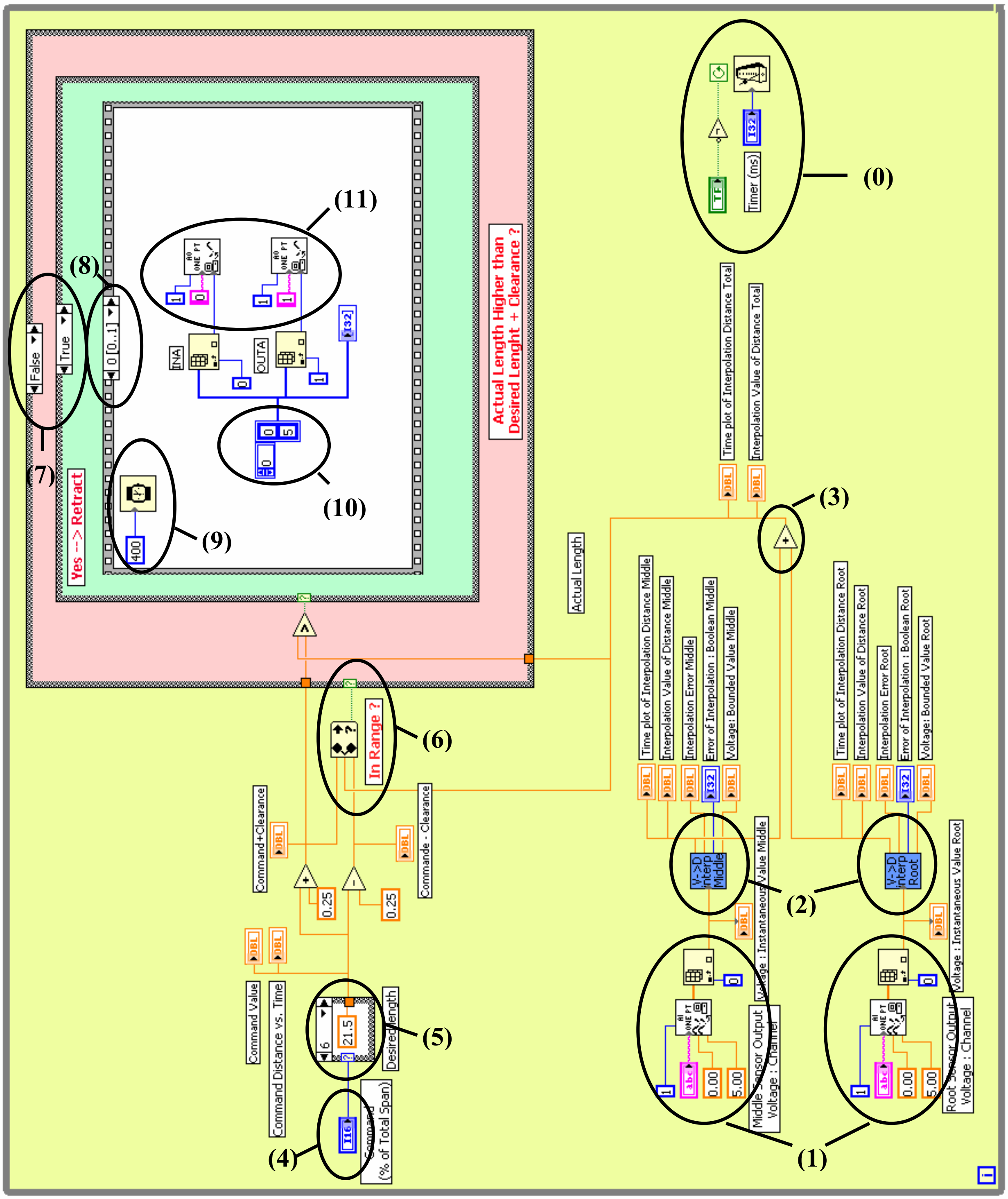

Figure 66 : LabView Control Program - Second Generation Prototype with Continuous Sensing

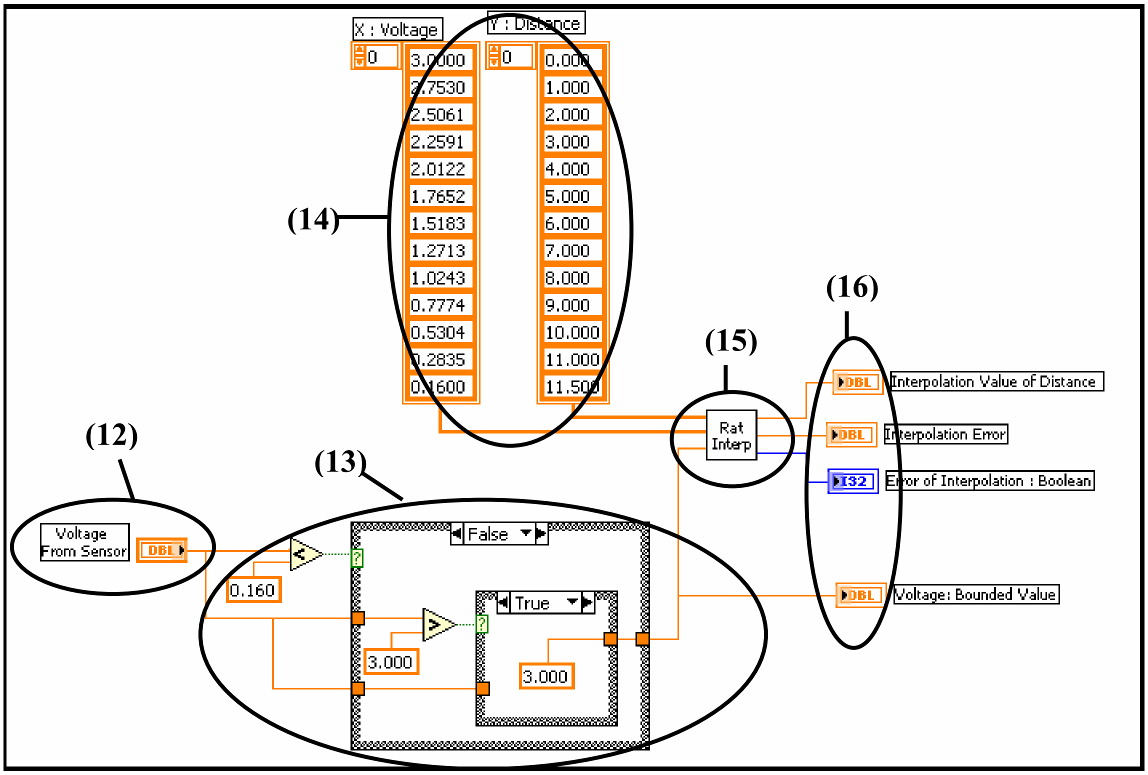

Figure 67 : Extrapolating Function

Let us clarify the LabView control program presented in figure 66.

(0) – The control system is inserted into a time loop, referred as Timer in the User Interface (see figure 68)

(1) – Output voltages from the two sensors are extracted from the terminal through the DAC and called separately into the loop

(2) – For each sensor, the output voltage is transformed into a distance through the Extrapolating Function, based on the calibration of the sensor

(3) – The extrapolated distances from the two sensors are summed up to get the actual length of the wing

(4) – Simultaneously, the control program calls the Command from the user – in percent of the total wing span - through the User Interface (see figure 68)

(5) – This Command in percent of the total wing span is transformed into an actual length in inches

(6) – The actual length is compared to the Command Length: Is it within the range of the Command length +/- a certain clearance (that can be adjusted). The smaller the clearance, the more precise the control

(7) – If the actual length is in the defined range, a set of 0V voltages is sent to the valves. In the illustrated case, the actual length is out of the defined range. The next step is to represent the two cases possible by comparing: Is the actual length above the higher range limit or bellow the lower range limit? A separate case-window is created for each case. In the illustration, the actual length is higher than the higher range limit

(8) – Once the case is defined, a set of actions can be initiated. Each action set is built in a sequence of two frames.

(9) – Each frame is time limited: the action will be performed until the timer expires. Note that the total of the two frame timers should be equal to the main loop timer value.

(10) – In every case, the first frame will correspond to an action period (extension/retraction generated by sending 0V/5V to the appropriate set of valves) and the second frame will correspond to a period of rest (0V is sent to all the valves to close them) in order to let the pneumatic effects happen and dissipate.

(11) – Simultaneously the command signals are sent to the valves

Let’s now describe the subprogram interpolating functions used to transform the output voltage of each sensor in a length in inches. Once of these Interpolation Programs is displayed on figure 67.

(12) – The voltage from the length sensor, called by the main control program, is the input of the interpolation function. There is an interpolation function for each program.

(13) – In case voltage discrepancies (sensor voltage being higher than the higher expected value or lower than the lowest expected value), the function needs to be protected in order to give meaningful values. Therefore a bounding function is created. The bounded voltage is the first input to the rational interpolation function provided by LabView.

(14) – A set of calibration values is also input into the rational interpolation function. One of the vectors represents length points; The other vector is filled with the corresponding values of voltage.

(15) – The rational interpolation function uses the calibration vectors to calculate and output the value of distance corresponding to the input value of voltage

(16) – The outputs of this window are sent to the output of the function in the main program.

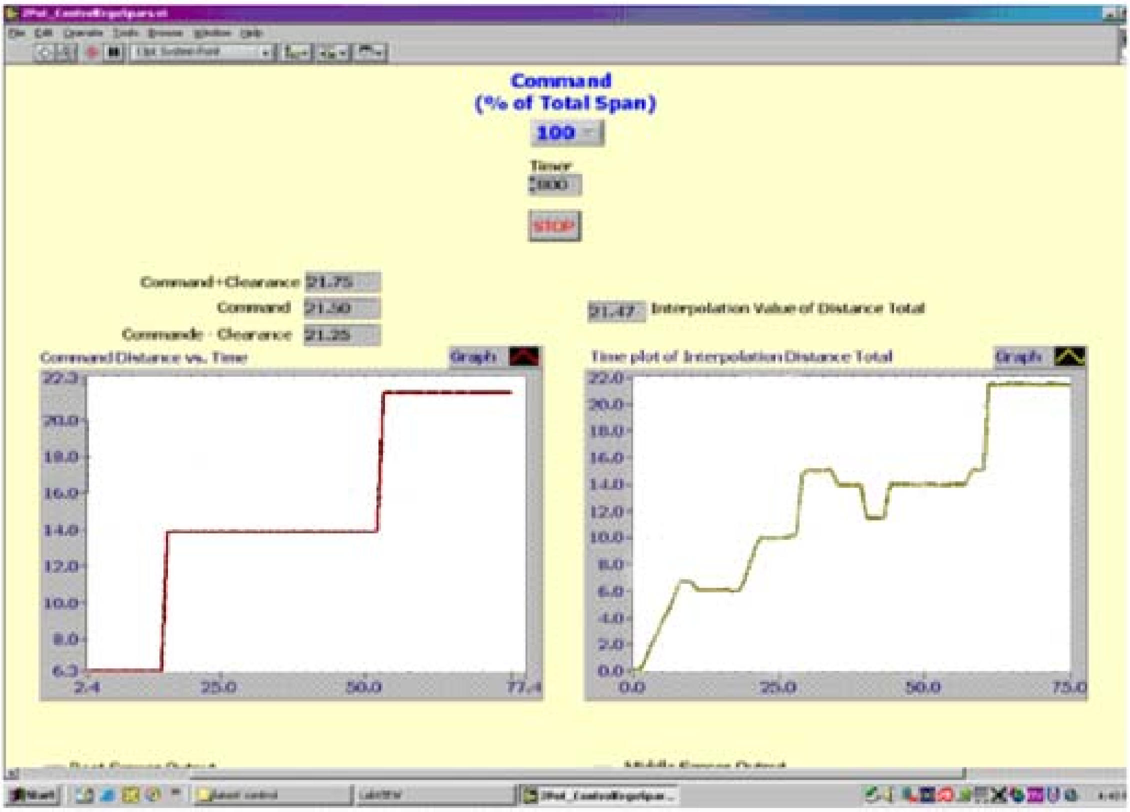

Command
(% of Total Span)
100

Timer
800

Command+Clearance 21.75
Command 21.50
Commande - Clearance 21.25

21.47 Interpolation Value of Distance Total

Figure 68 : User Interface

5.2.2. Performance of the control program.

The performance of the control program is a factor relatively hard to asses since it depends on numerous factors, which influence in a more or less drastic fashion the precision of the controller. Let's identify each of these factors and define their weight on the controller's accuracy:

- The main loop timer value (see legend 0 on previous figure): it defines how frequently the sensors output are collected and compared to the user command. Theoretically, the more frequent the comparison, the faster the controller will react.

- The individual action frames timer value (see legend 9 on previous figure): Let us recall that for each main loop timer value, two individual frames follow each other (action and rest). It was determined that since the main loop timer value is on the order of 400 to 800 ms, the rest period should be about the same length as the action period in order to let the pneumatic effects happen and dissipate. Making a rest period to short relative to the action period may result in a delay in the next action period, and extensively may cause the actuator to respond in an unwanted manner.
- The clearance on the total length tolerated by the control program: this parameter is defined at the comparison stage - between the actual length and the desired length (see legend 6 on previous figure). The clearance (negative or positive discrepancy) drives directly the overall precision of the controller. However, it is crucial to remember that below a certain value of clearance the pneumatic effects do not have enough time to dissipate. As a result, the wing span keeps oscillating around the desired length and never reaches stability.
- The operating pressure for the extension and retraction of the actuator: This parameter defines the amplitude of the pneumatic effects. If the pressure is too high, the wing will increase or decrease fast, with very large increments, which will most likely result in an overshoot of the desired length. If the operating pressure is too low, it will take several cycles of the main time loop before the actuators actually start to react to the inputs of pressure because there are friction forces as well as compressibility effects to overcome.

- The aerodynamic forces supported by the wing: the higher the aerodynamic forces, the higher pressure is required to actuate the wing. The initial time response is greatly affected as well.

A general rule would be to make sure that the rest time is long enough, and that a large pressure is matched with a very small main loop timer value. Conversely, a low pressure should be matched with a larger main loop timer value.

It was experimentally determined that the following combination of parameters was satisfying: Main loop timer of 400 ms, Action frame timer of 200ms and rest frame timer of 200ms, Imprecision (clearance) of 0.25" , which represents 0.65% of the total wingspan, Actuating pressure of 30 PSI. For the given values, the error was recorded to be:

- 0.65% average for a retraction case from 100% to 80% wingspan in 2 seconds
- 0.33% average for a retraction case from 100% to 60% wingspan in 3.6 seconds
- 0.0% average for a retraction case from 100% to 80% wingspan in 4 seconds

Figure 69 presents an example of usage of the controller: the top screen displays a distance command sequence given by the user, plotted versus a computer time unit. The bottom screen displays the actual length of the wing given by the length sensors, plotted versus the same time unit. A comparison of those plots shows the response delay of the spars and also that the spar sometime overshoots the desired length be fore the controller forces it back to the desired position. Additionally, the last four teeth of the test shows a time lag at about mid-height, which corresponds to the stiction that prevents the small part of the tube from retracting until the required pressure is attained and the force is overcome.

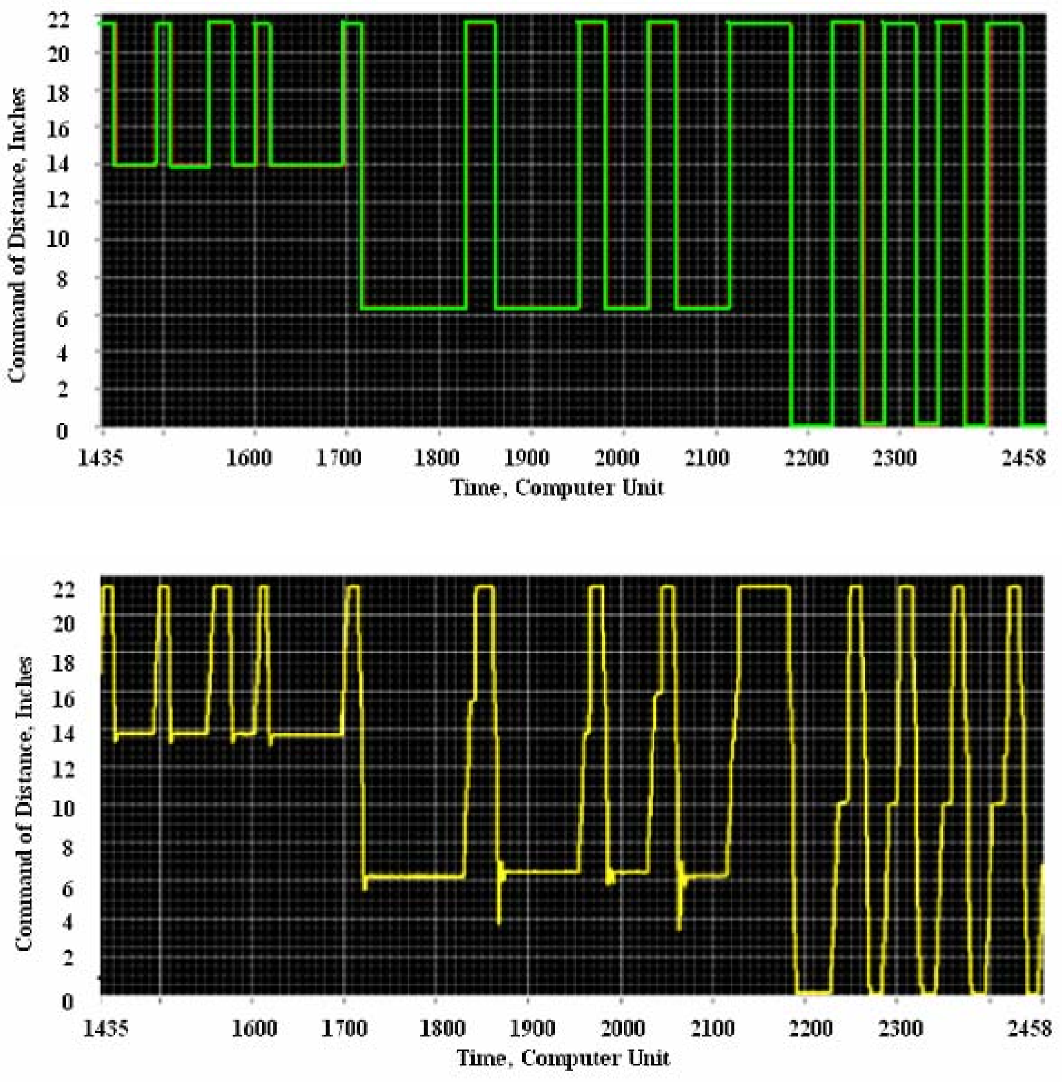

Figure 69: Controller Test Example

5.3. The Telescopic Wing Skin and Ribs: Design and Manufacturing

5.3.1. Skin design and Manufacturing

The Second Generation prototype was designed around the two coupled Ergo-Help actuators placed side by side. Due to the loading requirements, the actuators happened to be rather bulky, which was a challenge for the general design of the wing since both actuators had to be fitted inside the wing.

The smallest airfoil shape was design using the NACA 0013 base equation and adapting the chord so that the two telescopic tubes contour could be contained in it. The two larger shapes were designed to allow en even clearance of 0.060” everywhere around the smaller one. Figure 70 illustrates the design of the telescopic wing airfoil design:

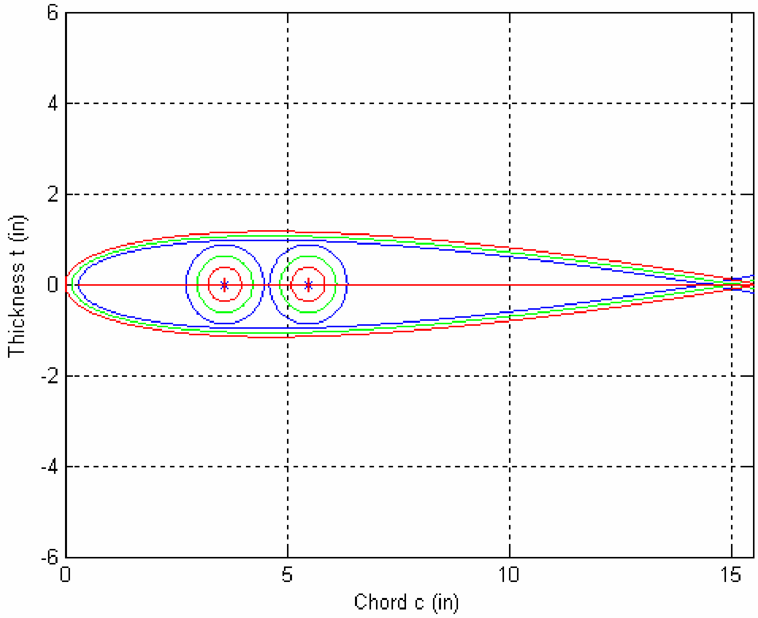

Figure 70: Telescopic Wing Airfoil Design

The manufacturing of the hollow shells for the Second Generation Prototype's wing was composed of several steps. First, thin aluminum templates of the dimensions illustrated on the previous figure were cut out of an aluminum plate using a programmable milling machine. Two templates of each size are required in order to cut airfoils out of stiro foam using hot wire technology.

Once those airfoils are cut, they are wrapped with a layer of Teflon paper, two layers of fiberglass, and another layer of Teflon paper. The purpose of Teflon paper is to prevent the fiberglass from sticking to the foam. Additionally, experience showed that two layers are enough to produce a 0.040" thin taut shell.

At this point, it is critical to verify that the trailing edge of the airfoil is not too long/short, since it can hardly be rectified after curing. The wrapped foam airfoil is then place back in its foam bed and in a vacuum bag be fore being cured at 180F for a minimum of 12 hours. Note that every step in the manufacturing process has to be very carefully executed to avoid bumps and wrinkles on the shell, or worse, that the shell twists during curing.

Also, an inch of span should be added to the airfoil to account for potential melting areas on the edges. Once the airfoil in its bed is cured, the inside foam can be removed by simply pulling on the Teflon paper. Additional steps as sanding and painting are required to ensure smoothness of the shells surface. During every operation it is safe to keep the foam core inside the shell to make sure the structure of the fibers is not going to be damaged.

5.3.2. Ribs design and Manufacturing

The contour design for the airfoil ribs were discussed in the previous section. However, each of them had to be manufactured in different way to be attached at the right location on the spar. The ribs were cut in a 0.25” thick aluminum plate, and the areas described on the above figures were removed in order to make the pieces lighter and provide room for the sensors electric cables and the pneumatic tubes.

The root section rib is slid on the two spars and rests on their attachment piece.

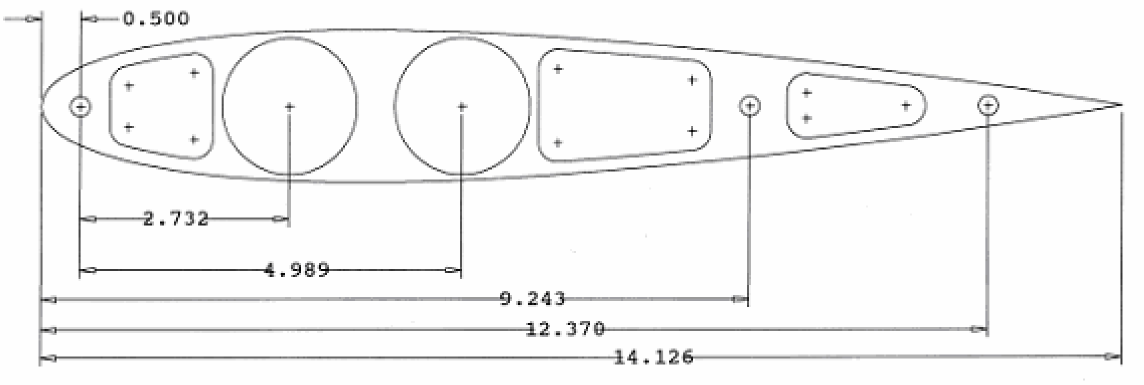

Figure 71: Root Section Rib

The middle section rib was machined so that two screws can be used to tighten and solidly fix the rib at the tip of the spars’ middle section.

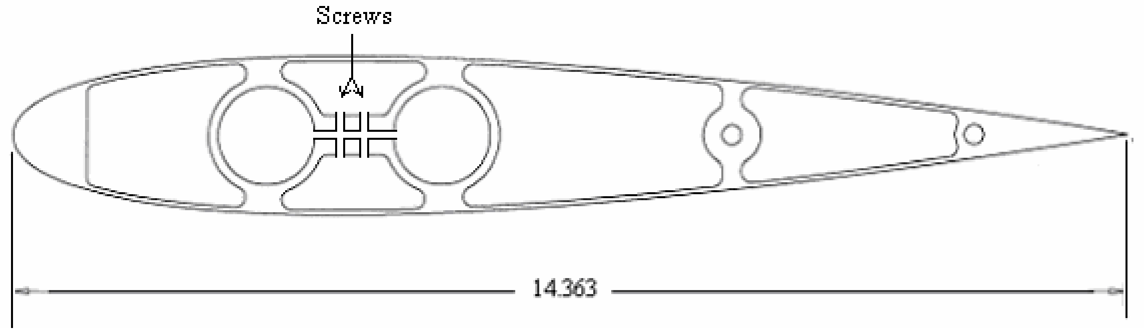

Figure 72: Middle Section Rib

The tip rib section was not completely extruded because it is located at the tip and faces the exterior of the wing. However, some areas were carved to make it lighter, and two squared pockets were created to fit and attach to the end caps of the spars.

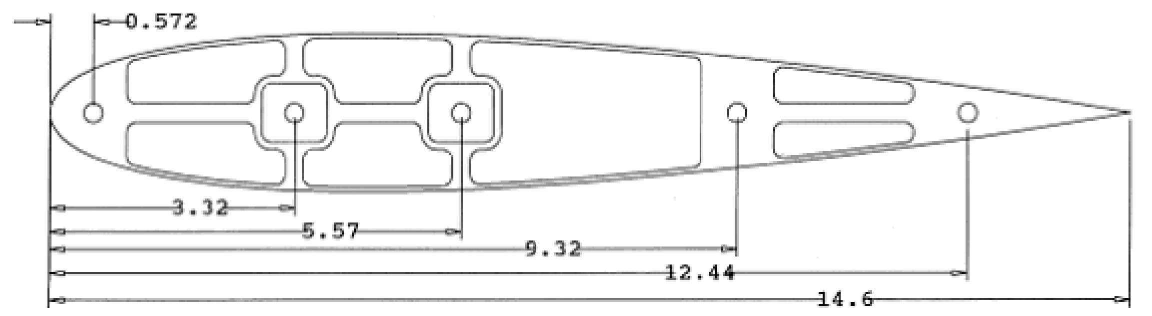

Figure 73: Tip Section Rib

The next section provides detailed pictures of the wing assembly and specifically of the rib sections attached to the spar

5.4. Integrated Wing

The next set of pictures displays details of the Second Generation Prototype being un-mounted.

Figure 74: SGP - Fully Extended Configuration

The tip element of the wing is mounted and attached to the actuators by means of two screws. Once those are removed, the tip element can be slid out

Figure 75 shows detail of the tip of the middle element once the tip element is removed. The actuators and the middle element sensor can be seen on figure 76, as well as two spacers on the far right and far left, which role is to prevent the sensor to be damaged or displaced during retraction of the tip element.

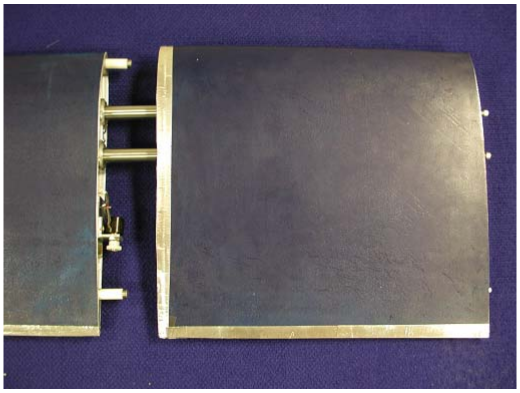

Figure 75: SGP - Tip Element Removal

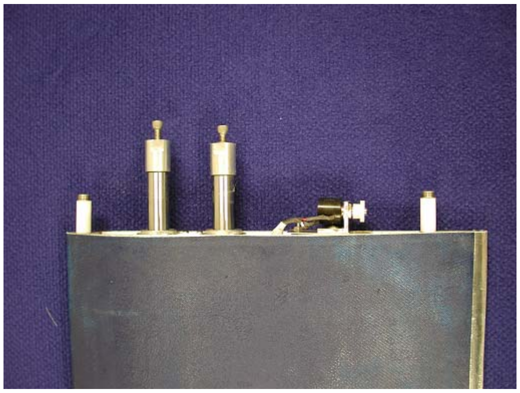

Figure 76: SGP - Tip Element Removed

The two following pictures show details of the rack mounted inside the removed tip element and a top view of the middle element, specifically the sensor mounting.

Figure 77: SGP - Tip Element: Rack Mounting

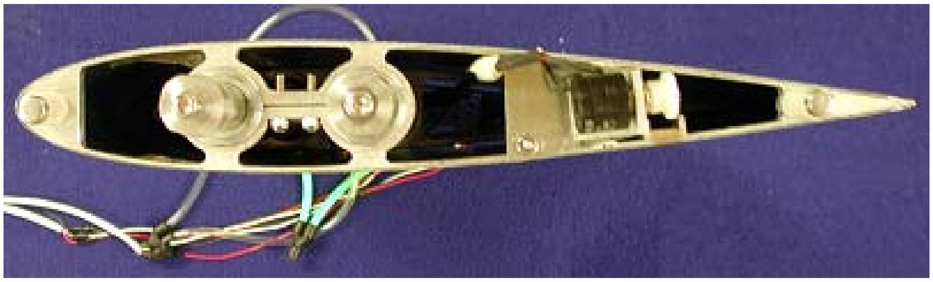

Figure 78: SGP - Middle Element: Attachment and Sensor

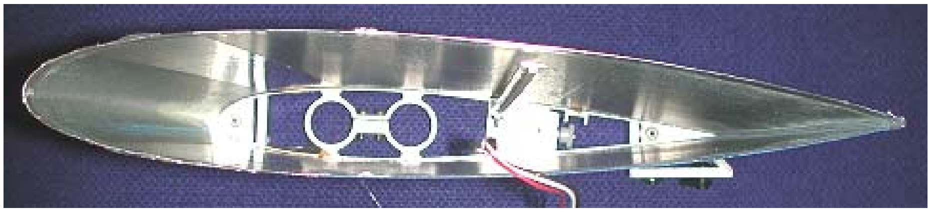

Figure 79: SGP - Middle Element: Rack Mounting

Once the tight screws are removed, the middle element can be removed. Figure 80 shows detail of the tip of the root element once the middle element is removed. However, note that the sensor can not be seen since it was mounted underneath the rib to not be in the way of the middle element retracting.

Figure 80: SGP - Middle Element Removal

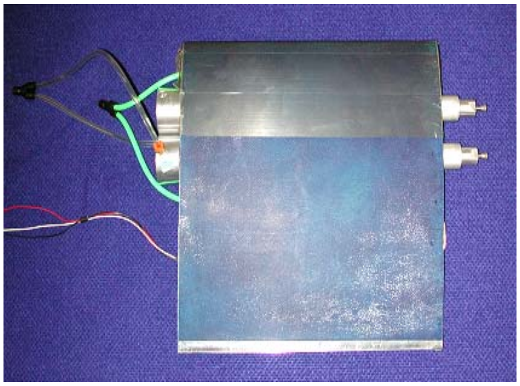

Figure 81:SGP - Middle Element Removed

The next figure display a top view of the root element of the wing, on which can be noticed the tight screw that attached the rib to the spars, and the sensor as well as a guide to force the rack against the pinion.

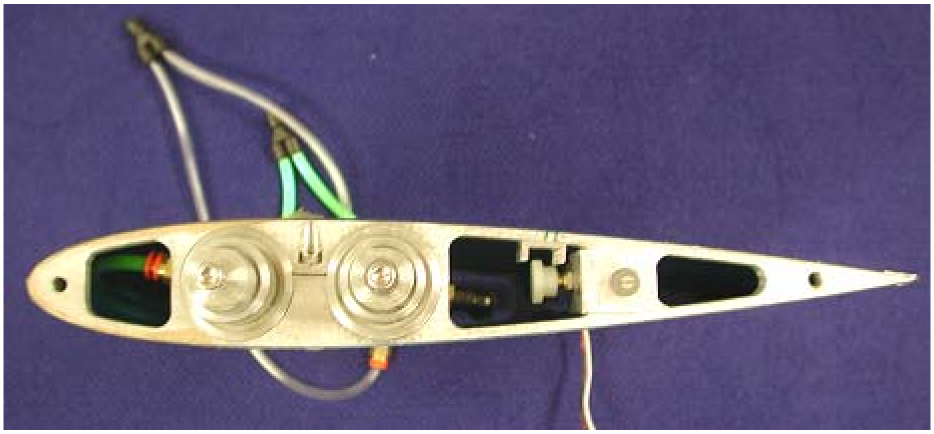

Figure 82: SGP - Root Prototype Attachment and Sensor

After the root skin element is removed the bare pistons can be observed:

Figure 83: SGP - Actuators: Base Attachment

Figure 84: SGP – Actuator

5.5. Analysis of performance

5.5.1. Theoretical Aerodynamic Performance

Lift and induced drag theoretical values were calculated as described in the earlier section using the CFD program X-Foil. The parasite drag values for the second generation prototype are shown in table 7. It is important to mention that the values obtained did not account for the Aspect Ratio, but were only dependent on the airfoil geometry and the Reynolds number. The sets of parasite drag values obtained seemed to diverge drastically above a 14 degrees angle of attack; therefore it was decided to account for a constant value of parasite drag, equal the 14 degrees value, above this angle.

5.5.2. Wind Tunnel Testing: Test Setup

The wind tunnel tests of the full scale wing were conducted at the Glenn L. Martin Wind Tunnel facility at University of Maryland in March 2004.

The test section is 7.75’ high x 11.04’ wide, and the flow speed ranges from 2mph to 230mph (ie. from M=0.0 to M=0.3). The experiments were conducted on a six-component yoke type balance with the following component precision: Lift: 0.1 lbs, Drag: 0.05 lbs, Pitch: 0.1 ft-lbs, Yaw: 0.1 ft-lbs, Roll: 0.25 ft-lbs, Side Force: 0.1 lbs.

Table 7: Parasite Drag Coefficients for given Reynolds Numbers

Re	227,390	284,390	341,120
α (˚)	C_{Dp}	C_{Dp}	C_{Dp}
0	0.00937	0.00818	0.00749
1	0.01043	0.00921	0.00841
2	0.0119	0.0111	0.01039
3	0.01442	0.01351	0.01286
4	0.01905	0.01743	0.01637
5	0.02539	0.02312	0.02164
6	0.03556	0.03165	0.02858
7	0.05362	0.04543	0.04126
8	0.18305	0.08646	0.0688
10	0.19871	0.15882	0.09927
12	0.21137	0.16943	0.21067
14	0.22773	0.17996	0.22119
16	0.24151	0.19189	0.23926
17	0.25486	0.20275	0.25448
18	0.26912	0.21363	0.26612
19	0.28107	0.22525	0.28158
20	0.29517	0.23631	0.2925
21	0.00937	0.00818	0.00749
22	0.01043	0.00921	0.00841
23	0.0119	0.0111	0.01039
24	0.01442	0.01351	0.01286

The wing was mounted vertically on the floating wind tunnel floor, which is directly mounted on the balance. All forces and moments were measured and it was ensured that the aerodynamic center of the wing was aligned with the center of the balance in order to simplify the interpretation of the wind tunnel data. The telescopic wing was tested at three free-stream velocities (20mph, 25mph, and 30mph) and thus Reynolds numbers (227390, 284290, and 341120), at four different spans (40%, 60%, 60% and 80%), and for angles of attack varying from 0 to after stall (estimated between 18 and 24 degrees). Additionally, two foam-core/ fiberglass solid wings, of spans corresponding to the fully-retracted and fully-extended telescopic wing configurations, were tested to verify the order of magnitude of the forces. The test matrix for the telescopic and solid wings is shown next page.

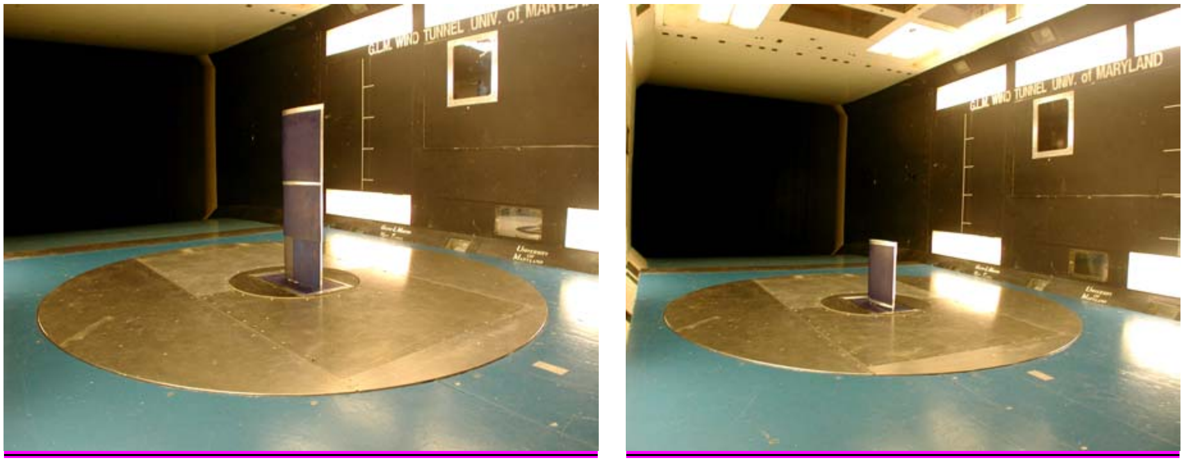

Figure 85: Pneumatic Telescopic Wing mounted in the Glenn L. Martin Wind Tunnel in Extended and Retracted Configurations

Table 8: Test Matrix of Angles of Attack for given Re and Wingspan Configuration

	Wingspan			
Re	16.5”	23.1”	30.8”	38.5”
227,390	0° – 24°	0° – 24°	0° – 24°	0° – 24°
227,390	0° – 24°	0° – 24°	0° – 24°	0° – 24°
227,390	0° – 24°	0° – 24°	0° – 24°	0° – 24°

5.5.3. Characteristics of the Second Generation Prototype

The main airfoil section is NACA 0013 based, with a chord of 14.625”. The wingspan can vary between 16.5” and 38.5”. Seams are reduced at the changes of airfoil section using an aluminum lip.

5.5.4. Expected Results

Considering the wing tunnel results of the previous design[40,41] (stiff hollow telescopic skin elements), and that the aerodynamic performance should be improved after reducing the seams, we expect the experimental maximum Lift to Drag ratio to be about 85% to 90% of the theoretical result in all for all of the three wing spans considered.

5.5.5. Wind Tunnel tests results – Test I:

The next figures show Lift Coefficient (C_L), Drag Coefficient (C_D) and Lift to Drag ratio (L/D) for the telescopic wing in its retracted configuration (40% of maximum span) and in its extended configuration (100% of maximum span). The plots also show theoretical predictions and the solid wing data. Additionally, the following results are only presented for a wind speed of 20 mph, or a Reynolds Number of 227,390, since very similar trends were observed at the other test speeds.

The lift curves, for both configurations, show a pretty good agreement between the three cases (Telescopic Wing, Finite Wing Theory and Solid Wing), even though the theoretical curves seems slightly lower that the two experimental curves. However, in both cases the solid wing shows a constant slightly higher value of lift. Figure 86 also shows that the solid wing stalls 2 degrees earlier than the telescopic wing.

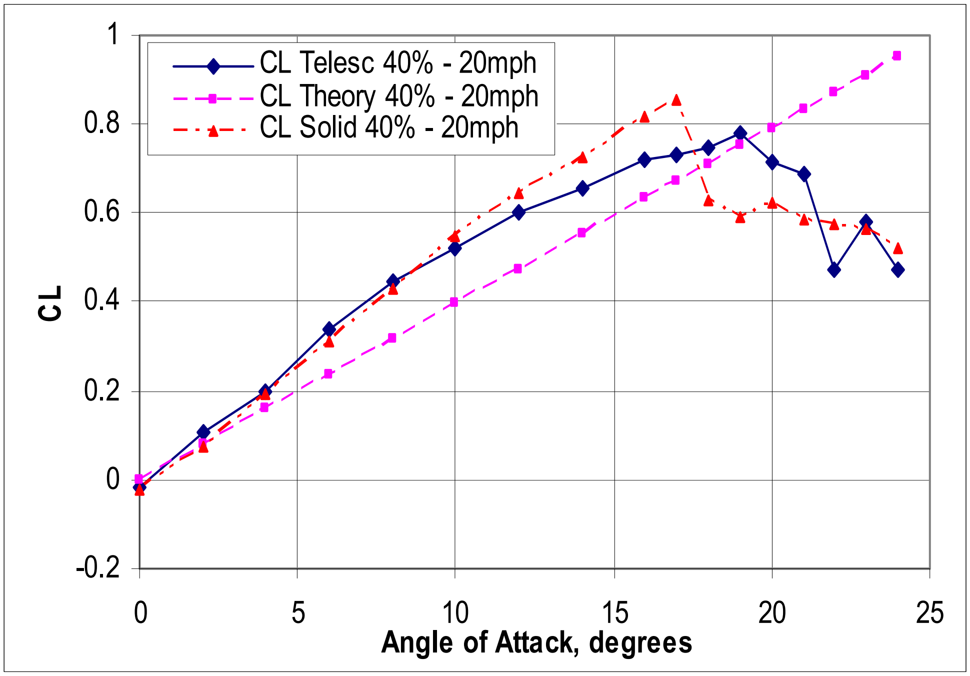

Figure 86: Lift Coefficient vs. Angle of Attack in Retracted Configurations at Re=227,390

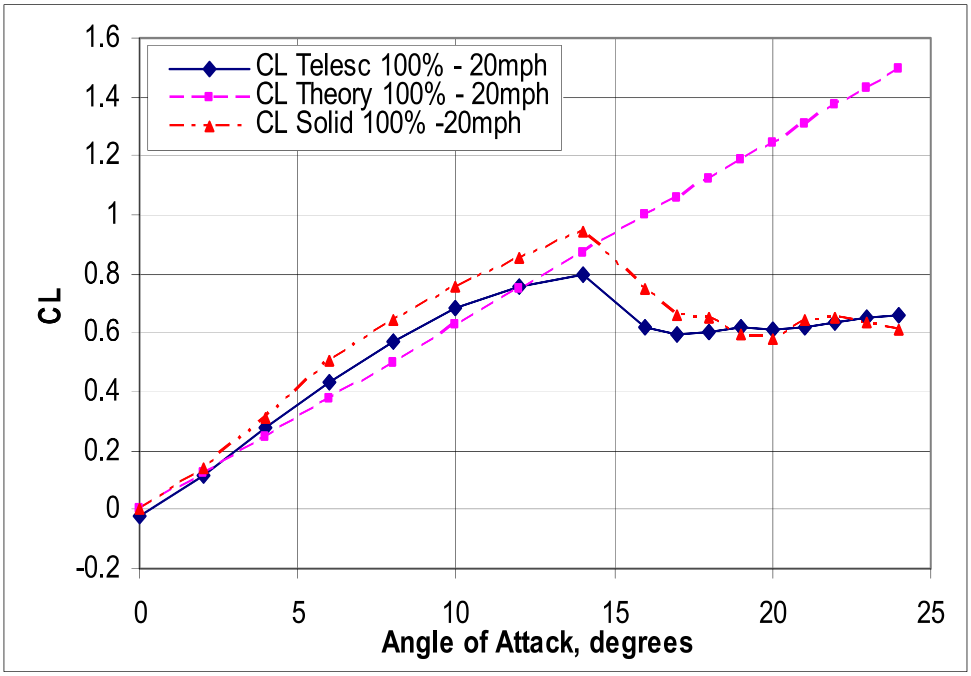

Figure 87: Lift Coefficient vs. Angle of Attack in Extended Configurations at Re=227,390

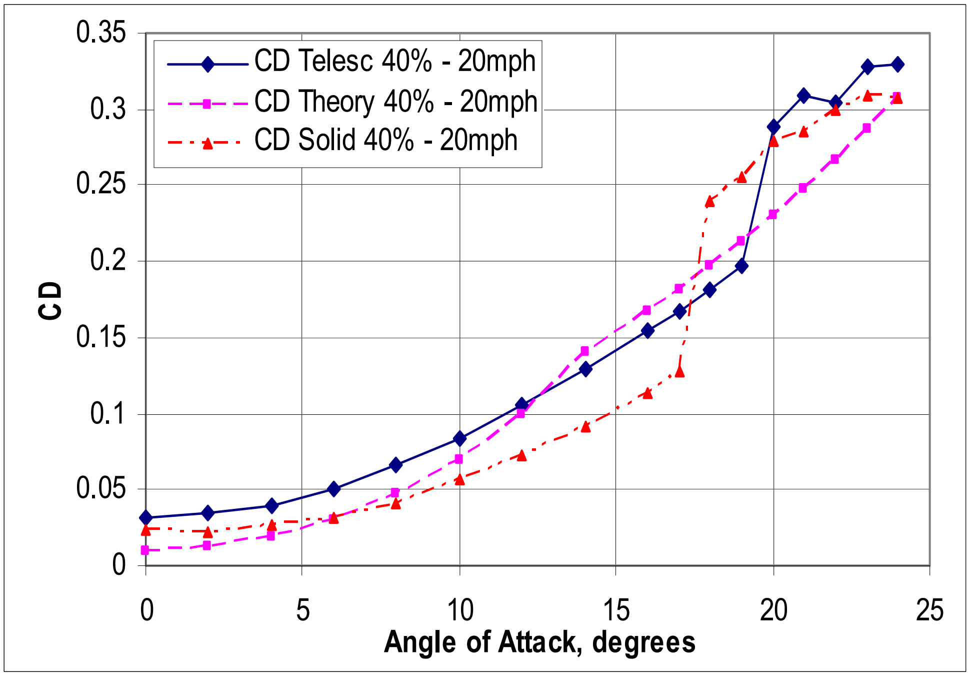

Figure 88: Drag Coefficient vs. Angle of Attack in Retracted Configurations at Re=227,390

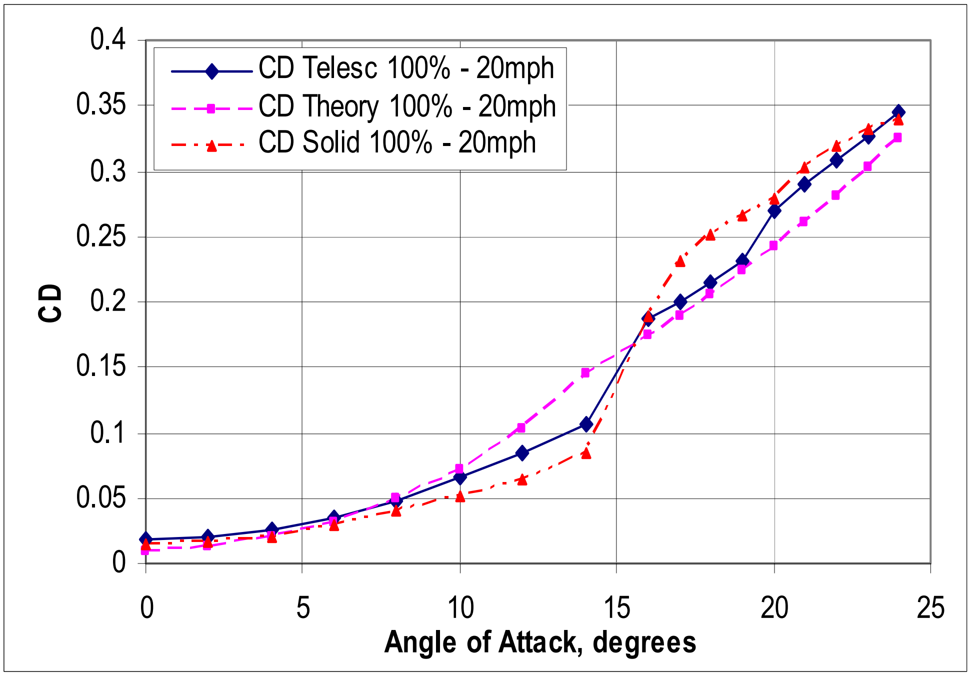

Figure 89: Drag Coefficient vs. Angle of Attack in Extended Configurations at Re=227,390

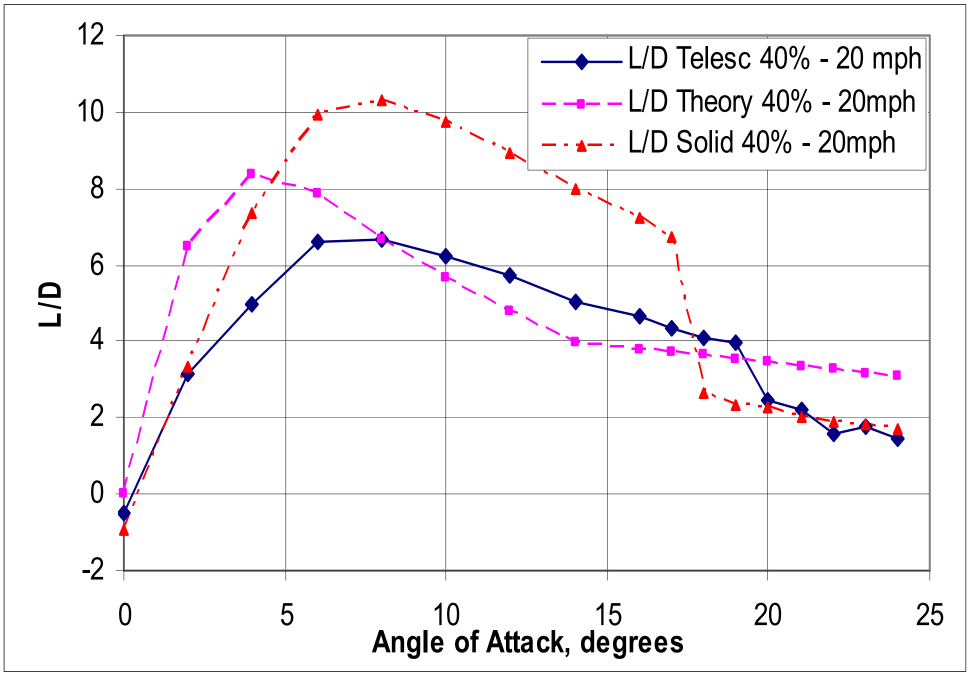

Figure 90: Lift to Drag Ratio vs. Angle of Attack in Retracted Configurations at Re=227,390

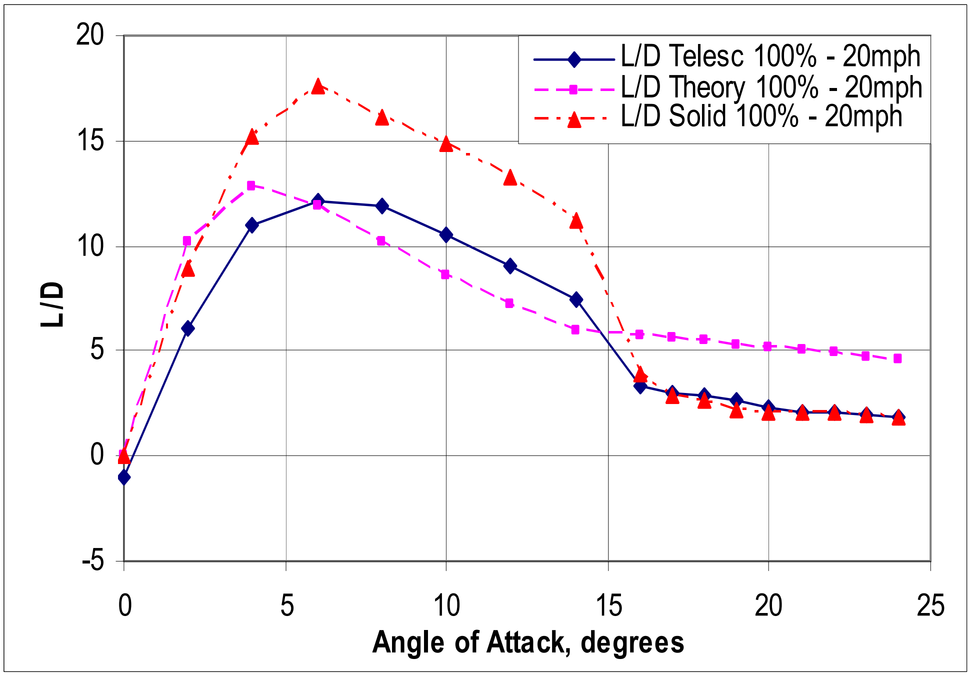

Figure 91: Lift to Drag Ratio vs. Angle of Attack in Extended Configurations at Re=227,390

The drag curves are in good agreement and again, the trends are very similar in both extended and retracted configurations. Nevertheless, the solid wing appears to generate consistently less drag than the telescopic wing. The theoretical value of drag being strongly dependent on the induced drag, which is a function of lift, does not show an abrupt change at the stall angle, but overall the experimental curves match fairly well the theoretical curve.

These discrepancies in lift and drag values for the telescopic wing can potentially be explained by the relative flexibility of the telescopic skin. As the angle of attack increases, the lower surface of the airfoil could potentially be deformed by pressure. This would result in a cambered airfoil that would produce less lift and more drag, as opposed to a symmetric airfoil of similar geometry – for instance, this would be the result expected if a NACA 2413 and a NACA 0013 were to be compared[13]. However, this change in the airfoil section should be accompanied by a delay in stall, which was not consistently observed. For example, Figure 86 shows a delay in the stall angle for the telescopic wing, but Figure 87 does not, or very slightly. Note that this expected slight change in stall angle could be hidden due to testing imprecision.

The differences in lift and drag appear minor but are more profoundly displayed on the Lift to Drag ratio plots (Figures 90 and 91). In the retracted configuration (40% of the maximum span), the telescopic wing underperforms the Theoretical curve by 17% peak to peak which could possibly be justified by the seams at the junction of the telescopic wing skin element. The telescopic wing underperforms the Solid wing curve by approximately 30%. In the extended configuration, the telescopic wing underperforms the Theoretical curve by about 8% peak to peak, and the Solid wing curve by approximately 30%. It is not clear why the solid wing outperforms the theoretical and telescopic curves in such a drastic manner. However, a bending of the mounting spars of the solid wings was observed during testing, which could influence the exactitude of the measured values.

5.5.6. Wind Tunnel Tests Results – Tests II.

Several points of the previous results were not completely explained, and it seemed like most of the incertitude could come from the telescopic model having manufacturing flaws. Therefore, another telescopic wing model and a new solid model (100% wing span) were created taking into account the previous results, and tested in the wind tunnel. Additionally, more attention was paid to the problem of the seams between the different telescopic skins: the question is how much and how do those seams affect the aerodynamic results. Also, it was decided to use a very smooth surfaced tape along the span of the telescopic wing in order to reduce friction, particularly at the leading edge. It was then important to identify the impact of this tape on the surface, since it is located in an area were the boundary layer should be attached. Finally, the wing was deployed in the wind at different angles of attack in order to identify the types of pressures required to actuate the wing under aerodynamic loads in both directions. Complete results of these tests can be found in Appendix III.

The first step that was taken in order to clarify the first wind tunnel test results was to compare the new solid wing with the previous one. A lot of care was taken to ensure that the attachment system would not fail or bend. Half inch threaded rod was epoxyed into the new airfoil, which was bolted through the aluminum mounting plate.

Figures 92 through 94 present the comparison of the aerodynamic performances for the two solid wings of span 100%, at speed 25mph. The closeness of the results proves that the differences encountered in the first series of tests did not involve the solid airfoil, but rather the telescopic wing. However, it appears that the first solid wing model encountered stall earlier than the telescopic wing and also the new solid wing model. This can be explained by the small bending that was observed.

The amount of drag produced by the two solid wing models is very similar up 14 degrees, and then the differences get larger, due to the part of drag due to the lift (induced drag). Finally, the Lift to Drag ratios are extremely close, which shows that the results for the first solid wing model can be used. Note that these are observed as well at 20mph and 30mph.

Figure 92: Comparison of Lift Coefficients for the two Solid Wing models, at 100% span and 25mph

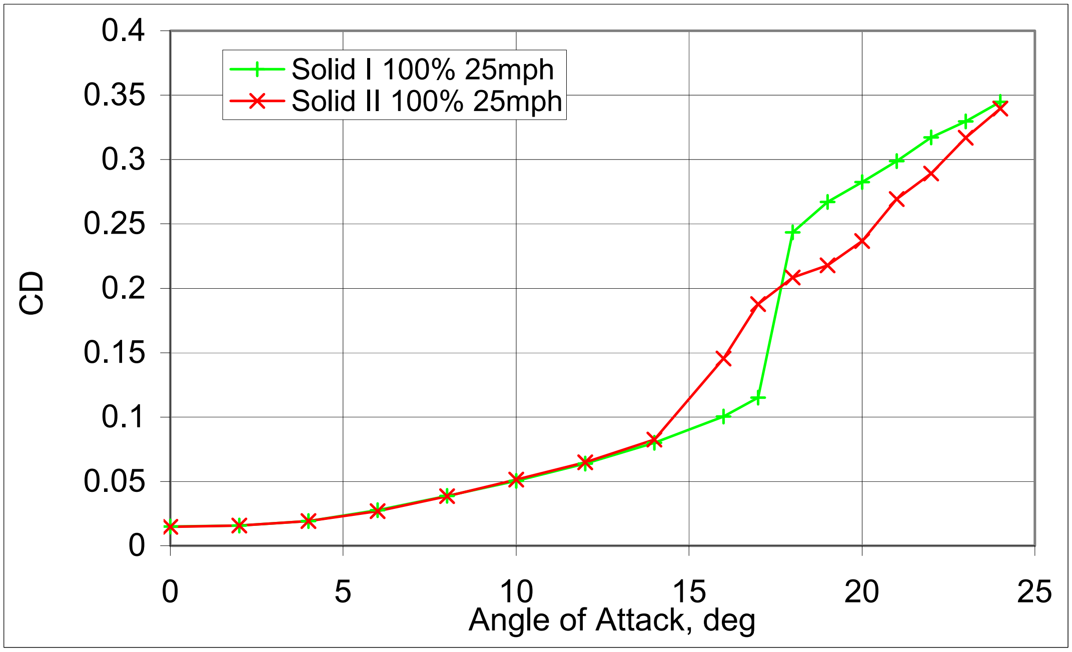

Figure 93: Comparison of Drag Coefficients for the two Solid Wing models, at 100% span and 25mph

Figure 94: Comparison of Lift to Drag Ratios for the two Solid Wing models, at 100% span and 25mph

It is now clear that the unexplained difference between the solid wing's performance and the telescopic wing's performance was due to the telescopic wing. A comparison of the two telescopic wing models and the solid wings can help identifying the issue, using the second model without covering the seams between the telescopic skins (No Tape). Figure 95 through 97 display a comparison of the aerodynamics performance of the two telescopic wings and the solid wing. Looking at the first telescopic model and the second telescopic model with free seams (No Tape), lift values are pretty similar but the first model generates more drag consistently, which results in a much lower lift to drag ratio curve. This confirms that the first model's manufacturing flaws had a very important impact on the wing's performance (the middle elements of the telescopic wing was twisted during curing and was leaving a large opening at the seam). The same conclusions can be drawn at the different wingspans and at 20mph and 30mph.

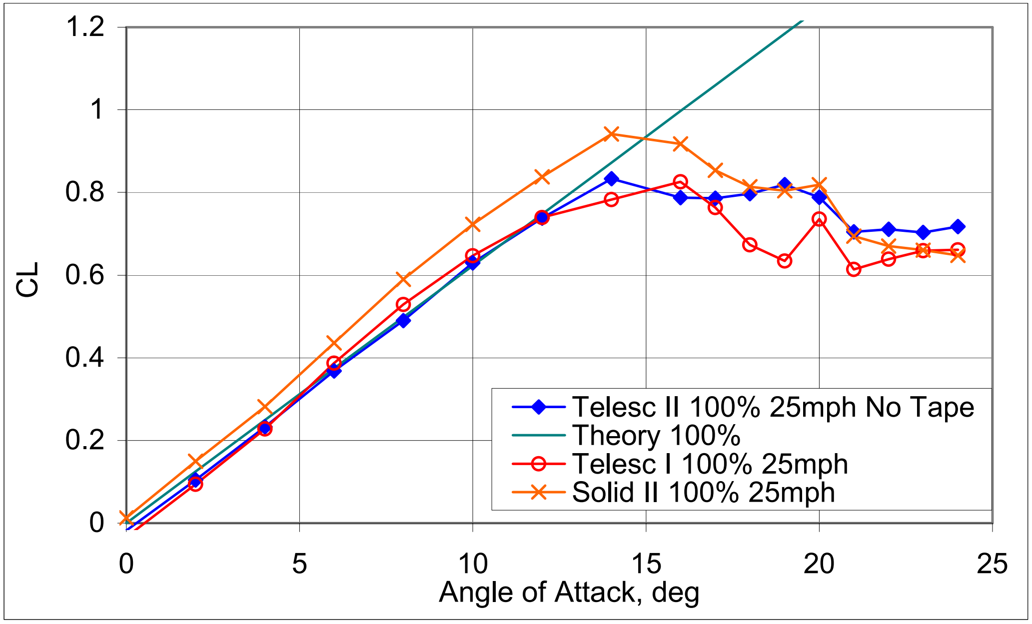

Figure 95: Comparison of Lift Coefficients for the Solid Wing and the two Telescopic Wings, at 100% span and 25mph

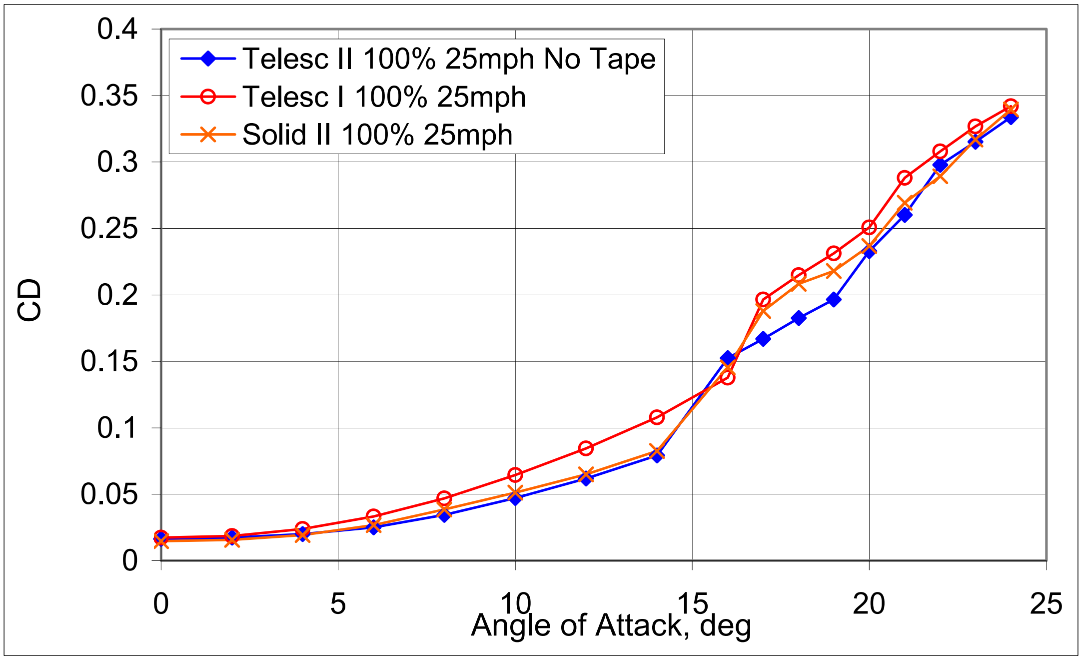

Figure 96: Comparison of Drag Coefficients for the Solid Wing and the two Telescopic Wings, at 100% span and 25mph

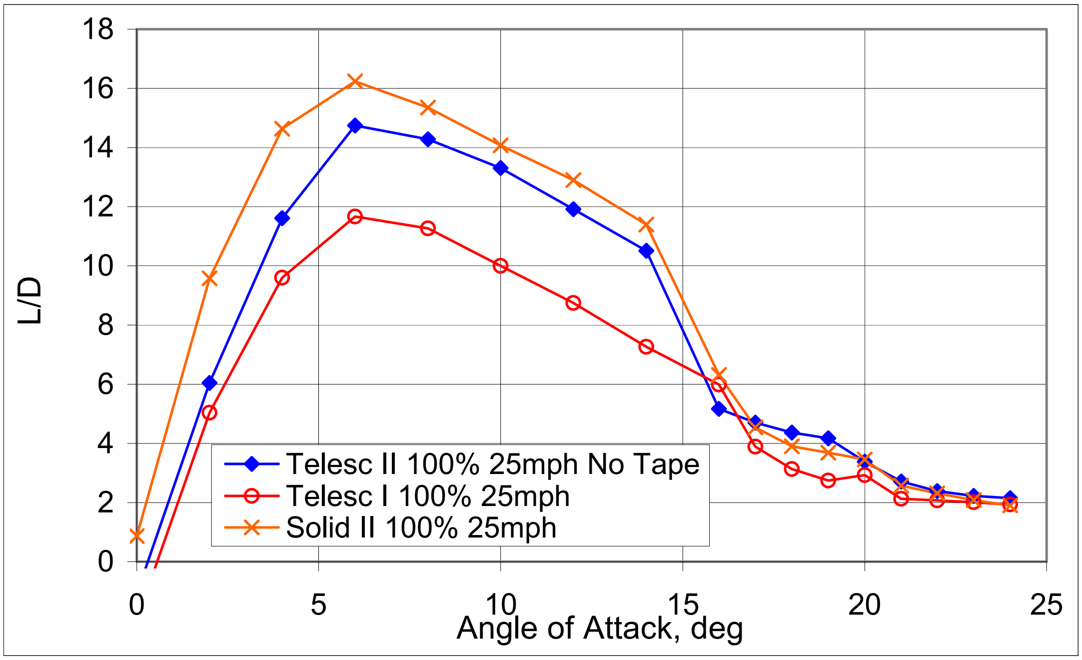

Figure 97: Comparison of Lift to Drag Ratios for the Solid Wing and the two Telescopic Wings, at 100% span and 25mph

Now, the impact of the seams at the interface of the telescopic skin elements on the aerodynamic results can be identified using thin aluminum foil tape. The results are compared for the second model of the telescopic wing with the seams covered and uncovered. Figure 98 through 100 illustrates these results.

It appears that covering the seams affects the both lift and drag values. When the seams are covered, lift and drag are improved consistently and more so when the airfoil approached stalls. It also appears that the influence of the seams is more important on the lift. As a result, lift to drag ratio can be improved by up to 10% for certain wingspan at higher speed (60% wing span at 30 mph).

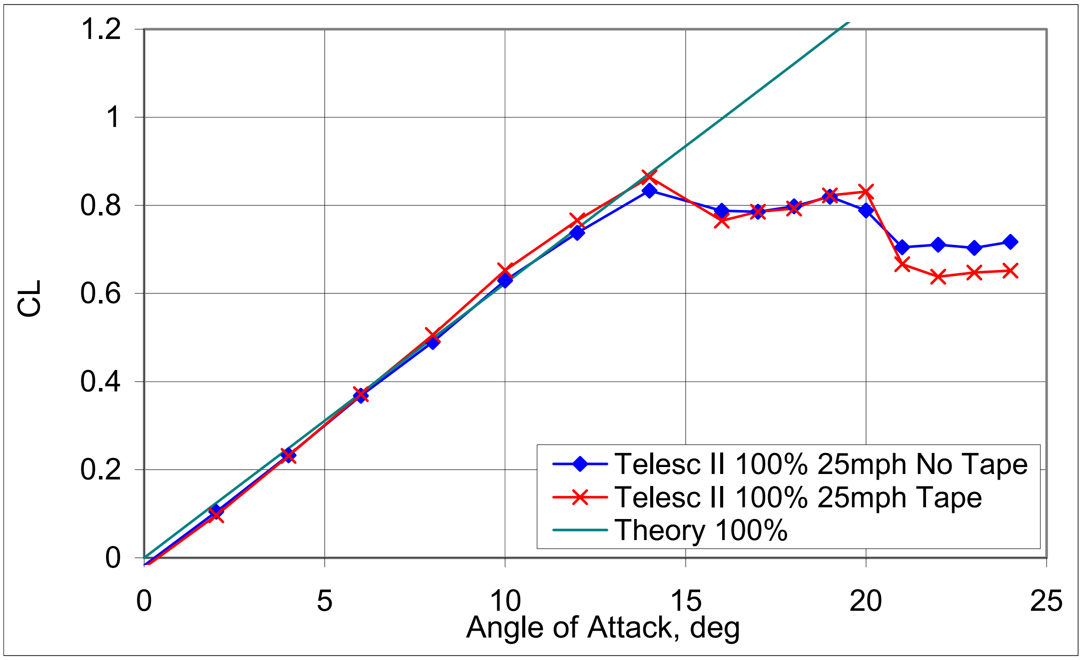

Figure 98: Comparison of Lift Coefficients for the second Telescopic Wing model, at 100% span and 25mph – Impact of the Seams

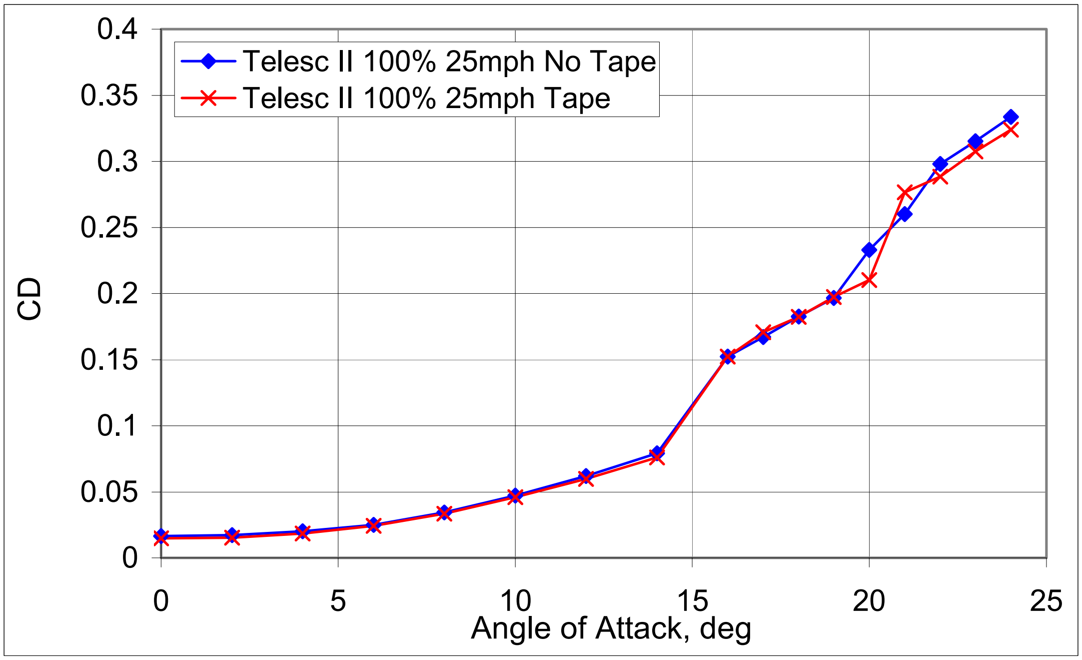

Figure 99: Comparison of Drag Coefficients for the second Telescopic Wing model, at 100% span and 25mph – Impact of the Seams

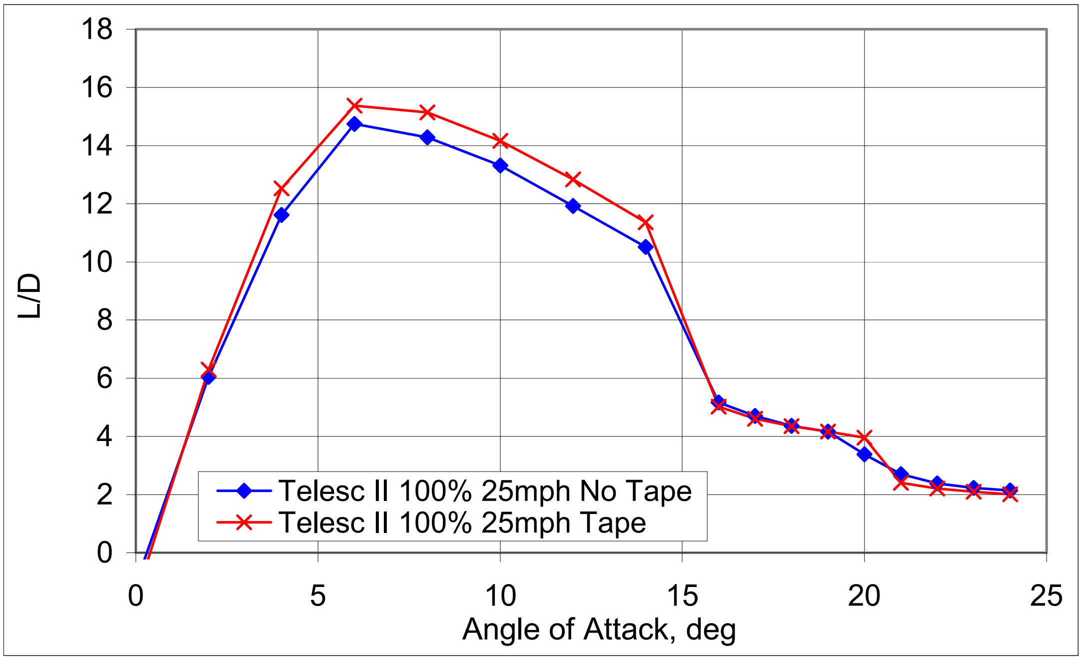

Figure 100: Comparison of Lift to Drag Ratios for the second Telescopic Wing model, at 100% span and 25mph – Impact of the Seams

Finally, the solid wing model was studied in the wind tunnel with friction tape on its surface, in the same pattern as the telescopic wing. Then the tape was removed and the tests were repeated. This helps identif the effect of this tape on the performance of the telescopic wing. Figures 101 through 103 present the results of this test. The lift curves are really close together all the way to stall. It appears consistently (the same results is observed at 20mph and 30mph) that the wing stalls earlier when it wears friction tape on its surface. As a result drag is also slightly different when the angle of attack approached 14 degrees. The Lift to Drag ratios are then very similar in both cases. This gives us an indication that the performance of the telescopic wing should not be affected by the presence of the friction tape on its surface.

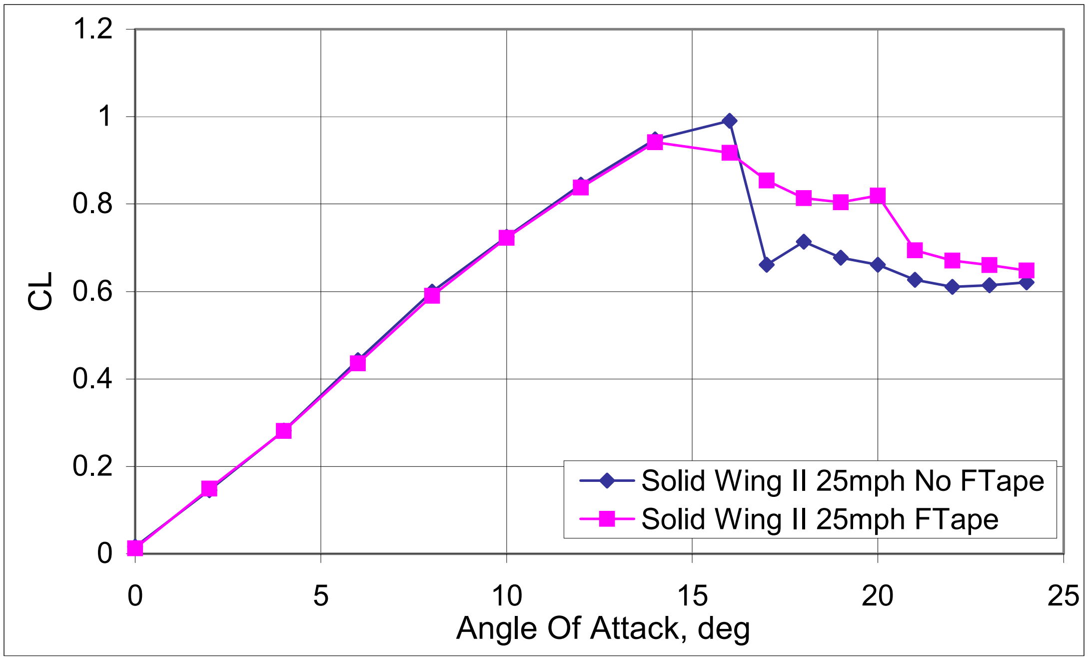

Figure 101: Comparison of Lift Coefficients for Solid wing model, at 100% span and 25mph – Impact of the friction tape.

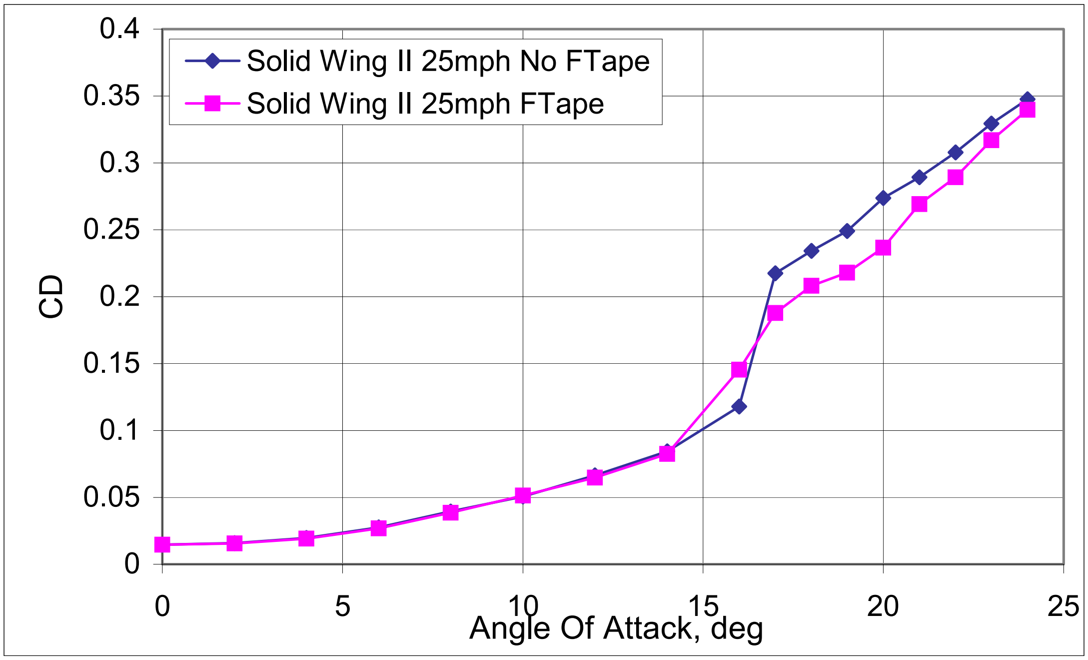

Figure 102: Comparison of Lift Coefficients for Solid wing model, at 100% span and 25mph – Impact of the friction tape.

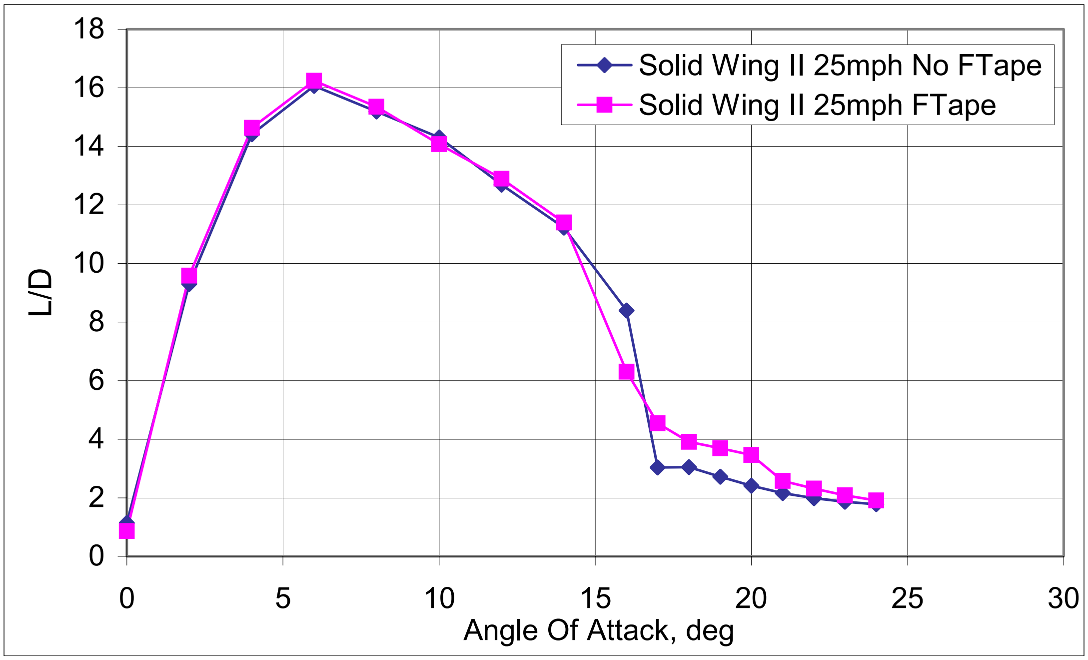

Figure 103: Comparison of Lift Coefficients for Solid wing model, at 100% span and 25mph – Impact of the friction tape.

Note that the conclusions drawn previously are based on a very good repeatability of the aerodynamic results through a range of wing span going from 40% to 100%, and a range of speeds going from 20mph to 30mph. The next table presents the maximum lift to drag ratio values for both the extended and retracted configuration, and at the lowest and highest test speeds.

Table 9: Comparison of the Max. Lift to Drag Ratios at Two Different Speeds (or Reynolds Numbers)

	40% of maximum span		100% of maximum span	
Max L/D	20 mph	30mph	20mph	30mph
Telescopic Wing	9 (α=8 degrees)	9 (α=8 degrees)	14.4 (α=6 degrees)	14.6 (α=6 degrees)
Finite Wing Theory	8.5 (α=4 degrees)	9.5 (α=4 degrees)	13 (α=4 degrees)	14 (α=4 degrees)
Solid Wing	10.5 (α=8 degrees)	11 (α=6 degrees)	15.8 (α=8 degrees)	16.2 (α=6 degrees)

Finally, the wing was deployed in the wind at different angles of attack in order to identify the types of pressures required to actuate the wing under aerodynamic loads in both directions. This systematic characterization of the telescopic wing proves that it can be extended and retracted under aerodynamic loads with pressures as low as 25 psi at low speeds.

Table 10: Extension and Retraction Pressures under Aerodynamic Load

V_∞=20mph	Extension Pressure	Retraction Pressure
AoA= 0 deg	25 psi	40 psi
AoA= 5 deg	25 psi	40 psi
AoA= 10 deg	25 psi	40 psi
AoA= 15 deg	25 psi	45 psi
AoA= 18 deg	25 psi	45 psi

V_∞=30mph	Extension Pressure	Retraction Pressure
AoA= 0 deg	30 psi	40 psi
AoA= 5 deg	30 psi	40 psi
AoA= 10 deg	30 psi	45 psi
AoA= 15 deg	30 psi	45 psi
AoA= 18 deg	30 psi	45 psi

Note that the retraction pressures are consistently lower than the extension pressures. This is expected since the force required to push a piston is proportional to its surface, and the retraction surfaces are smaller than the extension surfaces on the pistons.

Chapter 6: Conclusions and Future Work

Morphing wing technology has been used on manned aircraft over the years, but never on a UAV. Morphing the wing geometry enhances not only the aerodynamic performance, but also the endurance and range of a given airplane. This allows a single aircraft to perform various mission requirements. This paper considers the design, development and testing of a pneumatic telescopic wing. Key elements of the wing consist of a pneumatic telescopic spar, rigid airfoil skins and rib elements. The telescopic wing assembly has the ability to undergo a 230% change in aspect ratio while supporting aerodynamic loads. Preliminary structural analysis suggests that this wing concept is in fact feasible for a small-scale UAV. Wind tunnel test were conducted in the Glenn L. Martin Wind Tunnel at University of Maryland in March 2004 and July 2004. Data from these tests were compared to the theoretical results and confirm that the aerodynamic performance of the telescopic wing suffers slightly of parasitic drag created by the seams of the wing sections and of a softer skin. Nevertheless, in its fully deployed condition the telescopic wing can achieve lift to drag ratios as high as 17, which is as high as its solid foam core wing counterpart. In addition, the wing can be deployed and retracted under aerodynamic load, up to stall and beyond, with pressures as low as 25psi and 45psi.

Future work will involve improvement of the manufacturing techniques to provide stiffer and geometrically perfect telescopic skins in order to guarantee that bending does not cause extra friction during deployment. Fairings will also be developed to seal the seams at all stages of deployment or retraction of the spars. Future work will also involve the determination of the stability and control characteristics as well as the aero-elastic properties of the pneumatic telescopic wing. Ultimately, it is expected that pneumatic morphing wings can be mounted on a UAV to provide roll control.

Recent theoretical study of variable wingspan wing shows advantages such as drag reduction range increase and good roll motion control[42] .

the telescopic wing is a portion of a larger research program on morphing technology at the University of Maryland. In the future, variable aspect ratio, variable wing sweep and variable camber will be combined in a single aircraft's wing.

Appendix I: Wind tunnel results for the first generation prototype

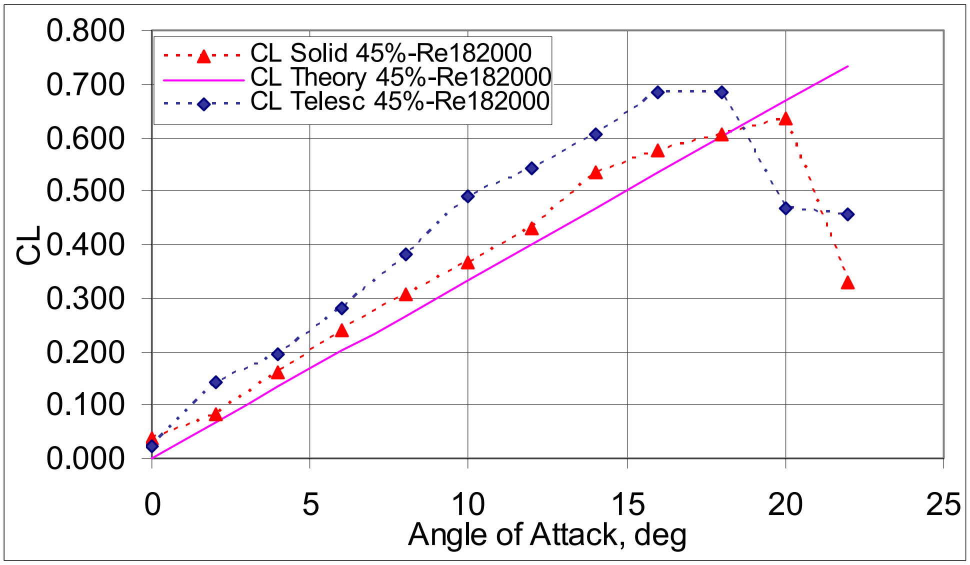
CL Solid 45%-Re182000
CL Theory 45%-Re182000
CL Telesc 45%-Re182000
CL
0.800
0.700
0.600
0.500
0.400
0.300
0.200
0.100
0.000
0
5
10
15
20
25
Angle of Attack, deg

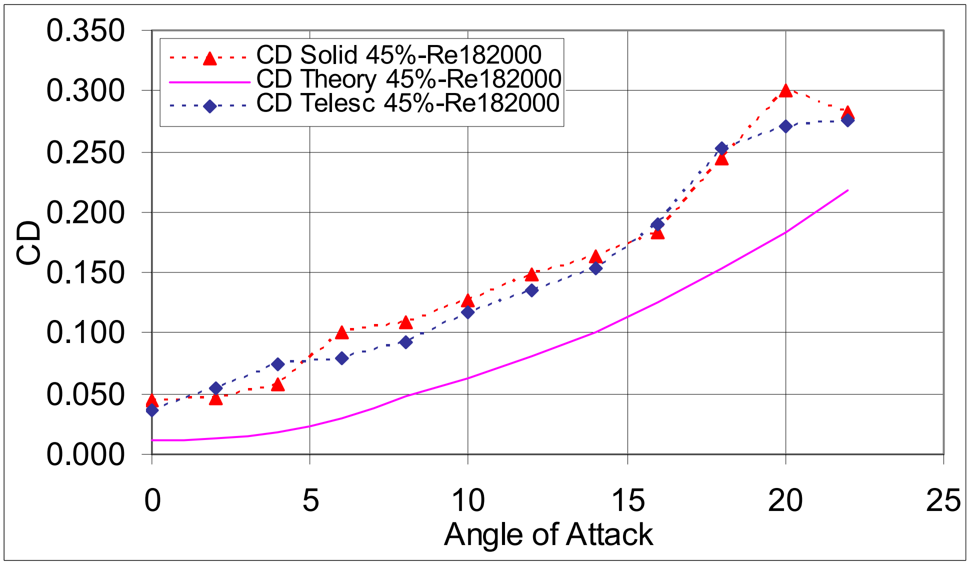
CD Solid 45%-Re182000
CD Theory 45%-Re182000
CD Telesc 45%-Re182000
CD
0.350
0.300
0.250
0.200
0.150
0.100
0.050
0.000
0
5
10
15
20
25
Angle of Attack

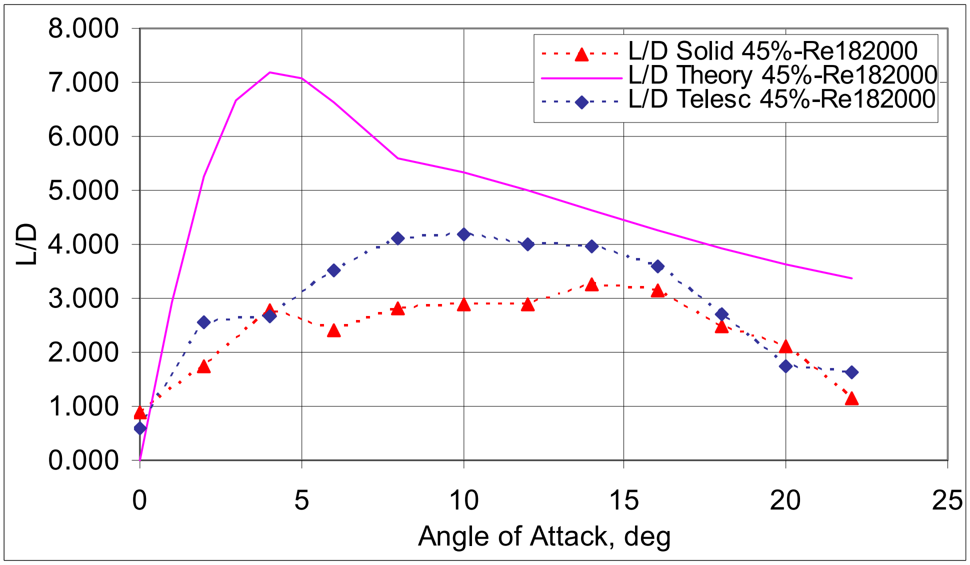
L/D Solid 45%-Re182000
L/D Theory 45%-Re182000
L/D Telesc 45%-Re182000
L/D
8.000
7.000
6.000
5.000
4.000
3.000
2.000
1.000
0.000
0
5
10
15
20
25
Angle of Attack, deg

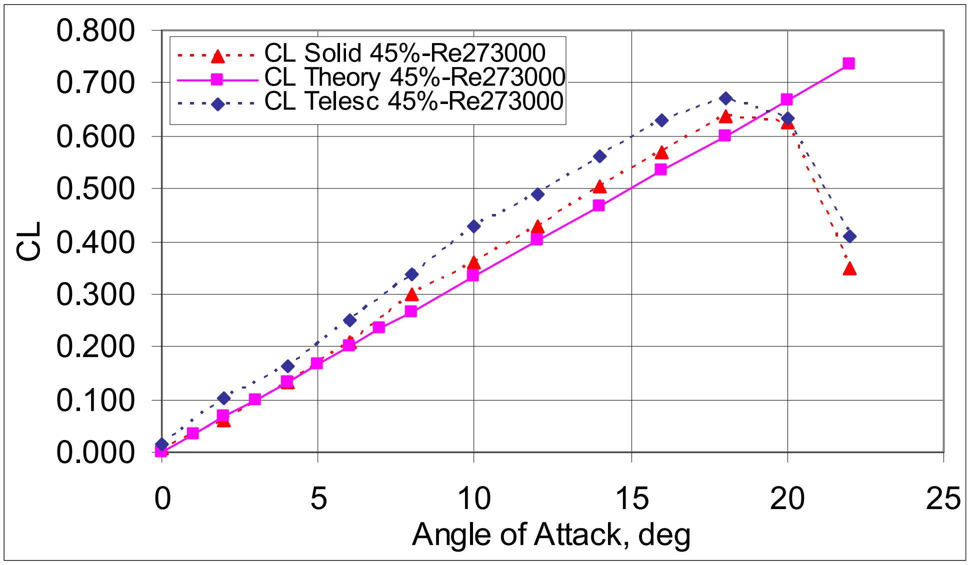

CL Solid 45%-Re273000
CL Theory 45%-Re273000
CL Telesc 45%-Re273000
CL
0.800
0.700
0.600
0.500
0.400
0.300
0.200
0.100
0.000
0
5
10
15
20
25
Angle of Attack, deg

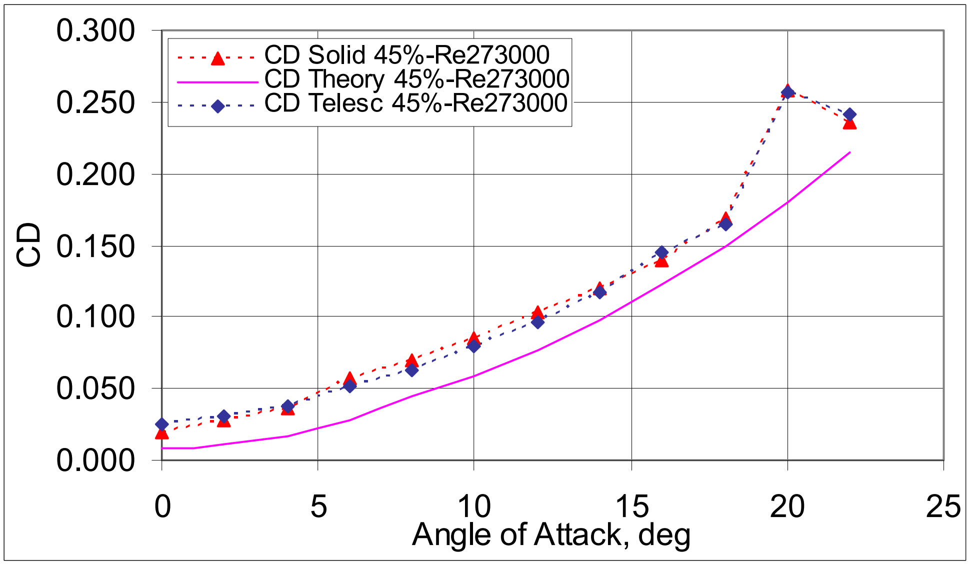

CD Solid 45%-Re273000
CD Theory 45%-Re273000
CD Telesc 45%-Re273000
CD
0.300
0.250
0.200
0.150
0.100
0.050
0.000
0
5
10
15
20
25
Angle of Attack, deg

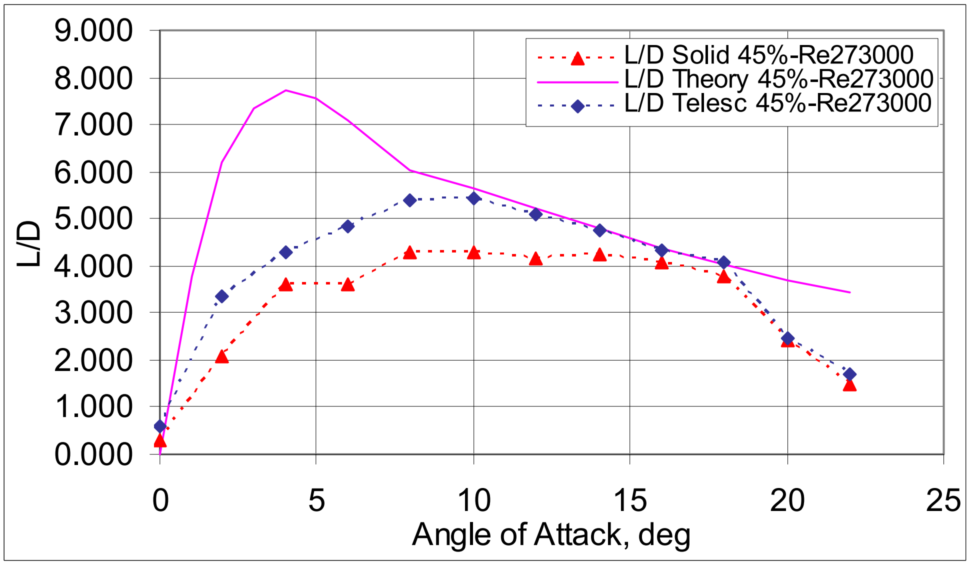

L/D Solid 45%-Re273000
L/D Theory 45%-Re273000
L/D Telesc 45%-Re273000
L/D
9.000
8.000
7.000
6.000
5.000
4.000
3.000
2.000
1.000
0.000
0
5
10
15
20
25
Angle of Attack, deg

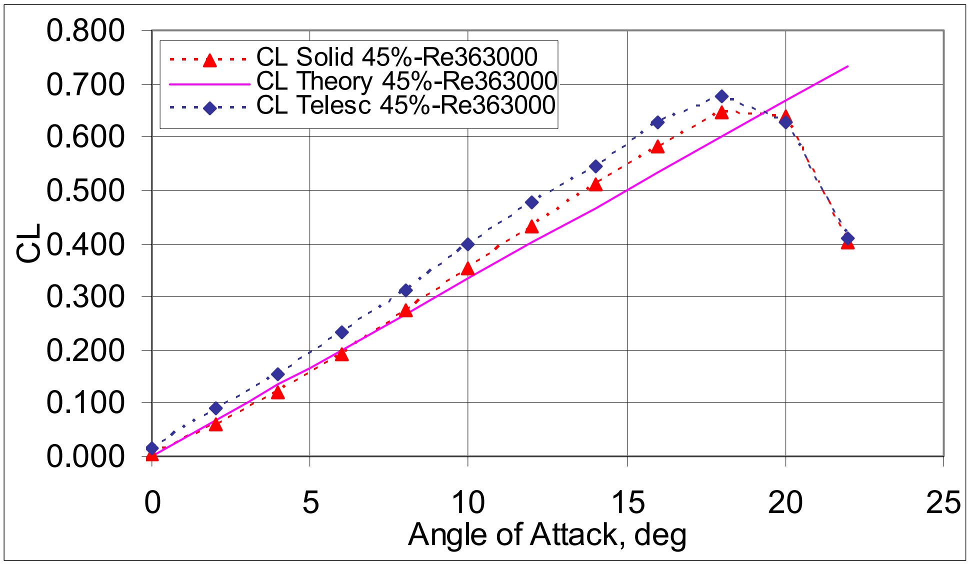
CL Solid 45%-Re363000
CL Theory 45%-Re363000
CL Telesc 45%-Re363000
CL
0.800
0.700
0.600
0.500
0.400
0.300
0.200
0.100
0.000
0
5
10
15
20
25
Angle of Attack, deg

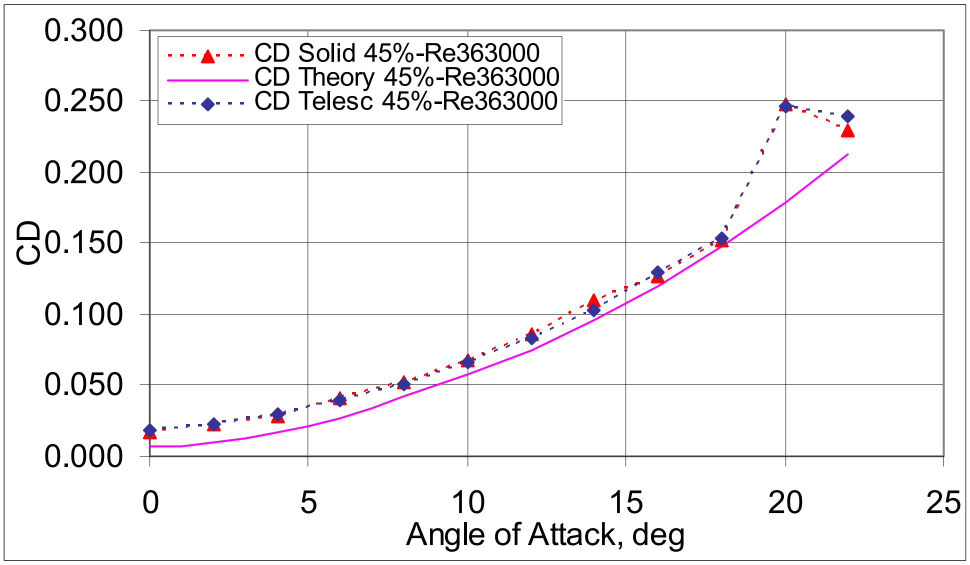
CD Solid 45%-Re363000
CD Theory 45%-Re363000
CD Telesc 45%-Re363000
CD
0.300
0.250
0.200
0.150
0.100
0.050
0.000
0
5
10
15
20
25
Angle of Attack, deg

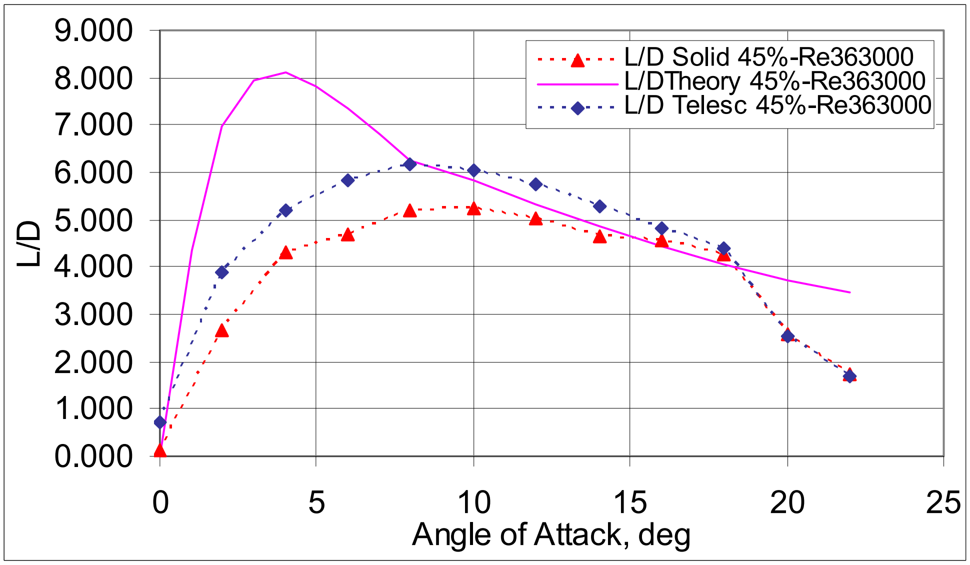
L/D Solid 45%-Re363000
L/DTheory 45%-Re363000
L/D Telesc 45%-Re363000
L/D
9.000
8.000
7.000
6.000
5.000
4.000
3.000
2.000
1.000
0.000
0
5
10
15
20
25
Angle of Attack, deg

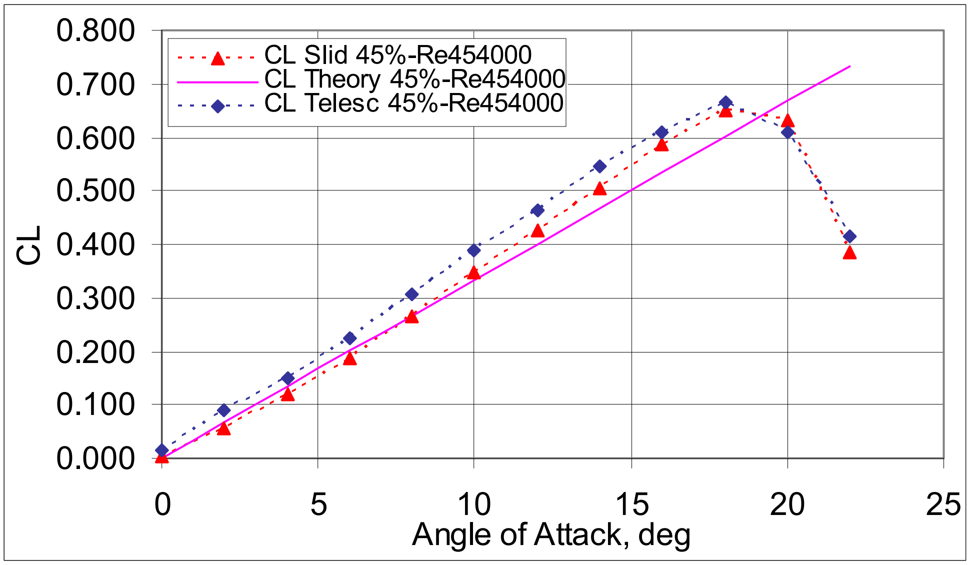
0.800
0.700
0.600
0.500
0.400
0.300
0.200
0.100
0.000
CL
0
5
10
15
20
25
Angle of Attack, deg
CL Slid 45%-Re454000
CL Theory 45%-Re454000
CL Telesc 45%-Re454000

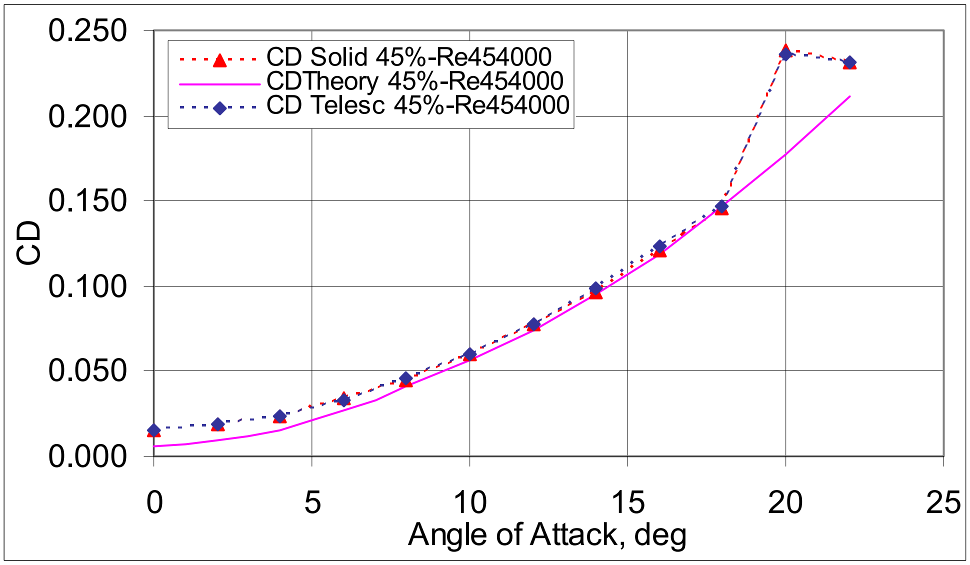
0.250
0.200
0.150
0.100
0.050
0.000
CD
0
5
10
15
20
25
Angle of Attack, deg
CD Solid 45%-Re454000
CDTheory 45%-Re454000
CD Telesc 45%-Re454000

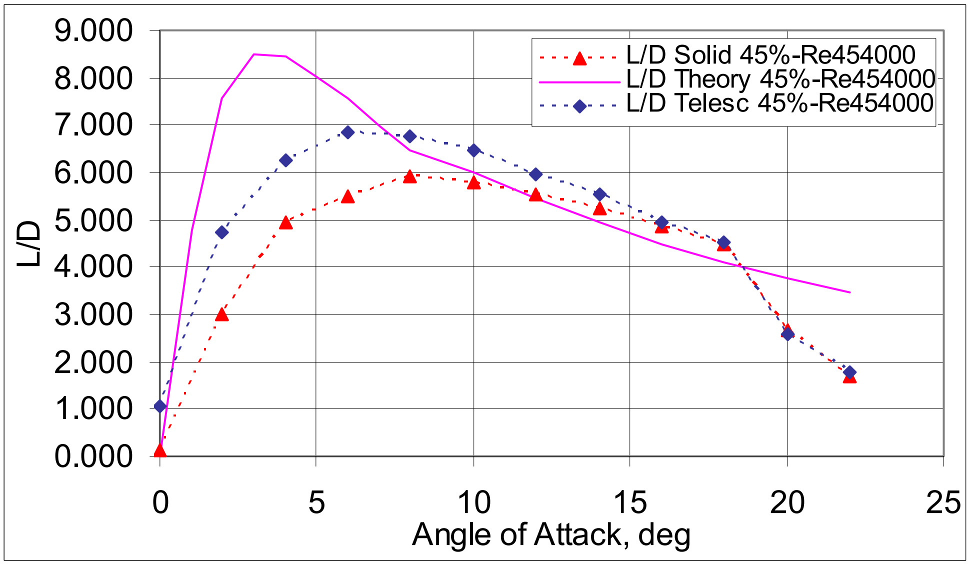
9.000
8.000
7.000
6.000
5.000
4.000
3.000
2.000
1.000
0.000
L/D
0
5
10
15
20
25
Angle of Attack, deg
L/D Solid 45%-Re454000
L/D Theory 45%-Re454000
L/D Telesc 45%-Re454000

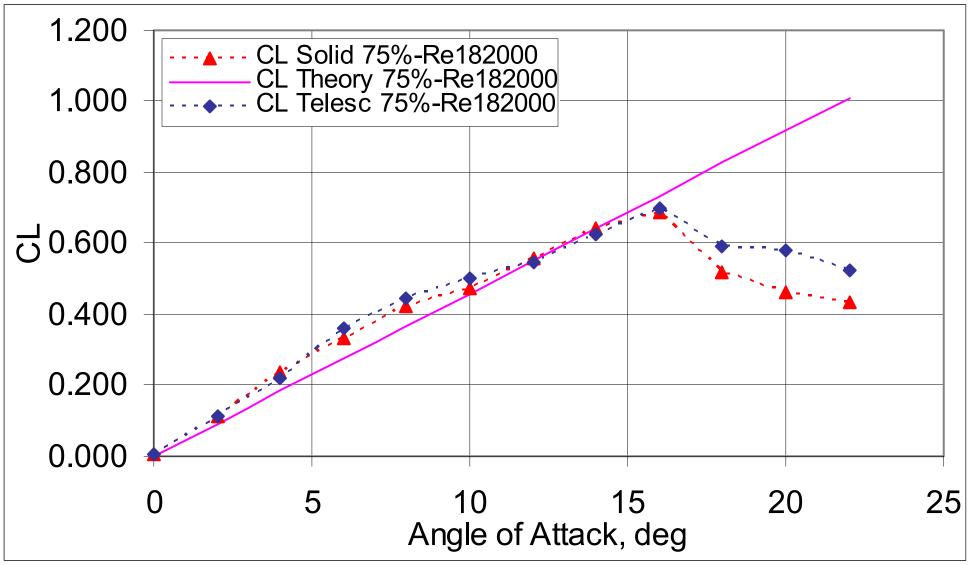
1.200
1.000
0.800
0.600
0.400
0.200
0.000
CL
CL Solid 75%-Re182000
CL Theory 75%-Re182000
CL Telesc 75%-Re182000
0
5
10
15
20
25
Angle of Attack, deg

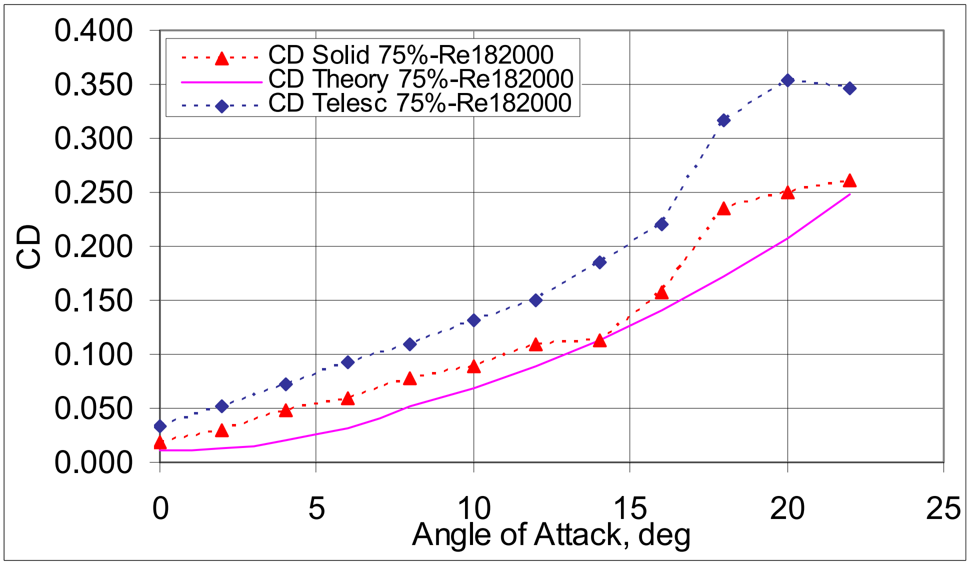
0.400
0.350
0.300
0.250
0.200
0.150
0.100
0.050
0.000
CD
CD Solid 75%-Re182000
CD Theory 75%-Re182000
CD Telesc 75%-Re182000
0
5
10
15
20
25
Angle of Attack, deg

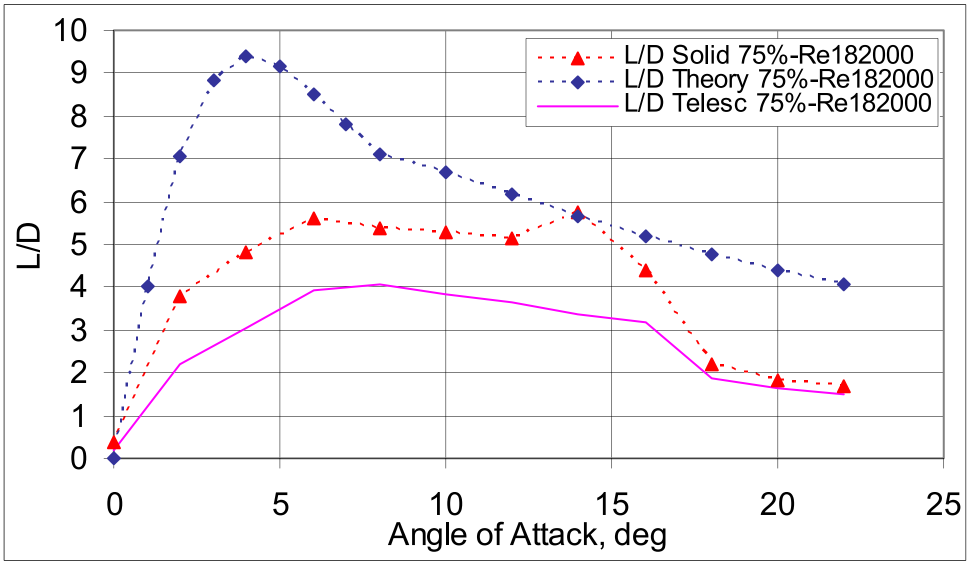
10
9
8
7
6
5
4
3
2
1
0
L/D
L/D Solid 75%-Re182000
L/D Theory 75%-Re182000
L/D Telesc 75%-Re182000
0
5
10
15
20
25
Angle of Attack, deg

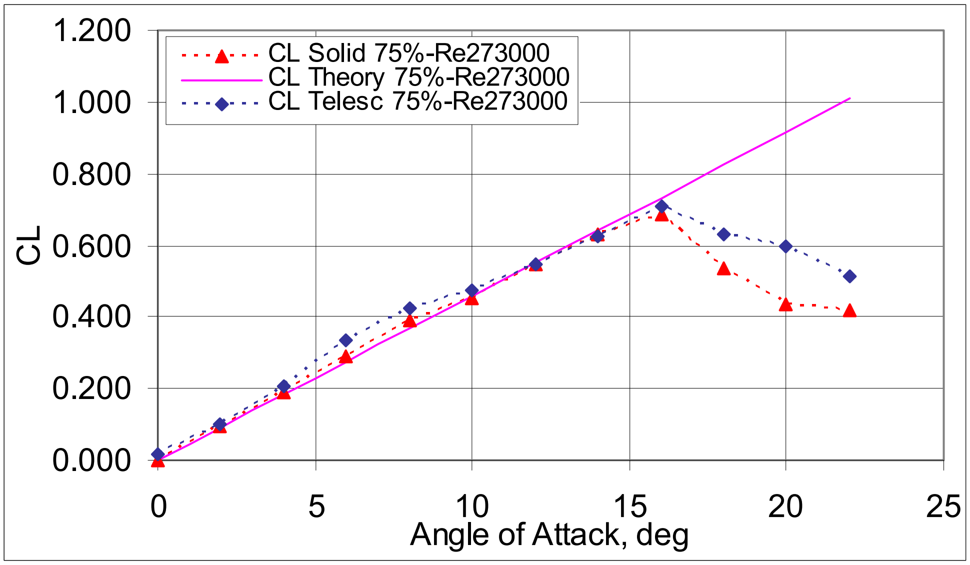
CL Solid 75%-Re273000
CL Theory 75%-Re273000
CL Telesc 75%-Re273000
CL
1.200
1.000
0.800
0.600
0.400
0.200
0.000
0
5
10
15
20
25
Angle of Attack, deg

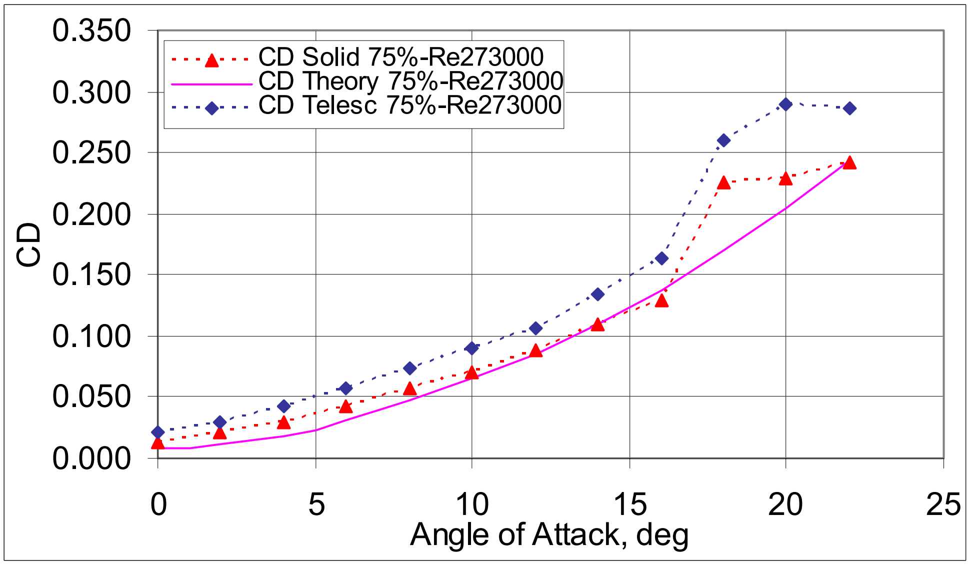
CD Solid 75%-Re273000
CD Theory 75%-Re273000
CD Telesc 75%-Re273000
CD
0.350
0.300
0.250
0.200
0.150
0.100
0.050
0.000
0
5
10
15
20
25
Angle of Attack, deg

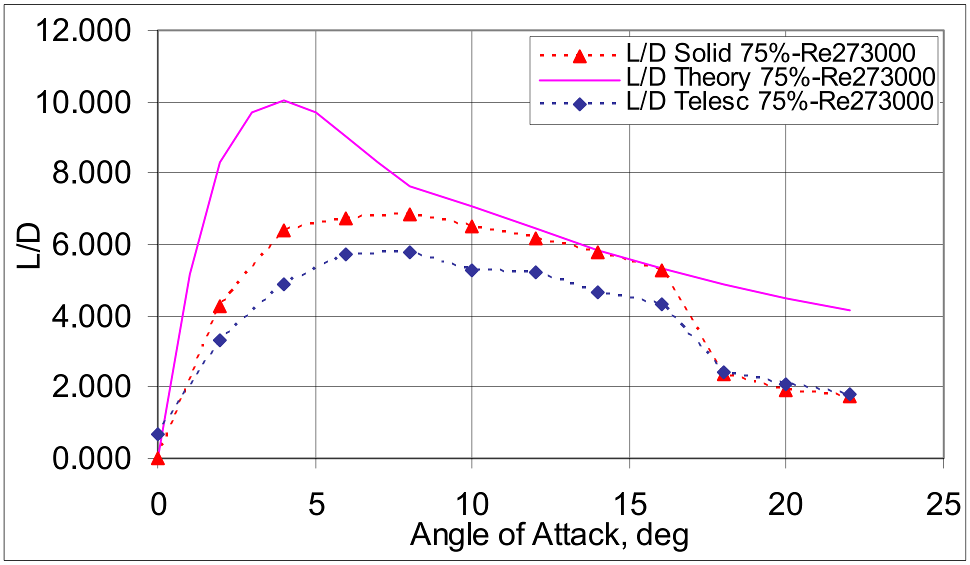
L/D Solid 75%-Re273000
L/D Theory 75%-Re273000
L/D Telesc 75%-Re273000
L/D
12.000
10.000
8.000
6.000
4.000
2.000
0.000
0
5
10
15
20
25
Angle of Attack, deg

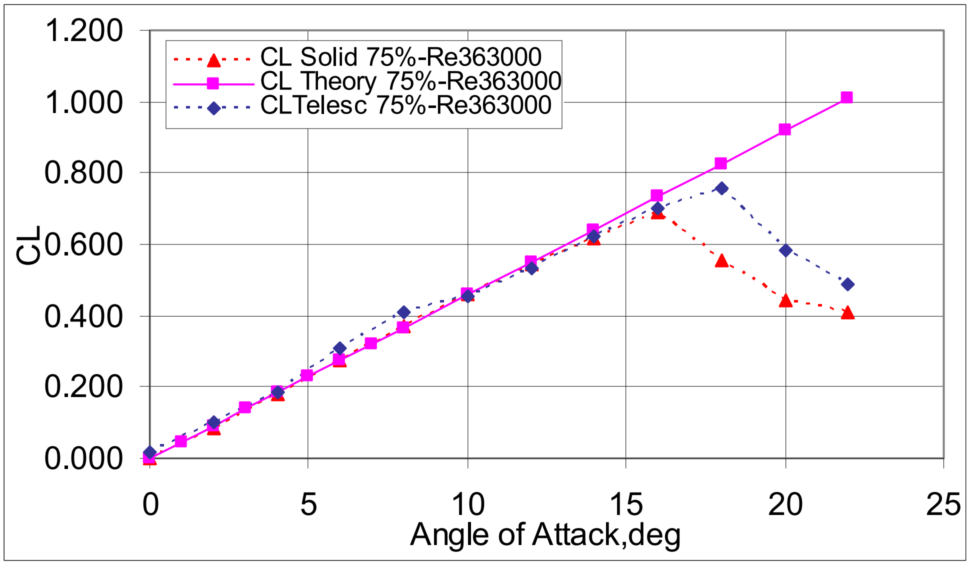
CL Solid 75%-Re363000
CL Theory 75%-Re363000
CLTelesc 75%-Re363000
CL
1.200
1.000
0.800
0.600
0.400
0.200
0.000
0
5
10
15
20
25
Angle of Attack,deg

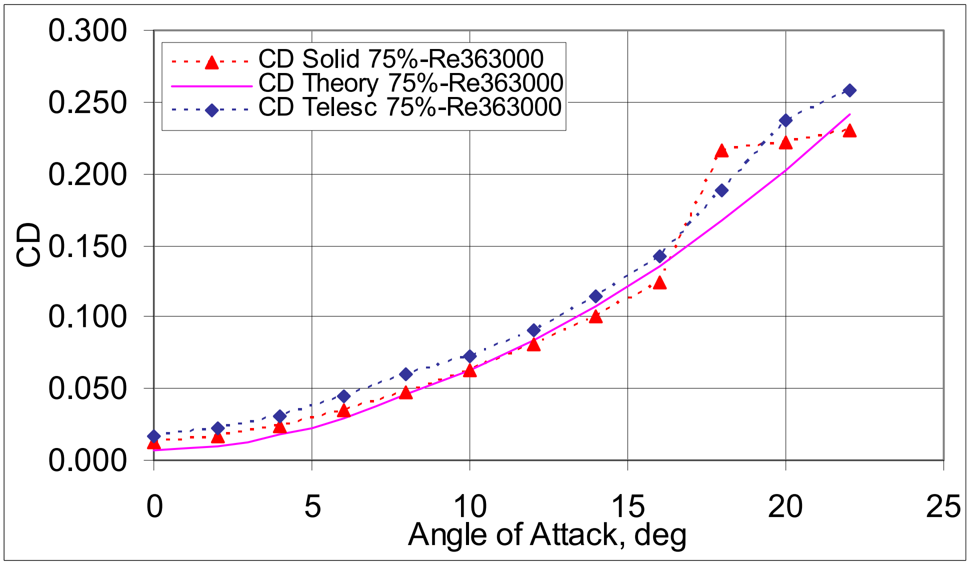
CD Solid 75%-Re363000
CD Theory 75%-Re363000
CD Telesc 75%-Re363000
CD
0.300
0.250
0.200
0.150
0.100
0.050
0.000
0
5
10
15
20
25
Angle of Attack, deg

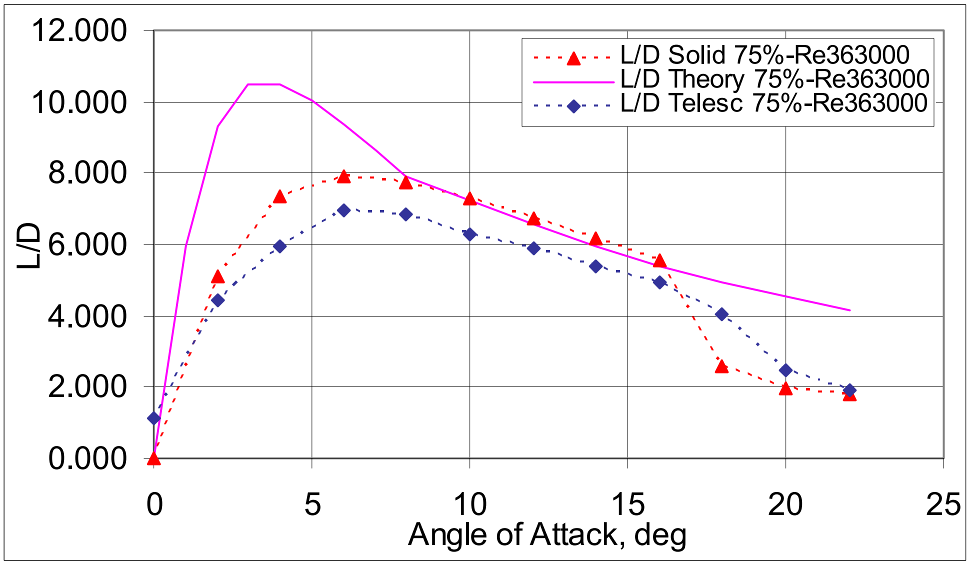
L/D Solid 75%-Re363000
L/D Theory 75%-Re363000
L/D Telesc 75%-Re363000
L/D
12.000
10.000
8.000
6.000
4.000
2.000
0.000
0
5
10
15
20
25
Angle of Attack, deg

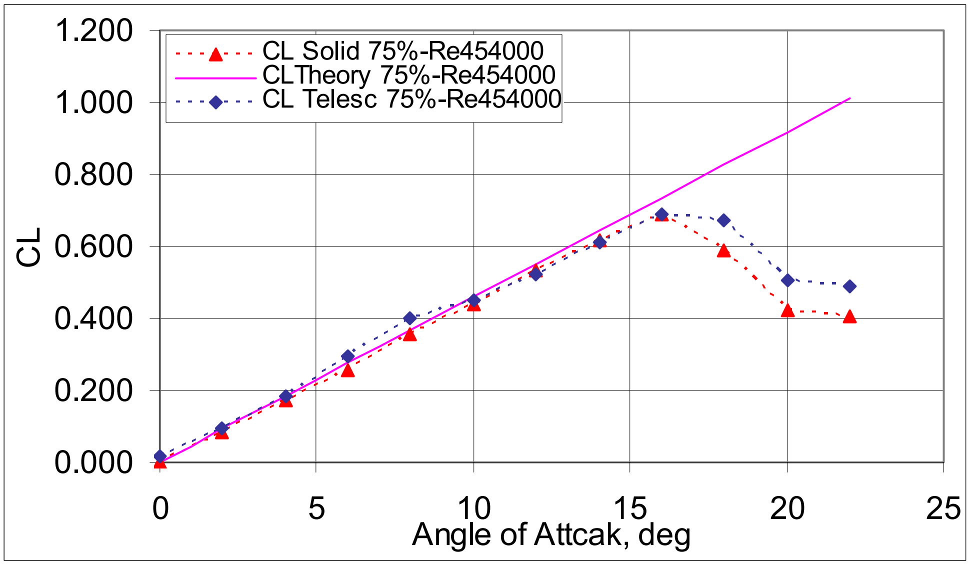
CL Solid 75%-Re454000
CLTheory 75%-Re454000
CL Telesc 75%-Re454000
CL
1.200
1.000
0.800
0.600
0.400
0.200
0.000
0
5
10
15
20
25
Angle of Attcak, deg

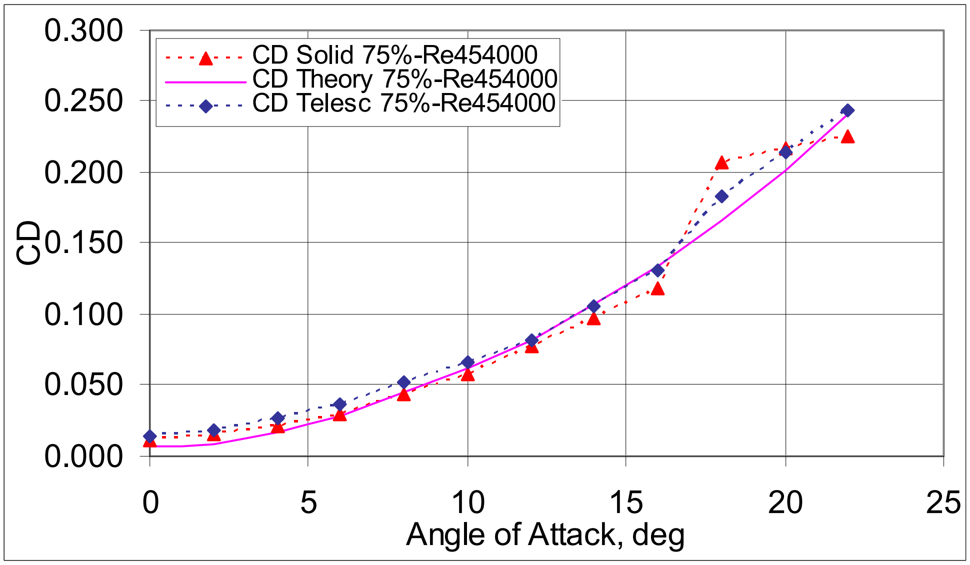
CD Solid 75%-Re454000
CD Theory 75%-Re454000
CD Telesc 75%-Re454000
CD
0.300
0.250
0.200
0.150
0.100
0.050
0.000
0
5
10
15
20
25
Angle of Attack, deg

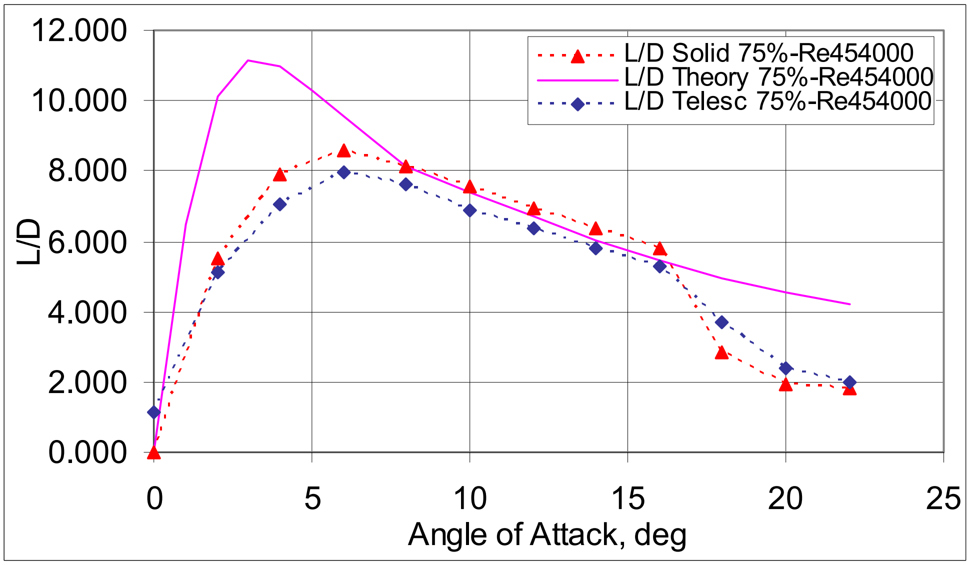
L/D Solid 75%-Re454000
L/D Theory 75%-Re454000
L/D Telesc 75%-Re454000
L/D
12.000
10.000
8.000
6.000
4.000
2.000
0.000
0
5
10
15
20
25
Angle of Attack, deg

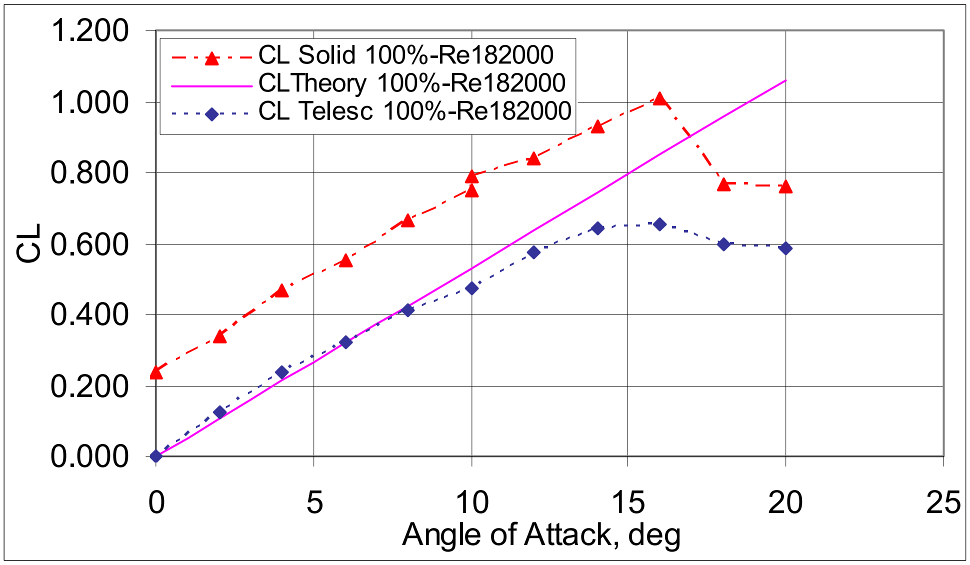
CL Solid 100%-Re182000
CLTheory 100%-Re182000
CL Telesc 100%-Re182000
CL
1.200
1.000
0.800
0.600
0.400
0.200
0.000
0
5
10
15
20
25
Angle of Attack, deg

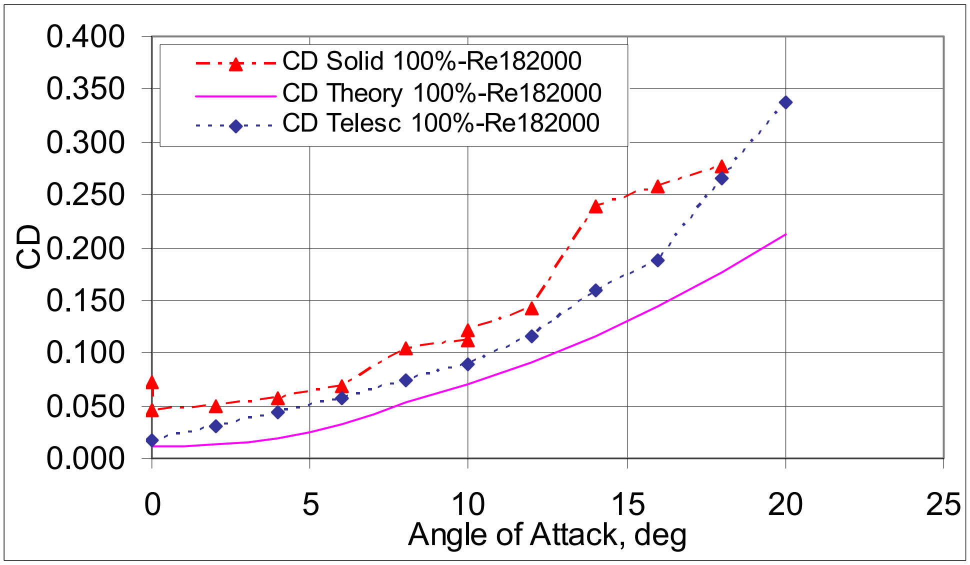
CD Solid 100%-Re182000
CD Theory 100%-Re182000
CD Telesc 100%-Re182000
CD
0.400
0.350
0.300
0.250
0.200
0.150
0.100
0.050
0.000
0
5
10
15
20
25
Angle of Attack, deg

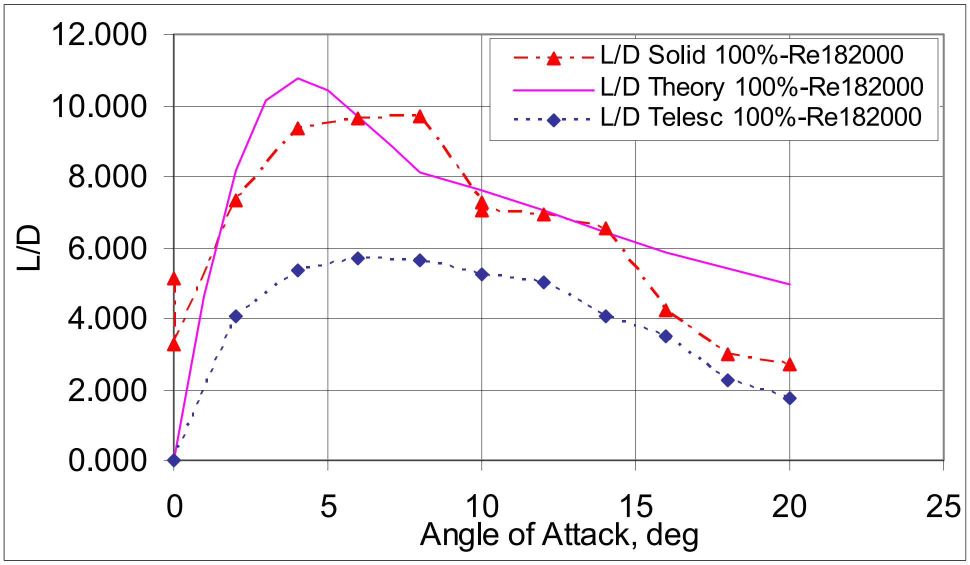
L/D Solid 100%-Re182000
L/D Theory 100%-Re182000
L/D Telesc 100%-Re182000
L/D
12.000
10.000
8.000
6.000
4.000
2.000
0.000
0
5
10
15
20
25
Angle of Attack, deg

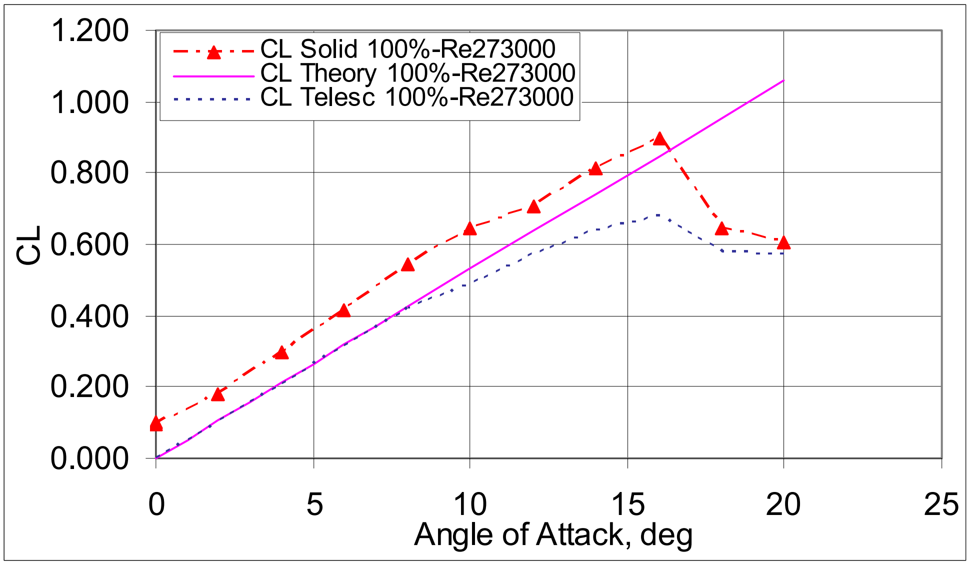
CL Solid 100%-Re273000
CL Theory 100%-Re273000
CL Telesc 100%-Re273000
CL
1.200
1.000
0.800
0.600
0.400
0.200
0.000
0
5
10
15
20
25
Angle of Attack, deg

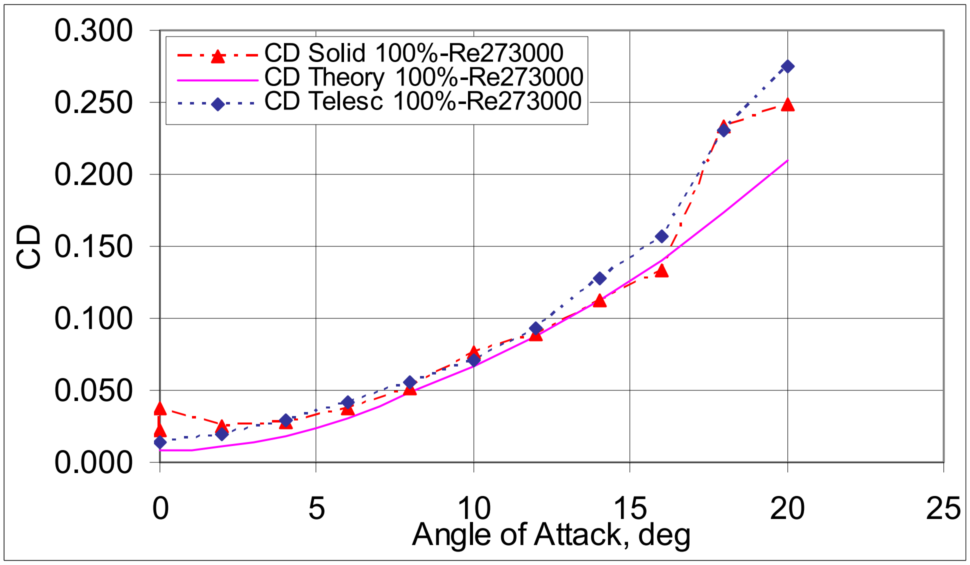
CD Solid 100%-Re273000
CD Theory 100%-Re273000
CD Telesc 100%-Re273000
CD
0.300
0.250
0.200
0.150
0.100
0.050
0.000
0
5
10
15
20
25
Angle of Attack, deg


L/D Solid 100%-Re273000
L/DTheory 100%-Re273000
L/D Telesc 100%-Re273000
L/D
14.000
12.000
10.000
8.000
6.000
4.000
2.000
0.000
0
5
10
15
20
25
Angle of Attack, deg

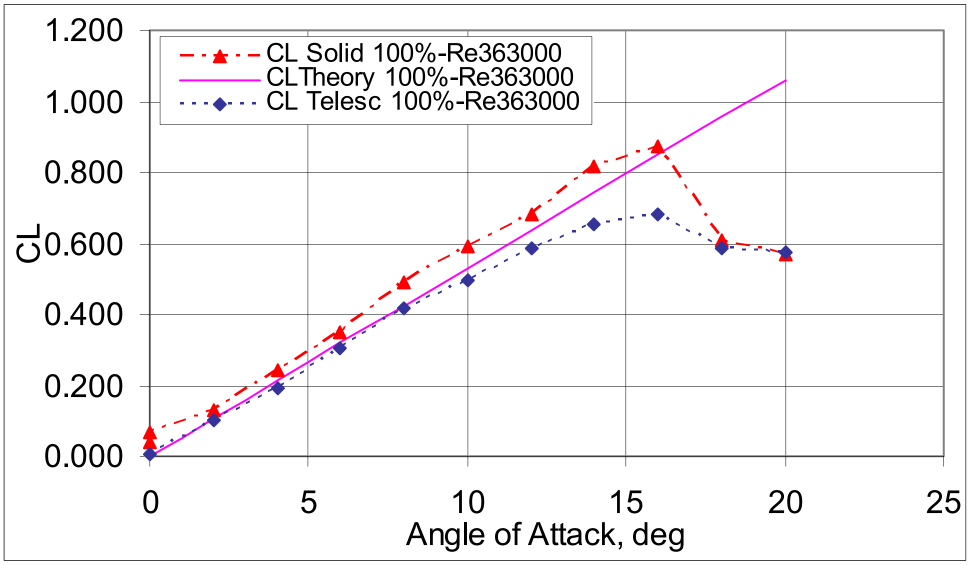
1.200
1.000
0.800
0.600
0.400
0.200
0.000
CL
0
5
10
15
20
25
Angle of Attack, deg
CL Solid 100%-Re363000
CLTheory 100%-Re363000
CL Telesc 100%-Re363000

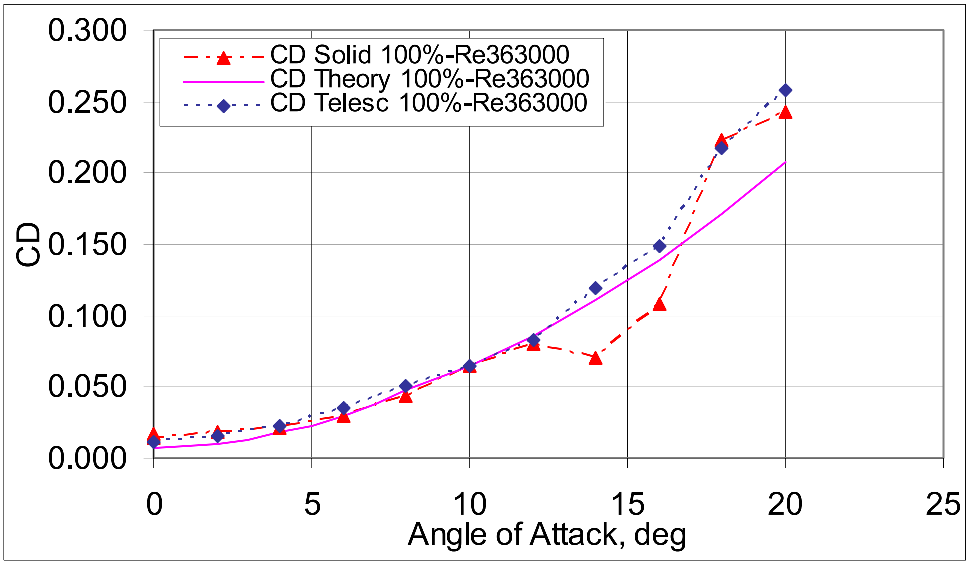
0.300
0.250
0.200
0.150
0.100
0.050
0.000
CD
0
5
10
15
20
25
Angle of Attack, deg
CD Solid 100%-Re363000
CD Theory 100%-Re363000
CD Telesc 100%-Re363000

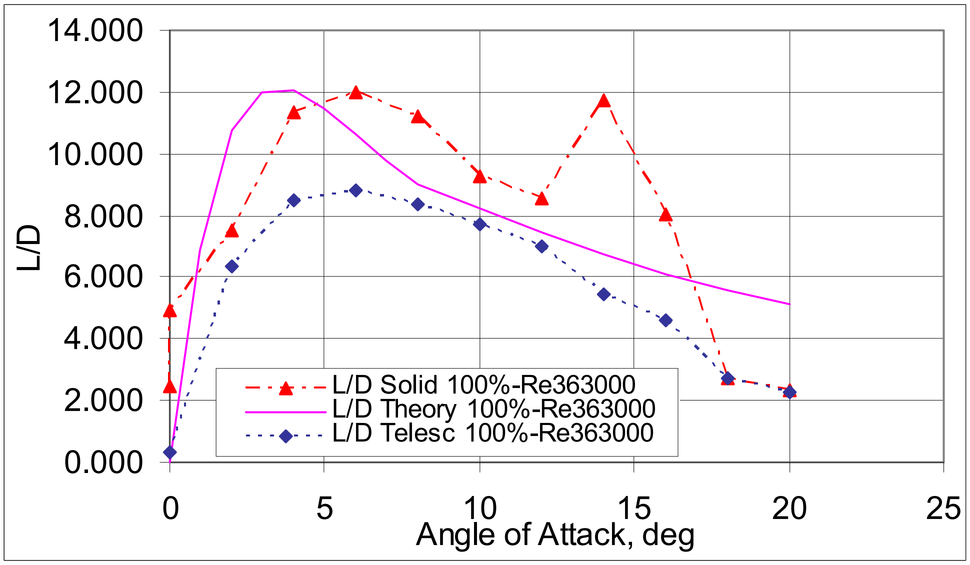
14.000
12.000
10.000
8.000
6.000
4.000
2.000
0.000
L/D
0
5
10
15
20
25
Angle of Attack, deg
L/D Solid 100%-Re363000
L/D Theory 100%-Re363000
L/D Telesc 100%-Re363000

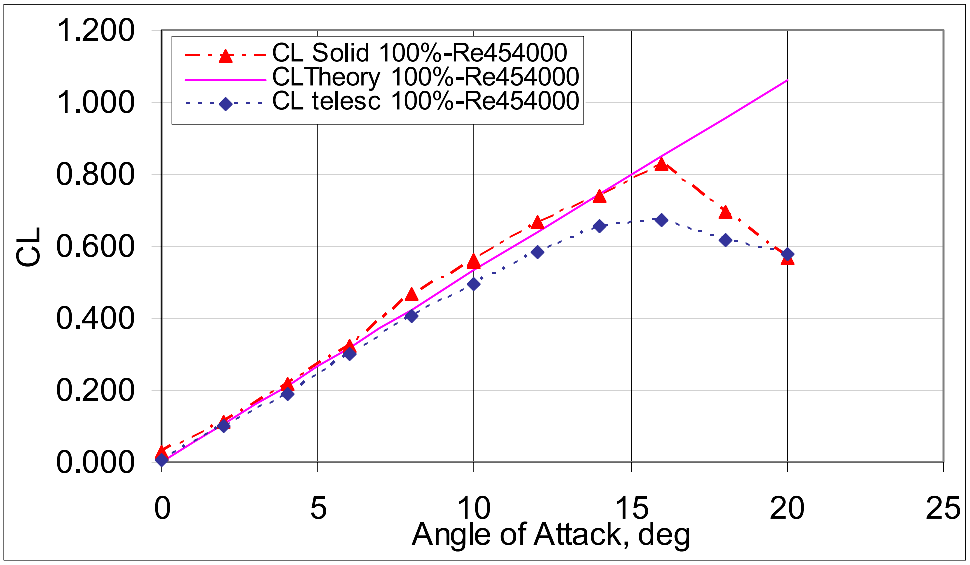
CL Solid 100%-Re454000
CLTheory 100%-Re454000
CL telesc 100%-Re454000
CL
1.200
1.000
0.800
0.600
0.400
0.200
0.000
0
5
10
15
20
25
Angle of Attack, deg

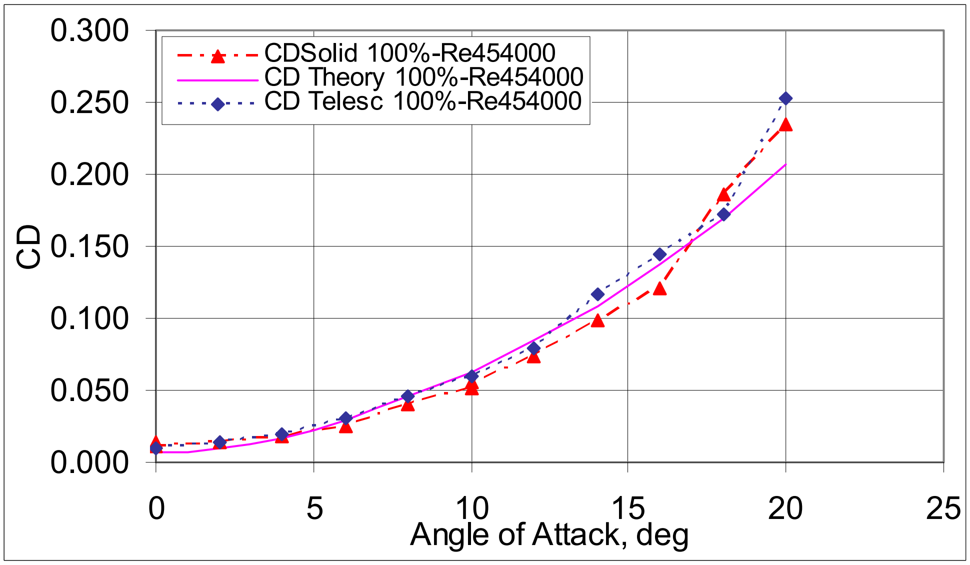
CDSolid 100%-Re454000
CD Theory 100%-Re454000
CD Telesc 100%-Re454000
CD
0.300
0.250
0.200
0.150
0.100
0.050
0.000
0
5
10
15
20
25
Angle of Attack, deg

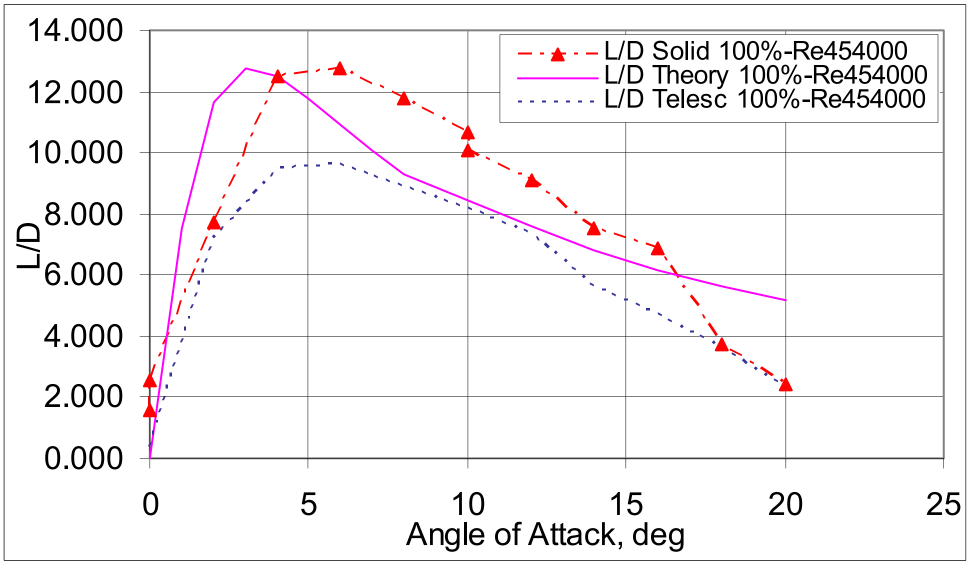
L/D Solid 100%-Re454000
L/D Theory 100%-Re454000
L/D Telesc 100%-Re454000
L/D
14.000
12.000
10.000
8.000
6.000
4.000
2.000
0.000
0
5
10
15
20
25
Angle of Attack, deg

Appendix II: Wind tunnel results for the Second Generation Prototype – Test I

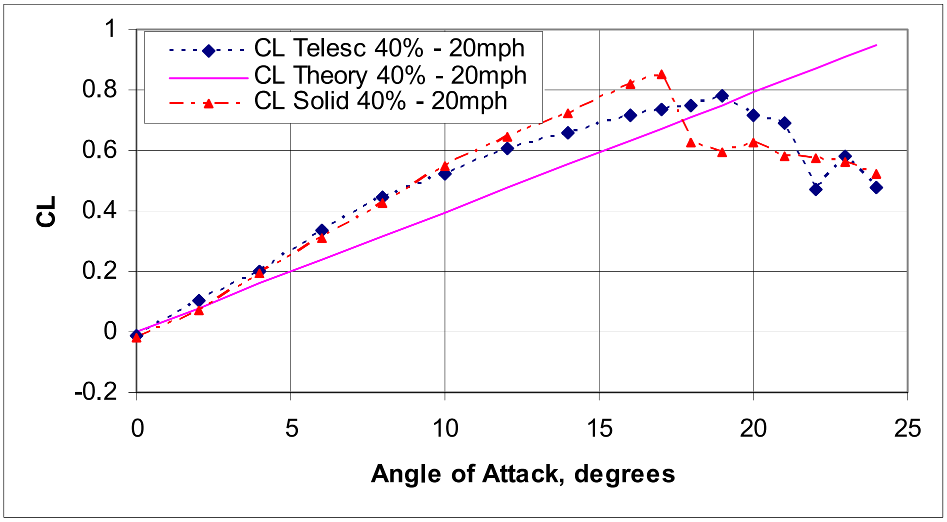
CL Telesc 40% - 20mph
CL Theory 40% - 20mph
CL Solid 40% - 20mph
CL
1
0.8
0.6
0.4
0.2
0
-0.2
0
5
10
15
20
25
Angle of Attack, degrees

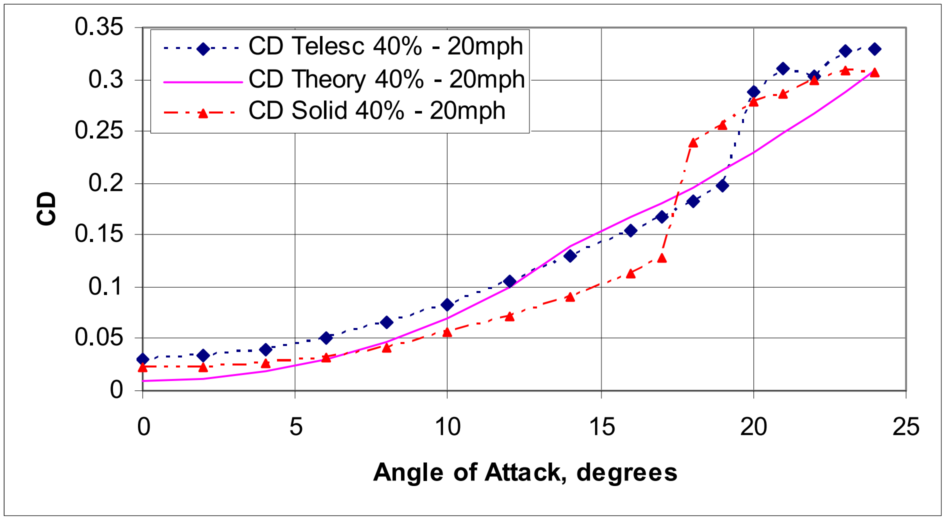
CD Telesc 40% - 20mph
CD Theory 40% - 20mph
CD Solid 40% - 20mph
CD
0.35
0.3
0.25
0.2
0.15
0.1
0.05
0
0
5
10
15
20
25
Angle of Attack, degrees

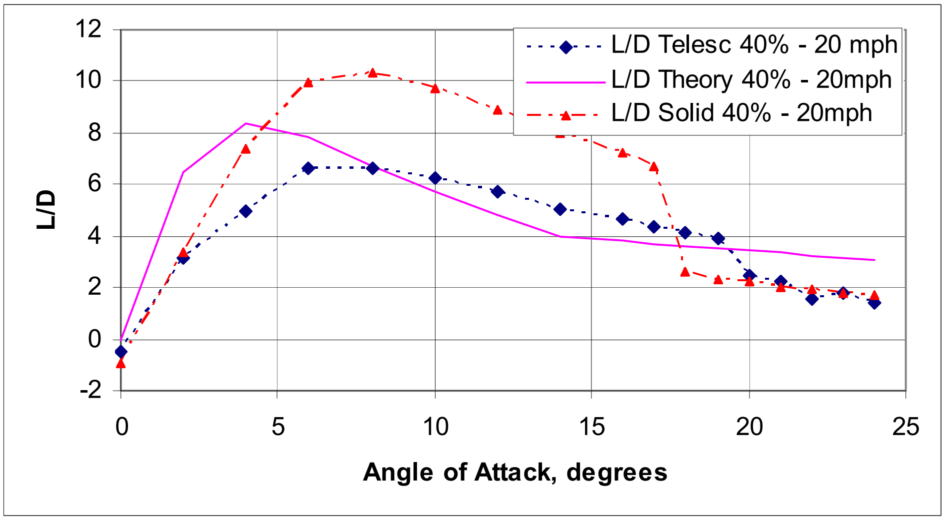
L/D Telesc 40% - 20 mph
L/D Theory 40% - 20mph
L/D Solid 40% - 20mph
L/D
12
10
8
6
4
2
0
-2
0
5
10
15
20
25
Angle of Attack, degrees

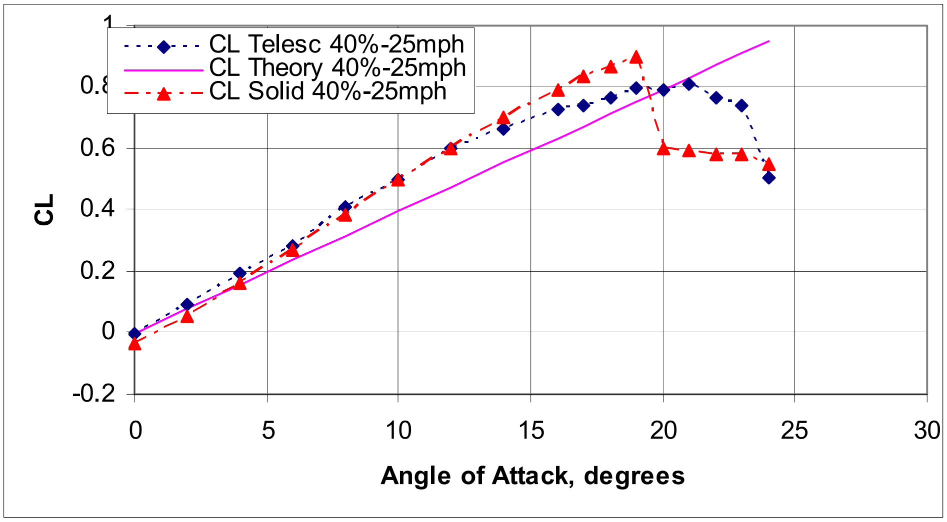
CL Telesc 40%-25mph
CL Theory 40%-25mph
CL Solid 40%-25mph
CL
1
0.8
0.6
0.4
0.2
0
-0.2
0
5
10
15
20
25
30
Angle of Attack, degrees

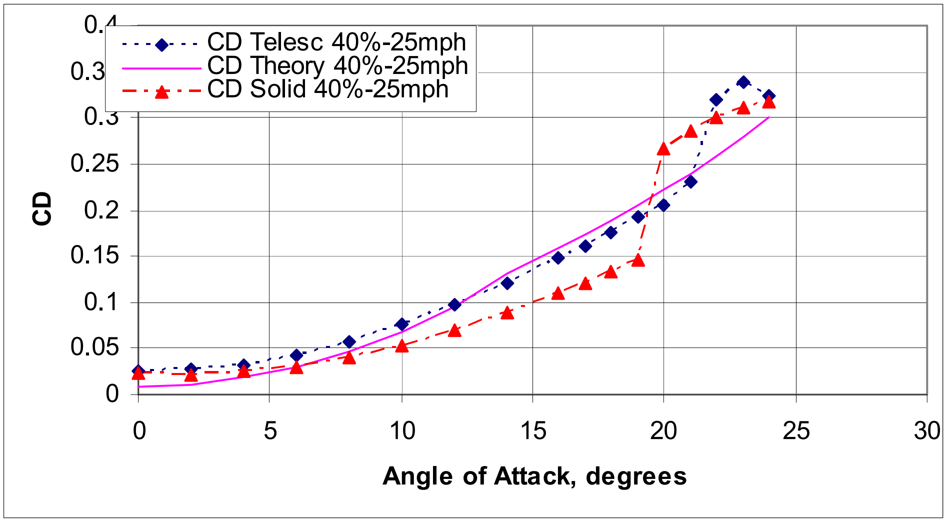
CD Telesc 40%-25mph
CD Theory 40%-25mph
CD Solid 40%-25mph
CD
0.4
0.35
0.3
0.25
0.2
0.15
0.1
0.05
0
0
5
10
15
20
25
30
Angle of Attack, degrees

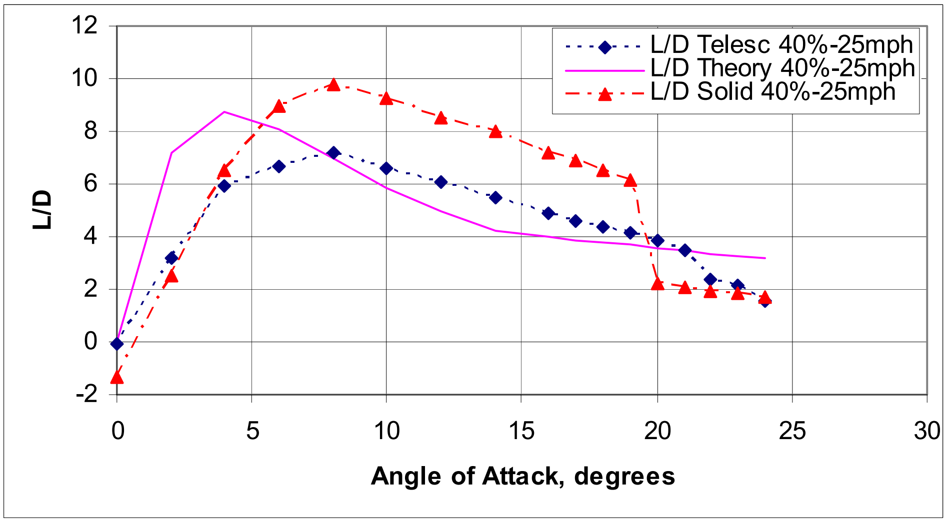
L/D Telesc 40%-25mph
L/D Theory 40%-25mph
L/D Solid 40%-25mph
L/D
12
10
8
6
4
2
0
-2
0
5
10
15
20
25
30
Angle of Attack, degrees

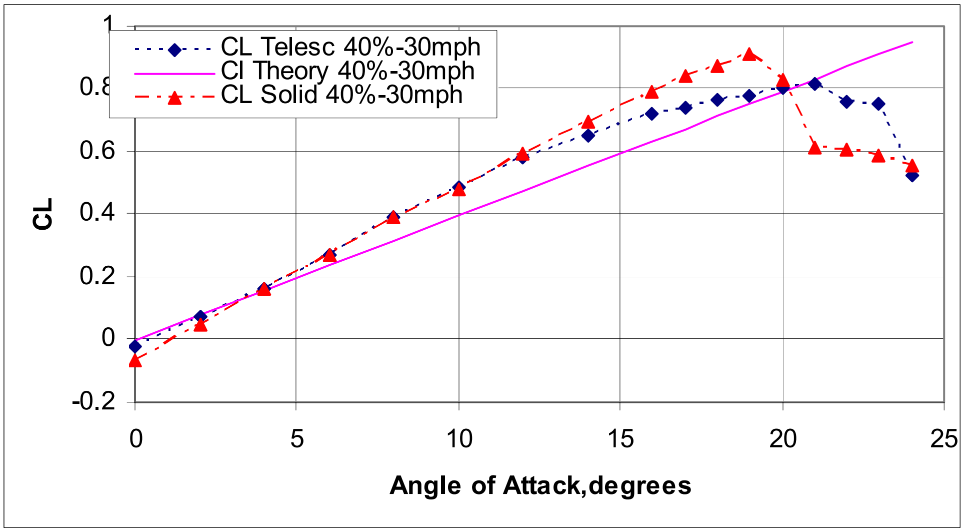
CL Telesc 40%-30mph
Cl Theory 40%-30mph
CL Solid 40%-30mph
CL
1
0.8
0.6
0.4
0.2
0
-0.2
0
5
10
15
20
25
Angle of Attack,degrees

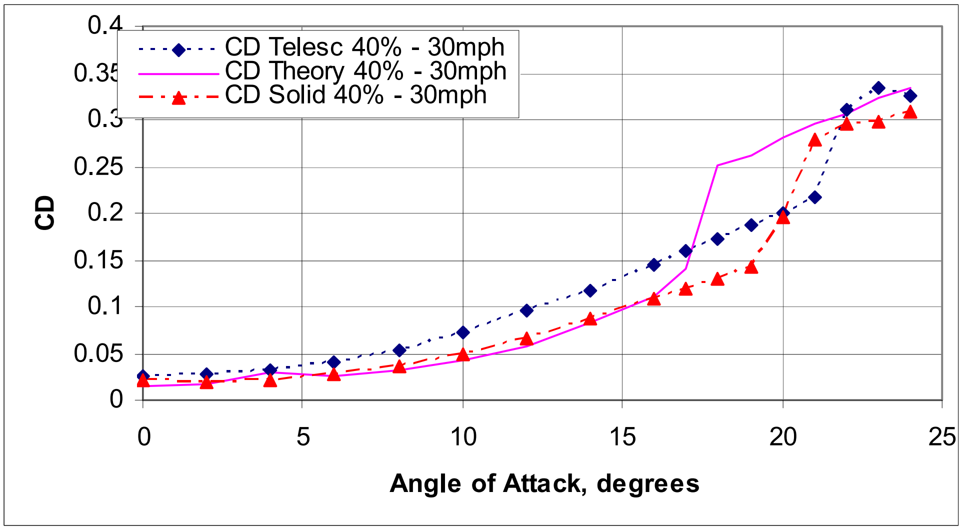
CD Telesc 40% - 30mph
CD Theory 40% - 30mph
CD Solid 40% - 30mph
CD
0.4
0.35
0.3
0.25
0.2
0.15
0.1
0.05
0
0
5
10
15
20
25
Angle of Attack, degrees

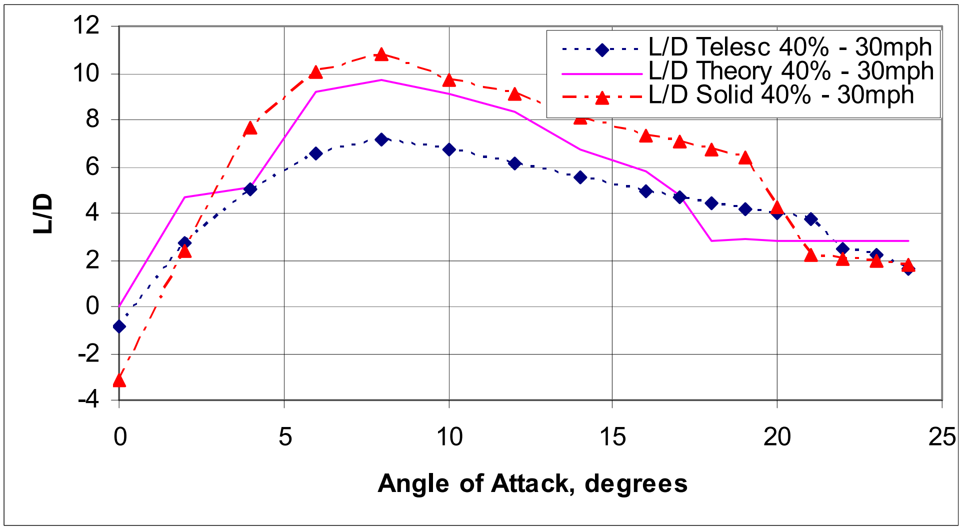
L/D Telesc 40% - 30mph
L/D Theory 40% - 30mph
L/D Solid 40% - 30mph
L/D
12
10
8
6
4
2
0
-2
-4
0
5
10
15
20
25
Angle of Attack, degrees

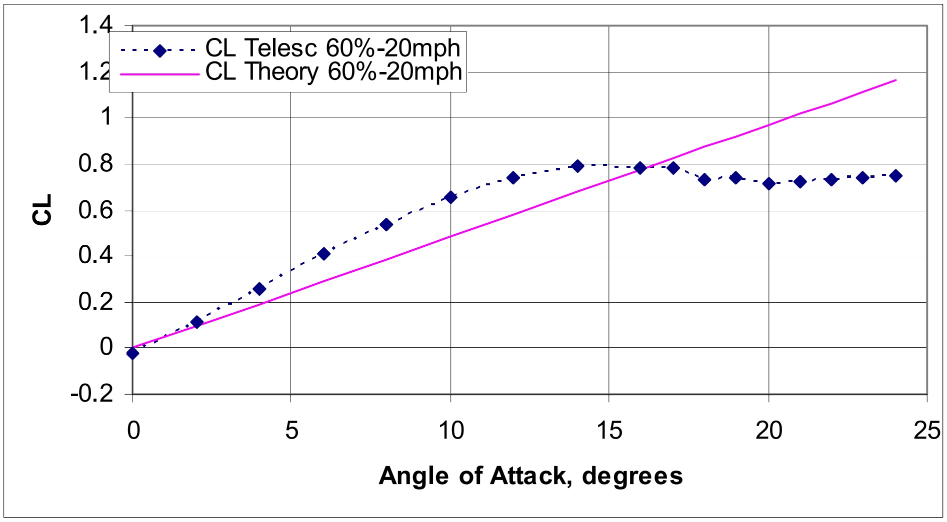
CL Telesc 60%-20mph
CL Theory 60%-20mph
CL
1.4
1.2
1
0.8
0.6
0.4
0.2
0
-0.2
0
5
10
15
20
25
Angle of Attack, degrees

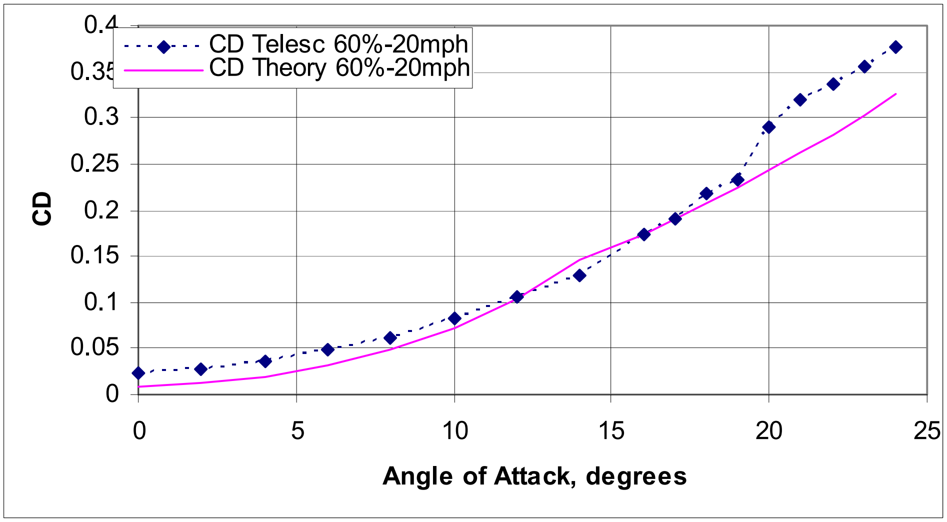
CD Telesc 60%-20mph
CD Theory 60%-20mph
CD
0.4
0.35
0.3
0.25
0.2
0.15
0.1
0.05
0
0
5
10
15
20
25
Angle of Attack, degrees

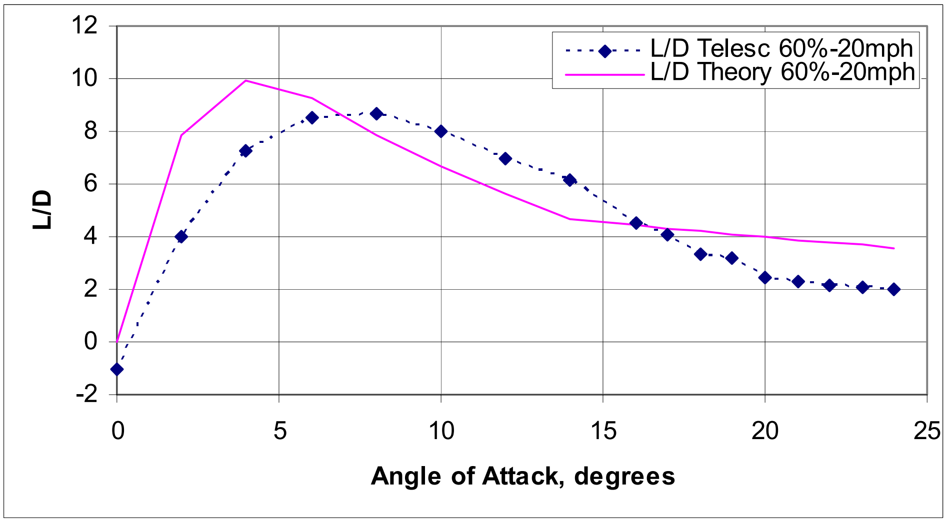
L/D Telesc 60%-20mph
L/D Theory 60%-20mph
L/D
12
10
8
6
4
2
0
-2
0
5
10
15
20
25
Angle of Attack, degrees

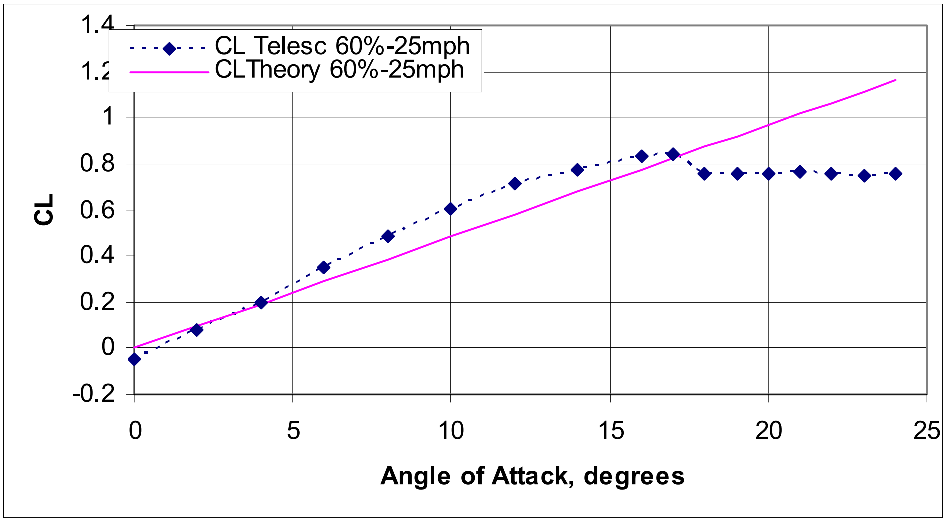

CL Telesc 60%-25mph
CLTheory 60%-25mph
CL
1.4
1.2
1
0.8
0.6
0.4
0.2
0
-0.2
0
5
10
15
20
25
Angle of Attack, degrees

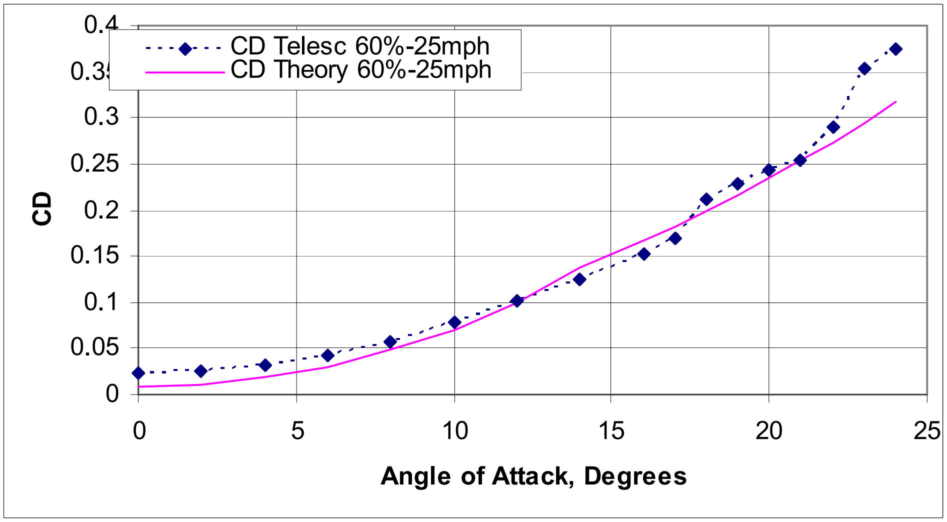

CD Telesc 60%-25mph
CD Theory 60%-25mph
CD
0.4
0.35
0.3
0.25
0.2
0.15
0.1
0.05
0
0
5
10
15
20
25
Angle of Attack, Degrees

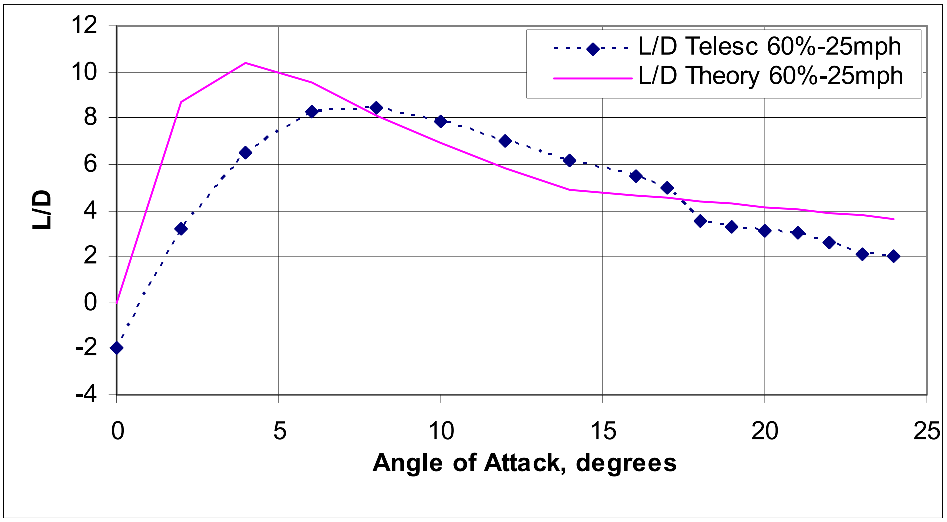

L/D Telesc 60%-25mph
L/D Theory 60%-25mph
L/D
12
10
8
6
4
2
0
-2
-4
0
5
10
15
20
25
Angle of Attack, degrees

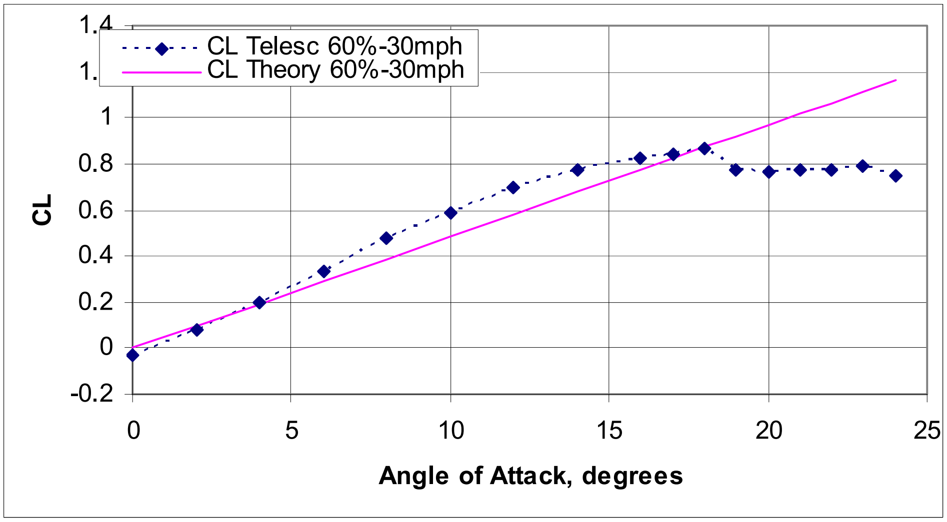
CL Telesc 60%-30mph
CL Theory 60%-30mph
CL
1.4
1.
1
0.8
0.6
0.4
0.2
0
-0.2
0
5
10
15
20
25
Angle of Attack, degrees

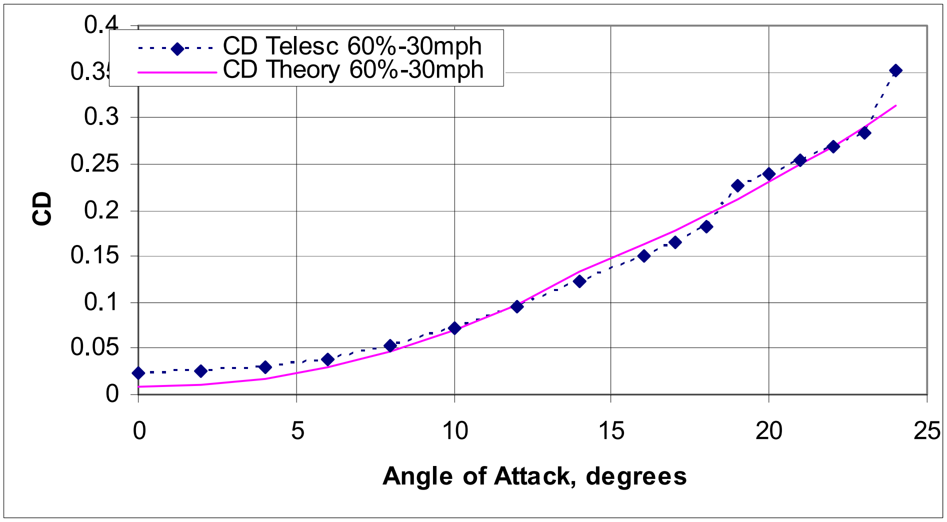
CD Telesc 60%-30mph
CD Theory 60%-30mph
CD
0.4
0.35
0.3
0.25
0.2
0.15
0.1
0.05
0
0
5
10
15
20
25
Angle of Attack, degrees

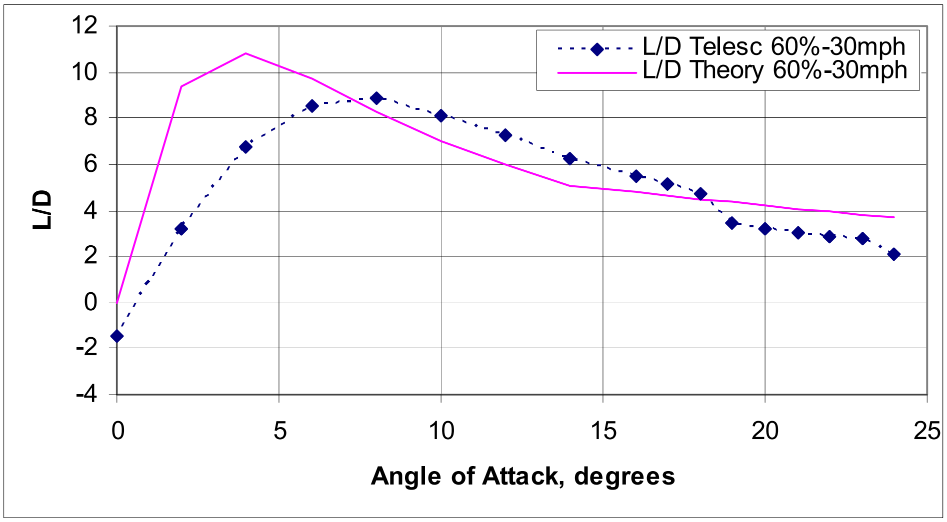
L/D Telesc 60%-30mph
L/D Theory 60%-30mph
L/D
12
10
8
6
4
2
0
-2
-4
0
5
10
15
20
25
Angle of Attack, degrees

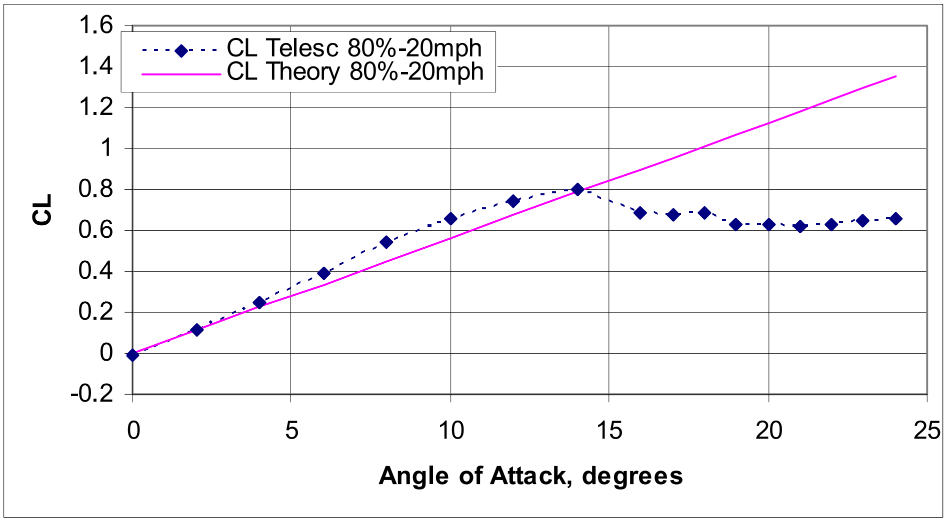
CL Telesc 80%-20mph
CL Theory 80%-20mph
CL
-0.2
0
0.2
0.4
0.6
0.8
1
1.2
1.4
1.6
0
5
10
15
20
25
Angle of Attack, degrees

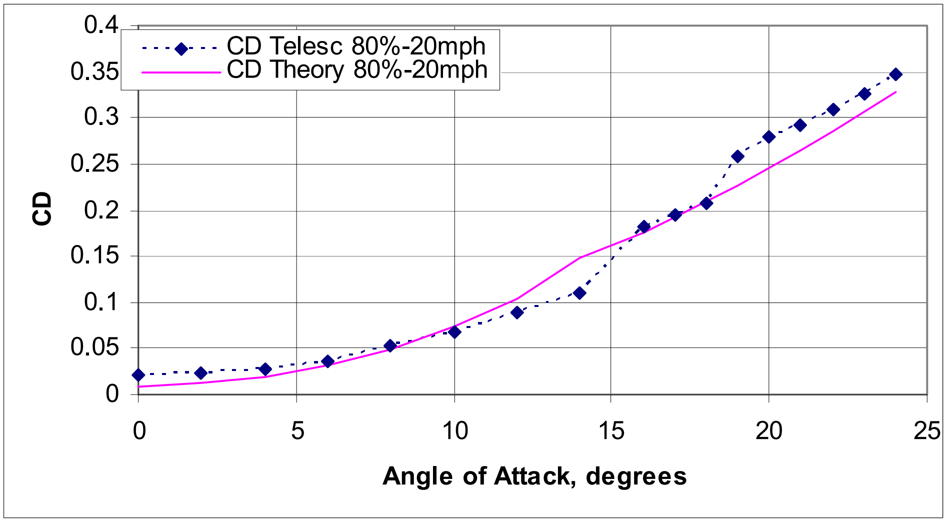
CD Telesc 80%-20mph
CD Theory 80%-20mph
CD
0
0.05
0.1
0.15
0.2
0.25
0.3
0.35
0.4
0
5
10
15
20
25
Angle of Attack, degrees

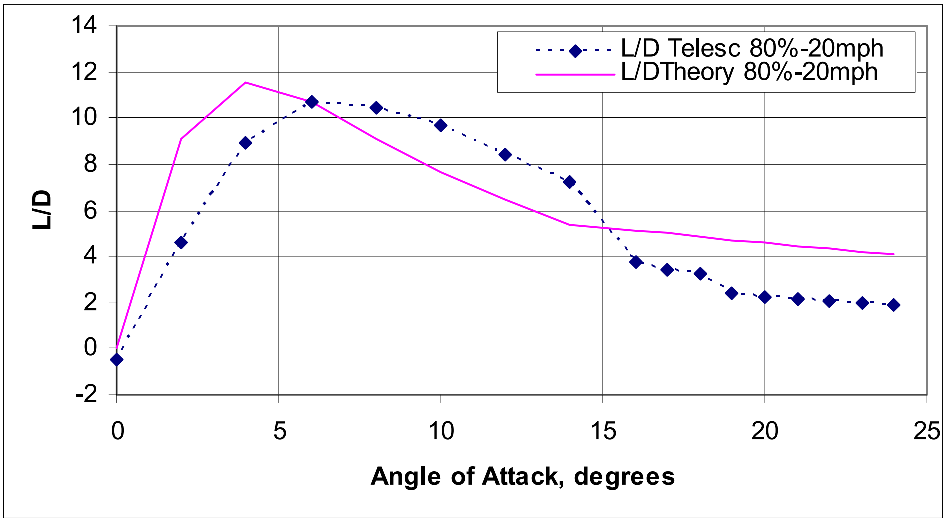
L/D Telesc 80%-20mph
L/DTheory 80%-20mph
L/D
-2
0
2
4
6
8
10
12
14
0
5
10
15
20
25
Angle of Attack, degrees

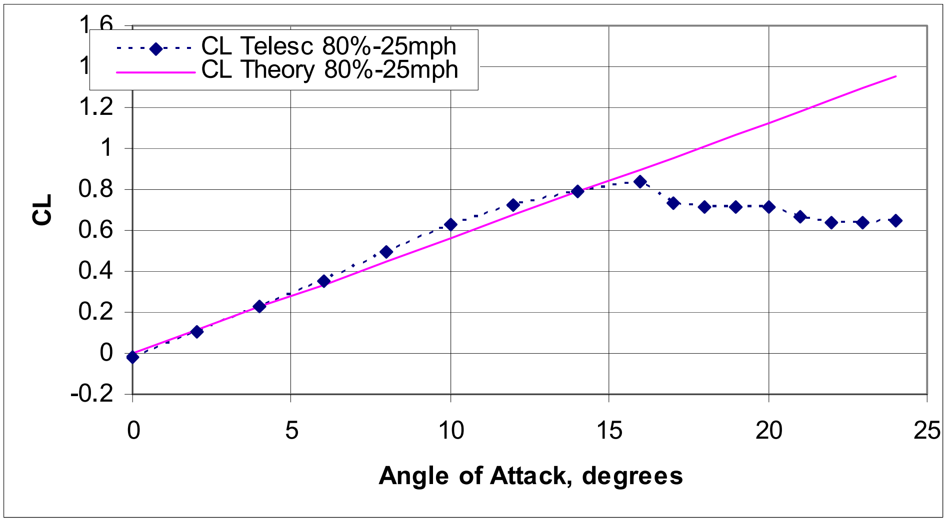
1.6
1.4
1.2
1
0.8
0.6
0.4
0.2
0
-0.2
CL
0
5
10
15
20
25
Angle of Attack, degrees
CL Telesc 80%-25mph
CL Theory 80%-25mph

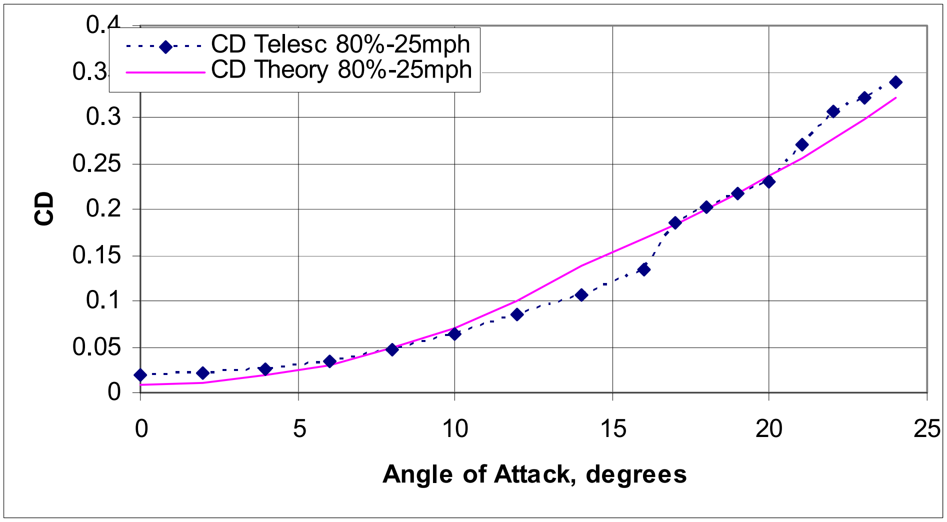
0.4
0.35
0.3
0.25
0.2
0.15
0.1
0.05
0
CD
0
5
10
15
20
25
Angle of Attack, degrees
CD Telesc 80%-25mph
CD Theory 80%-25mph

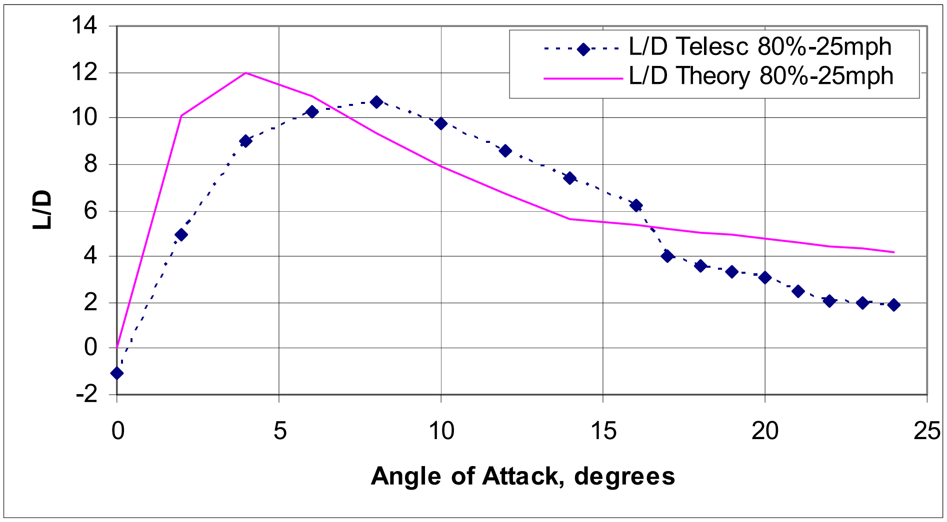
14
12
10
8
6
4
2
0
-2
L/D
0
5
10
15
20
25
Angle of Attack, degrees
L/D Telesc 80%-25mph
L/D Theory 80%-25mph

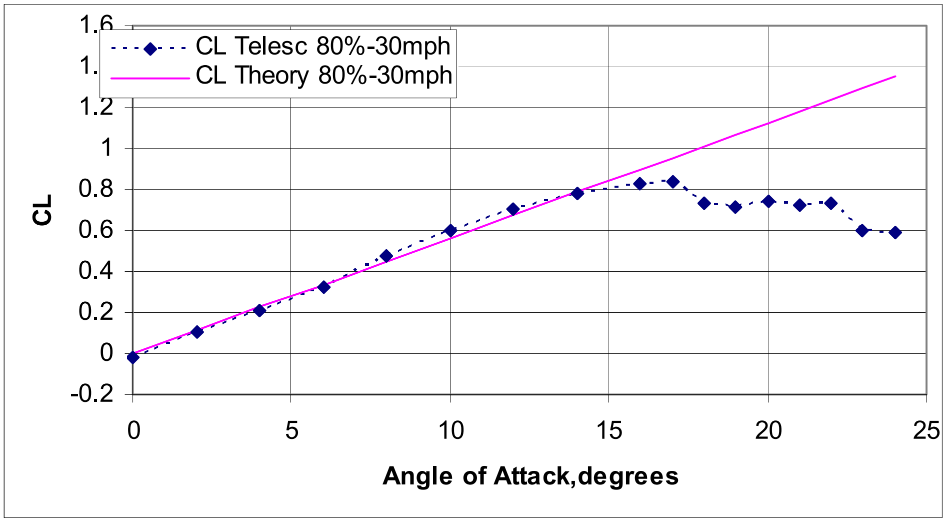
CL Telesc 80%-30mph
CL Theory 80%-30mph
CL
1.6
1.
1.2
1
0.8
0.6
0.4
0.2
0
-0.2
0
5
10
15
20
25
Angle of Attack,degrees

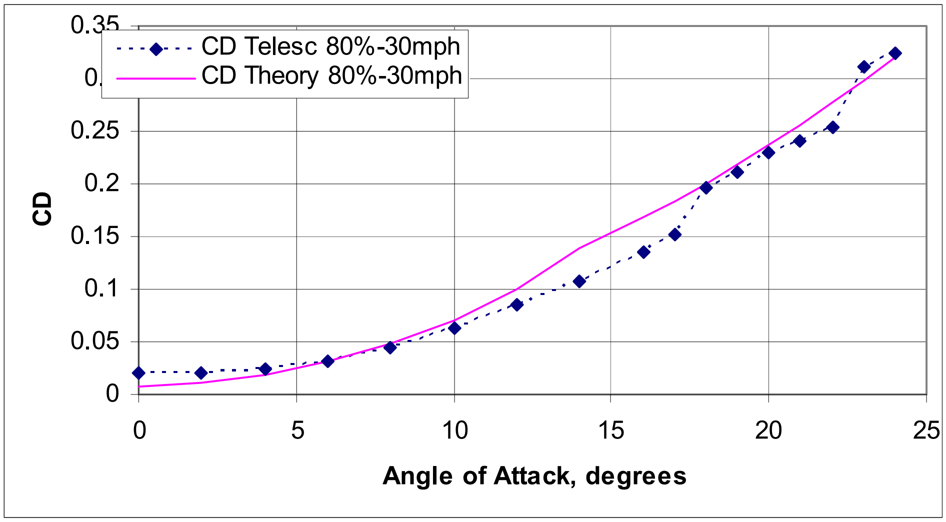
CD Telesc 80%-30mph
CD Theory 80%-30mph
CD
0.35
0.
0.25
0.2
0.15
0.1
0.05
0
0
5
10
15
20
25
Angle of Attack, degrees

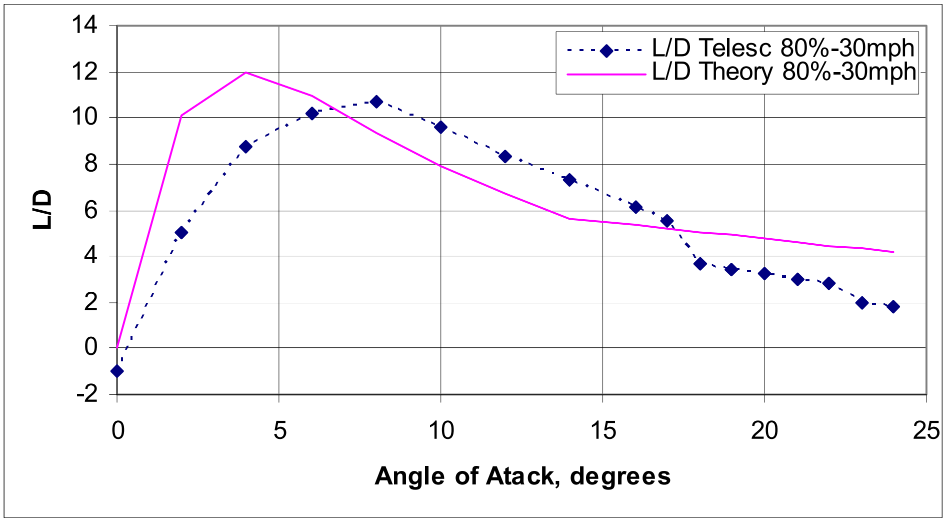
L/D Telesc 80%-30mph
L/D Theory 80%-30mph
L/D
14
12
10
8
6
4
2
0
-2
0
5
10
15
20
25
Angle of Atack, degrees

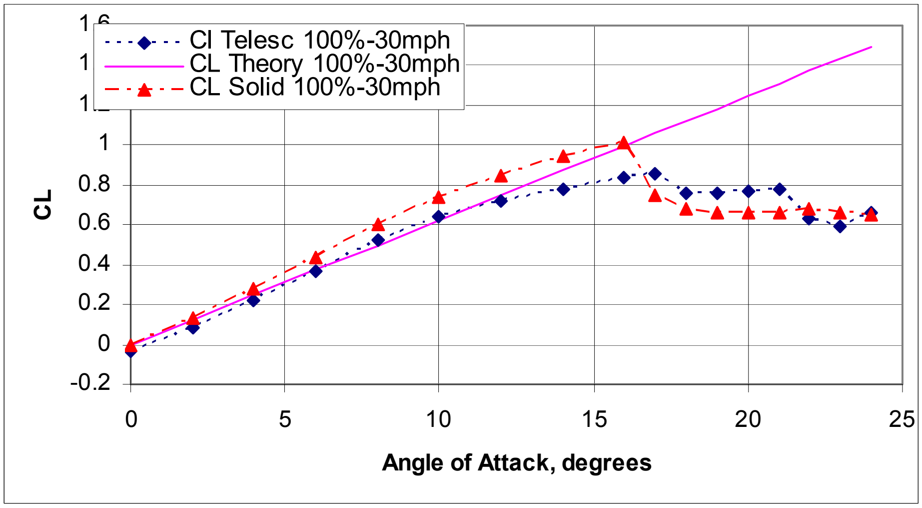

Cl Telesc 100%-30mph
CL Theory 100%-30mph
CL Solid 100%-30mph
CL
1.6
1
1
1
0.8
0.6
0.4
0.2
0
-0.2
0
5
10
15
20
25
Angle of Attack, degrees

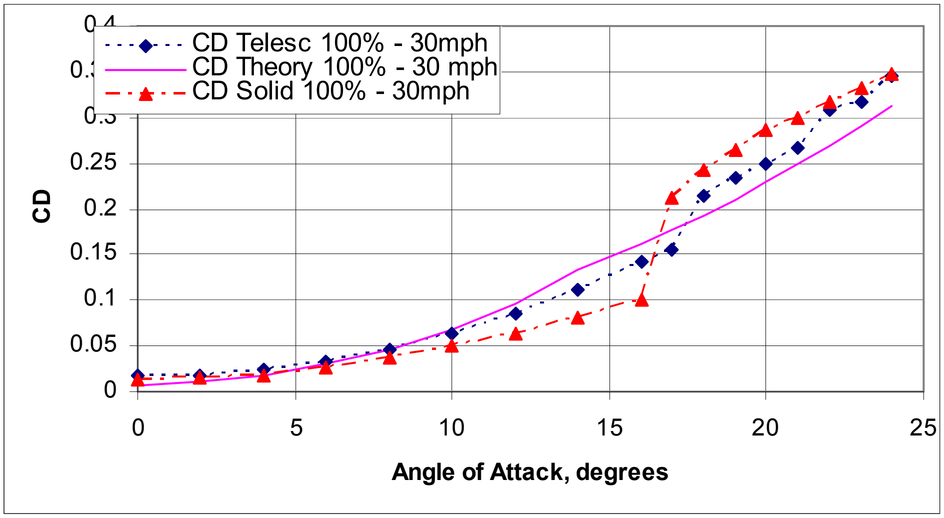

CD Telesc 100% - 30mph
CD Theory 100% - 30 mph
CD Solid 100% - 30mph
CD
0.4
0.3
0.3
0.25
0.2
0.15
0.1
0.05
0
0
5
10
15
20
25
Angle of Attack, degrees

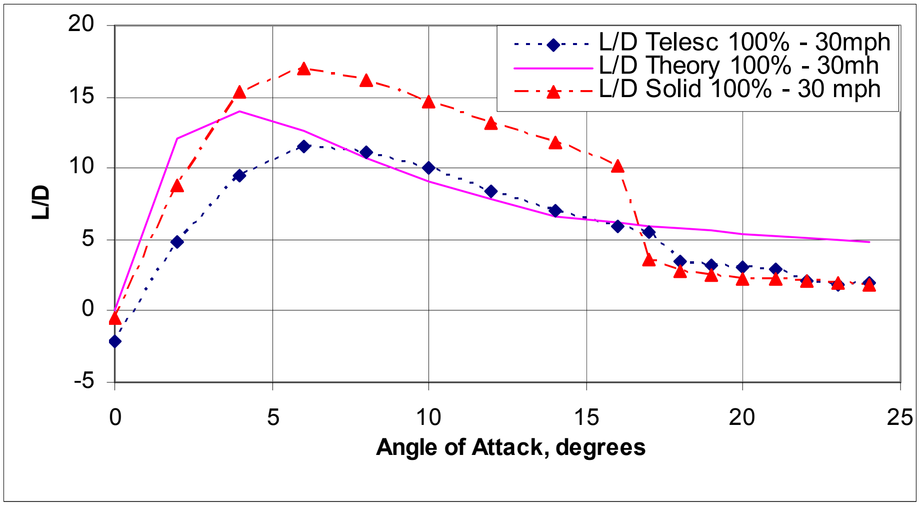

L/D Telesc 100% - 30mph
L/D Theory 100% - 30mh
L/D Solid 100% - 30 mph
L/D
20
15
10
5
0
-5
0
5
10
15
20
25
Angle of Attack, degrees

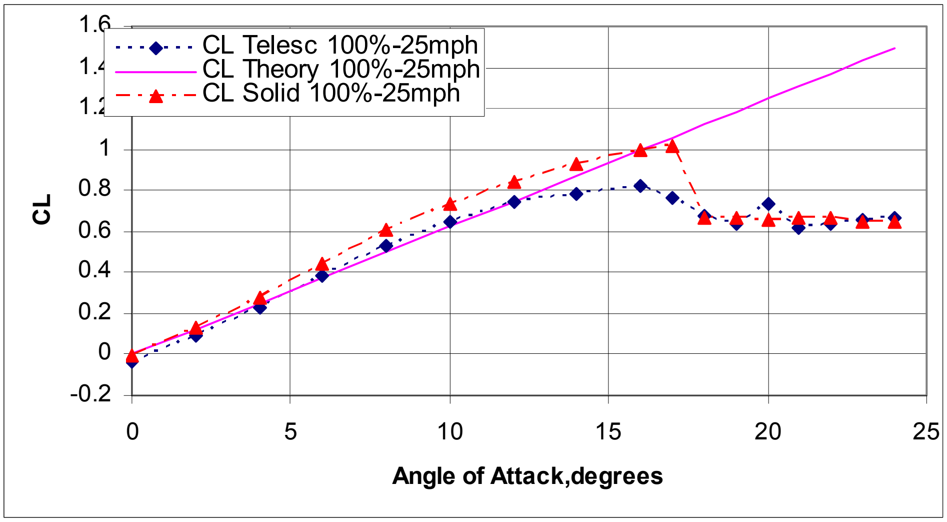
CL Telesc 100%-25mph
CL Theory 100%-25mph
CL Solid 100%-25mph
CL
1.6
1.4
1.2
1
0.8
0.6
0.4
0.2
0
-0.2
0
5
10
15
20
25
Angle of Attack,degrees

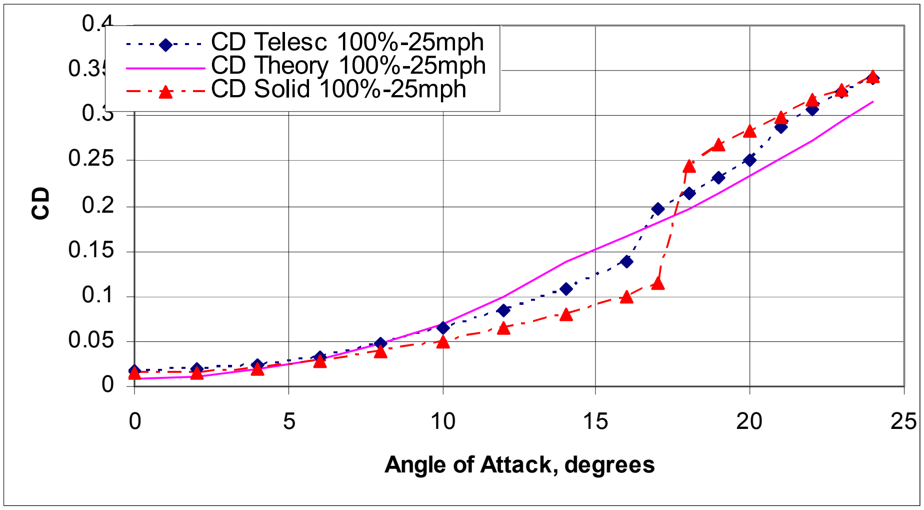
CD Telesc 100%-25mph
CD Theory 100%-25mph
CD Solid 100%-25mph
CD
0.4
0.35
0.3
0.25
0.2
0.15
0.1
0.05
0
0
5
10
15
20
25
Angle of Attack, degrees

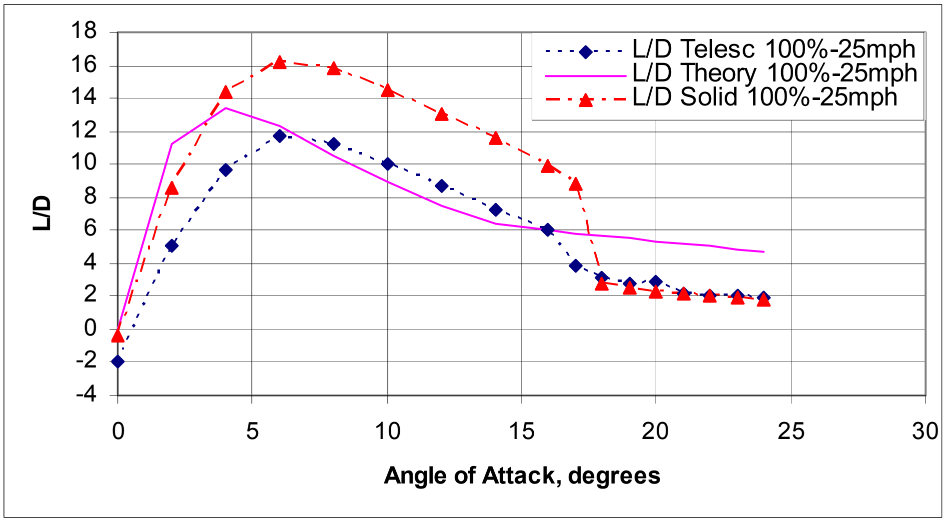
L/D Telesc 100%-25mph
L/D Theory 100%-25mph
L/D Solid 100%-25mph
L/D
18
16
14
12
10
8
6
4
2
0
-2
-4
0
5
10
15
20
25
30
Angle of Attack, degrees

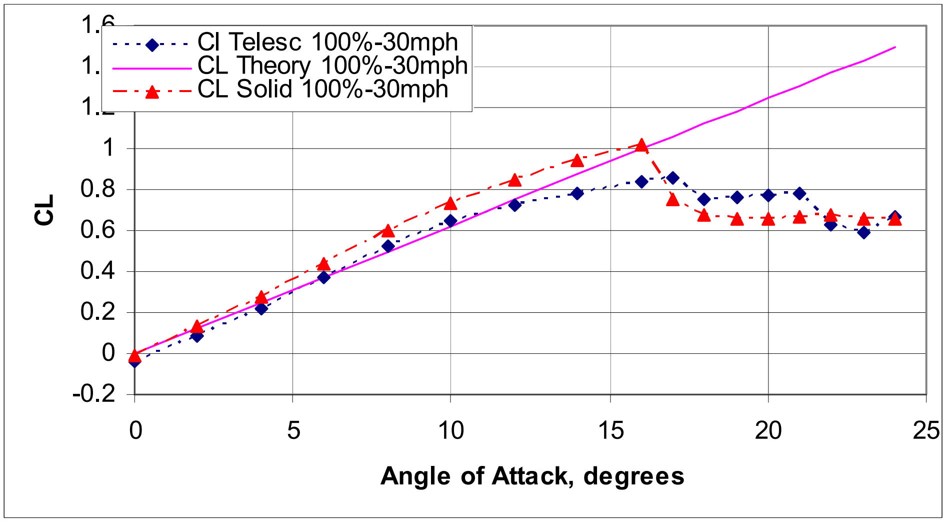

Cl Telesc 100%-30mph
CL Theory 100%-30mph
CL Solid 100%-30mph
CL
1.6
1
0.8
0.6
0.4
0.2
0
-0.2
0
5
10
15
20
25
Angle of Attack, degrees

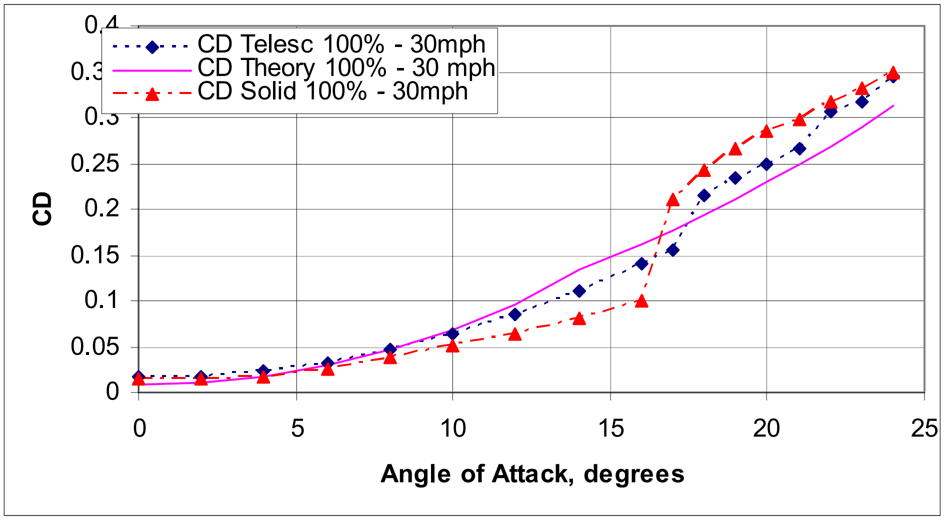

CD Telesc 100% - 30mph
CD Theory 100% - 30 mph
CD Solid 100% - 30mph
CD
0.4
0.25
0.2
0.15
0.1
0.05
0
0
5
10
15
20
25
Angle of Attack, degrees

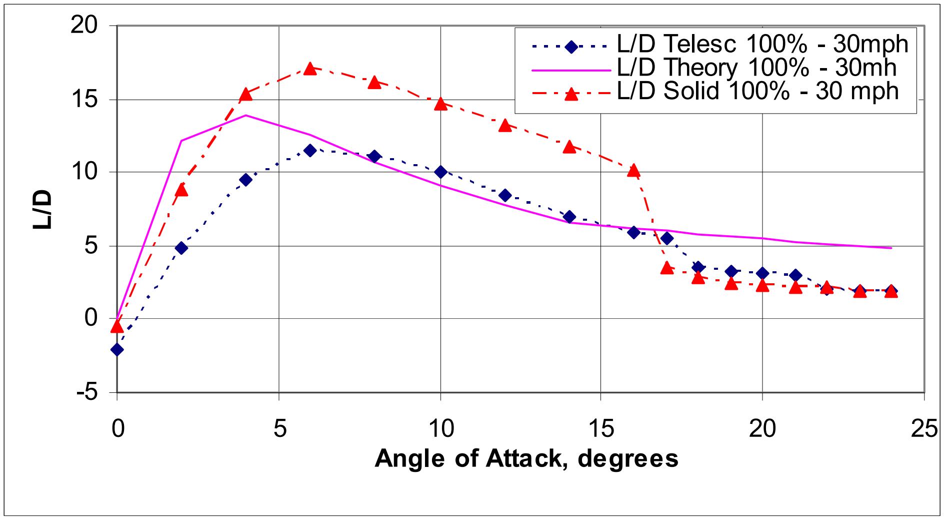

L/D Telesc 100% - 30mph
L/D Theory 100% - 30mh
L/D Solid 100% - 30 mph
L/D
20
15
10
5
0
-5
0
5
10
15
20
25
Angle of Attack, degrees

Appendix III: Wind tunnel results for the Second Generation Prototype – Test II

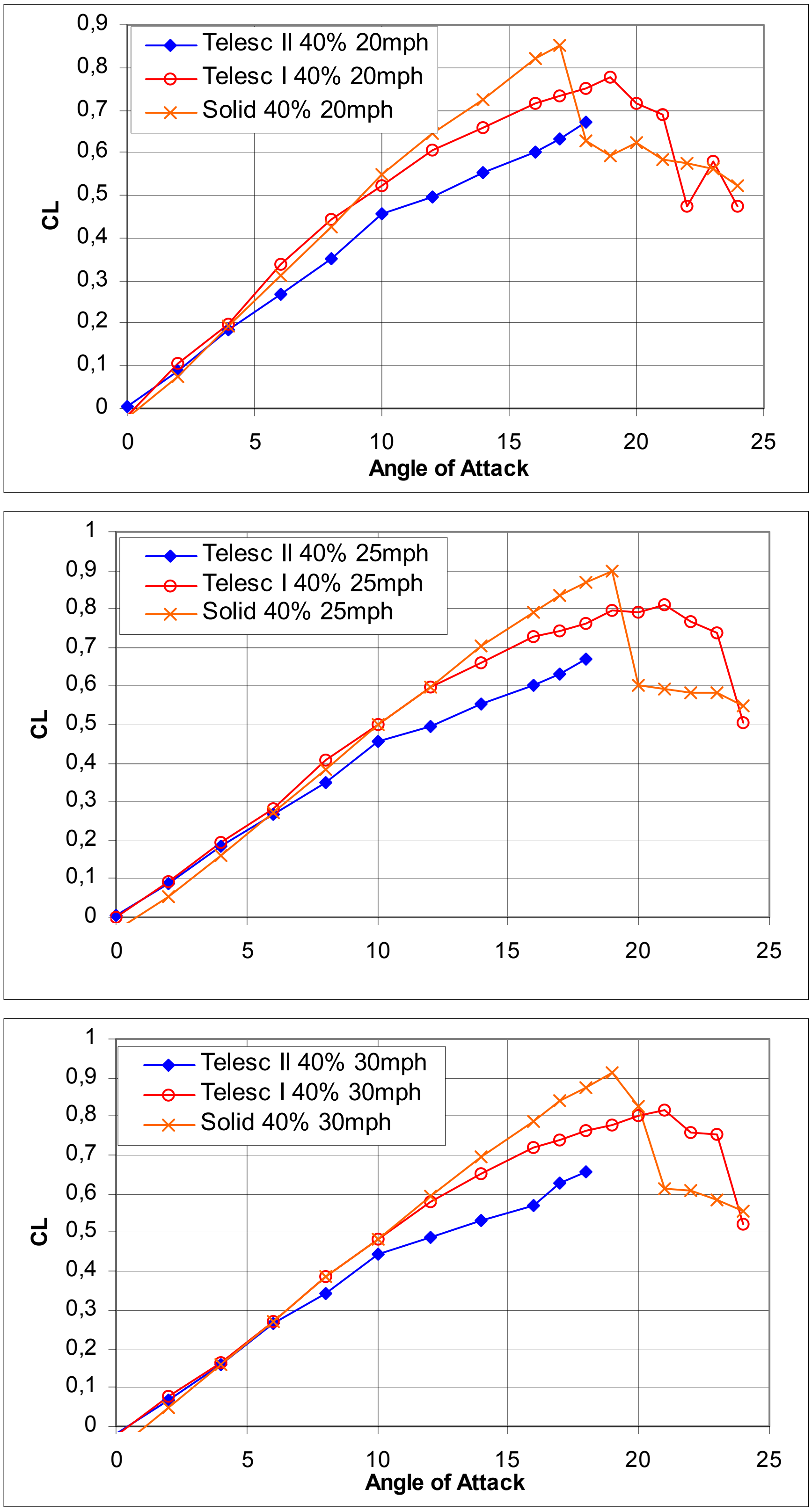

Comparison of Lift Coefficient for the two telescopic wings and the solid wing – 40%, at different free stream velocities

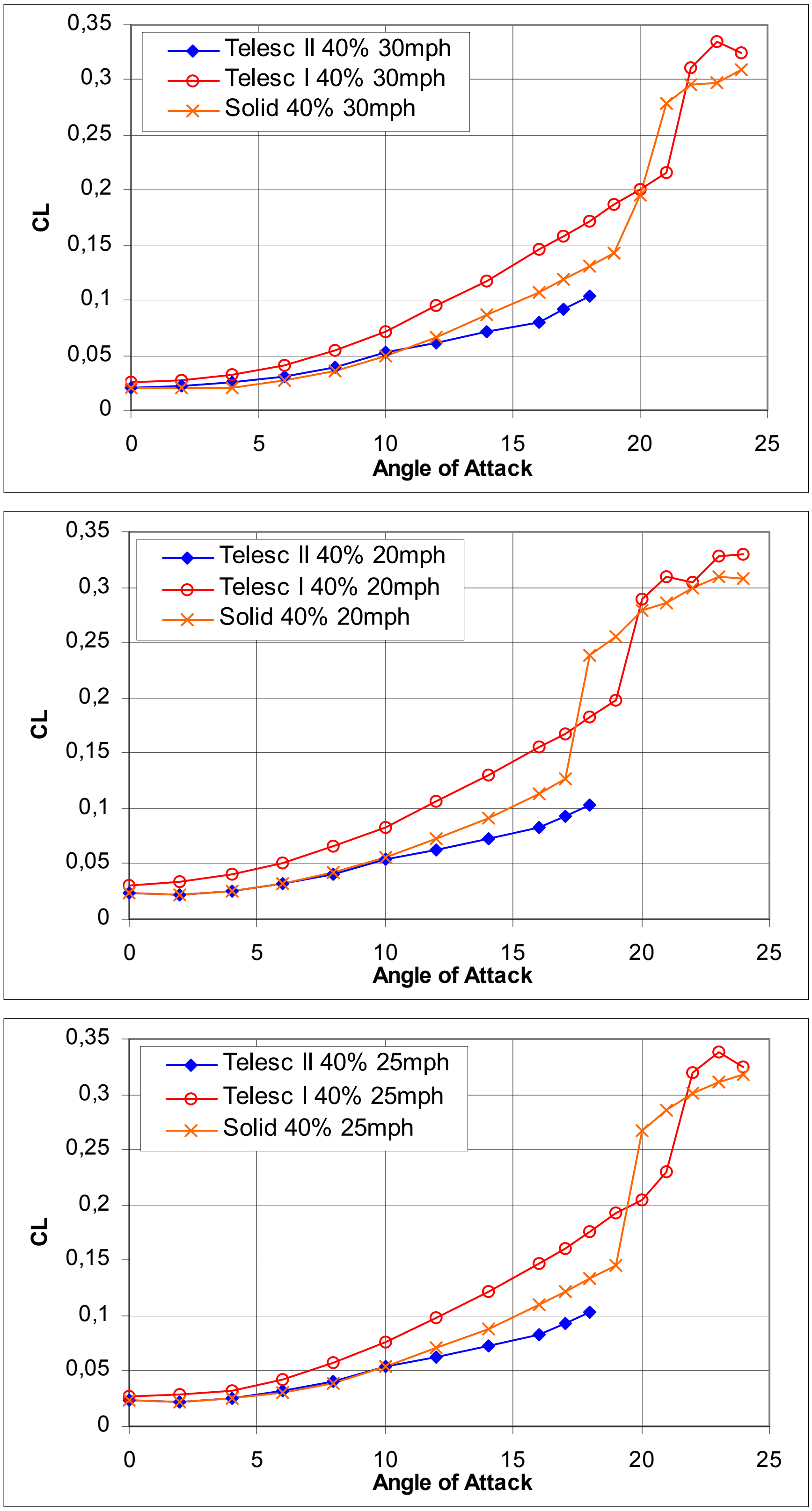

Comparison of Drag Coefficient for the two telescopic wings and the solid wing – 40%, at different free stream velocities

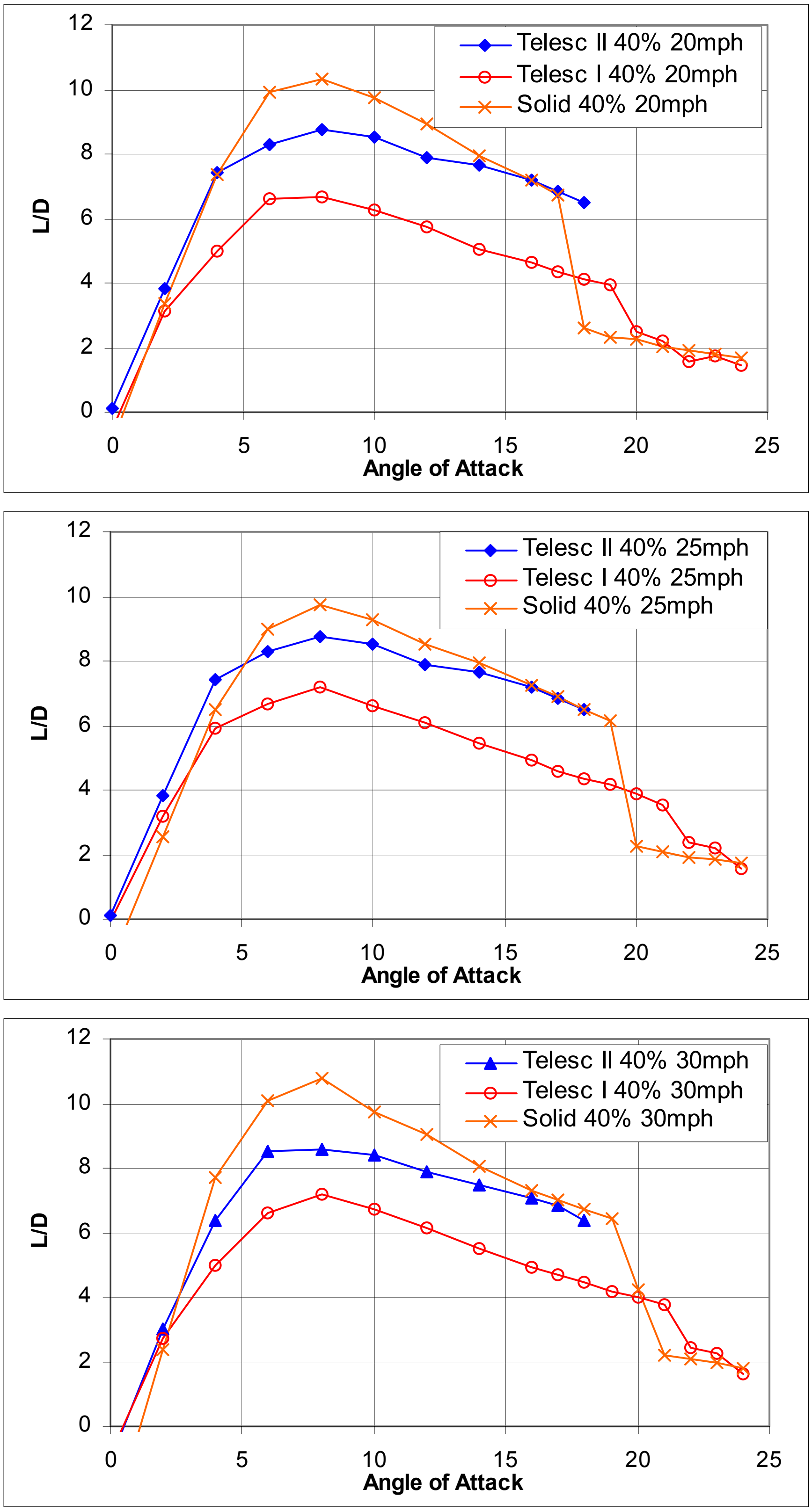

Comparison of Lift to Drag Ratio for the two telescopic wings and the solid wing – 40%, at different free stream velocities

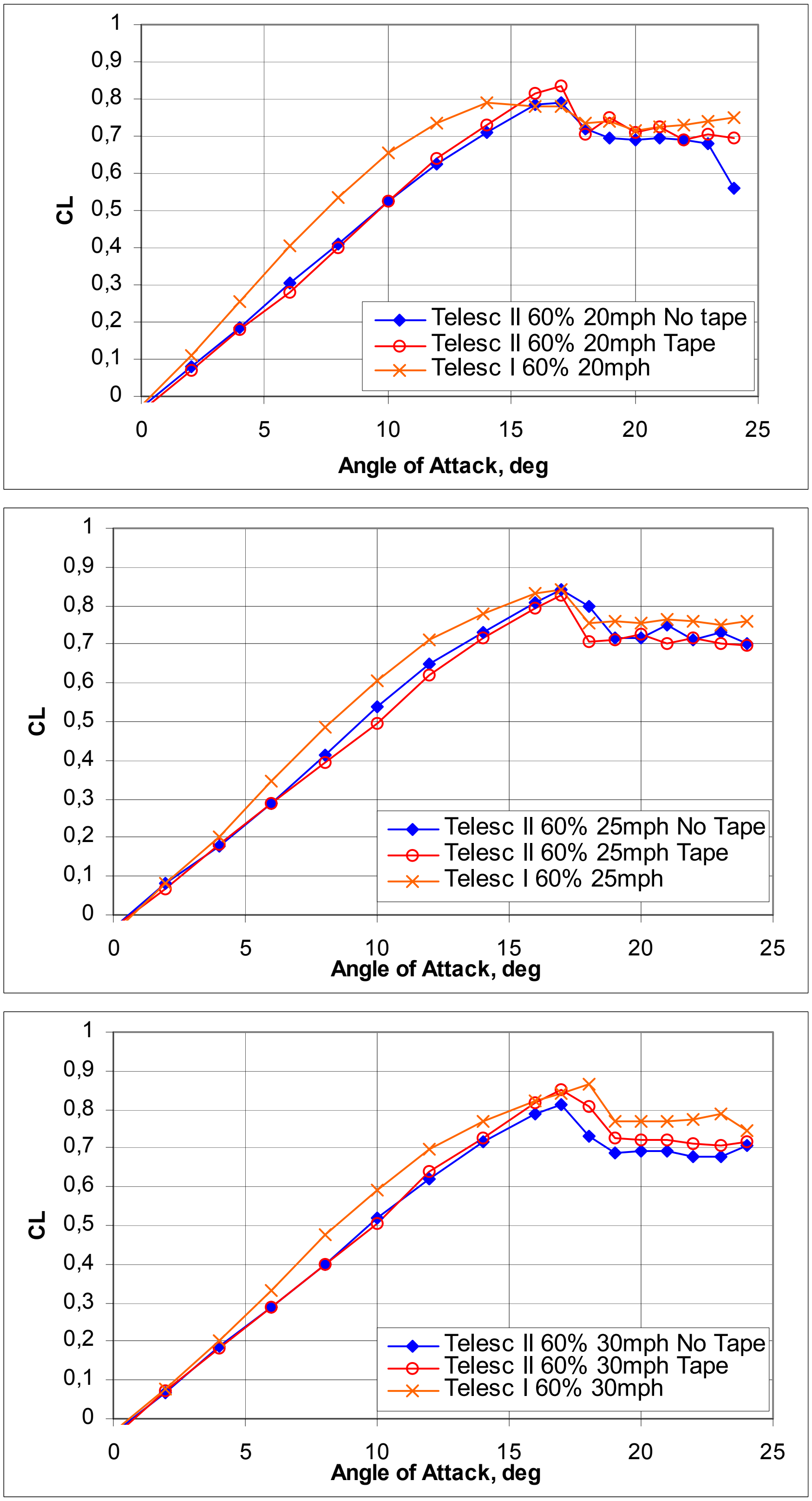

Comparison of Lift Coefficient for the two telescopic wings and influence of the Seams – 60%, at different free stream velocities

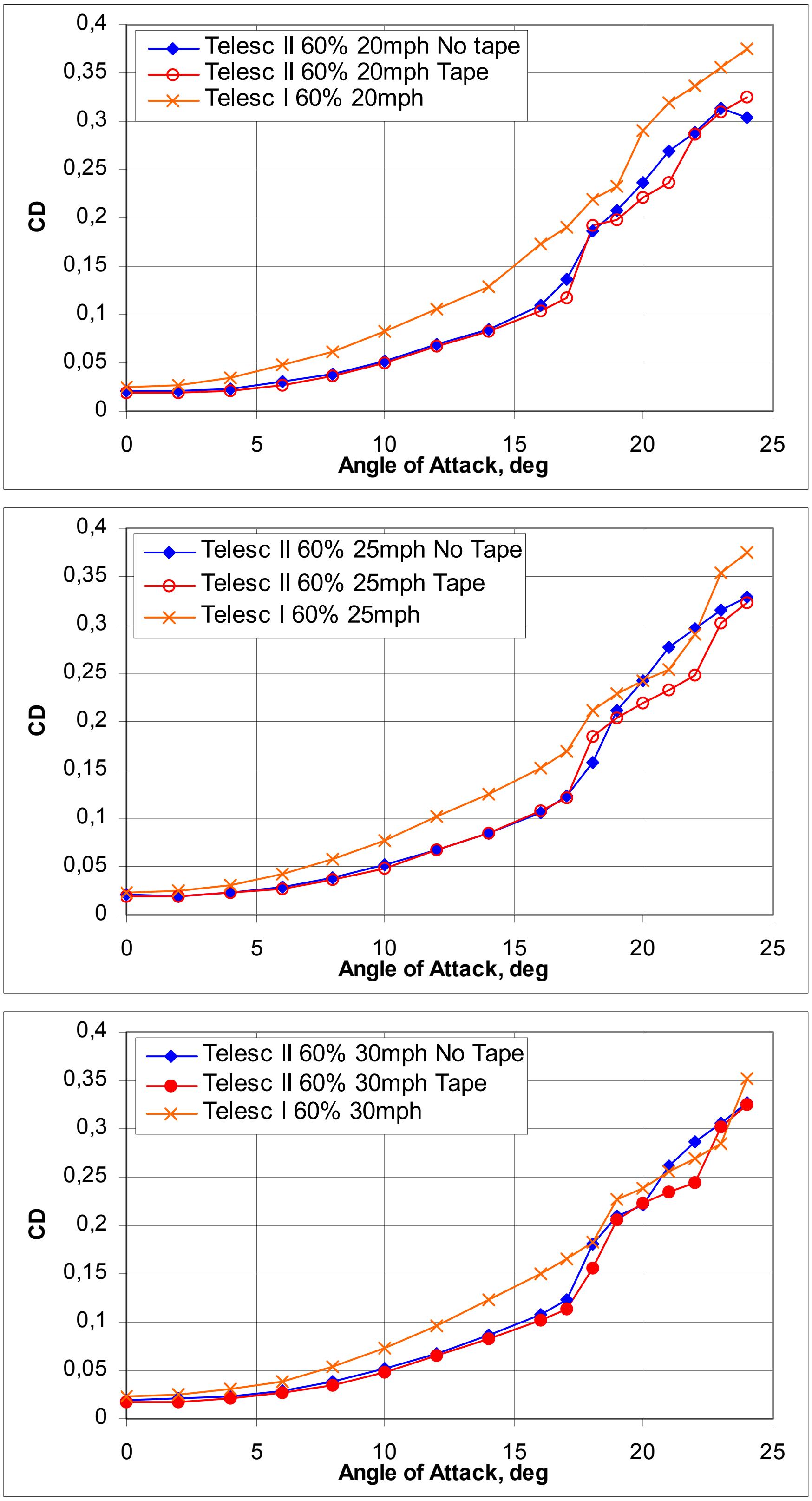

Comparison of Drag Coefficient for the two telescopic wings and influence of the Seams – 60%, at different free stream velocities

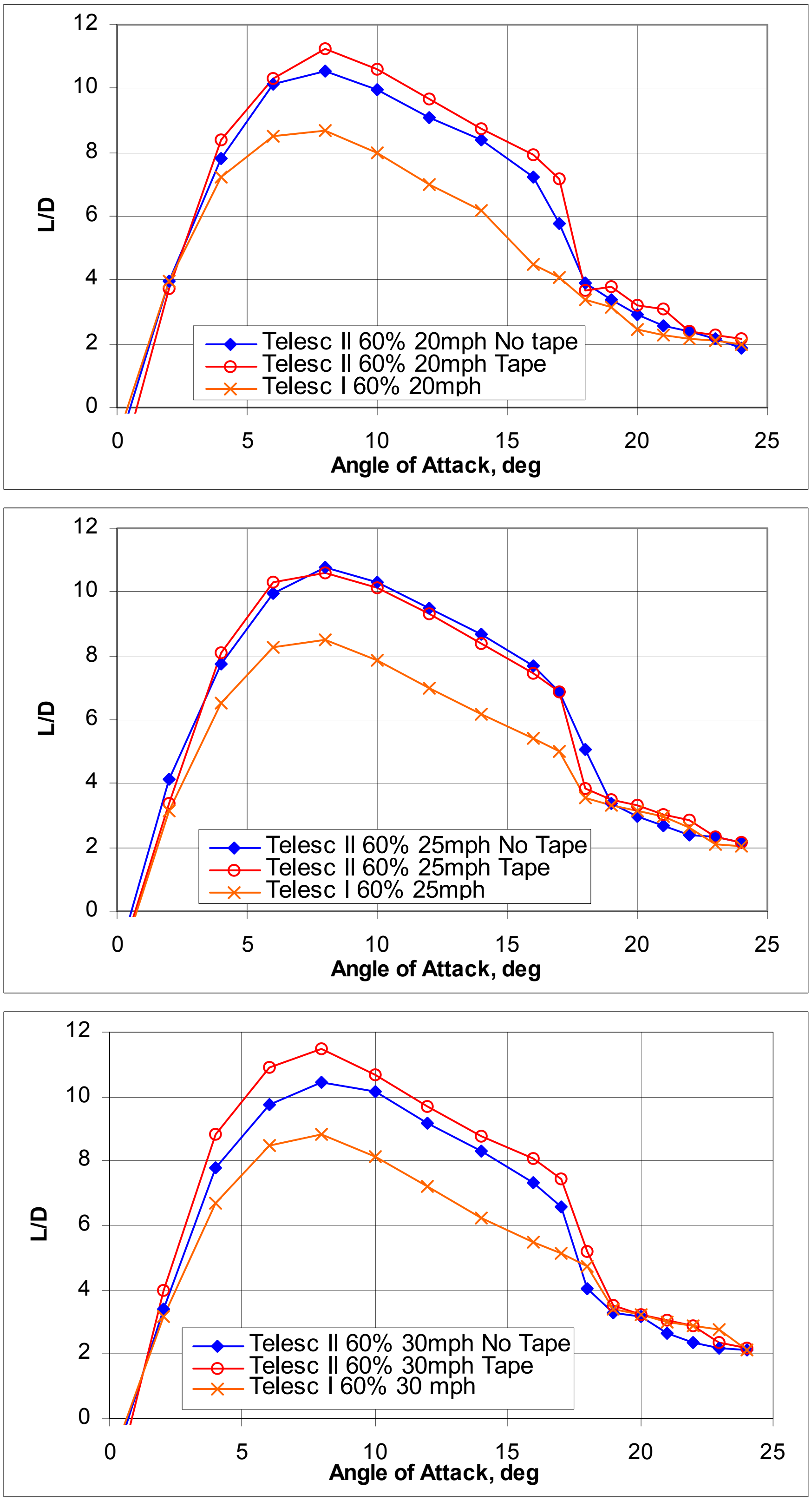

Comparison of Lift to Drag Ratio for the two telescopic wings and influence of the Seams – 60%, at different free stream velocities

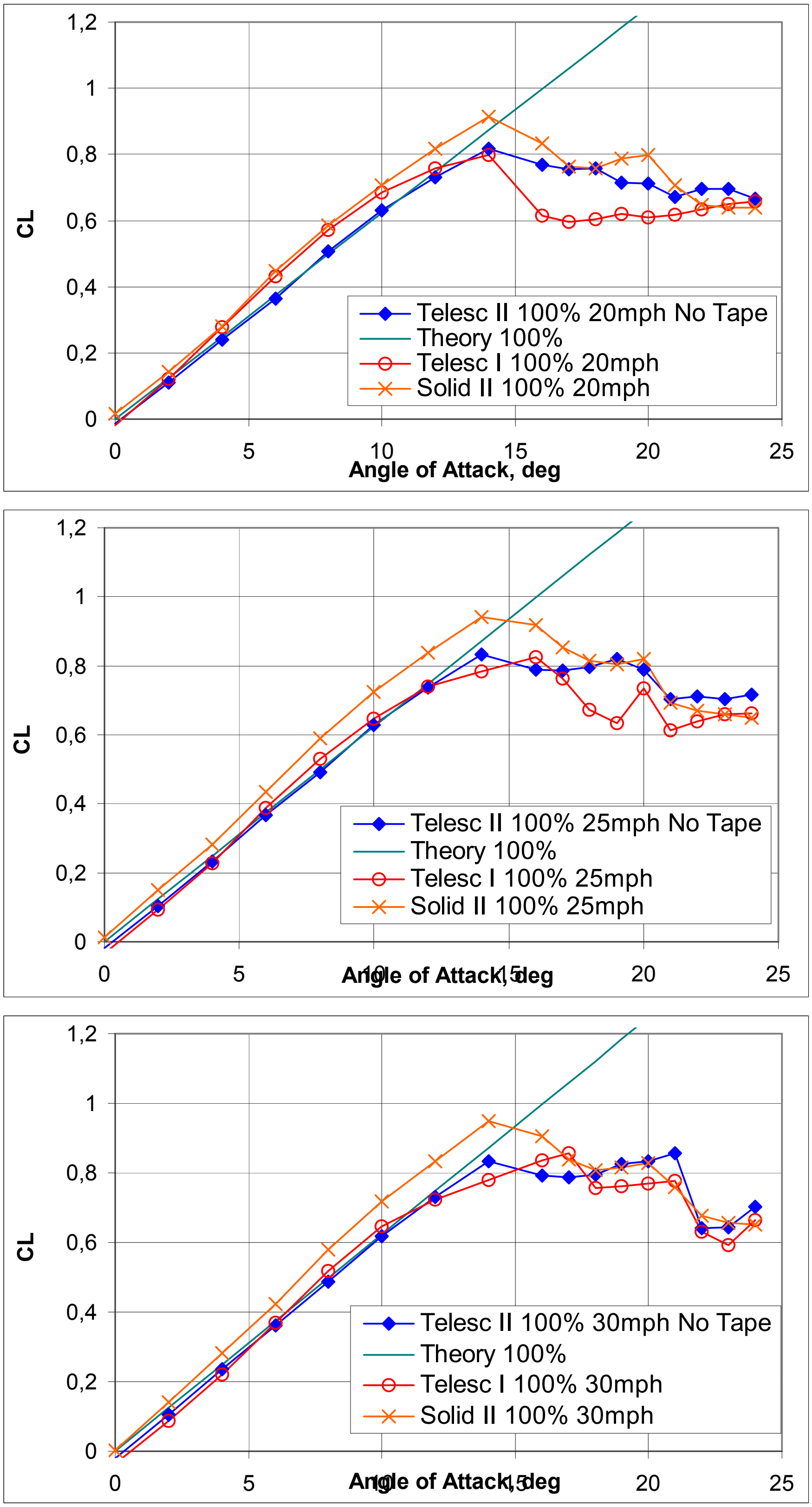

Comparison of Lift Coefficient for the two telescopic wings and the Solid Wing – 100%, at different free stream velocities

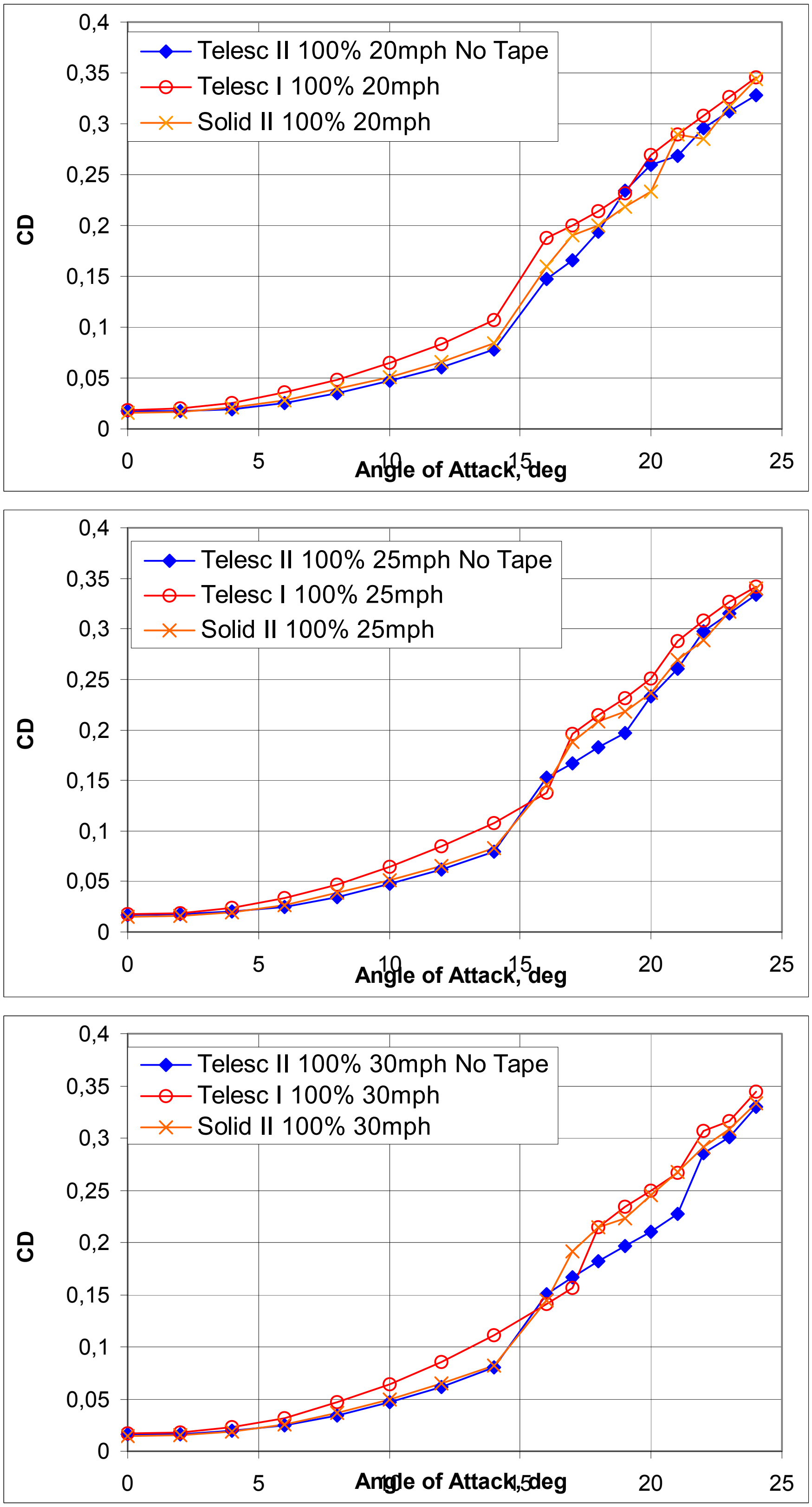

Comparison of Drag Coefficient for the two telescopic wings and the Solid Wing – 100%, at different free stream velocities

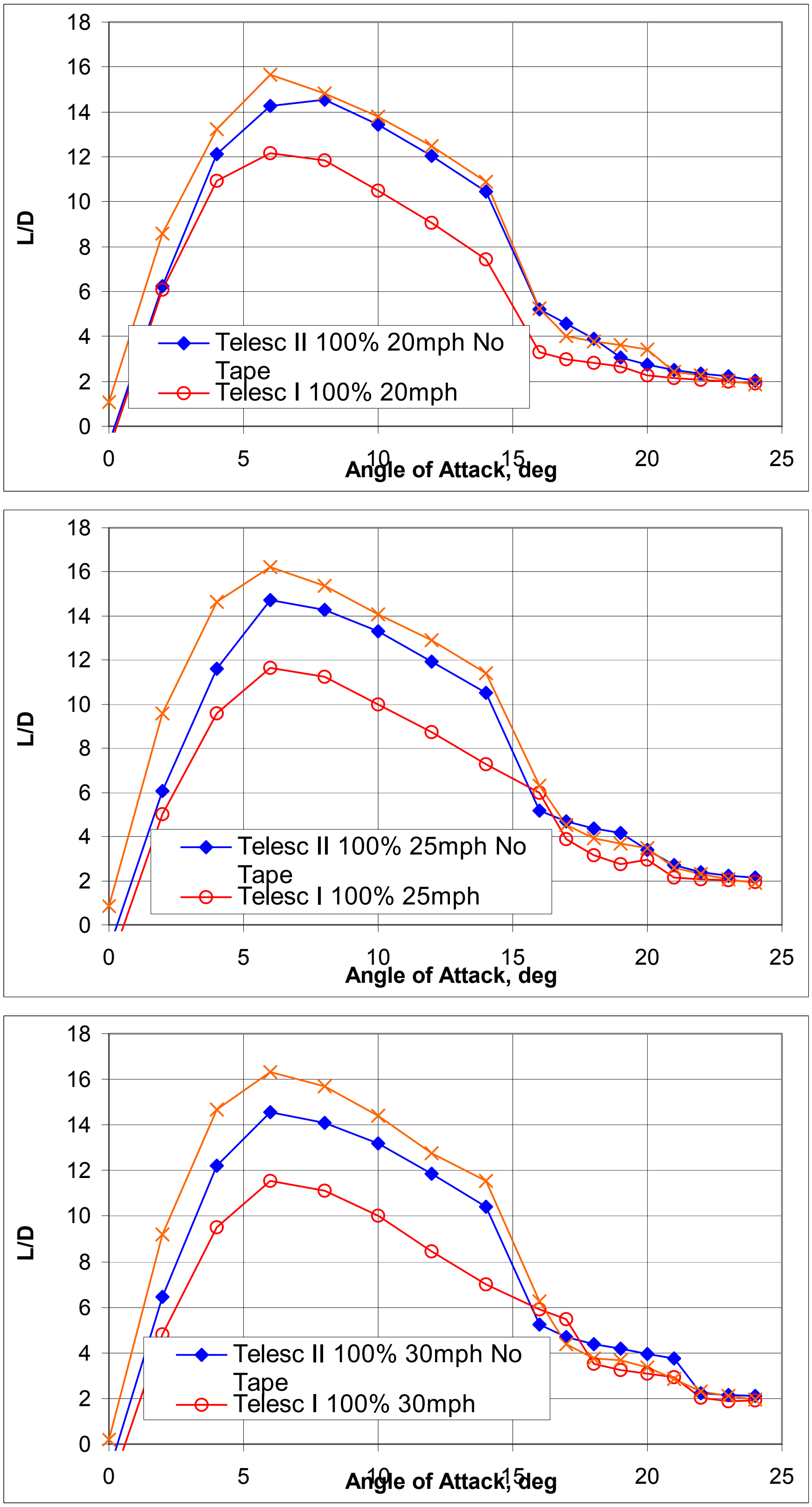

Comparison of Lift to Drag Ratio for the two telescopic wings and the Solid Wing – 100%, at different free stream velocities

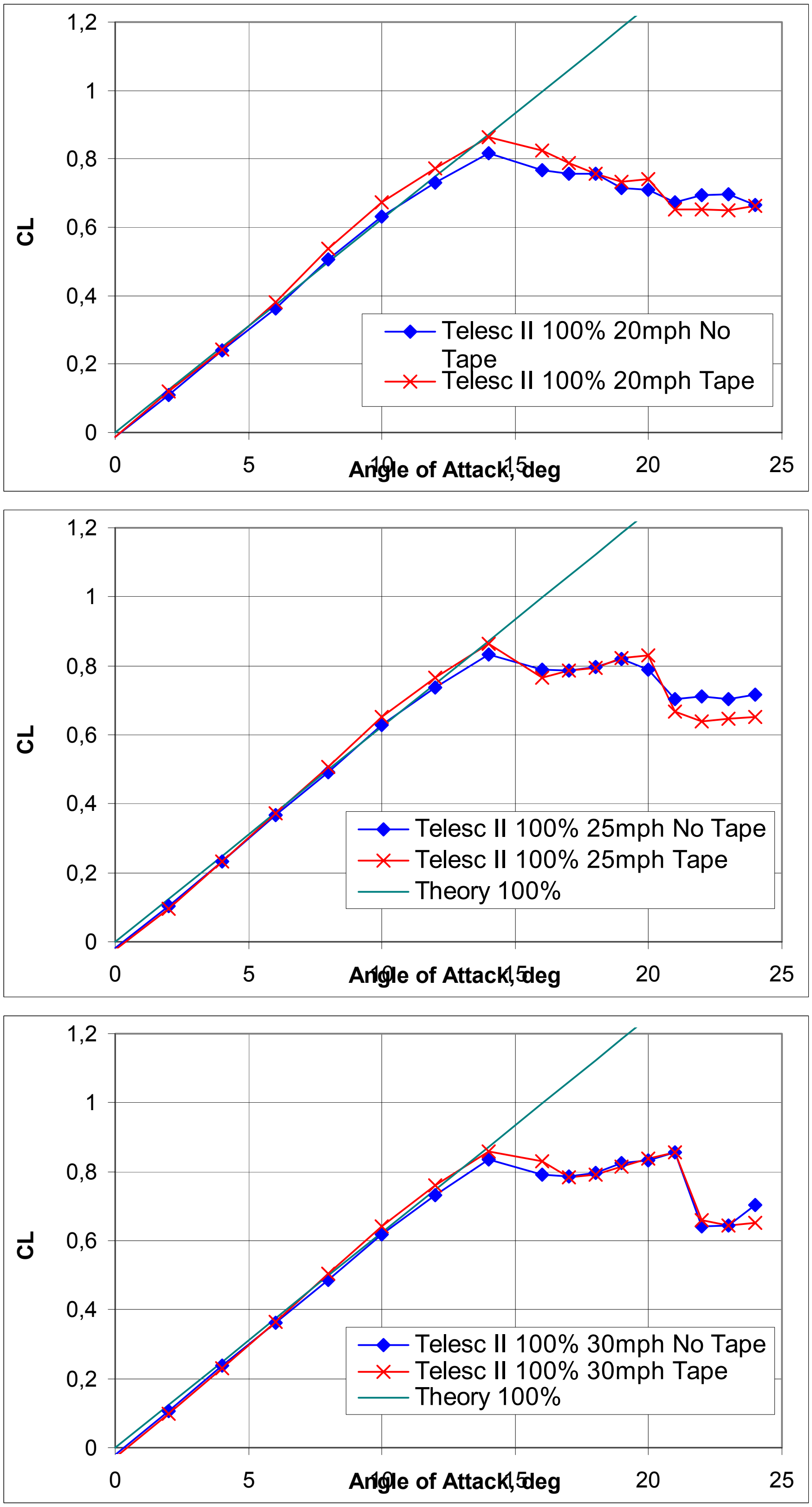

Comparison of Lift Coefficient, Influence of the Seams – 100%, at different free stream velocities

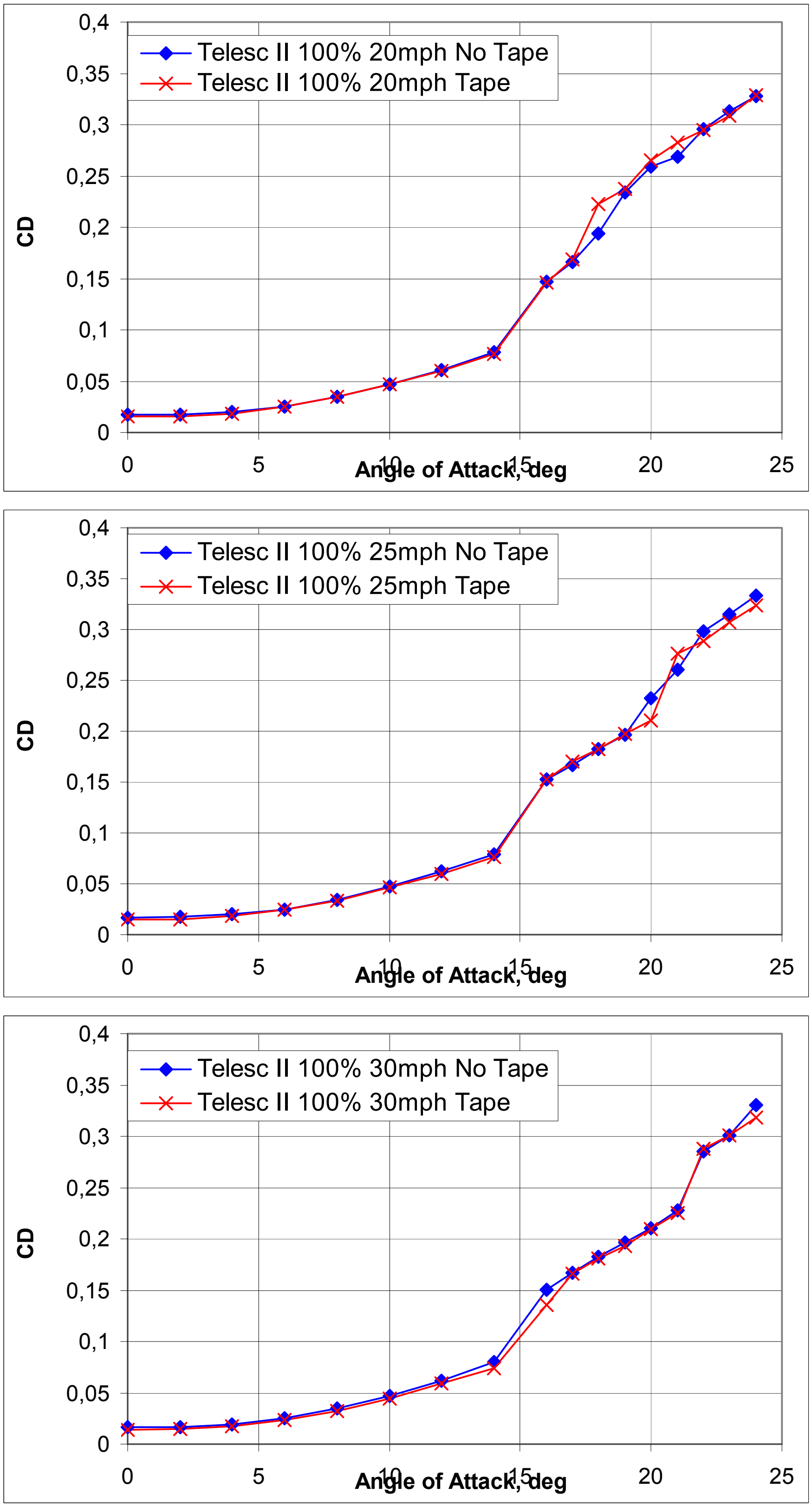

Comparison of Drag Coefficient, Influence of the Seams – 100%, at different free stream velocities

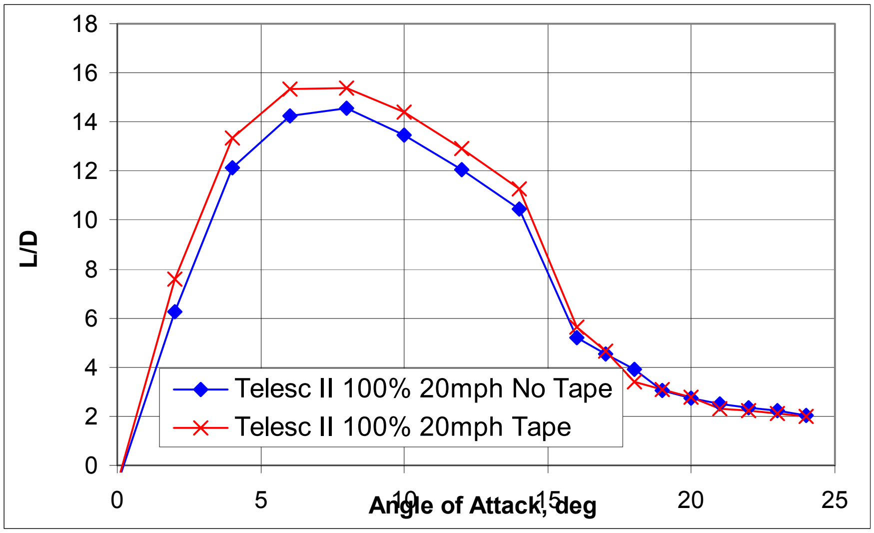

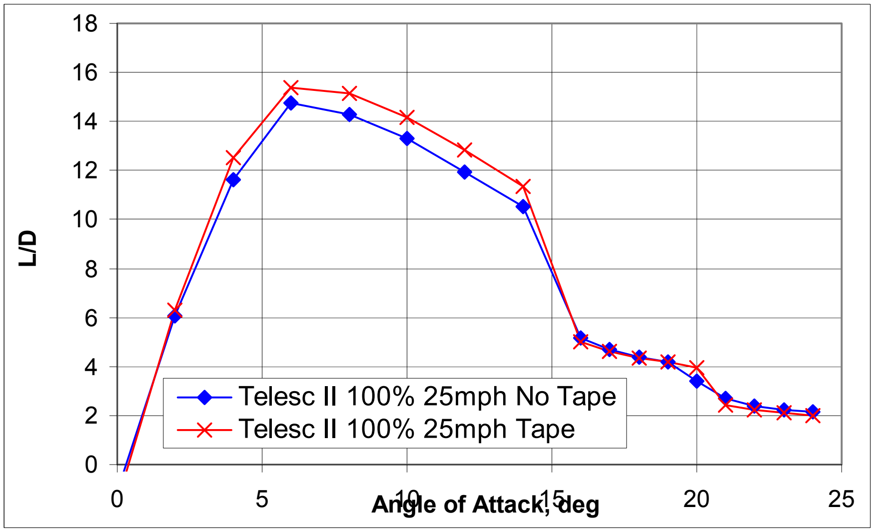

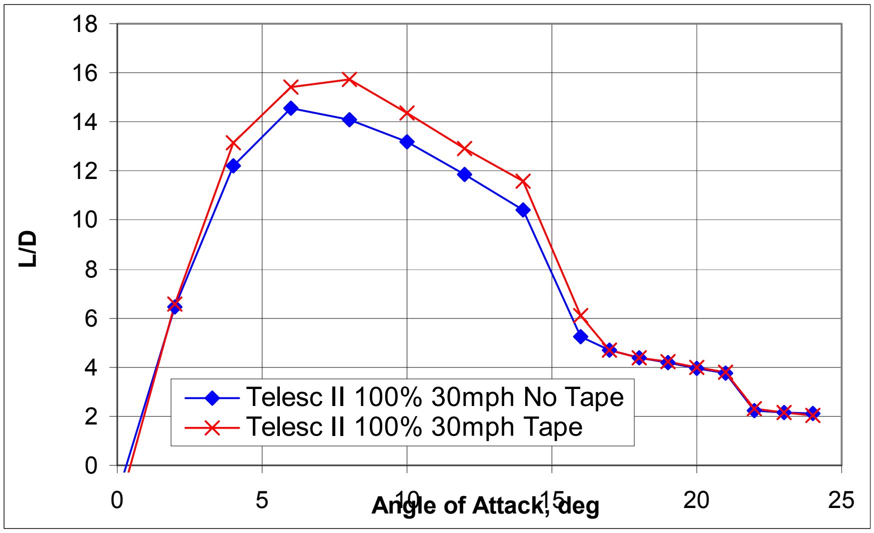

Comparison of Lift to Drag Ratio, Influence of the Seams – 100%, at different free stream velocities

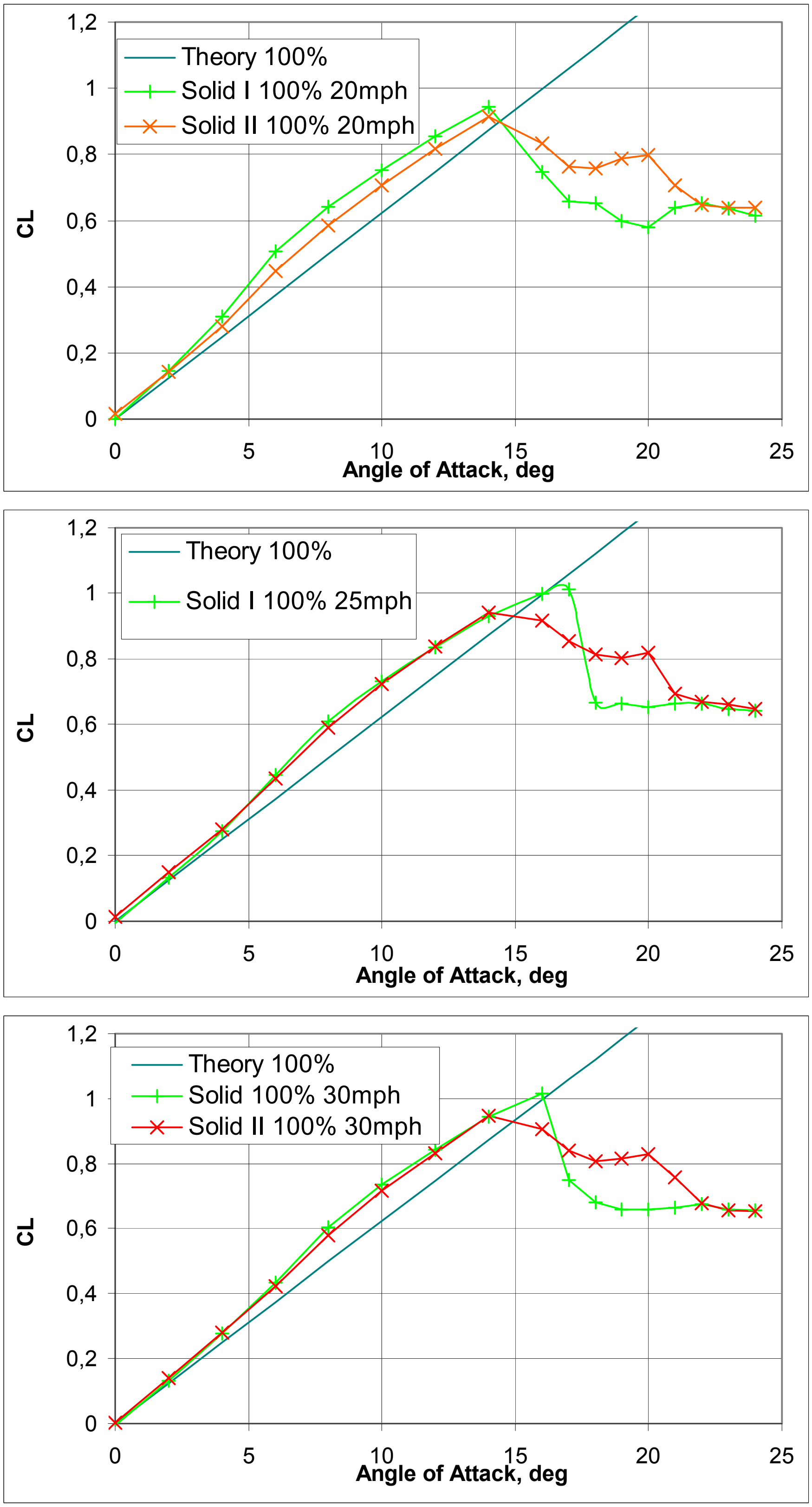

Comparison of Lift Coefficient for the two Solid Wings– 100%, at different free stream velocities

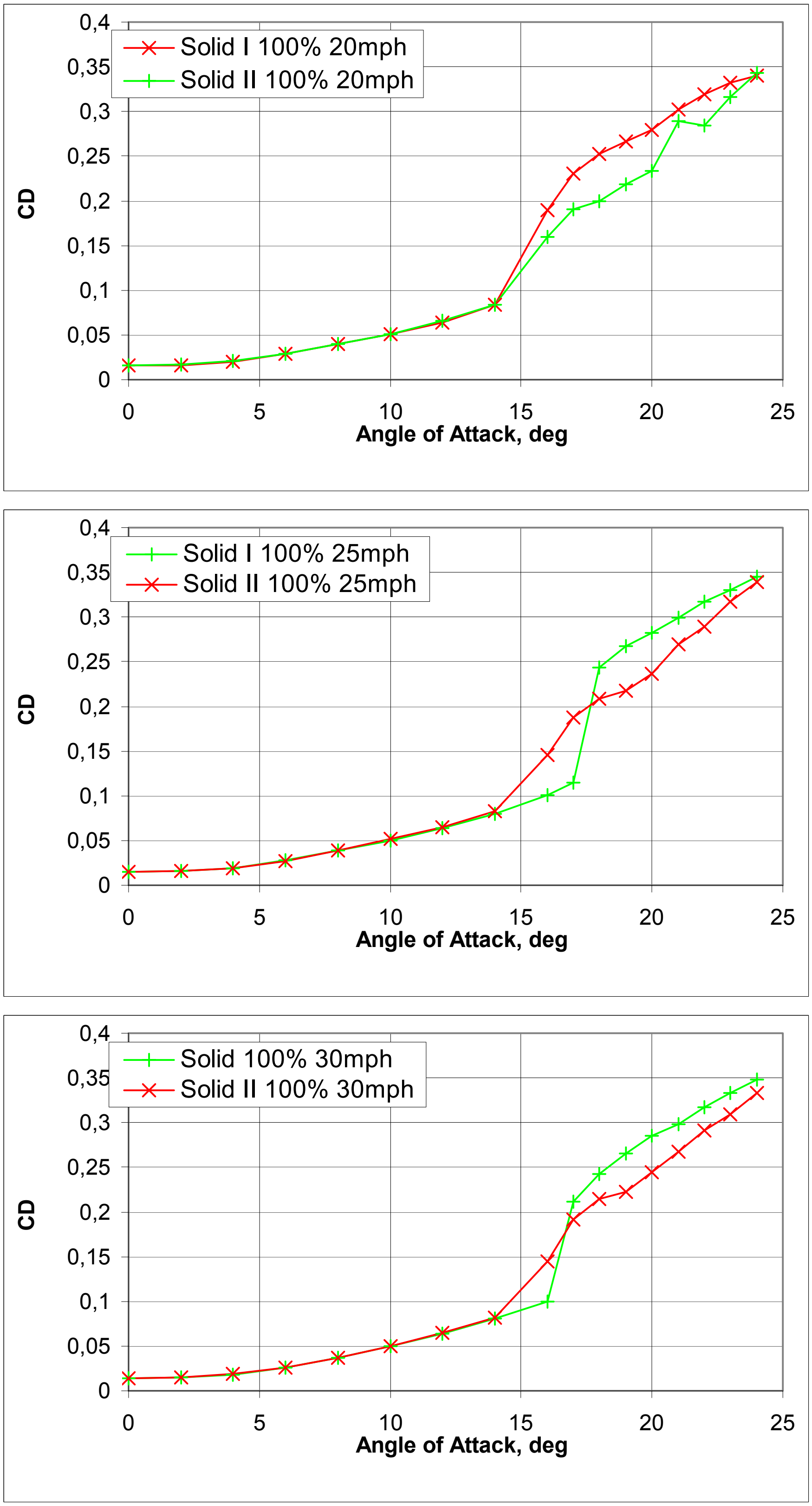

Comparison of Drag Coefficient for the two Solid Wings– 100%, at different free stream velocities

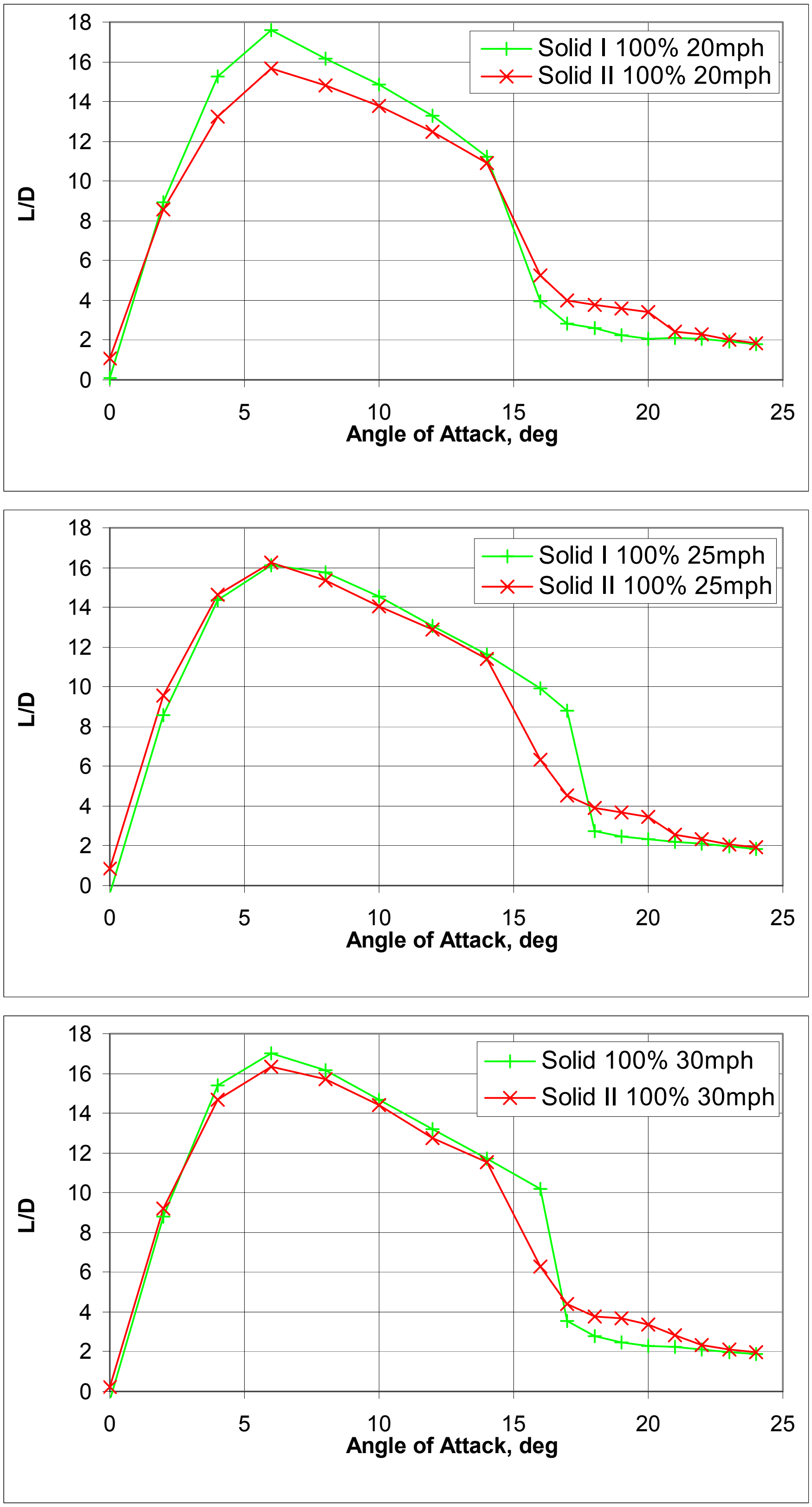

Comparison of Lift to Drag Ratio for the two Solid Wings– 100%, at different free stream velocities

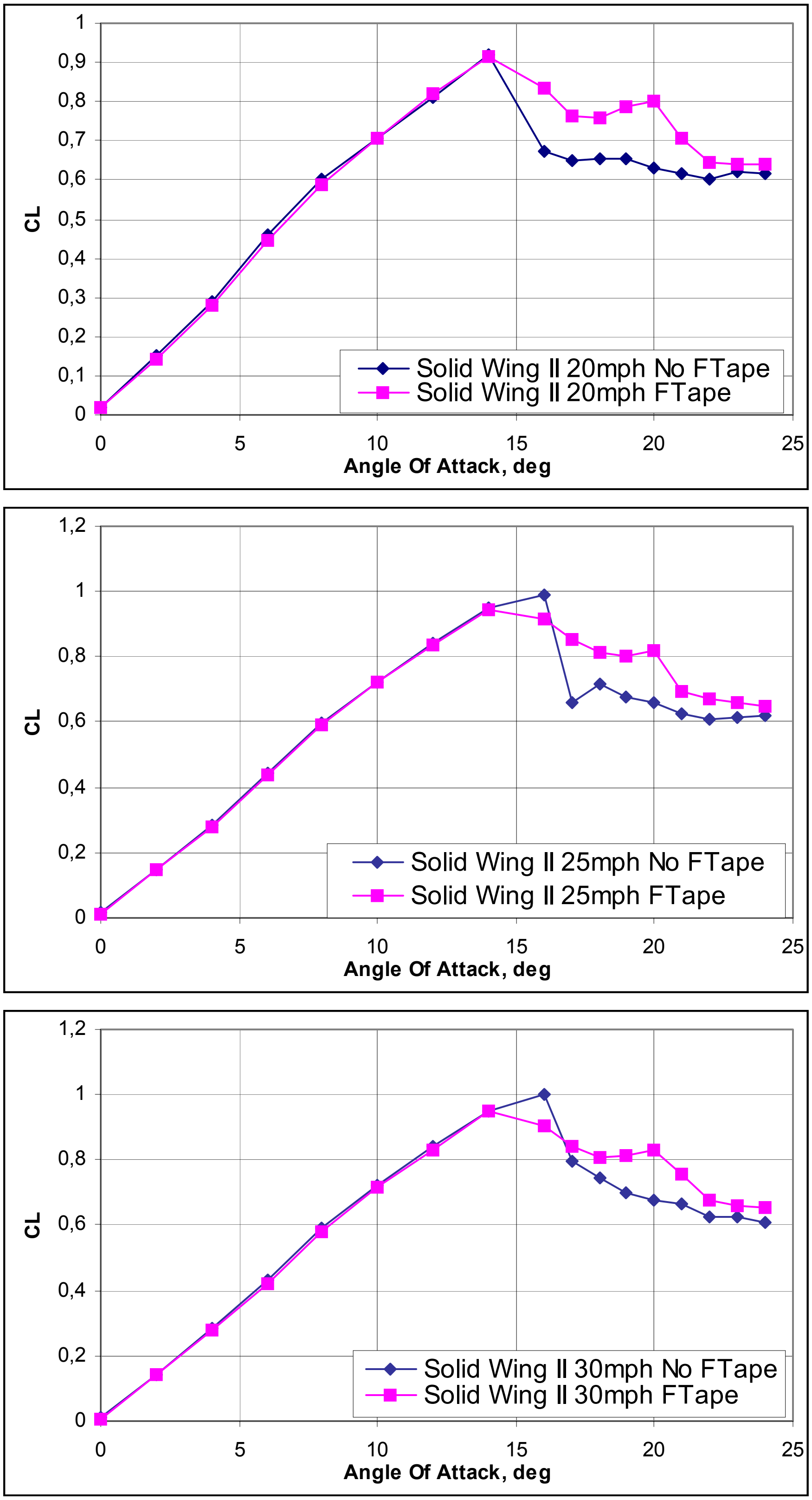

Comparison of Lift Coefficient for the Solid Wings II– 100%, Effect of the Friction Tape, at different free stream velocities

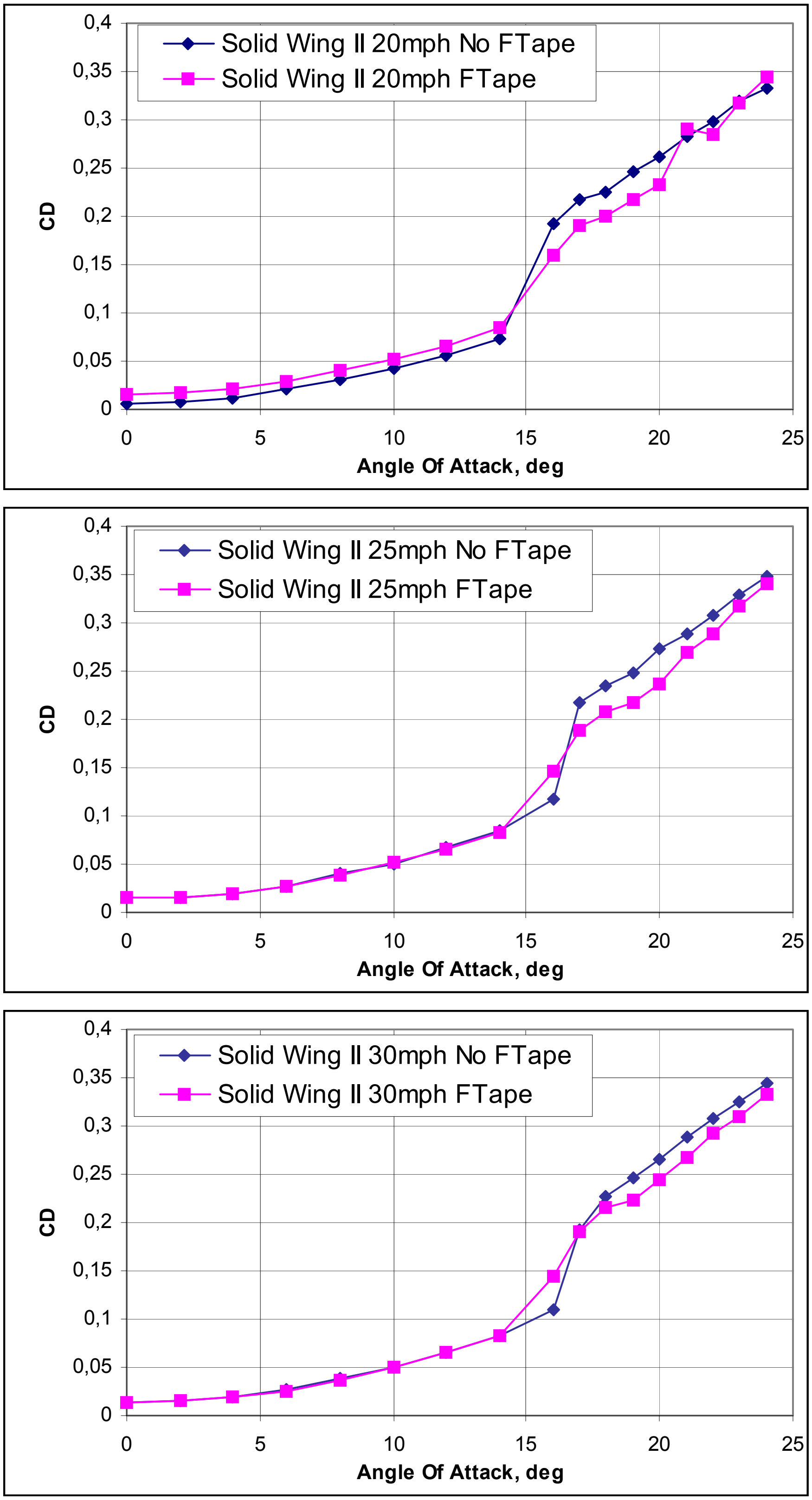

Comparison of Drag Coefficient for the Solid Wings II– 100%, Effect of the Friction Tape, at different free stream velocities

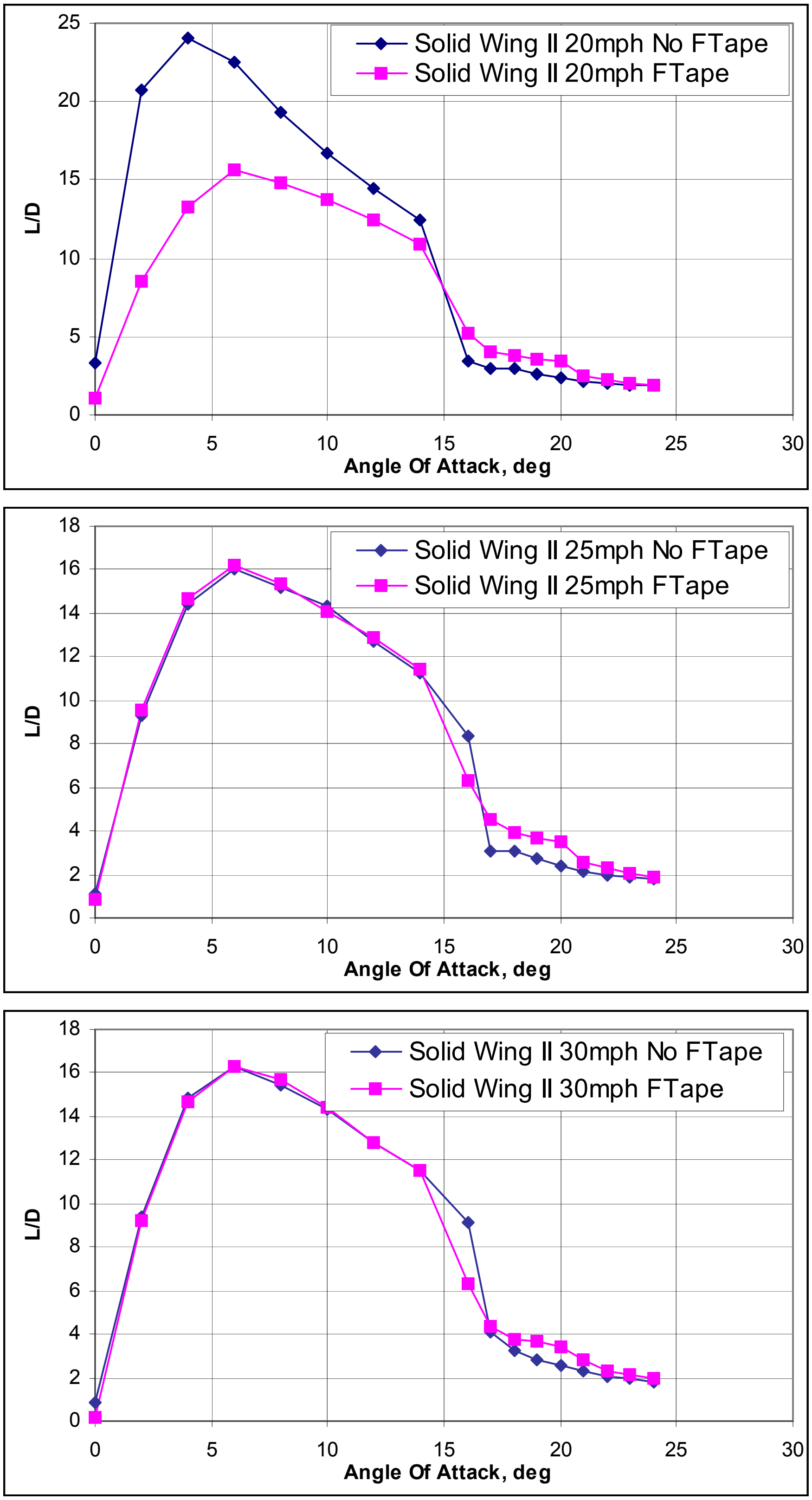

Comparison of Lift to Drag Ratio for the Solid Wings II– 100%, Effect of the Friction Tape, at different free stream velocities

Appendix IV: Root Moment Derivation

Integration Formulae Used

- $$\int \sqrt{a^2 - X^2}\,dX = \frac{X}{2}\sqrt{a^2 - X^2} + \frac{a^2}{2} Sin^{-1}\left(\frac{X}{a}\right)$$

  $$\int X\sqrt{a^2 - X^2}\,dX = -\frac{1}{3}\left(a^2 - X^2\right)^{3/2}$$

  $$\int \frac{dX}{Sin\left(AX\right)} = \frac{1}{A}\ln\left(\tan\left(\frac{AX}{2}\right)\right)$$

Lift Distribution and Constants

- $$q(X) = \rho_\infty V_\infty \Gamma_o \sqrt{1 - \left(\frac{2X}{b}\right)^2} = C_1\sqrt{C_2}\sqrt{a - X^2}$$

  $$C_1 = \rho_\infty V_\infty \Gamma_o$$

  $$C_2 = \frac{4}{b^2}$$

  $$a = \frac{1}{\sqrt{C_2}} \qquad A = \frac{1}{a}$$

Strain and Moment Derivation

- $\frac{dV}{dX} = -q(X)$ and $\frac{dM}{dX} = V$

Strain Derivation and Boundary Condition

- $$-V(X) = \int q(X)dX = C_1\sqrt{C_2}\left[\frac{X}{2}\sqrt{a^2 - X^2} + \frac{a}{2}Sin^{-1}\left(\frac{X}{a}\right)\right] + D_1$$

  $$V(0) = 0 \Rightarrow D_1 = C_1\sqrt{C_2}\left[\frac{X}{2}\sqrt{a^2 - X^2} + \frac{a}{2}Sin^{-1}\left(\frac{X}{a}\right)\right]$$

Moment Derivation and Boundary Conditions

- $$M(X) = \int V(X)dX = -\frac{C_1\sqrt{C_2}}{2}\left[-\left(a^2 - X^2\right)^{3/2}\right] - \frac{C_1\sqrt{C_2}}{2}a^2\left[\frac{1}{A}\ln\left(\tan\frac{AX}{2}\right)\right]$$
$$\ldots\ldots\ldots\ldots\ldots\ldots\ldots\ldots\ldots\ldots - D_1X + D_2$$

$$M(L) = 0 \Rightarrow D_2 = \frac{C_1\sqrt{C_2}}{2}\left[-\left(a^2 - L^2\right)^{3/2}\right] + \frac{C_1\sqrt{C_2}}{2}a^2\left[\frac{1}{A}\ln\left(\tan\frac{AL}{2}\right)\right] + D_1L$$

Root Moment

- $$M(0) = -\frac{C_1\sqrt{C_2}}{2}\left[-\frac{1}{3}\left(a^2\right)^{3/2}\right] + 0 - 0 + D_2$$

$$M(0) = -\frac{C_1\sqrt{C_2}}{2}\left[-\frac{1}{3}\left(a^2\right)^{3/2}\right] + \frac{C_1\sqrt{C_2}}{2}\left[-\left(a^2 - L^2\right)^{3/2}\right]$$
$$\ldots\ldots\ldots\ldots + \frac{C_1\sqrt{C_2}}{2}a^2\left[\frac{1}{A}\ln\left(\tan\frac{AL}{2}\right)\right]$$
$$\ldots\ldots\ldots\ldots + L\left(C_1\sqrt{C_2}\left[\frac{X}{2}\sqrt{a^2 - X^2} + \frac{a}{2}Sin^{-1}\left(\frac{X}{a}\right)\right]\right)$$

BIBLIOGRAPHY

1. *Future Advances in Aeronautical Systems,* Gallington et al., "Chapter 6: Unmanned Aerial Vehicles", 1996.
2. Aircraft Office. *NASA's Wallops Flight Facility*. http://www.wff.nasa.gov /~apb/
3. BAA 01-42, Addendum 7, *Special Focus Area: Morphing Aerial Aircraft Structures (MAS)*.
4. R. W. Wlezien, G. C. Horner, A. R. McGowan, S. L. Padula, M. A. Scott, R. J. Silcox, and J. O. Simpson; "The Aircraft Morphing Program", AIAA Paper No. 1998-1927, AIAA/ASME/ASCE/AHS/ASC Structures, Structural Dynamics, and Materials Conference and Exhibit, 39th, and AIAA/ASME/AHS Adaptive Structures Forum, Long Beach, CA, Apr. 20-23, 1998
5. J. Bowman and B. Sanders, T. Weisshaar,; "Evaluating the Impact of Morphing Technologies on Aircraft Performance", AIAA Paper No. 2002-1631, 43rd AIAA/ASME/ASCE/AHS/ASC Structures, Structural Dynamics, and Materials Conference
6. Anderson, John D., Jr. *Introduction to Flight*, 4th Edition, McGraw-Hill Book Company, New York, 2000, pg 226-229 and 404-415.
7. Anderson, John D., Jr. *Fundamental of Aerodynamics*, 2nd Edition, McGraw-Hill Book Company, New York, 2001.
8. Hayden Kenneth L., "Aircraft Wing Construction", United States Patents Office, Patent Number 2,056,188, 1936.

9. Sarh, Branko, “Convertible fixed wing aircraft”, United States Patents Office, Patent Number 4,986,493, 1990.
10. David E. Gevers, Gevers Aircraft, Inc., “Multi-Purpose Aircraft”, United States Patents Office, Patent Number 5,645,250, July 1997.
11. J. Lin, and D. Cadogan, J. Huang and V. Alfonso Feria, “An Inflatable Microstrip Reflectarray Concept for Ka-Band Applications,” AIAA Paper No. 2000-1831, 41st AIAA/ASME/ASCE/AHS/ASC Structures, Structural Dynamics, and Materials Conference & Exhibit, April 3-6, 2000, Atlanta, Georgia.
12. J.E. Murrray, J.W., Pahle, S.V. Thorton, S. Vogus, T. Frackowlak, J.D. Mello, and B. Norton, “Ground and Flight Evaluation of a Small-Scale-Winged Aircraft”, AIAA Paper No. 2002-0820, AIAA Aerospace Sciences Meeting & Exhibit 40th, Reno, NV, Jan. 14-17, 2001.
13. Benson, Tom, “Wright Brothers’ Wing Warping,” NASA Glenn Research Center,
14. Max M. Munk, “Note on the relative Effect of the Dihedral and the Sweep Back of Airplane Wings”, NACA TN 177, 1924
15. Busemann, A., “Aerodynamic Lift at Supersonic Speeds”, Ae. Techl. 1201, Rep. No. 2844 (British A.R.C., February 3, 1937), Bd. 12, Nr. 6, October 3, 1935, pp. 210-220
16. Robert L. Perry, “Variable Sweep: A Case History of Multiple Re-Innovation,” the Rand Corporation, California, 1966

17. John E. Lamar, "A Theoretical Study of the Effect of Pivot Location on the Aerodynamic-Center Movement of Variable-Sweep Wings in Compressible Flow", NASA TN D-4635, Langley Research Center

18. Laurence K. Loftin. Jr. *Quest for Performance: The Evolution of Modern Aircraft*.

19. www.worldhistory.com/wiki/G/General-Dynamics-F-111.htm

20. www.worldhistory.com/wiki/B/B-1-Lancer.htm

21. www.fas.org/nuke/guide/usa/bomber/b-1b.htm

22. www.worldhistory.com/wiki/F/F-14-Tomcat.htm

23. www.fas.org/man/dod-101/sys/ac/f-14.htm

24. http://arc.cs.odu.edu:8080/dp9/getrecord/oai_dc/1974343677/oai:inf.cs.cmu.edu:pub/168/495900

25. H. Abbott and Albert E. Von Doenhoff, *Theory of Wing Sections*, 2nd Edition, Dover, New York, 1959

26. www.zenithair.com/stolch801/design/design.html

27. Sheryll Goecke Powers and Lannie D. Webb, "Flight Wing Surface Pressure and Boundary-Layer Data Report from the F-111 Smooth Variable-Camber Supercritical Mission Adaptive Wing", NASA Technical Memorandum 4789, June 1997.

28. Ed Pendleton, Denis Bessette, Pete Field, Gerry Miller, and Kenneth Griffin, "The Active Aeroelastic Wing Flight Research Program - Technical program and model analytical development", AIAA Paper No. 1998-1972, AIAA/ASME/ASCE/AHS/ASC Structures, Structural Dynamics, and

Materials Conference and Exhibit, 39th, and AIAA/ASME/AHS Adaptive Structures Forum, Long Beach, CA, Apr. 20-23, 1998, Collection of Technical Papers. Pt. 4 (A98-25247 06-39)

29. P. Scott Zink, Dimitri N. Mavris, Peter M. Flick, Michael H. Love, “Impact of Active Aeroelastic Wing Technology on Wing Geometry Using Response Surface Methodology”, presented at CEAS/ AIAA/ ICASE/ NASA Langley International Forum on Aeroelasticity and Structural Dynamics, Williamsburg, VA, June 1999.
30. Richard V. Whitney, “Goodyear's Inflatoplane and Project Wagmight”, AAHS Journal, V/ol. 45, No. 2 - Summer 2000.
31. J. E. Murray, J. W. Pahle, S. V. Thornton, S. Vogus, T. Frackowiak, J. D. Mello, and B. Norton. “Ground and flight evaluation of a small-scale inflatable-winged aircraft”, AIAA Paper No. 2002-0820, AIAA Aerospace Sciences Meeting & Exhibit, 40th, Reno, NV, Jan. 14-17, 2002
32. Albert George Fischer, “Semi-rigid aircraft wing”, US patent 3,987,984, October 1976.
33. Griggs Robinson Post Henderson and Smith, LLP, “Extendable/Retractable Airfoil Assembly for Fixed Wong Aircraft”, International Patent Application Number PCT/US98/07103, Filed in April 1998.
34. “Telescopic Wing Tips”, United States Patents Office, Patent Number 2,056,188
35. D. Cadogan, W. Graham and T. Smith, ILC Dover Inc., Frederica, DE ; “Inflatable and Rigidizable Wings for Unmanned Aerial Vehicles”, AIAA

Paper No. 2003-6630, 2nd AIAA "Unmanned Unlimited" Conf. and Workshop & Exhibit

36. Beer, Ferdinand P. Johnston, E. Russel, Jr., *Mechanics of Materials*, Second Edition, McGraw-Hill Book Company, 1992, pg 191, 423 - 424.
37. T. D. Burton, *Introduction to Dynamic Systems Analysis*, McGraw-Hill Book Company, 1994, pg 85-87.
38. X-Foil Program, Released under GNU General Public License; Mark Drela, MIT Department of Aeronautics and Astronautics.
39. ERGO-HELP, Inc. 2466 E. Oakton St., Arlington Heights, IL 60005
40. J. Blondeau, J. Richeson and D. Pines; “Design of a Morphing Aspect Ratio Wing Using an Inflatable Telescoping Spar”, AIAA Paper No. 2003-1718, 44th AIAA/ASME/ASCE/AHS/ASC Structures, Structural Dynamics, and Materials Conference.
41. J. Blondeau and D. Pines; “Wind Tunnel Testing of a Morphing Aspect Ratio Wing Using an Pneumatic Telescoping Spar”, AIAA Paper No. 2003-6659, 2nd AIAA "Unmanned Unlimited" Conf. and Workshop & Exhibit.
42. J. Bae, T. Seigler, D. Inman, I. Lee, “Aerodynamic and Aeroelastic Considerations of a Variable-Span Morphing Wing”. AIAA Paper 2004-1726 45th AIAA/ASME/ASCE/AHS/ ASC Structures, Structural Dynamics & Materials Conference